Improving performance of catalysts for water electrolysis

The MnOx case

Frydendal, Rasmus

Publication date:
2015

Document Version
Publisher's PDF, also known as Version of record

Improving performance of catalysts for water electrolysis: *The MnO_x case*

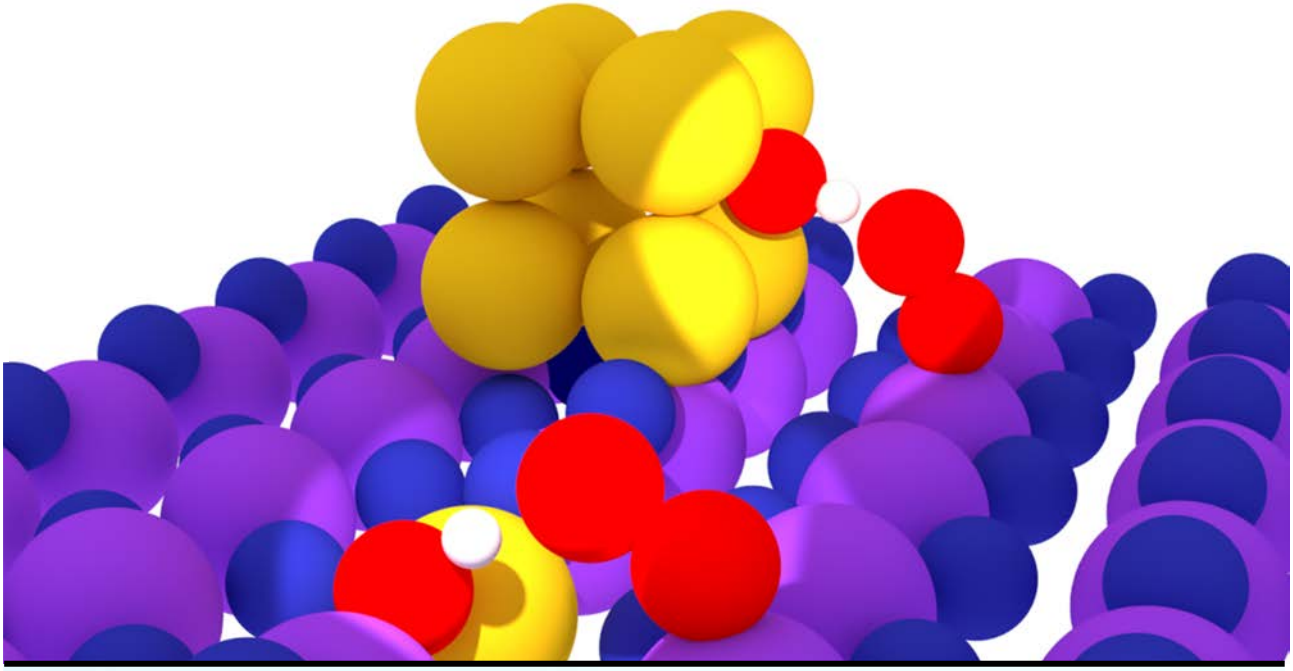

Rasmus Frydendal
Department of Physics
Technical University of Denmark
August 2015

Improving performance of catalysts for water electrolysis: The MnO_x case

Ph.D. dissertation by

Rasmus Frydendal

Supervisor: Professor Ib Chorkendorff
Co-supervisor: Associate Professor Ifan E. L. Stephens

August 2015

Center for Individual Nanoparticle Functionality
Department of Physics
Technical University of Denmark

Front image
An atomic model of how gold atoms (the yellow spheres) and active Mn sites (purple spheres) can interact in stabilizing *OOH (O are the red spheres and H the white) on the surface, during oxygen evolution reaction. Such an interaction could lead to a higher efficiency of hydrogen producing devices.

Preface

This thesis is submitted in partial fulfillment of the requirements for the Ph.D. degree from the Technical University of Denmark (DTU). The work was accomplished at the Department of Physics and the Center for Individual Nanoparticle Functionality (CINF) under the supervision of Prof. Ib Chorkendorff and Associate Prof. Ifan E. L. Stephens. CINF is funded by the Danish Research Foundation, which is greatly acknowledged. The work presented herein was carried out between August 2012 and August 2015.

First of all, I would like to express my gratitude towards my supervisors for granting me the possibility to work in such a great and inspiring environment. I thank you both for your support, general guidance and many suggestions that motivated me throughout this project. Furthermore, I would also like to thank all my colleagues at CINF and the former Catalysis for Sustainable Energy (CASE). It has truly been a fantastic time and three years where I have had the chance to learn so much from all of you. In particular the persons I was lucky enough to work with deserves a special thanks: Björn Wickman, Anders Nierhoff, Katarzyna Janik, Mathilde Raad Lilliedal, Paolo Malacrida, Dowon Bae, Bastian Mei, Anastasia Permyakova, Brian Seger, Jacqueline McAnulty, Federico Masini, Mauro Malizia, Jan Rossmeisl, Michael Busch and Niels Halck. Robert Jensen and Kenneth Nielsen have also been invaluable with their knowledgeable help. Furthermore, Brian Knudsen have throughout my project been a loyal companion in the office and I have always appreciated the useful and useless discussions about everything and nothing. In the later part of the project I have had the pleasure of working more closely with Arnau Verdaguer-Casadevall in what I hope will be a long and exciting adventure. So far it has certainly been a great experience.

A part of the project was spent at the Chemical Engineering Department, Stanford University, a visit supervised by Prof. Thomas F. Jaramillo. I am very grateful for the chance of visiting this highly competent and friendly research group. In particular I would like thank both Linsey Seitz and Thomas Jaramillo

for being great and welcoming hosts.

The luck I have had at work is nevertheless surpassed by my luck in meeting Elisa. You have been a fantastic colleague but continues to be an even more amazing girlfriend. Thank you for all your help and ideas in both the project and later thesis writing, a contribution which can not be overestimated. I can think of nothing better than travelling the world with you in search of new places and things to discover.

Finally, I would like to thank my family for always being immensely supportive and for creating such a happy and peaceful place back on Fyn. Going there always provided me with new energy that I could bring to my workplace.

Kongens Lyngby, 28^{th} July 2015
Rasmus Frydendal

Abstract

This Ph.D. thesis presents work on non-noble metal oxide catalysts for the oxygen evolution reaction, OER. This reaction is currently a bottleneck in electrolyzer technologies, which are promising for energy storage purposes. In particular, Polymer Electrolyte Membrane, PEM, cells are attractive for decentralised hydrogen stations. PEM electrolyzers rely on scarce noble metals to achieve high efficiency and durability, which limits the scalability of the technology. Finding new catalysts for OER is therefore a thriving research field with new materials being reported frequently.

However, many of these new reports include little information about stability, which is evaluated solely from short term electrochemical testing. The first part of this project was therefore dedicated to designing a meaningful stability protocol. Manganese oxide thin films were prepared with sputter deposition and the stability was evaluated with Electrochemical Quartz Crystal Microbalance measurements combined with Inductively Coupled Plasma - Mass Spectrometry. The results showed that a stable electrochemical performance can be achieved, while a constant mass loss is occurring. The proposed protocol can guide future research efforts in evaluating novel materials for the OER.

Unfortunately, most non-noble metal based OER catalysts reported to this date work in alkaline solutions, where cheap NiFe electrodes are already utilized in commercial systems. For acidic media, relevant for the acidic membrane in PEM electrolyzers, there is a lack of strategies aimed at designing catalysts without noble metals. It turns out that MnO_2 is a stable material in the OER relevant potential range in acid. In this project, MnO_2 thin films were therefore prepared to evaluate their usefulness for PEM electrolyzers. Anodic dissolution of MnO_2 was found to be an issue and a strategy is presented for stabilizing the surface. From density functional theory calculations it was found that titanium could segregate to surface sites prone to dissolution. Thus, MnO_2 thin films were modified with titanium using a reactive co-sputtering method and tested in acid. The results indicate that the stability could be improved with more

than 40 %, while the activity decreased with 10 %.

Finally, for MnO_2 to be useful as an OER catalyst in PEM cells, the activity should be improved. Mixtures of manganese oxide and gold have been reported to exhibit activity enhancements and, hence, a final part of the thesis focus on this system. Mixed thin films were prepared, which exhibited five times higher current density compared to pure Mn oxides. X-ray Diffraction measurements indicated that Au domains of approximately 3 nm were important for this enhancement. Furthermore, from an in-situ X-ray Absorption Spectroscopy study it was found that Mn oxidises at a more cathodic potential when Au is nearby. This experimental study serves as a starting point for understanding the beneficial interaction between gold and manganese oxides.

Dansk Resumé

Denne Ph.D. afhandling præsenterer ny forskning indenfor metaloxid katalysatorer til elektrokemisk oxygen udvikling, OER. Denne reaktion er en flaskehals for elektrolyse, der er en lovende teknologi til energilagring. Især er Polymer Electrolyte Membrane, PEM, systemer attraktive for decentraliseret hydrogen produktion. Disse systemer bruger ædelmetaller for at opnå høj effektivitet og holdbarhed, hvilket begrænser deres skalerbarhed. Jagten på nye katalysatorer til denne reaktion er derfor et vigtigt forskningsområde og nye materialer bliver publiceret hyppigt.

Mange af disse nye materialer er dog ikke testet for stabilitet, udover kortsigtet elektrokemisk karakterisering. Første part af dette projekt er derfor dedikeret til at designe en meningsfuld protokol til at teste stabilitet. Mangan oxid tyndfilm blev deponeret med sputter deposition og stabiliteten testet med Electrochemical Quartz Crystal Microbalance kombineret med Inductively Coupled Plasma - Mass Spectrometry. Resultaterne viste at stabil elektrokemisk ydeevne kunne opnås samtidig med at et konstant massetab fandt sted. Den foreslåede protokol kan guide fremtidige evalueringer af nye katalysatorer til oxygen udvikling.

Blandt nye katalysatorer til OER, der ikke er baseret på ædelmetaller, virker langt de fleste og bedste kun i basiske opløsninger, hvor billige NiFe katalysatorer allerede bliver brugt kommercielt. I syre, relevant for PEM celler, er der en mangel på strategier til at finde stabile og billige materialer. Her er MnO_2 et unikt materiale, idet det er stabilt og aktivt i et OER relevant potentialevindue. I dette projekt testes MnO_2 derfor som OER katalysator i syre. Instabilitet ved høje anodiske potentialer er et problem og derfor udvikledes en strategi for stabilisering af dette materiale. Ved brug af density functional theory blev det fundet at titanium kan migrere til de overfladepositioner der er mest ustabile. Derfor modificeredes MnO_2 med titanium ved hjælp af en co-sputtering metode og disse tyndfilm blev testet i svovlsyre. Resultaterne viste at massetabet kunne sænkes med mere end 40 %, imens aktiviteten faldt med kun 10 %.

For at MnO_2 kan bruges som OER katalysator i PEM elektrolysesystemer skal aktiveten også forbedres. Mangan oxid blandet med guld har vist sig at give store aktivitetsforbedringer og derfor omhandler den sidste del af projektet disse blandinger. Mangan oxid og guld blev co-deponeret og en femdobling af strømdensiteten kunne opnås. Ved Røntgendiffraktion blev det fundet at 3 nm store gulddomæner har stor betydning for aktivitetsforbedringen. Endvidere blev in-situ Røntgenabsorption brugt til at karakterisere oxidationstrin for Mn i tyndfilmene. Det viste sig at Mn oxideres ved mere katodiske potentialer når Au er til stede. Disse studier udgør et solidt udgangspunnkt for bedre forståelse af interaktionen mellem guld og mangan oxid.

List of publications

Appended Publications

Paper I

Benchmarking the Stability of Oxygen Evolution Reaction Catalysts: The Importance of Monitoring Mass Losses
Rasmus Frydendal, Elisa A. Paoli, Brian P. Knudsen, Björn Wickman, Paolo Malacrida, Ifan E.L. Stephens, Ib Chorkendorff
ChemElectroChem, 2014, Volume **1**, pages 2075-2081

Paper II

Enhancing Activity for the Oxygen Evolution Reaction: the Beneficial Interaction of Au with Mn and Co Oxides
Rasmus Frydendal, Michael Busch, Niels B. Halck, Elisa A. Paoli, Peter Krtil, Ib Chorkendorff, Jan Rossmeisl
ChemCatChem, 2014, Volume **7**, pages 149-154

Paper III

Toward an active and stable catalyst for oxygen evolution in acidic media: Ti-stabilized MnO_2
Rasmus Frydendal, Elisa A. Paoli, Ib Chorkendorff, Jan Rossmeisl, Ifan E.L. Stephens
Accepted for publication in Advanced Energy Materials

Paper IV

In-situ investigation of Au-MnO_x thin films with improved activity for the oxygen evolution reaction
Rasmus Frydendal, Linsey Seitz, Dimosthenis Sokaras, Tsu-Chien Weng, Dennis Nordlund, Ib Chorkendorff, Ifan E.L. Stephens, Thomas F. Jaramillo
In preparation

Other publications - not appended

Paper V

Iron-Treated NiO as a Highly Transparent p-Type Protection Layer for Efficient Si-Based Photoanodes
Bastian Mei*, Anastasia A. Permyakova*, Rasmus Frydendal*, Dowon Bae, Thomas Pedersen, Paolo Malacrida, Ole Hansen, Ifan E.L. Stephens, Peter C. K. Vesborg, Brian Seger, Ib Chorkendorff
Journal of Physical Chemistry Letters, 2014, Volume **5**, pages 3456-3461
* These authors contributed equally to the manuscript.

Paper VI

Oxygen Evolution on Well-defined Mass-Selected Ru and RuO_2 Nanoparticles
Elisa A. Paoli, Federico Masini, Rasmus Frydendal, Davide Deiana, Christian Schlaup, Mauro Malizia, Thomas W. Hansen, Sebastian Horch, Ifan E.L. Stephens, Ib Chorkendorff
Chemical Science, 2014, Volume **6**, pages 190-196

Paper VII

Enabling direct H_2O_2 production through rational electrocatalyst design
Samira Siahrostami, Arnau Verdaguer-Casadevall, Mohammadreza Karamad, Davide Deiana, Paolo Malacrida, Björn Wickman, Maria Escudero-Escribano, Elisa A. Paoli, Rasmus Frydendal, Thomas W. Hansen, Ib Chorkendorff, Ifan E.L. Stephens, Jan Rossmeisl
Nature Materials, 2013, Volume **12**, pages 1137-1143

Paper VIII

Crystalline TiO_2: A Generic and Effective Electron Conducting Protection Layer for Photo-anodes and -Cathodes
Bastian Mei, Thomas Pedersen, Paolo Malacrida, Dowon Bae, Rasmus Frydendal, Ole Hansen, Peter C. K. Vesborg, Brian Seger, Ib Chorkendorff
The Journal of Physical Chemistry C, 2015, Volume **119**, pages 15019-15027

Paper IX

Fine-tuning the activity of oxygen evolution catalysts: The effect of oxidation pretreatment on size-selected Ru nanoparticles
Elisa Antares Paoli, Federico Masini, Rasmus Frydendal, Davide Deiana, Paolo Malacrida, Thomas W. Hansen, Ib Chorkendorff, Ifan E.L. Stephens
Submitted, 2015

List of Acronyms

ALD ..... Atomic Layer Deposition

BCE ..... Before Common Era (same as BC - Before Christ)

CAES ..... Compressed Air Energy Storage

CE ..... Common era (same as AD - Anno Domani)

DSA ..... Dimensionally Stable Anodes

DFT ..... Density Functional Theory

EIA ..... U.S. Energy Information Administration

EQCM .... Electrochemical Quartz Crystal Microscopy

EROI ..... Energy Return Of (Energy) Invested

ETP (2DS) Energy Technologies Perspective (2 degrees scenario)

EWG ..... Energy Watch Group - organization

EXAFS ... Extended X-ray Absorption Fine Structure

GGA ..... Generalized Gradient Approximation

Gt ..... Gigaton

HER ..... Hydrogen Evolution Reaction

HHV ..... Higher Heating Value

HOR ..... Hydrogen Oxidation Reaction

ICP-MS .. Inductively Coupled Plasma - Mass Spectroscopy

IEA ..... International Energy Agency

LHV ..... Lower Heating Value

Mbd ..... Million barrels (oil) per day

Mtoe ..... Million ton oil equivalent

NP ..... NanoParticle

OECD .... Organisation for Economic Co-operation and Development

OER ..... Oxygen Evolution Reaction

OPEC .... Organization of the Petroleum Exporting Countries

ORR ..... Oxygen Reduction Reaction

PEM ..... Polymer Electrolyte Membrane (also Proton Exchange Membrane)

PHS ..... Pumped Hydropower Storage

QCM ..... Quartz Crystal Microbalance

RDE ..... Rotating Disk Electrode

RHE ..... Reversible Hydrogen Electrode

RPBE .... Revised Perdew-Burke-Ernzerhof

RRDE .... Rotating Ring Disk Electrode

SEM ..... Scanning Electron Microscopy

STM ..... Scanning Tunneling Microscopy

T&D ..... Transmission and Distribution

TEM ..... Transmission Electron Microscopy

TWh ..... Terawatt hour

UHV ..... Ultra High Vacuum

WEO ..... World Energy Outlook

XPS ..... X-ray Photoelectron Spectroscopy

XRD ..... X-ray Diffraction

XAS ..... X-ray Absorption Spectroscopy

XANES ... X-ray Absorption Near Edge Spectroscopy

Contents

Chapter 1

Introduction

The aim of this thesis is to investigate new electro-catalysts for the oxygen evolution reaction, which is key to improve the feasibility of water electrolysis. Water electrolysis in turn holds great potential as a technology for storing electrical energy as a chemical. This brief "bottom-up" motivation is meaningful for researchers in the field, however, for others it may be of greater interest to know why electrochemical production of hydrogen is relevant in the bigger scope of things. In the following I will therefore attempt a top-down motivation to why the world needs energy storage technologies. As a starting point for the introduction, the current energy landscape will be presented along with the global distribution of resources. The challenge of future energy demand is then discussed and finally energy storage will be introduced.

1.1 A world divided in energy

In the last decades, energy related issues, such as finite fossil fuel resources and climate changes, have lead to serious debates among the world's policy makers. Excellent examples are the Conference of the Parties, COP, sessions of the UN Framework Convention on Climate Change, which have been held since the mid 90's all around the world. In these sessions the worlds leaders aim to set an ambitious framework for the future emission of green house gasses, which are closely related to how each country produces its energy. Unfortunately, it has proven extremely difficult to reach binding agreements between the parties, despite the fact that most leaders seem aware of the urgency of the situation.

However, it is perhaps not so surprising that it is difficult to reach agreements when comparing the distribution of population to distribution of energy consumption in the world. The distribution of population is illustrated in figure 1.1, which shows a map of the world where every country size is normalized to the size of its population.

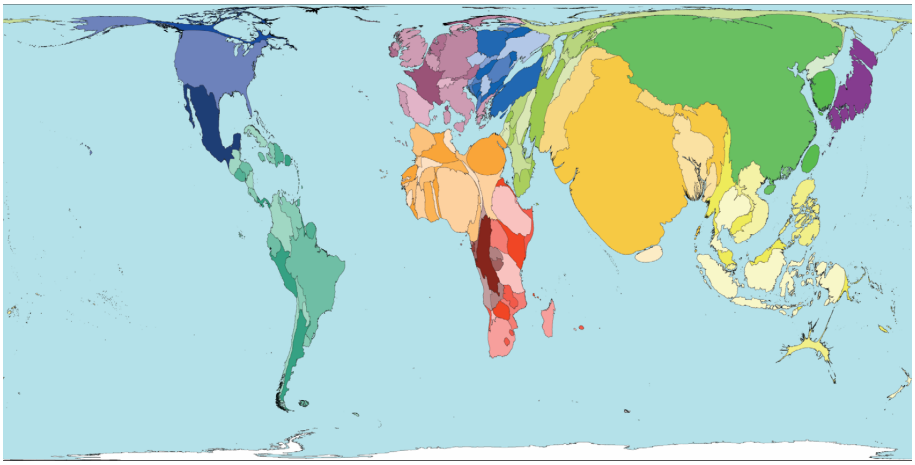

Figure 1.1: Map of the world where each country size is proportional to its population. Taken from [1].

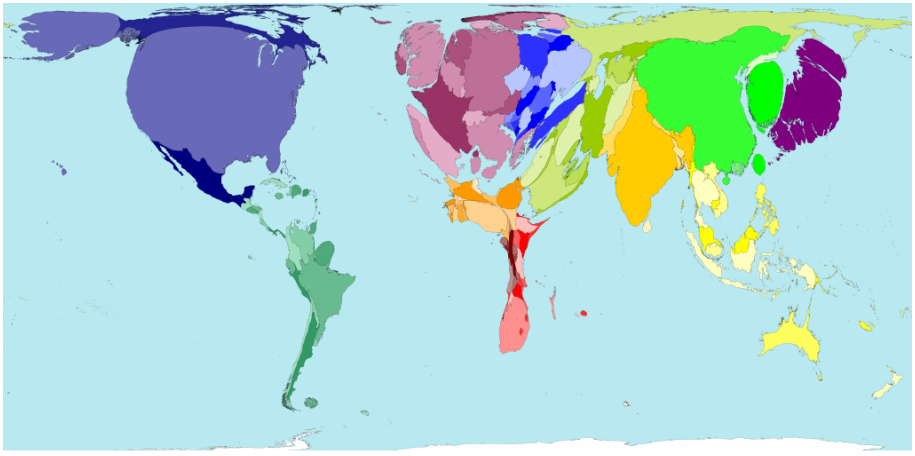

Figure 1.2: Map of the world where each country size is proportional to its fuel consumption. Taken from [1].

From the population distribution it is clear that countries such as China and India contain a disproportionate amount of people compared to the geographic area. In comparison to this map, an illustration of fuel consumption distribution, figure 1.2, shows that the amount of energy spent throughout the world is markedly different from the distribution of people. In the fuel consumption map the US is approximately the size of India and China combined and the European region is significantly larger than South America and Africa where very little energy is consumed. The effect of this skewed energy/population ratio can also be seen from figure 1.3, where a measure of living standard, the Human Development Index, is plotted for a selection of countries as function of the electricity consumption per capita.

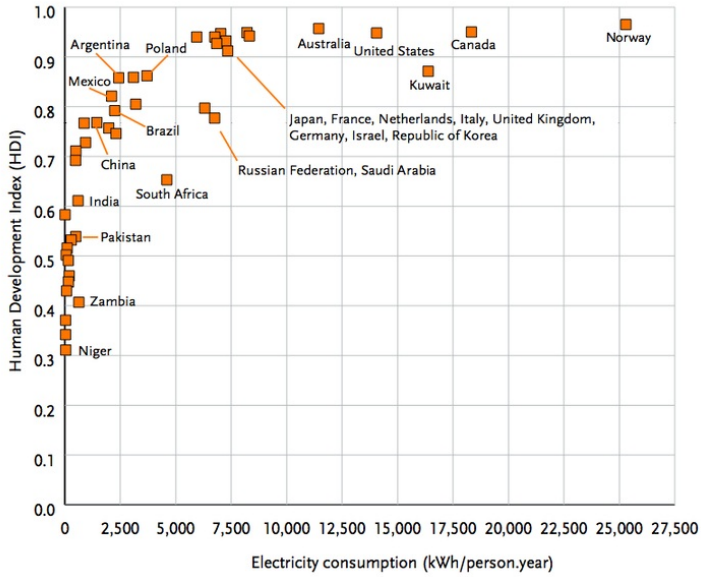

Figure 1.3: Plot of the Human Development Index, HPI, as function of electricity consumption per person per year. The HPI is a measure of living standards. Figure taken from [2]

Although the data from figure 1.3 is from 2005, the difference in energy consumption is astonishing. More recent data from the BP Statistical Review of World Energy 2015 [3] is shown in figure 1.4, where consumption per capita of oil, natural gas and coal is shown for the US, China and India in year 2013. From this data, the US consumes more than three times as much energy per capita as China, who in turn consumes more than four times as much as India. Understandingly, countries with very low living standards wish to improve their situation; the world energy consumption is therefore bound to increase.

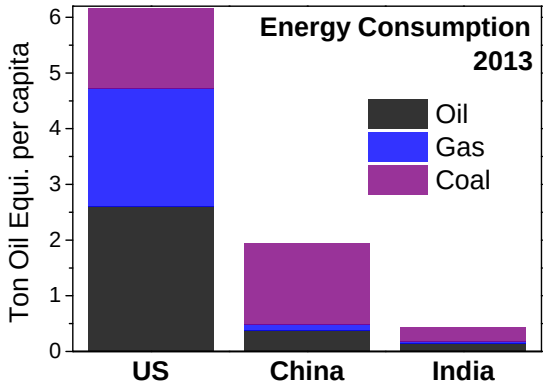

Figure 1.4: Bar plot of the energy consumption per capita from US, China and India. Only the three major fuels, oil, gas and coal are included. Numbers are from [3].

As a thought experiment, let's assume India and China would reach the living standard of the US and consume the same amount of energy per capita. The increase in energy consumption for this scenario would correspond to almost 13000 Mtoe/year (million ton oil equivalent) or equivalent of the total primary energy consumption of the whole world in 2013. While this example is rather extreme, it certainly shows that these highly populated countries have a lot of catching up to do, in terms of living standards, growth of economy and therefore in energy consumption. The increasing oil consumption among these countries is also evident from recent historic consumption data from BP Statistical review of the world 2015 [3], which is shown in figure 1.5.

The oil consumption for Asia Pacific, Africa and the middle east is clearly increasing. Specifically for Asia Pacific, the consumption went from 13 Mbd (million barrels per day) to 30.8 Mbd in the period of 1989 to 2014, equivalent of 236 % increase in 25 years. In the same period the combined consumption in North America and Europe & Eurasia actually decreased slightly. This is naturally only valid for oil which does not give the full picture. For all regions the consumption of natural gas has increased since 1989, however, with Asia Pacific approximately tripling their consumption. Furthermore, coal consumption has gone down in Europe, stagnated in North America and more than doubled in Asia Pacific.

The above examples and graphs highlight the fact that energy is closely linked to economic growth and living standards and that developing countries will consume a lot more energy in the years to come. So far the population growth has not been taken into account. From a historic perspective the human population has been growing slowly for many years and even in the period 4000 before common era, BCE, to 1000 common era, CE, the population only doubled ap-

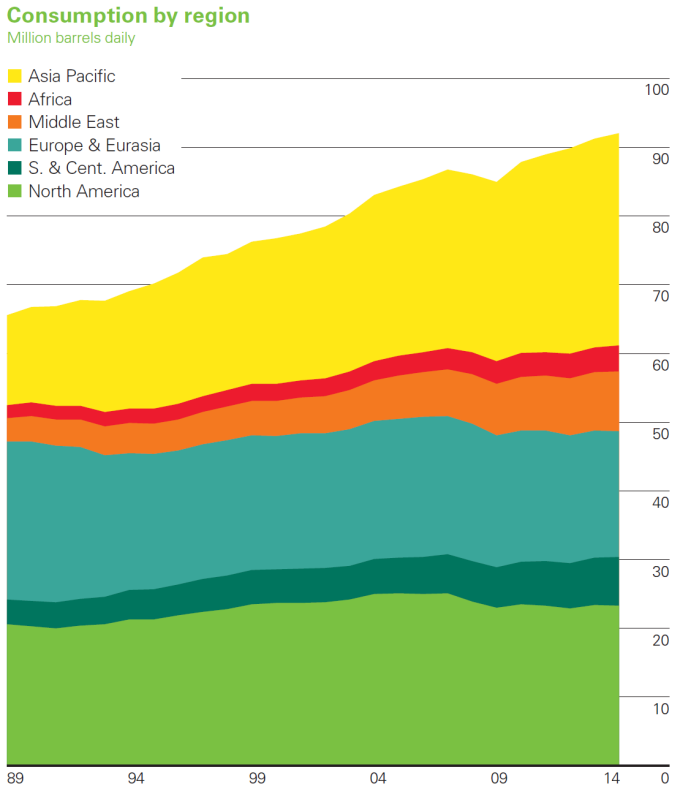

Figure 1.5: The worlds oil consumption divided in regions, plotted from 1989 to 2014. Figure taken from [3].

proximately every thousand years. It was not until the 17th century and the industrial revolution that the growth accelerated dramatically and between year 1600 and 1800 the population doubled so that 1 billion people lived on the earth simultaneously. Between year 1900 and 2000 the population more than tripled. Recent development of the human population can be seen in figure 1.6, where both population numbers and annual growth rates are plotted.

The annual growth rate can be expected to remain positive until around 2070. However, before then it is most likely that we will reach around 10 billion people. The increase in population means that more energy is required to provide for approximately an extra China and India. Provided the new population require what corresponds to the energy consumed in the US per capita, we can add another 13000 Mtoe to the consumption. Energy forecasters expect that world energy consumption will increase with an average annual rate of 1.1 % up until

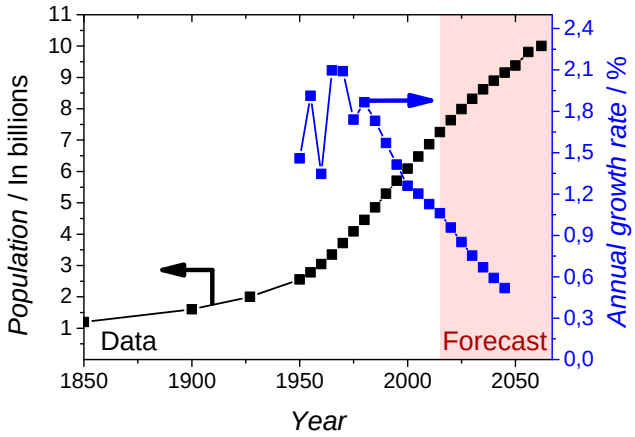

Figure 1.6: A plot of the world population (in black) and annual growth rates (in blue) from 1850 to 2062. The numbers from 2015 and 2062 are forecasts. Data taken from [4].

2040, which corresponds to an increase of 37 % from 2014 [5]. Although the exact numbers from such forecasts can vary dramatically, it is certain that we will need to produce significantly more energy in the coming decades.
The question is how this vast amount of energy will be provided. The numbers presented here has so far been in Mtoe, which can seem somewhat arbitrary. As an example of the magnitudes, one of the largest wind turbines ever built is the Vestas V-164 which can deliver 8 MW. If this turbine was to run with 8 MW as power output non-stop for a year it would produce 0.006 Mtoe. The windmills in Denmark deliver between 25 and 30 % of the nominal power as electricity averaged over a year [6]. In other words, 13000 Mtoe/year consumption could be covered with approximately 7.3 mio. 8 MW wind turbines, assuming the deliver 30 % of the nominal power. Note that the world currently has an installed wind power capacity of around 370 GW [7], or what corresponds to about 46000 8 MW turbines.
In 2014 oil, natural gas and coal resources provided 86 % of the worlds primary energy consumption. Is it possible for these traditional resources to fill the gap? In the energy sector there is still optimism regarding this prospect, however, it should be noted that forecasting the production and predicting the fossil fuel reserves are not straightforward tasks. This is illustrated in 1.7a and b.
In figure 1.7a oil production forecasts from three annual reports of the US Energy Information Administration, EIA, are plotted. It is evident that the actual production in 2010 was lower than predicted and in the latest report the expectations for 2020 and 2025 have decreased significantly since 2004. In figure 1.7b the so called proven reserves are taken from BP Statistical Review of World

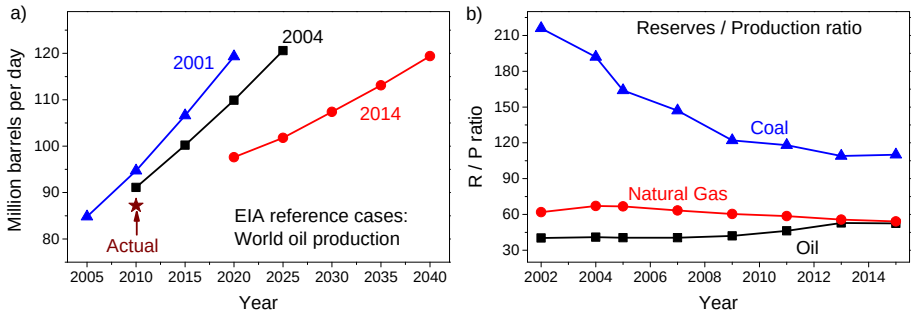

Figure 1.7: a) Forecasts of the worlds oil production from the US Energy Information Administration, EIA. In blue is their forecast from 2001, in black from 2004 and in red from 2014. Based on [5, 8, 9] b) Reserves/production ratios for the three major fuels in the period 2002 to 2014. Based on statistics from [3, 10–16].

Energy annual reports. Especially for the coal reserves there is a drastic change in the evaluation from 2002 to 2014. The predictions also vary significantly dependent on the source, exemplified in figure 1.8 showing the forecast from Energy Watch Group, EWG, a non-profit organization of scientists.

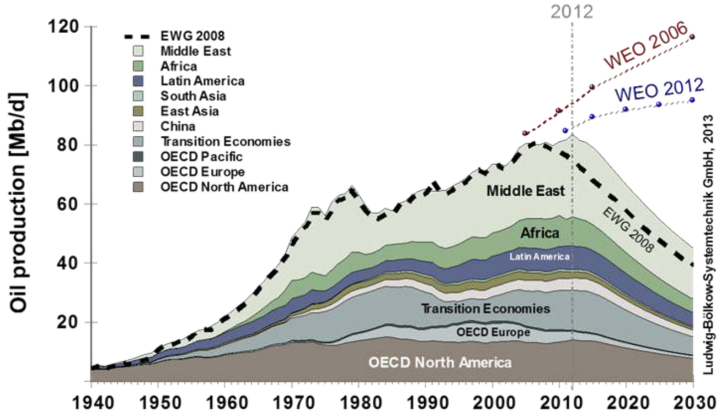

Figure 1.8: World oil production from 1940 to 2030, divided into regions. The number from 2012 are predictions. The dashed black line represents the scenario predicted by the Energy Watch Group in 2008. The red dotted line represents the International Energy Agency's outlook from 2006 and the blue dotted line their outlook from 2012. Figure taken from [17].

The forecast from EWG in 2013 clearly shows a different picture than the one from EIA and in their view the global oil production should decrease already

from this year. So the question about whether the traditional energy sources can cover our future energy demand is certainly not an easy one to answer. Much of the optimism regarding new oil exploration is further complicated by the locations and extraction methods necessary to make it profitable. In recent years the "fracking miracle" in the US has been put under scrutiny and independent researchers claim that the future production levels from some of the new US tight oil and shale gas sites are grossly overestimated [18]. While these sites are certainly rich in resources, the total cost of extraction is difficult to assess. From an environmental point of view, hydraulic fracturing and horizontal drilling are highly controversial methods, requiring large amounts of water and chemicals. The methods may, among other effects, cause significant contamination of water supply as well as air pollution [19]. From an economic point of view, the energy return on (energy) invested, EROI, for tight oil and shale gas resources are far lower than for the more traditional oil wells. EROI is a ratio of how much a unit of input energy will return as output [20]. This ratio must be above 1 for any feasible process, regardless of market value of the product. The decreasing EROI for oil is partly due to the "easy oil first" approach, but also to the technical advances over time allowing for oil to be found and extracted almost anywhere. In figure 1.9 EROI ratios are shown for the different resources.

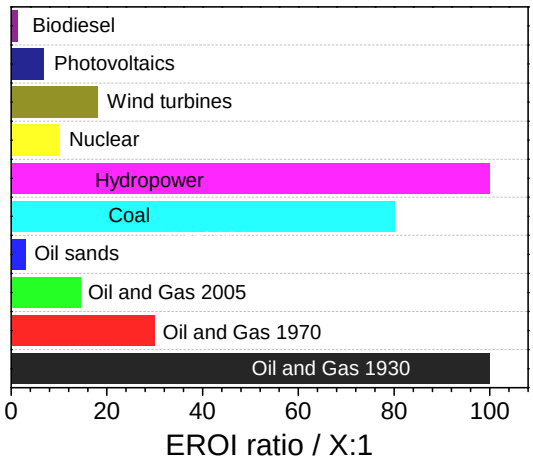

Figure 1.9: A bar plot of calculated Energy Return on (Energy) Invested, EROI, for various energy sources. The EROI numbers are taken from [21].

These values are taken from Murphy and Hall (2010) [21] but as the authors note, EROI ratios are complex and can vary significantly dependent on the research group or organization behind the calculation. However, it is clear that the energy return for oil and gas has decreased over time and is now approaching the values found for wind turbines. In fact, the more recently discovered

tight oil sites may have EROI ratios lower than 5. This is a huge shift from the traditional oil wells where the EROI ratios could exceed 100. From the EROI analyses and forecasts from energy agencies a picture is emerging. The traditional resources might still be plentiful, but the expected rates of production may become a limiting factor. As established earlier, the world's energy demand is increasing and for this reason alone it is vital that the renewable resources are exploited to a much larger degree than they currently are. The second major driver for increasing energy production from renewables is the environmental impact of burning fossil fuels, which have lead to unprecedented high levels of CO_2 in the atmosphere. The climate change discussion has a lot of momentum these years and there are numerous reports predicting the consequences of the ever increasing CO_2 emissions [22–25]. Although the full effect of the emissions is impossible to predict with our current knowledge, it is certainly a risky experiment we are carrying out on "laboratory earth". An interesting example from the International Energy Agency, IEA, is shown in figure 1.10, where the global CO_2 emissions from the energy sector are plotted together with an evaluation of a so called global carbon budget. The background for this model is a scenario which takes into account recent pledges from dominant countries and the carbon budget is evaluated as the amount of CO_2 we can emit while only raising the global temperature with 2 °C by 2050 [26]. According to that model we will have spent the budget in 2040 where the emissions of CO_2 are not even expected to peak.

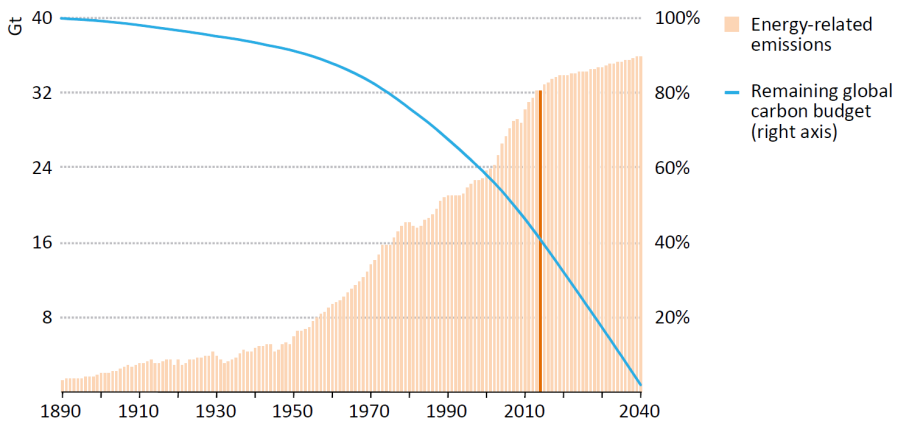

Figure 1.10: CO_2 emissions in Gt in the period 1890 to 2040, shown as bars and on the left axis. The blue line and the right side axis represents remaining global carbon budget from a scenario based on recent pledges from the worlds policy makers. Numbers from 2014 are predictions. Figure from [26].

1.2 The renewables - what is the challenge?

As mentioned above, 86 % of the worlds primary energy consumption in 2014 was provided by the traditional fossil fuel resources, oil, natural gas and coal. The remaining 14 % consists of nuclear, hydro and other renewables. The other renewable resources include wind, solar, geothermal and biomass which combined provide 2.5 % of the worlds primary energy [3]. The big question is whether it is possibly to increase this value significantly. In 2014 an estimated 250 billion US dollars were invested globally in renewable energy sources, of which photovoltaics and onshore windturbines received the most [27]. While this investment seems a staggering amount, the installed renewables are not likely to meet the targets of the 2 °C plan from IEA, which aim for 10225 TWh power generated in 2025 from renewables, an increase of approximately 100 % compared to 2013 [27]. Many countries are still struggling with making large integration of renewables feasible and it is clear that regional and national subsidy schemes are key to further implementation. However, one aspect is the market and public willingness to invest in these technologies, another is to evaluate the potential power reserve available. As mentioned above for oil, gas and coal the reserves are investigated yearly but are not considered to be very accurate. For renewables the ultimate reserve is the highly useful fusion generator located approximately 150 billion meters above us, a star known as the Sun. In fact, on earth we receive approximately 170000 TW of radiation from the sun, of which close to a third is reflected back [28]. Assuming we can harvest that energy with 10 % efficiency, we would have to cover approximately 0.016 % of the earth's land surface with solar panels to produce 20 TW [28]. It is also worth noting that solar and wind power are potentially much more distributed resources compared to fossil fuels. With widespread installation of wind turbines and solar panels it is possible that the future energy landscape will contribute to a markedly different and more equal political environment, compared to today.

A key factor to consider is the intermittent nature of solar and wind power, which can not be turned on and off in the same manner as fossil fuel based plants. When the sun shines or the wind blows power generation is possible, but when it is dark or there is no wind there is nothing to gain from these sources. This intermittency is exemplified in figure 1.11, where Danish electricity demand and wind power generation is shown for a two-week period in May 2015. The demand fluctuates between 2.5 and 4.7 GW, but the wind power fluctuates between close to zero and 4 GW. There are also times when the wind power generation exceeds the demand, which means the excess power must be exported. Denmark has an ambitious plan to expand the electricity generation from wind power up to 50 % of the national consumption. In 2014 a new record level was reached, where 39.1 % of the national electricity consumption was covered by wind turbines [29]. In figure 1.11 an example is given for doubling the wind power production. With such a doubling there are longer periods where the wind power exceeds the

demand, but there are still periods where the wind power is far from enough.

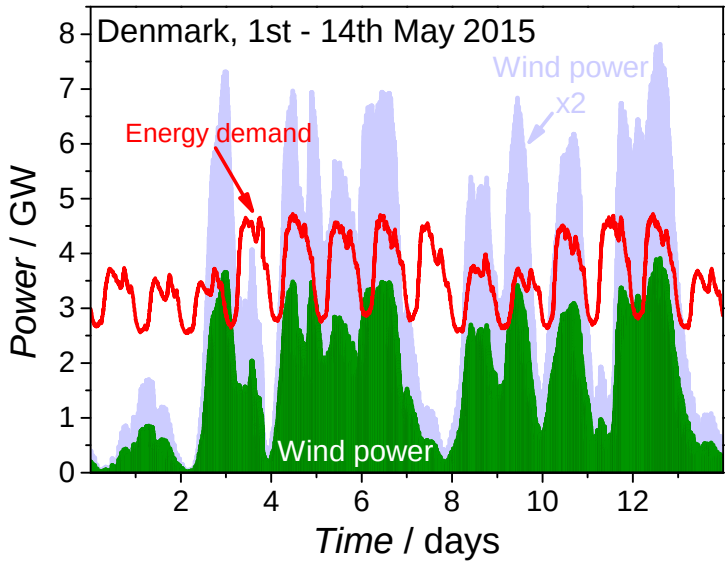

Figure 1.11: Energy demand, red line, and wind power production, in green, for a two week period in January 2014, Denmark. In shaded blue, the doubled wind power production is shown. Data from [30].

Integration of a significant amount of renewables in the energy infrastructure will put the electricity grid under a high degree of stress. The existing fossil fuel power plants will have to accommodate for the fluctuating sources, which could lead to lower efficiencies due to non-optimal operation. A way to mitigate this is to dramatically increase the export and import options so that larger regions can share the load. However, there is no guarantee that southern Europe will import electricity every time northern Europe experience periods of wind and vice versa. Smart grids are also expected to alleviate some of the problems with fluctuating power supply by turning electricity demanding utilities into intelligent components of the grid. Essentially these utilities will follow the electricity supply and spend energy when there is excess (cheap) electricity and be on stand by when there is low (expensive) supply [31]. However, for the smart grids to make a significant impact energy storage technologies must be implemented. For example, the IEA expects energy storage technology capacity to reach 8 % of the total power generation capacity in 2050, under their ETP 2DS proposal [32]. Among these technologies are: pumped hydropower, flywheels, batteries, thermal storage, supercapacitors and hydrogen production with electrolysis. Hydrogen production with electrolysis presents a promising technology, where electricity is used to produce a chemical which can be stored

and used for power generation. The advantages of electrolysis are high energy density, quick response times, zero carbon footprint and potential use in large scale [33]. In figure 1.12 a comparison of the various energy storage technologies can be seen, based on power scale and discharge duration. Hydrogen production can cover large scale operation and are suited for response and discharge in a dynamic range between hours and whole seasons.

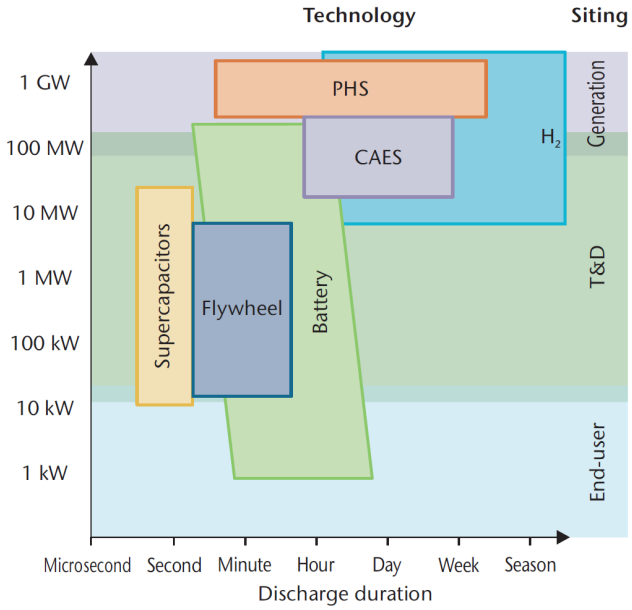

Figure 1.12: An overview graph showing various energy storage technologies. The comparison is based on the power scale as function of discharge duration. The power scale is divided into three main applications, end-user, transmission and distribution (T&D) and generation. Other technologies included on this chart are Supercapacitors, Flywheel, Battery, Pumped Hydro Storage (PHS) and Compressed Air Energy Storage (CAES). Figure taken from [32].

Furthermore, a major advantage for hydrogen production is the option of generating a high value fuel which can be used in the transport sector. With small scale fuel cell systems the hydrogen can be converted into electrical energy in cars, trucks or boats. Hydrogen is also used as a feedstock in various chemical processes and is already produced at a large scale. Currently, most of this hydrogen is made from methane and only 8 GW of electrolysis is currently installed worldwide [34]. Therefore, a shift to electrolysis for hydrogen production has an extremely large potential for reducing CO_2 emissions as well as providing energy storage and sustainable fuels for the future energy infrastructure. In the following section an introduction to electrolyzers will be presented.

1.3 Electrolyzer technologies

An electrolyzer is a device made for splitting water into hydrogen and oxygen by electrochemical means. Water splitting is an endothermic reaction so energy is required for it to proceed. In an electrolyzer this energy is supplied as an electrical current passed through the electrochemical cell. A simple schematic of an electrolyzer cell can be seen in figure 1.13. The electrolyzer as a device is then a series of these cells connected to deliver the rate of hydrogen needed. In acidic electrolyte, water is oxidised into oxygen and solvated protons at the anode. The protons are then conducted through the electrolyte (can be an ion conducting membrane) and reduced to form hydrogen gas at the cathode. The necessary inputs are therefore water and electricity. The potential applied per cell determines the efficiency.

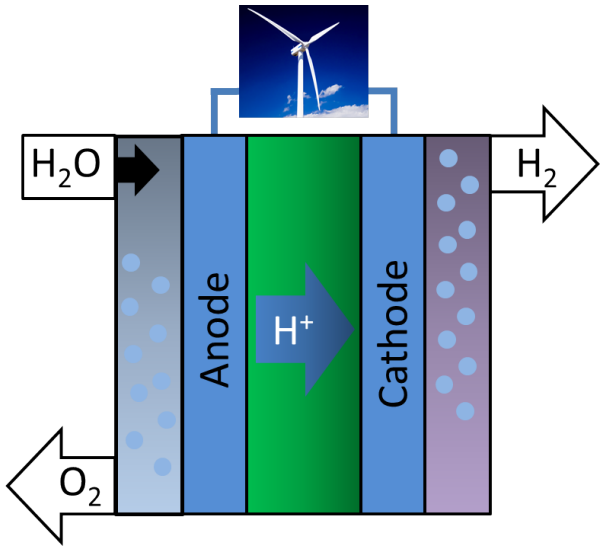

Figure 1.13: In a Polymer Exchange Membrane cell, the electrolyte is a proton conducting membrane. In electrolysis mode water is oxidised at the anode, generating oxygen gas and protons. The protons are then transferred through the electrolyte to the cathode where they are reduced to form hydrogen gas.

The existing electrolyzer technologies are divided by the type of electrolyte being used. The electrolyte is a key component, providing ionic conductivity while being electronically insulating. Traditionally, alkaline electrolytes have been used for this purpose and in particular concentrated potassium hydroxide. This type of electrolyzer was the first to be commercially available and can deliver stable performance up to 15 years with efficiencies in the range of 40-80 % [32,35]. The advantages of this technology lie in their technological maturity and the

cheap materials that can be used as catalysts. A more elaborate description of these catalysts will be given in section 2.5. Both for the anode and cathode Ni based materials can be used as electrodes in alkaline systems. At this point it should be noted that while the potential necessary for driving the reaction at the oxygen electrode is approximately the same in alkaline and acid, the hydrogen electrode requires a larger driving force or overpotential in alkaline compared to acid electrolyte [36].

In contrast to the alkaline based cells, the Polymer Electrolyte Membrane cells, known as PEM cells, utilize a solid membrane, based on a proton conducting sulfonated teflon polymer. This type of membrane was originally developed by Dupont in the 1960's and is known as Nafion®. Today, many other brands exist, offering similar membranes with great performance and stability. Using this type of membrane allows for very thin (Membrane Electrode Assembly down to 0.5 mm [37]) but mechanically stable electrochemical cells leading to a highly compact electrolyzer design [38]. Furthermore, the superior ionic conductivity enables high current densities and low operation temperature facilitates fast start up times [39]. In figure 1.14 a comparison between the performances of the traditional alkaline electrolyzer and a PEM electrolyzer can be seen. They are compared on the basis of efficiency as function of the current density.

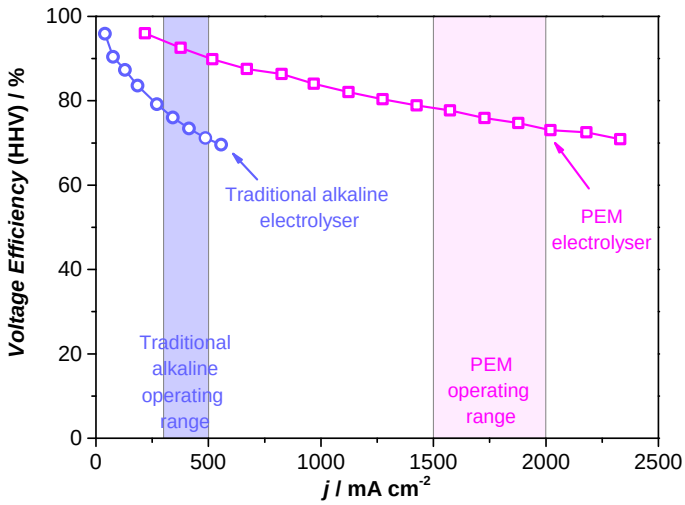

Figure 1.14: Figure showing the operational ranges of two types of electrolyzers. The voltage efficiency is plotted as function of the current density. For traditional alkaline electrolyzers an efficiency between 70 and 80 % means operating between 250 and 500 mA/cm^2. Conversely, the PEM electrolyzer can operate in the same efficiency range with current densities between 1500 and 2000 mA/cm^2. Data for this figure has been adapted from [39].

It is evident that while both can deliver high efficiency (>80 %), the PEM electrolyzers can do so at currents approximately four times higher. Other advantages are a simple gas separation due to the solid electrolyte and purity of hydrogen and oxygen produced [39]. The high current densities in PEM cells represent a big advantage over the alkaline systems, since very compact systems can handle a large power range without compromising the efficiency. With more compact systems the cost of other system components becomes lower. A disadvantage of PEM cells is that the acidic environment limits the number of stable materials that can be used. Currently only noble metal based materials are used as electrocatalysts. Not only does this increase the price of the overall system, it significantly limits the scalability due to the scarcity of these elements. As an example of that, the IEA estimated that 8 % storage capacity should be installed by 2050, as mentioned above. For 12.5 TW of power generation this means 1 TW storage. For 1 TW of PEM electrolysis approximately 10 years of annual production of iridium would be needed and half a year of annual platinum production just for the electrocatalysts, based on state of the art electrolyzers reported by Debe *et al.* [40, 41]. These estimations show that a search for alternative and abundant catalysts could have a huge impact on the commercialisation of the technology.

Solid alkaline membranes have emerged as a possible alternative to PEM, which exhibit some of the advantages from the acidic counterpart [42]. They can be fabricated very thin and therefore allow for the same type of cell design. At the same time the alkaline environment means that the selection of electrode materials are less constrained and abundant elements could be utilized [42]. However, they conduct OH^- with a larger resistivity than PEM and currently the stability and performance in the long term are not satisfactory. Finally, solid oxide cells operating at high temperature (higher than 600 °C) have been proposed for large scale electrolysis offering high efficiencies [43, 44]. This technology is still in its early stage and it is difficult to assess the potential. The high temperature leads longer time for start up and greater fabrication costs, however, there are advantages in fuel diversity and higher tolerance towards fuel impurities.

1.4 Thesis Outline

The overall focus of this thesis is to investigate alternative catalysts for the oxygen evolution reaction. Here I will present and discuss the main findings of the project.

Chapter 2 will be used for setting the scene in terms of explaining concepts of catalysis and water splitting. Naturally this thesis is build upon a massive amount of research done in the field over decades and this is useful to keep in mind. The most important findings from the literature will therefore be highlighted and discussed.

Chapter 3 encompasses experimental methods that have been used throughout this work. A small introduction to each method will be given along with how it has been employed here.

Chapter 4 represents the first main project. In the field of oxygen evolution new catalysts are reported rapidly but there is often a lack of tests dedicated to investigating mass loss processes. The aim of this chapter is to highlight the importance of stability testing for electrocatalysts. Here a viable test protocol is presented and used for a MnO_x thin film catalyst.

Chapter 5 introduces a new strategy for stabilization of a non-noble metal oxygen evolution electrocatalyst. The goal is to operate this catalyst in acidic environment, where currently only noble metal oxides can be used. As mentioned earlier in the introduction, the scale up of PEM electrolyzers suffers from the expensive and scarce materials used as catalysts for oxygen evolution. Our stabilization strategy is based on blocking the sites responsible for dissolution and this is tested experimentally for titanium modified MnO_2, prepared with reactive sputter deposition.

Chapter 6 addresses activity improvements for gold modified MnO_2 as catalyst for the oxygen evolution reaction. On a conceptual basis, reasons for activity enhancements reported in the literature are discussed and recent Density Functional Theory calculations are briefly introduced. From an experimental approach co-deposited Au-MnO_x thin films are characterized electrochemically and with in-situ X-ray Absorption Spectroscopy. A particular focus is put on the valency of Mn under reaction conditions when gold is present.

Chapter 7 presents the main conclusions described in the previous chapters and finally, a small outlook section finalizes this thesis.

The main papers and manuscripts produced during this project are appended after the bibliography.

Chapter 2

Electrocatalysis and the splitting of water

Electrocatalysis can be described as the study of catalysing reactions taking place at the interface between an electrode and an electrolyte. Already from this general and simple description it is evident that the field is highly interdisciplinary and so one must be familiar with both surface science and physical chemistry. The ultimate goal of electrocatalysis is to optimize the rate of electrochemical reactions by a careful choice of electrode material [45]. In water electrolysis, the electrochemical generation of hydrogen and oxygen occurs at such electrodes and their catalytic properties directly affect the efficiency of the process. This chapter serves as an introduction to the catalysis of water electrolysis. Special attention will be given to the oxygen evolution reaction and the development of finding catalysts for that reaction until now.

2.1 What is a catalyst?

Before describing the field of electrocatalysis, it is useful to have a definition of a catalyst. A catalyst increases the rate of a chemical reaction by providing a surface where the reactants can bind and react to form products with a lower energy barrier or activation energy [46]. This phenomenon is illustrated in figure 2.1, where "red-black" and "red-red" reacts to form "red-red-black". In gas or liquid phase the reaction proceeds slowly due to a high energy barrier despite the fact that the product has a lower free energy. This is shown in the diagram to the right in figure 2.1 as the blue curve. The slow rate is due to a short-lived

transition state that has a low probability of being formed. If, however, the reactants bind to a suitable catalytic surface, intermediates are stabilized and can react with lower energy barriers, shown as the red curve.

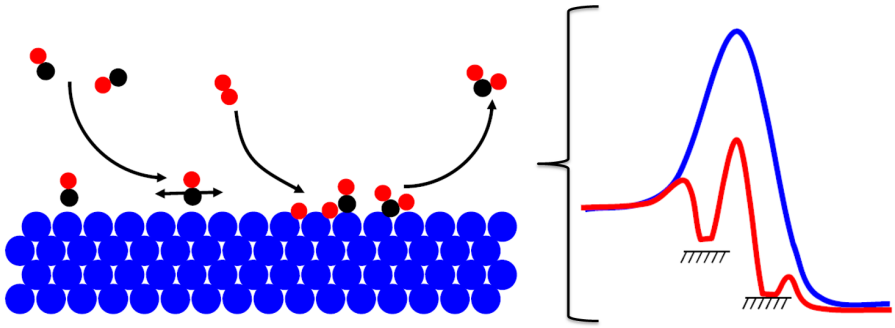

Figure 2.1: A cartoon depicting how catalysis works. The blue surface works to facilitate binding of reactants and intermediates, which can then break and form bonds. The overall energy barrier for the reaction can be lowered by the use of such catalytic surfaces. Notice that this simple explanatory figure is not appropriate for electrocatalysis, where the reactions can only proceed on electrode surfaces. However, the nature of the surface interaction is equally important.

As a result, the reaction can proceed at faster rates or the same rate can be achieved with less energy input. Thermal catalysis provides an intuitive example where the energy input is temperature. A new catalyst that decreases the operating temperature can make a chemical process much cheaper and a chemical plant (more) profitable. This simple explanation highlights the importance of catalysts and gives an impression of how they work. It is the binding of reactants, intermediates and products to the catalyst surface that lowers the energy barriers. However, any given surface that binds these species is not necessarily a good catalyst. In fact, it is crucial that the binding is balanced. This concept is famously described by the Nobel prize winner Paul Sabatier, who stated that the interactions between a catalyst and the reactants should be "just right" [47]. If the interaction is too weak reactants will not bind to the surface and no reaction takes place. If the interaction is too strong either reactants or products block the catalyst surface, causing little or no reaction to proceed. This concept has been demonstrated for many reactions and an example is shown in figure 2.2 with catalysts for electrochemical hydrogen evolution. In this example the energy of hydrogen adsorption is used as descriptor and the activity has a clear optimum [48, 49].
The left part of figure 2.2 shows Parson's attempt to quantify and understand the theoretical basis of the hydrogen evolution reaction, HER, from 1958 [48]. He found that i_0, exchange current density used to indicate catalyst activity,

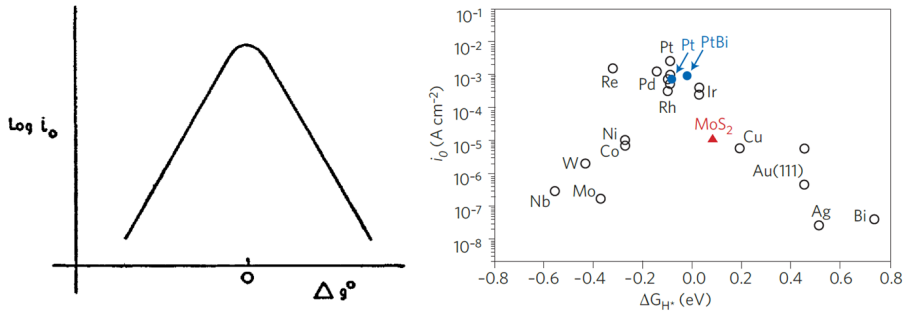

Figure 2.2: Figures showing the correlation between binding energy and rate of reaction for Hydrogen Evolution. In the left figure from [48] predicted exchange current density for hydrogen evolution is plotted as function of the heat of formation for hydrogen adsorption. In the figure to the right from [49], experimental values of exchange current densities for hydrogen evolution on various metals are plotted as function of calculated hydrogen binding energies.

should be maximised when the heat of formation for hydrogen on a catalyst surface is zero. To the right in figure 2.2 a much later work by Nørskov and co-workers shows that the hydrogen adsorption energy is a reasonably good descriptor despite the fact that some of the surfaces in the study oxidise under reaction conditions [49]. It also turns out that platinum is the best catalyst. Plots of catalyst activity as a function of one or more descriptors are also called a volcano plots. In the field of catalysis volcano shaped activity plots are used extensively and identifying a suitable descriptor for a reaction can be seen as the first step towards solid understanding and design principles.

2.2 Thermodynamics of electrode reactions

In electrocatalysis, the primary energy input is the potential difference over two electrodes, ΔU. Electrochemical reactions include the transfer of electrons between the electrode and reactants and the rate of this transfer can be tuned with ΔU. The electrodes are immersed in an electrolyte which provides ionic conductivity, due to a high concentration of protons or hydroxide ions. Furthermore, electrochemical reactions are reduction-oxidation, redox, reactions. They can always be divided into two half reactions, each proceeding at their respective electrode. The electrode at which oxidation of a reactant occurs is called the anode, whereas the electrode where a reduction occurs is called the cathode. The change in Gibbs free energy of formation for a reaction, ΔG_f, determines the equilibrium potential, U_{cell}, for a given electrochemical cell, consisting of two electronically connected electrodes immersed in an electrolyte.

This is formulated in equation 2.1 [50].

$$U_{cell} = \frac{-\Delta G_f}{nF} \tag{2.1}$$

where U_{cell} is the equilibrium potential also called reversible open circuit potential of the cell, F is the Faraday constant (96485 C/mol) and n the number of electrons transferred in the reaction. While this equation holds at standard conditions, the change in Gibbs free energy for a reaction vary with temperature and pressure. This variation can be calculated for the general reaction $jJ + kK \rightarrow mM$ as

$$\Delta G_f = \Delta G_f^0 - RT \ln(\frac{a_J^j \cdot a_K^k}{a_M^m}) \tag{2.2}$$

where ΔG_f^0 is the change in Gibbs free energy at standard conditions, R the gas constant, T the temperature and a denotes reactant activity; $a = \frac{P}{P_0}$. P is partial pressure and P_0 the standard pressure, 1 atm. Combining equation 2.1 and 2.2 gives the Nernst equation which relates the reversible open circuit potential to temperature and pressure (equation 2.3).

$$U_{cell} = U_{cell}^0 - \frac{RT}{nF} \ln(\frac{a_J^j \cdot a_K^k}{a_M^m}) \tag{2.3}$$

With these equations it is possible to evaluate the minimum potential difference needed to run a non-spontaneous reaction in an electrochemical cell, or similarly the maximum potential difference generated by a spontaneous reaction. However, the actual operating potentials, ΔU of such cells are typically significantly different from U_{cell}. The components of the operating voltage are the following:

$$\Delta U = U_{cell} \pm \eta \pm \Delta U_\Omega \pm \Delta U_t \tag{2.4}$$

In equation 2.4 "$\pm$" should be "+" for power consuming cells where non-spontaneous reactions are driven, whereas "$-$" should be used for power generating cells. η denotes the overpotential needed to drive the reaction when current is flowing due to non-ideal kinetics at the electrode interface. ΔU_Ω is the loss of potential difference due to resistance losses in the system and finally ΔU_t is the potential increase or decrease over time. Electrocatalysis deals with decreasing η by finding the best suited electrode material. The theoretical relation between overpotential η and current j is described in the Butler-Volmer equation:

$$j = j_0 \Big[\exp \frac{(1-\alpha)nF\eta}{RT} - \exp \frac{\alpha nF\eta}{RT} \Big] \tag{2.5}$$

In equation 2.5 j_0 is the exchange current density and α is a symmetry factor. The exchange current density is a quantity that defines the current flowing

in both directions when a reaction is in equilibrium. From equation 2.5 it is evident that a high i_0 results in higher currents for a given η. It is also noteworthy that the current is exponentially dependent on overpotential, η. At high overpotentials one of the two exponentials in equation 2.12 becomes negligible and a simpler version can be formulated. In semilogarithmic form this version is known as Tafel lines. Briefly, Tafel slopes indicate the change in potential for a ten-fold increase in current. From this definition it is obvious that lower Tafel slopes are desirable. Traditionally, electrochemical experiments have been conducted with the aim of determining the Tafel slope of reactions on specific electrode materials. It is commonplace in the literature to use Tafel slopes to phenomenologically deduce a reaction mechanism [51]. However, this requires several loaded assumptions, including the value of a symmetry factor, an adsorption isotherm, etc. Consequently I chose not to use such an approach for this thesis.

2.3 Water splitting in electrolyzers

Electrolysis is a general term describing the process of driving a non-spontaneous electrochemical reaction by applying a potential over two electrodes. This is in contrast to a potential difference generated from a spontaneous electrochemical reaction like in the case of fuel cells. In water electrolysis hydrogen and oxygen gasses are generated from water.

$$2H_2O\ (\text{liquid}) \rightarrow 2H_2\ (\text{gas}) + O_2\ (\text{gas}) \tag{2.6}$$

This is an energy demanding reaction with a change in Gibbs free energy of 237.2 kJ/mol at standard conditions. If this is done in an electrochemical cell, an electrolyzer, a potential difference of 1.23 V is required at room temperature and standard pressure. As discussed above, for any significant current a higher potential has to be applied in terms of overpotential and resistance losses. The efficiency of such a process is typically defined from the change in enthalpy of the reaction. The enthalpy can be taken for either water as a liquid (higher heating value, HHV, equivalent of 1.48 V) or as a gas (lower heating value, LHV, equivalent of 1.25 V) [50].

$$\text{efficiency} = \frac{1.48V}{V_c} \tag{2.7}$$

where V_c is the cell voltage. Note that for electrolyzers using the HHV results in higher efficiencies while for fuels cells in lower. The overall reaction can be split into half reactions, formulated in 2.9 and 2.8 for an acidic electrolyte.

$$4H^+ + 4e^- \rightarrow 2H_2\ (\text{gas}) \quad \text{Hydrogen Evolution} \tag{2.8}$$

$$2H_2O\ (\text{liquid}) \rightarrow O_2\ (\text{gas}) + 4H^+ + 4e^- \quad \text{Oxygen Evolution} \tag{2.9}$$

These two half reactions will be treated more carefully in the following subsections.

2.4 Hydrogen Evolution

The electrolytic evolution of hydrogen gas is one of the most, if not the most, studied electrochemical reactions throughout the history of electrochemistry as a research field. In fact, fundamental studies on hydrogen evolution has helped shape the modern understanding of electrochemical processes. It is a rather simple two electron transfer process where protons are reduced to form molecular hydrogen. The overall reaction in acid can be written as:

$$2H^+ (aq) + 2e^- \rightarrow H_2 (gas) \tag{2.10}$$

The equilibrium potential of this reaction is 0 V using the conventional electrochemical potential scale. In acidic environment, the reaction can be further split up into the following reaction steps:

$$H^+ (aq) + e^- + * \rightarrow H^* \text{ (Volmer)} \tag{2.11}$$

$$2H^* \rightarrow H_2 (gas) + 2^* \text{ (Tafel)} \tag{2.12}$$

$$H^* + e^- + H^+ \rightarrow H_2 (gas) + * \text{ (Heyrovsky)} \tag{2.13}$$

While it is commonly accepted that the first step is the Volmer process, it has proven difficult to understand whether the Tafel or Heyrovsky mechanism dominates [52]. Studies from Markovic *et al.* have shown experimentally that the surface structure plays a large role in which mechanism dominates. The Tafel step takes place on Pt(110) and Heyrovsky on Pt(100) [53]. However, for polycrystalline surfaces it is difficult to assess experimentally through kinetic measurements alone [54]. Despite this ambiguity in the understanding of hydrogen evolution there is only one intermediate, which is adsorbed hydrogen, H^*. The binding between a surface and this intermediate has turned out to be an exceptionally good descriptor for identifying active catalysts [48, 49, 52, 55–57]. The best known catalyst for the reaction is platinum which can catalyse the reaction at negligible overpotentials. Work done by Neyerlin *et al.* shows that with overpotentials down to 50 mV a current density of more than 1 A/cm^2 can be reached even for a loading as low as $50\mu g_{Pt}/cm^2$ [58]. It should also be noted that hydrogen evolution is significantly faster in acid compared to alkaline. This was shown in a study by Sheng *et al.*, where systematic rotating disk electrode measurements were used to elucidate the differences between HER in acid and alkaline [36]. In alkaline the overpotential needed to reach around 1.5 A/cm^2 is at least 100 mV higher than the same reaction in acid. An overview of the

range of active catalysts available for HER can be found in figure 2.3a and b for both acid and alkaline electrolytes.

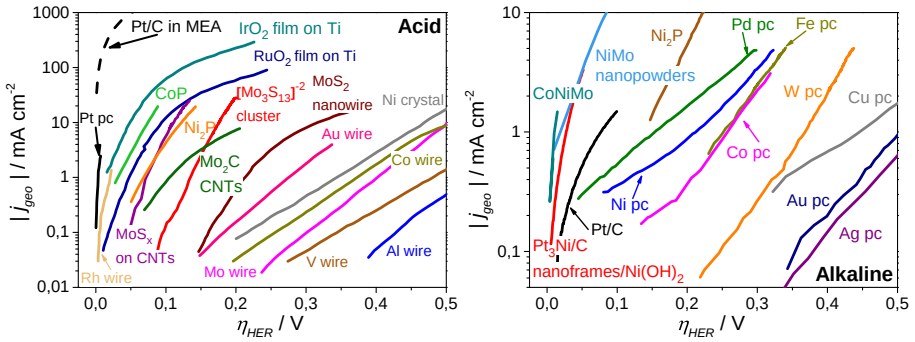

Figure 2.3: An overview of catalyst materials for HER. The logarithmic of the current density is plotted as function of overpotential. a) Catalysts tested in acidic solutions. Pt pc is from [36]. Pt/C in MEA is from [58]. IrO_2 and RuO_2 are films from [59]. CoP is from [60]. MoS_x on CNTs is from [61]. Ni_2P is from [62]. Mo_2C CNTs is from [63]. $[Mo_3S_13]^{-2}$ cluster is from [64]. MoS_2 nanowire is from [65]. Ni crystal is from [66]. Rh, Mo and Au wires are from [67]. Co, Cr and V wires are from [68]. Al wire is from [69]. b) Catalysts tested in alkaline solutions. CoNiMo is from [70]. NiMo nanopowders is from [71]. Pt/C and Pt_3Ni/C nanoframes/$Ni(OH)_2$ are from [72]. Ni_2P is from [62]. Pd pc, Ni pc, Fe pc, Co pc, W pc, Au pc, Ag pc and Cu pc are from [73].

2.5 Oxygen Evolution

Compared to HER the oxygen evolution reaction, OER, is more complex and involves several intermediates. As discussed in the previous section, the hydrogen electrode in an electrolyzer can run at appreciable current densities with lower than 50 mV overpotential using a very low amount of platinum. This is far from the situation at the oxygen electrode which imposes a large overpotential, more than 300 mV, at significant currents with a high loading of even the best catalysts. While 1.23 V_{RHE} is already highly oxidising, the substantial overpotential makes matters worse so that the selection of stable materials available for this electrode is rather narrow. For these reasons it has long been recognised as a great challenge in electrochemistry to find new active and stable catalysts for this reaction [74, 75]. In fact, a number of electrochemical processes besides water electrolysis depends on the oxygen evolution reaction including CO_2 and CO reduction, photoelectrochemical water splitting, electrowinning of metals and metal-air batteries. In this section an overview of the developments in the field of fundamental research for OER will be given.

The first attempts at understanding OER were made in the 1940's and 50's with, among others, Hickling [76], Rütschi [77] and later Bockris [78] reporting experiments with various electrode materials. The conclusions from the work of Hickling and Hill describe the difficulties in comparing the activities of different materials due to large variance in Tafel slope dependent on current density and measurement procedure. These issues are still haunting researchers today where the comparison of electrode materials from different groups is complicated by different preparation and experimental methods. Hickling and Hill tested twelve metals as anodes and for all of them substantial overpotentials were needed to drive the reaction. Some of these results can be seen in figure 2.4, where the overpotentials needed to reach 10 mA/cm^2 for seven electrode materials are shown.

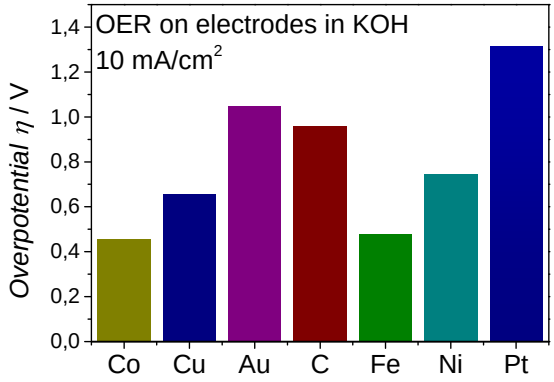

Figure 2.4: Comparison of overpotentials needed to drive 10 mA/cm^2 dependent on the choice of electrode material. The data is taken from [76] and represents one of the first attempts at systematically identifying a good catalyst for OER. The measurements were conducted at room temperature and in 1N KOH.

With the results from Hickling and Hill in 1946 the scene was set to understand why some metals were much more active than others. In the 1950's the first reports were therefore focused on plotting the activity as a function of various material properties such as lattice spacing or bond strength between metal and hydroxide ions, M-OH [77]. The latter descriptor was somewhat successful but it largely depended on the way the M-OH binding was calculated. However, it seemed evident that the interaction between an oxygen species and the metal was key to understanding the catalytic activity. In the 1960's, work by Winter [79], Boreskov [80] and Klier [81] added to the understanding of the metal-oxygen interaction, oxide to higher oxide formation and oxygen exchange on oxides. Nevertheless, it wasn't until 1980 that the knowledge of oxides was successfully combined with measurements of OER activity. This approach was famously

reported by Trasatti who constructed a volcano shaped activity plot based on the heat of transition from lower to higher oxide [82]. The impact of this report lies in the fact that oxide and not metallic properties are related to activity, which better reflect the electrode interface at the reaction conditions. At the same time the volcano plot suggests that an optimum at a specific formation energy exists so that experimentalists are provided with a design principle. In figure 2.5a reproduction of the analysis by Trasatti is shown, where the OER overpotential is plotted as a function of heat of transition from lower oxide to higher, ΔH_t^0.

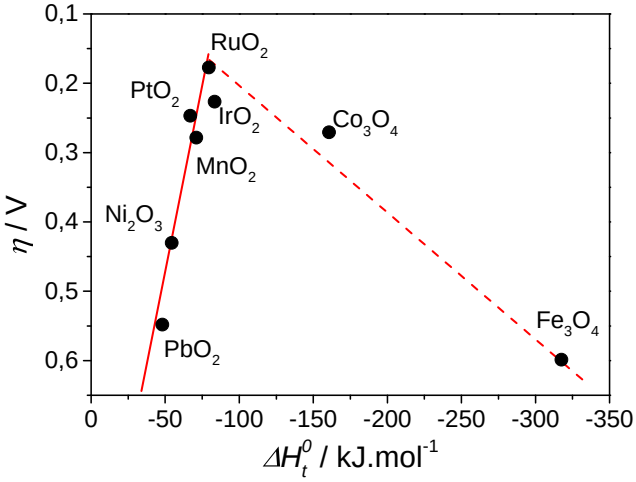

Figure 2.5: Volcano plot showing the overpotential for reaching approximately 1 mA/cm^2 for OER as a function of the heat of oxide transition ΔH_t^0. The data is digitized from [82] and only acidic measurements are included. Note that the for RuO_2, PtO_2, IrO_2, PbO_2 and MnO_2 the transition from III to IV oxidation state is considered, while for Ni_2O_3, Co_3O_4 and Fe_3O_4 the II to III. Furthermore, in the original volcano plot 1-3 values of overpotential are shown for each compound. For simplicity, only the overpotentials which fits the trend are shown here.

Later in the 1980's Bockris and Otagawa extended the understanding of oxides for OER by systematically investigating a series of perovskite materials based on Co, Fe, Ni and Mn [83]. A number of descriptors were investigated such as number of d-band electrons, heat of formation for the corresponding metal hydroxide, magnetic moment and stability limits.

In parallel with the scientific communities' efforts to understand the concepts behind OER activity, an important discovery had been made in one of the industrial research laboratories. Henry Beer had invented the so called Dimensionally Stable Anodes, DSA®, [45, 84], which were used with great success in the industrially important chlorine evolution process. The DSAs® were made

by thermal decomposition of metallic precursors on a titanium substrate, resulting in conductive mixed oxides. The active components of the oxides were Ru and Ir and they were mixed with Sn, Ta and Ti for better stability and selectivity. These electrodes were, as their name suggests, more stable under reaction conditions compared to the graphite anodes originally used for chlorine evolution. DSAs® also found use as OER electrodes, due to the high activity of Ru and Ir, and are still considered the state of the art for electrolysis in acidic environment [75, 85, 86].

2.5.1 Theoretical model for Oxygen evolution

These early reports have greatly inspired modern research efforts in describing the OER activity of metals and oxides. On the theoretical side developments in computational power and methodology have greatly aided the understanding of catalysis in general [49, 87]. For oxygen electrocatalysis a large step towards understanding oxygen reduction was reported by Nørskov and co-workers in 2004 [88]. They used a simple linear free energy model to relate the overpotential to the binding energies of intermediates. This model was later used to describe the OER on both metallic and oxide surfaces by Rossmeisl *et al.* [89, 90]. At this point it is useful to look into the reaction mechanism of OER. Several reaction mechanisms have been proposed but here we will consider one of the most common, which is also the one used in the free energy models. In acidic solution it can be written in the following way [89]. First a water molecule is dissociated into an adsorbed hydroxide and a solvated proton.

$$\mathrm{H_2O} + {}^* \rightarrow \mathrm{HO^*} + \mathrm{H^+} + \mathrm{e^-} \tag{2.14}$$

The hydroxide is further oxidised to adsorbed atomic oxygen.

$$\mathrm{HO^*} + \mathrm{H^+} + \mathrm{e^-} \rightarrow \mathrm{O^*} + 2(\mathrm{H^+} + \mathrm{e^-}) \tag{2.15}$$

From the adsorbed oxygen atom and a water molecule a superoxide, *OOH, can be formed

$$\mathrm{H_2O} + \mathrm{O^*} + 2(\mathrm{H^+} + \mathrm{e^-}) \rightarrow \mathrm{HOO^*} + 3(\mathrm{H^+} + \mathrm{e^-}) \tag{2.16}$$

Finally, molecular oxygen is formed and leaves the surface.

$$\mathrm{HOO^*} \rightarrow \mathrm{O_2(gas)} + 4(\mathrm{H^+} + \mathrm{e^-}) + {}^* \tag{2.17}$$

In these equations * denotes an active surface site. In alkaline environment the reaction mechanism looks slightly different but the intermediates are the same.

$$4\mathrm{OH^-} \rightarrow \mathrm{OH^*} + 3\mathrm{OH^-} + \mathrm{e^-} \tag{2.18}$$

$$\mathrm{OH^*} + 3\mathrm{OH^-} + \mathrm{e^-} \rightarrow \mathrm{O^*} + \mathrm{H_2O} + 2\mathrm{OH^-} + 2\mathrm{e^-} \tag{2.19}$$

$$O^* + H_2O + 2OH^- + 2e^- \rightarrow HOO^* + H_2O + OH^- + 3e^- \quad (2.20)$$

$$HOO^* + H_2O + OH^- + 3e^- \rightarrow O_2 + 2H_2O + 4e^- \quad (2.21)$$

The binding energies of the intermediates, O*, OH* and OOH* are central to the model put forward by Rossmeisl and co-workers. Using the quantum mechanical method Density Functional Theory, DFT, it is possible to calculate these energies on various surfaces such as metals and metal oxides. From the binding energies each step in the reaction mechanism can be evaluated and for a reaction step to be thermodynamically allowed the change in free energy should be zero or negative. When all steps are zero or downhill in energy the reaction can run at "significant" rates. The calculations are summarized in free energy diagrams as shown in figure 2.6, where a rutile (110) RuO_2 surface is used as catalytic surface.

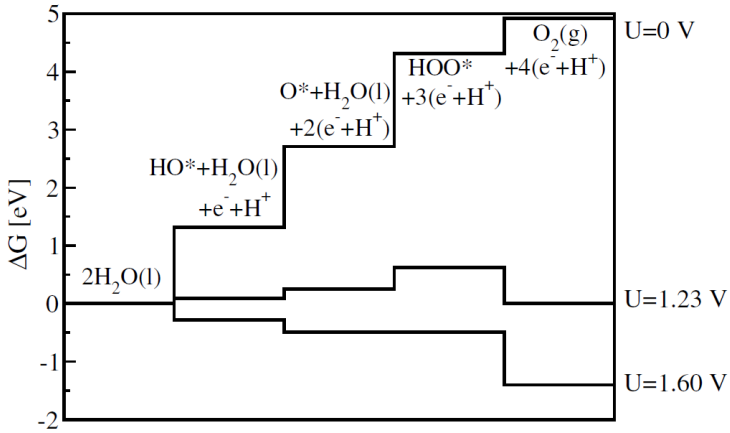

Figure 2.6: Free energy diagram for the oxygen evolution reaction based on the binding of intermediates to a rutile RuO_2 surface, shown for 0, 1.23 and 1.6 V. At the equilibrium potential, 1.23 V the first three steps are still not energetically favorable, which means that an extra overpotential is needed for the reaction to proceed at significant rates. Figure taken from [90].

The free energy profile of the reaction taking place at U= 0 V has all steps going uphill in energy and the final step is 4.92 V higher than the beginning. This value fits with the total energy needed to split water, which has so far been stated as 1.23 V per electron. When the potential is increased to 1.23 V it turns out that the energy profile is not flat, but instead three out of four steps are still uphill in energy. In fact, to get all steps flat or downhill it requires 1.60 V. For the ideal catalyst all steps would require 1.23 V to become flat. The

last step that becomes flat for RuO_2 is the third which includes the formation of $^*OOH$. For RuO_2 it was therefore concluded that the third step is potential determining, since the binding to $^*OOH$ is slightly too weak. It should be noted that energy barriers for each step are not directly taken into account. The thermodynamic analysis was also extended to predicting a volcano shaped activity plot based on a single descriptor, the binding to oxygen. This was justified based on the apparent correlation between binding energies for similar intermediates. Later it has been found that Brøndsted-Evans-Polanyi relations exists for the oxygen intermediates of OER on several surfaces, such as metals and oxides [91]. These relations correlate the energy of formation for transition states to the overall thermodynamic change in free energy of a reaction step [92, 93]. In other words, the energy barriers associated with a reaction can be described as a linear function of the change in free energy. With the DFT method and thermodynamic analysis in place a natural step forward was to extend the calculations to a large variety of materials. From such calculations universal scaling relations emerged [56,94–97]. Scaling relations provide a simple correlation between the binding energy of similar adsorbates independently from the surface. In this way the binding energies of $^*OH$ or $^*OOH$ are correlated to the binding energy of $^*O$. By averaging over a large number of oxides it was found that the adsorption energy of $^*OOH$, $\Delta E_{^*OOH}$, could be described as a function of $\Delta E_{^*OH}$ in the following equation:

$$\Delta E_{^*OOH} = \Delta E_{^*OH} + 3.2\,\text{eV} \tag{2.22}$$

Independently of the nature of the oxides there is a constant offset of 3.2 eV between step 1 (equation 2.14) and step 3 (equation 2.16) in the reaction mechanism. For the ideal catalyst this difference is 2.46 eV, since two electrons and protons are transferred from step 1 to 3. The discrepancy between the ideal catalyst and the best possible catalyst following these scaling relations is 0.74 eV or 0.37 eV per step which is close to the predicted overpotential of RuO_2. Notice that even though the offset is the same for all of the oxides it doesn't mean that they are all as good as RuO_2. The predicted overpotential of 0.37 V only results from optimal splitting of the 3.2 eV offset into two steps and therefore the 0.37 V is a minimum overpotential. For OER catalysis it is therefore seemingly impossible to find a simple surface with the ideal binding energies to all intermediates. This limitation is shown in figure 2.7, where the theoretically predicted overpotential is shown for various oxides as a function of a single descriptor [94]. The descriptor in this case is the difference in Gibbs free energy for $^*O$ and $^*OH$ adsorption. While these theoretically predicted overpotentials relate to a thermodynamic allowance of the reaction, the comparison to experimental current densities is not straightforward. However, the trends found from such analyses are in good agreement with experiments and, in fact, the overpotential needed to drive 10 mA/cm^2 on flat surfaces match to the theory within 100-200 mV for most materials [75, 94].

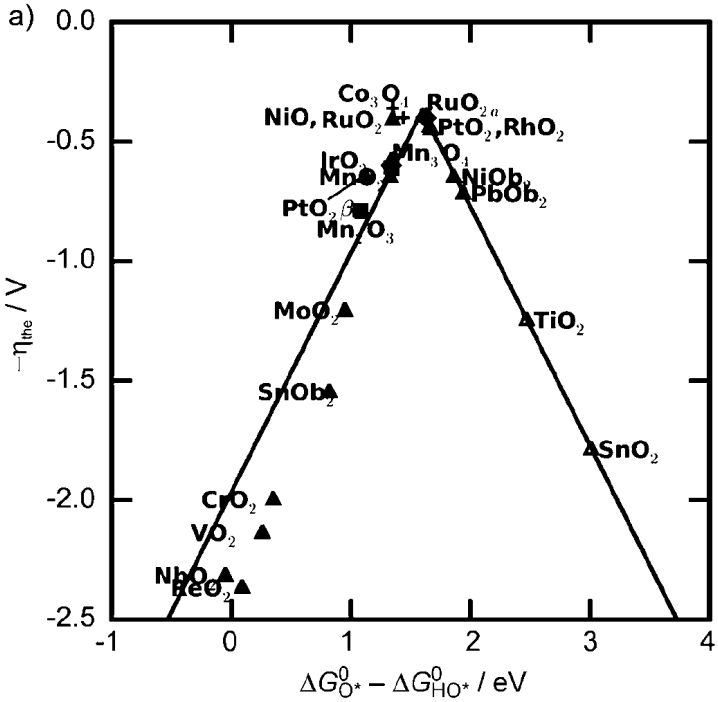

Figure 2.7: Volcano shaped activity plot for oxygen evolution on various oxide surfaces. The activity is shown as overpotential needed for all reaction steps to be downhill in energy, which is then plotted as function of the difference in free energy for step 1 and 3, $\Delta G^0_{O^*} - \Delta G^0_{HO^*}$. The points are calculated values for the indicated surfaces, while the solid lines are derived from scaling relations between the OER intermediates. The figure is from [98].

2.5.2 Recent experimental advances

With theory and experiments in good agreement, it is evident that RuO_2 is a unique catalyst for OER, which has been shown in several studies [40, 99–101]. Unfortunately, as it has been mentioned earlier, ruthenium is a scarce element produced as a by-product in platinum extraction. It is therefore problematic to use for technologies that are to be scaled up to the terawatt level [102]. At the same time the stability of RuO_x based electrodes have turned out to be unsatisfactory for long lifetime of electrolyzers and many commercial anodes for electrolysis instead use iridium or mixtures of the two [41, 103]. Iridium is even more scarce and therefore a search for alternative catalysts has long been the focus in the research field. The experimental progress can be divided into efforts aimed at acidic electrolytes and efforts aimed at alkaline electrolytes.

In acidic electrolyte, relevant for PEM cells, most experimental studies are focused on understanding and improving the noble metal oxides, RuO_x and IrO_x. In a study by Reier *et al.* Ru, Ir and Pt electrodes were studied for activity towards OER [100]. They paid special attention to the electrochemical active surface area which was determined by CO adsorption prior to activity measurement. Here it should be noted that addressing the electrochemical surface area for oxides is not well established due to a lack of accurate methods [74]. However, for metallic surfaces it can be done with high precision; to a first degree the electrochemically formed oxide area should not vary much from the initial metallic. On this basis Ru outperformed Ir and Pt. At the same time it was also evident that Ru nanoparticles were too unstable under the reaction conditions. This can be seen in figure 2.8 where the activity is normalised to the amount of CO adsorbed.

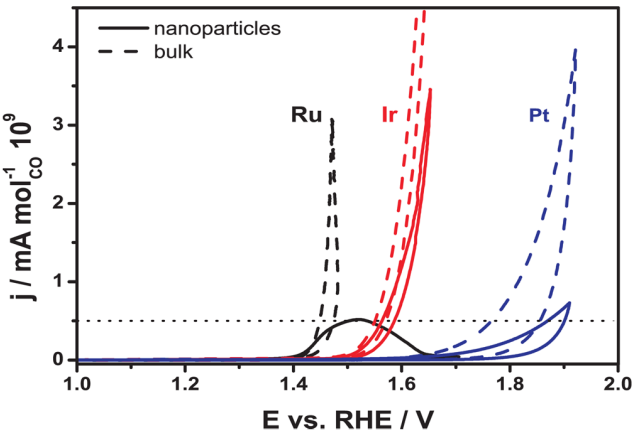

Figure 2.8: Comparison of results for anodic polarisation of Ru, Ir and Pt polycrystalline disks (bulk) and nanoparticles. Ru is shown in black, Ir in red and Pt in blue. Bulk measurements are indicated with dashed lines while nanoparticles are in solid lines. The current is normalised with the amount of CO adsorbed on the surface, based on electrochemical CO stripping. Figure taken from [100].

Since the activity of RuO_x based catalysts is high compared to other oxides, it is interesting to investigate whether further activity enhancements are possible. It has indeed been shown to be the case in various studies, where especially mixtures with Ni or Co stand out [104–107]. A theoretical model explaining these enhancements has recently been proposed on the basis of an extended thermodynamical analysis [108]. In this model the adsorption of *OOH, which was shown to be a limiting factor, can be stabilized by introducing a hydrogen acceptor close to the catalytic site. If this acceptor can retrieve the hydrogen atom from *OOH (and regenerate) at potentials close to OER, the overpoten-

tial could be decreased for surfaces that are limited by a too weak adsorption of *OOH compared to *OH. Essentially, a selective stabilization of OOH by immediate splitting into adsorbed H and O_2 is proposed to occur on active Ru sites with an oxidised Ni or Co site as neighbour.
Just as it can be complicated to compare Tafel slopes from different materials prepared differently, it can be quite difficult to document activity enhancements from mixed oxides appropriately. First, it is important that the pure oxide is actually performing as good as possible, which is why proper benchmarking is critical [109, 110]. Second, the reason for improvements can be manifold. Depending on preparation method a big contributor is increase in surface area, which changes the current measured directly. Other examples are increase in conductivity and change in electrode-electrolyte interface [111, 112].

In order to better understand the influence of surface structure on catalytic activity, single crystal studies have proven very useful for investigations of the oxygen reduction reaction [113–119]. However, this is not trivial for OER due to difficulties in preparation of oxide single crystals and reconstruction taking place under reaction conditions [120]. From a report by Trasatti and co-workers in 1986, early works on geometric effects are analysed [121] and it was argued that polycrystalline and single crystal studies often suffer from poor characterization of the surface structure during reaction conditions. From their own electrochemical experiments the (110) surface of rutile RuO_2 exhibited a change in Tafel slope as a function of the overpotential and a roughening of the surface during testing. Unfortunately, that study did not include any surface science methods to confirm the expected crystalline orientation. The overall goal of these early studies was to map out Tafel slopes as a function of the surface structure. This phenomenological approach, although theoretically valid, have achieved little success in OER due to difficulties in reproducibility for similar materials across different research groups. More recent studies have focused on systematically preparing comparative surfaces, exemplified by work from Shao-Horn and co-workers, who compared the activity of (110) and (100) oriented surfaces on rutile RuO_2 and IrO_2 [122]. They found that the more open (100) surfaces on both RuO_2 and IrO_2 exhibited increase in activity over the (110) orientation. They argue that it could be related to a higher surface density of coordinatively undersaturated metal sites, CUS, which Rossmeisl et al proposed to be the active site [90]. It should here be noted that those experiments were performed in alkaline solution. There is much to learn from studying well-defined surfaces of RuO_2 and IrO_2 which are the state of the art catalysts. It is particularly valuable to use such experimental evidence of active sites as input for more accurate and realistic DFT calculations. If a close agreement between theory and experiments can be established the insight gained could accelerate rational design of oxygen evolution catalysts.

In practical devices the catalyst has to be nanostructured to maximise the surface area and minimise catalyst loading. For Ru and Ir based catalysts it is

therefore compelling to investigate the activity of well defined nanoparticles. Compared to the opposite reaction ORR where there is a large amount of work in this area [123–129], there are only few studies available for OER [105, 130]. From those experiments it was suggested that changing the size from 45 to 15 nm lead to increased current densities for OER. Investigations of particle size effects are related to which facets or sites that are active, and a decrease in particle size generally leads to a higher fraction of undercoordinated sites vs. flat terrace sites. According to DFT calculations the binding to intermediates on flat terrace sites results in activity trends that match experimental values [90, 94, 131, 132]. The binding on undercoordinated sites are instead expected to be radically different [133] and would not be expected to play a dominant role in the reaction. From such considerations it is expected that smaller particles exhibit lower specific activity, but possibly higher mass activity [40]. Another related research effort is focused on substituting the noble metal core with a more abundant element, while keeping the activity constant. This has been done successfully for IrNi nanoparticles by Strasser and co-workers [134–136]. $IrNi_{3.3}$ particles exhibited a mass activity 10 times higher than rutile IrO_2 particles. The recent efforts for finding better OER catalysts in acid is summarized in figure 2.9, where the current is normalised to geometric surface area. It is clear from this plot that only noble metal oxides are considered and currently no other materials are being reported as alternatives.

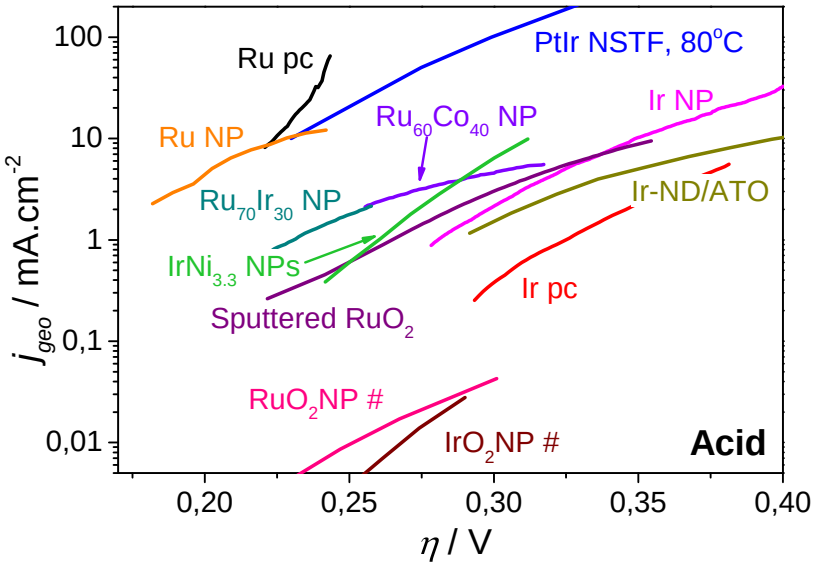

Figure 2.9: Overview plot of recent studies on OER catalysts tested in acidic media. Ru polycrystalline sample (pc), Ru NP, Ir pc and Pt pc are from [100]. PtIr NanoStructured Thin Film (NSTF) is from [41]. $Ru_{70}Ir_{30}$ NP and $Ru_{60}Co_{40}$ NP are from [106]. $IrNi_{3.3}$ is from [134]. Ir-ND/ATO (antimony-doped tin oxide) is from [136]. RuO_2 NP and IrO_2 NP are from [101], where the current is normalised to an area estimated from particle size analyses, indicated by #. Sputtered RuO_2 is from [137], which is appended as paper I.

2.5.2.1 Progress in alkaline media

A far larger group of materials can withstand the reaction conditions in alkaline electrolytes. This is quickly realized by scanning through the Pourbaix diagrams of the elements, where most stable compounds are shown as function of pH and electrochemical potential [138]. A renewed interest in perovskite materials has been taken by the group of Shao-Horn, who tested a set of oxides with the aim of finding design principles for activity towards OER [139]. Inspired by the earlier work of Bockris and co-workers [83], they attempted to identify a suitable bulk property that could relate to the OER activity of a group of perovskites. They successfully constructed a volcano shaped activity plot based on the filling of the e_g band and identified $Ba_{0.5}Sr_{0.5}Co_{0.8}Fe_{0.2}O_{3-x}$ as a highly active catalyst. The e_g band filling was argued to be a suitable descriptor for OER due to strong overlap of this particular orbital with the oxygen adsorbate orbital. Thus, the e_g band filling should have a direct implication in the charge transfer from electrode to adsorbate and influence the binding strength. An optimum e_g band filling of 1 was proposed. Due to difficulties in measuring and

calculating the e_g band filling, Grimaud *et al.* later reported a similar finding where the O p-band center was used to describe the OER activity of double perovskites such as $Pr_{0.5}Ba_{0.5}CoO_{3-\delta}$ [140]. This descriptor could be found from DFT calculations and compared to oxidation state found with chemical titration techniques. In figure 2.10 the results of this work can be seen as a volcano shaped plot, indicating an optimum O p-band center of -1.7 eV relative to the Fermi level, E_F. With a higher O p-band center the oxides tend to become amorphous during OER testing, which was the case for $Ba_{0.5}Sr_{0.5}Co_{0.8}Fe_{0.2}O_{3-x}$ [141].

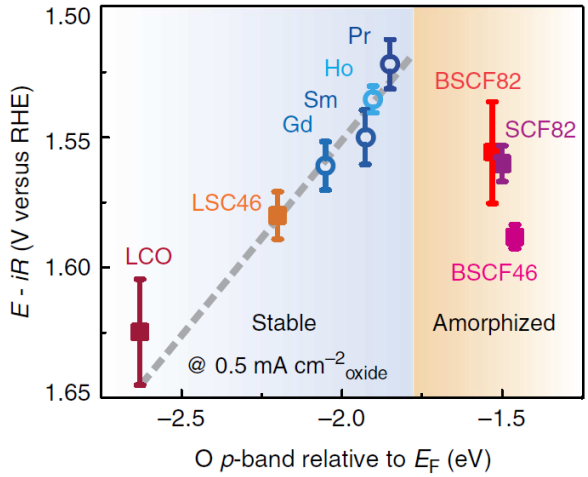

Figure 2.10: Volcano shaped activity plot for a range of perovskites. The activity is shown as the potential needed to reach 0.5 mA/cm^2 as function of the computed O p-band center. In the left side of the figure there are stable perovskite materials, which improve in activity as the O p-band center inceases. For high O p-bands some perovskite have been observed to become amorphous. The data is reproduced from [140].

Parallel to these efforts of relating bulk oxide properties to OER activity, other groups have focused on nickel or cobalt based catalysts [142] where especially Ni hydroxides mixed with iron have proven relevant. Boettcher and co-workers have measured on a range of electrodeposited transition metal oxides and found 2 nm thick $Ni_{0.9}Fe_{0.1}O_x$ able to reach 10 mA/cm^2 at only 340 mV overpotential. The advantage of measuring such thin films is that almost all the material can be considered active and roughness will not play a large role. A disadvantage is that it is challenging to characterize such thin layers and there could be a large dependence on interaction with the substrate. However, similar activities were reported by other groups [109,143–146]. Interestingly, Boettcher and co-workers later reported that pure NiO_x is not very active on its own but,

due to inherent iron contamination from alkaline solutions and glassware, most Ni electrodes are in fact doped with iron [147]. This has spurred further investigations into mixed nickel-iron oxides. Friebel *et al.* used a combination of X-ray Absorption Spectroscopy, electrochemical measurements and DFT calculations to propose a model explaining the activity of mixed $NiFeO_x$ [148]. Contrary to the common understanding that Ni provide the active site, they argue that highly active Fe-sites in a Ni hydroxide matrix are responsible for the low overpotential of these mixed catalysts. The X-ray Absorption technique is particularly useful in combination with DFT calculations since it allows for a very accurate determination of both oxidation state and local structure of the metal atoms, which can then be used as input in the calculations. Furthermore, the bad performance of pure iron hydroxides is argued to be due to bad conductivity of γ-FeOOH. A similar conclusion was reached in a study on mixed cobalt-iron hydroxides, from Burke *et al.* For this material addition of iron leads to improvements in activity up to around 50 % Fe content, after which phase separation and bad conductivity seemingly lead to a decrease. The primary methods employed by Burke *et al.* are electrochemical measurements on electrodeposited samples combined with in-situ studies of the potential dependent resistivity.

These studies mark an interesting new era in electrocatalysis, where new understanding arises from combinations of methods, rather than phenomenologically relying on pure electrochemical parameters such as Tafel slope and exchange current density. An additional focus point in the field of OER is the benchmarking of a large range of materials to allow for better comparison. Especially the Joint Center for Artificial Photosynthesis, JCAP, stands out in this aspect with dedicated groups working on comparing catalysts for both HER and OER [109, 110]. In two comprehensive studies McCrory *et al.* test a large number of catalysts with a simple electrochemical protocol. The primary parameters resulting from the protocol are overpotential needed to reach 10 mA/cm^2, roughness factor based on pseudocapacitance, Faradaic efficiency and change in activity after 2 hours. It should be noted that even though almost all known catalysts are tested, only Ru, Ir and Pt are active in acidic environment. To sum up this section of the most active catalysts for OER in alkaline environment a unified Tafel is shown in figure 2.11.

2.5.2.2 Manganese based OER catalysts

Manganese based catalysts for OER represent another interesting case, which in many studies has been inspired by nature [151, 153–155]. This is due to the manganese-calcium complex responsible for the turnover of molecular oxygen in photosystem II. Manganese is also an extremely abundant element, among the most available transition metals, and it is considered environmentally friendly [102, 156, 157]. Finally, it is one of the few transition metal oxides with a stable solid phase in the OER relevant potential region in acidic conditions that is also

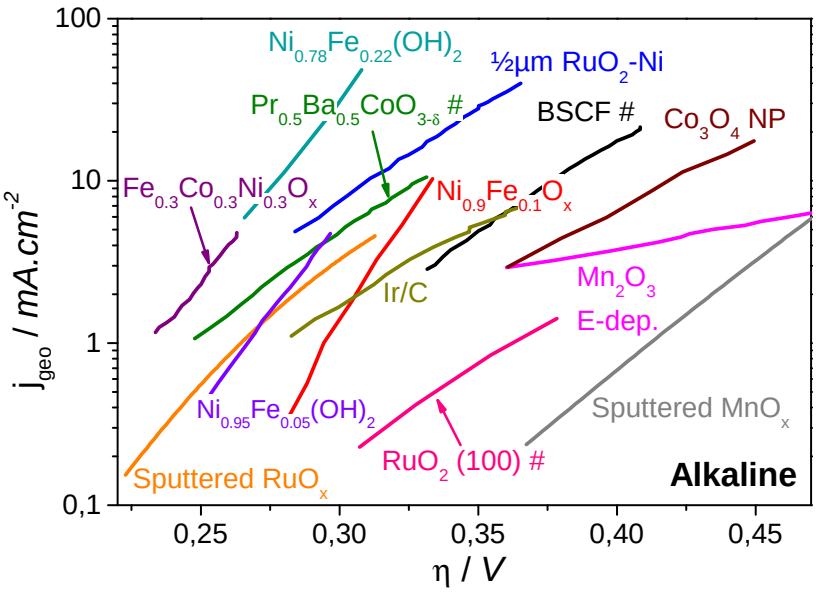

Figure 2.11: Overview plot of recent experiments with OER catalysts tested in alkaline media. $Ni_{0.78}Fe_{0.22}(OH)_2$ is from [149], $Fe_{0.3}Co_{0.3}Ni_3O_x$ is from [144], RuO_2-Ni is from [104], $Pr_{0.5}Ba_{0.5}CoO_{3-\delta}$ is from [140], $Ni_{0.95}Fe_{0.05}(OH)_2$ is from [147], $Ni_{0.9}Fe_{0.1}O_x$ is from [150], Ir/C is from [151], BSCF is from [139], $RuO_2(100)$ is from [122], Co_3O_4 is from [152] and Mn_2O_3 E-dep is from [151]. Sputtered RuO_x and MnO_x is from this project. # denotes that the surface area is evaluated from particle size analysis instead of geometric.

catalytically active [138].

Some of the first manganese based OER catalysts to be reported were made with thermal decomposition, inspired by the success of DSAs®, by Morita *et al.* in 1977-79 [158–160]. It was concluded that both β-MnO_2 and α-Mn_2O_3, on either Ti or Pt, and their mixtures could be used as anodes for oxygen evolution, even though they were inferior to RuO_2 based electrodes. The electrodes were tested in both acid and alkaline electrolytes. Ti substrates yielded better adhesion for the catalyst, while using a Pt substrate resulted in better conductivity. It was further speculated that oxygen vacancies in the catalyst layer provide the necessary conductivity, which decreases upon prolonged oxidation of the electrode due to an increase of oxygen content. This effect could be responsible for a slow deactivation of the catalyst activity when measured at high current density or potential over time. The existence of various Mn oxides (MnO, Mn_3O_4, Mn_2O_3, MnO_2 and several different crystalline phases) has also lead to studies on the influence of the initial oxide on the OER activity, so-called structure-activity

relations [153, 156, 161–163]. In some reports Mn in a +3 state was concluded superior in terms of activity [162–166]. This view is supported by characterizations of Mn oxides before and in some instances after electrochemical testing. In a study from Su *et al.* surface stability of Mn oxides together with binding energies to the OER intermediates were evaluated using a combination of DFT and electrochemical measurements [131]. The DFT calculations suggested that at OER relevant potentials the MnO_2 phase was most stable, which is consistent with the bulk stability regions found in the Pourbaix diagram [138]. It is therefore unlikely that a +3 state of Mn would persist at the electrode surface at highly anodic potentials. Instead, it is likely that the preparation method and the resulting roughness or conductivity of the catalyst play a large role in determining an activity hierarchy. However, to elucidate the dependence on oxidation state in-situ techniques must be used so that the surface can be characterised under reaction conditions. Such studies are at this time not available for Mn based OER catalysts. A selection of active Mn based OER catalysts is shown in figure 2.12 as a Tafel plot. From that plot it is evident that even with one type of material, e.g. Mn oxides, the range of measured activities is rather large.

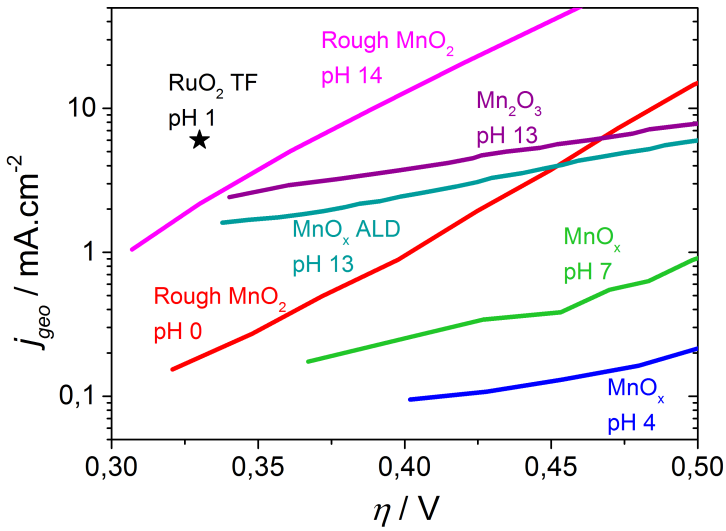

Figure 2.12: Overview plot of recent experiments with Mn based OER catalysts tested in various electrolytes. The Rough MnO_2 measurements in pH 0 (red) and 14 (magenta) are from [158], the MnO_x ALD (teal) is from [167], the Mn_2O_3 (purple) is from [151], the MnO_x (green) tested in pH 7 is from [168] and the MnO_x tested in pH 4 (blue) is from [165]. A RuO_2 thin film from [137] is shown as a black star.

2.5.3 Catalyst stability

In the previous sections it has been briefly mentioned that the OER catalysts have to survive in extremely harsh and oxidising conditions. It is therefore of utmost importance that new and active catalysts are actually stable in those conditions for an extended amount of time. However, while searching for new materials long term testing is not often a focus point and instead many groups turn to shorter electrochemical tests (2-24 hours) at either constant potential or constant current density. The question is whether these tests reveal any stability that can be extrapolated to the long term. A pure electrochemical test at constant current density have traditionally been the standard [109]. This type of test is justified by the operation mode such a catalyst would typically work under in an actual device. A certain amount of hydrogen is needed or a certain amount of energy is used and the electrolyzer is therefore likely to operate under constant current density. If the catalyst deactivates over time it leads to an increase in the applied potential in order to reach the constant current density. However, since the current is exponentially dependent on the overpotential small changes in potential lead to huge changes in current. So when measuring the potential at constant current the changes are normally within 50 mV, which may be judged acceptable from the researchers point of view. This type of test does not inform the researcher about any specific changes in the catalyst structure, purity or electrode thickness. More importantly it does not reveal when a complete loss of the catalyst material will occur. Such information must be analysed with other means which is the topic of this section.

Recently, stability tests have received increased attention in the field of OER, likely inspired by the importance that stability plays in the evaluation of ORR catalysts [169–174]. For Pt based ORR catalysts a typical accelerated stability test consists of 10000 cycles in a relevant potential range after which the loss of activity is reported [175–177]. The ORR proceeds at potentials where Pt is thermodynamically stable but the start-stop conditions in fuel cells can cause surface oxidation followed by reduction, resulting in loss of platinum [173]. Conversely, for OER catalysts many materials are prepared in a state that is not thermodynamically stable at potentials higher than 1.6 V_{RHE}. For prolonged operation at high current densities the surface is bound to change structure and this can lead to a loss of catalyst material. Such effects have been elegantly shown for a selection of noble metal oxides by Cherevko *et al.* [178–180]. In those studies an online Inductively Coupled Plasma-Mass Spectrometry (ICP-MS) system is used to measure corrosion products while the catalysts are under potential control. A short introduction to ICP-MS can be found in section 3.4.2. The results can be seen in figure 2.13 for Ru, Ir, Pt and Au, where dissolution rates and voltammetric profiles are shown. The potential is slowly scanned between 0 and 1.5 V_{RHE}, while the dissolved species are measured with the ICP-MS. Notice that for Ru the dissolution occurs solely at the peak potential whereas it is stable at all other potentials. This is in contrast to the other three metals,

which all dissolve upon reduction, although at a much lower rate compared to Ru.

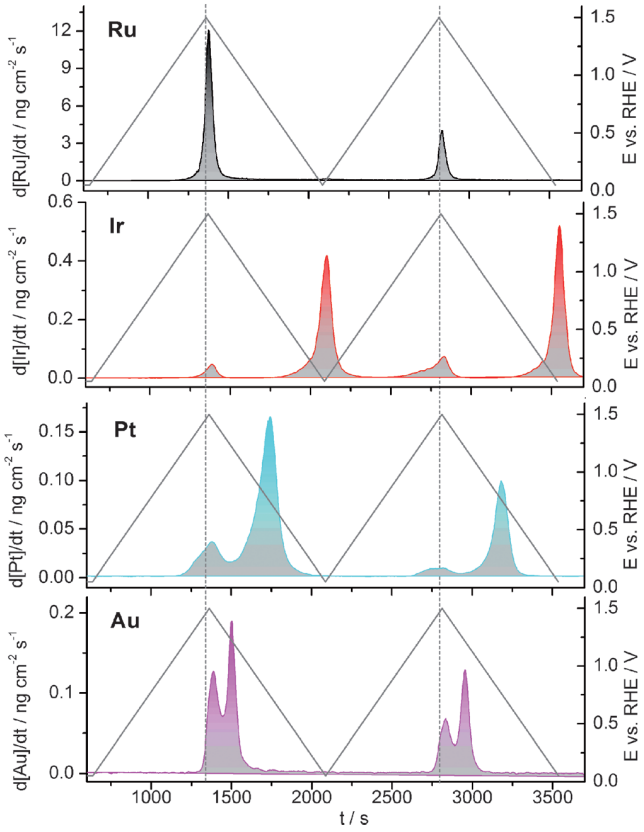

Figure 2.13: Figure showing the stability of Ru, Ir, Pt and Au under OER reaction conditions, from top to bottom respectively. The mass losses are measured with online Inductively Coupled Plasma-Mass Spectrometry systems and are plotted as function of time. The potential is indicated with the lines and second axes on the right. In this way, it is possible to directly correlate the amount of mass lost to the potential applied to the electrodes. Figure taken from [179].

With such a dissolution profile it is unlikely that Ru can be used in electrolyzers. Instead Ir appears as the best compromise between activity and stability. In fact, through annealing procedures it has been shown that IrO_x can be even more stable, reaching a mass loss rate of only 1 pg/cm^2/s at approximately 1.75 V_{RHE} [180]. For a realistic catalyst loading of 0.15 mg/cm^2 [41] this corrosion rate corresponds to just below 5 years of constant operation. However, since

IrO_x dissolves primarily at potentiodynamic conditions it is likely that the mode of operation will have a large impact on the lifetime, where less start-stops lead to a longer lifetime.

The dissolution products can in some cases be detected electrochemically with a separate electrode during a catalyst test. This is the case for ruthenium dissolving as RuO_4, which can be reduced at 1.1 V_{RHE} [181,182]. In practice, this type of test is carried out with a Rotating Ring Disk Electrode, RRDE, setup where the catalyst is loaded as a standard rotating disk and the separate electrode is positioned as a ring around the disk. This geometry allows for an accurate determination of the efficiency with which the ring picks up products from a reaction at the disk. A few groups have characterized Ru dissolution with this method and the Faradaic efficiency for RuO_4 formation is between 6 and 15 % [40,182,183]. It should be noted that this technique is also frequently used for the determination of Faradaic efficiency towards oxygen evolution [101,109,139]. A combination of RRDE and ICP-MS measurements were used by Markovic and co-workers [183] to elucidate trends of stability among the metals that can catalyse OER, see figure 2.14a. They found that the more unstable metals were also more active catalysts. In two other studies from the same group, focused on mixed Ru-Ir thin films [184] and $SrRuO_3$ [185], this argument is further supported. However, the trend found by Cherevko *et al.*, which can be seen in figure 2.14b, appears to be in contrast to the simple inverse stability-activity relationship.

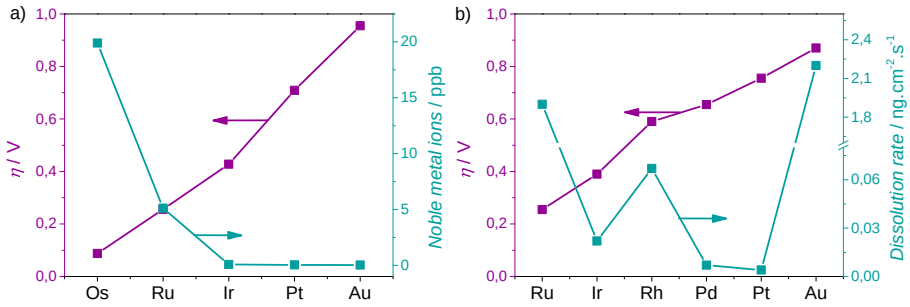

Figure 2.14: a) Stability and activity trends for Os, Ru, Ir, Pt and Au under a constant current density of 5 mA/cm^2. The stability is measured as concentration of metals in solution after test (ppb). The activity is shown as the overpotential needed to reach 5 mA/cm^{-2}. Data from [183]. b) Trends of activity and stability for Ru, Ir, Rh, Pd, Pt and Au under a constant current density of 0.8 mA/cm^2. The dissolution rate, in ng.cm^{-2}.s^{-1} is found with online ICP-MS at a constant current density of 0.8 mA/cm^{-2}. Note the scale break in the dissolution rate. The activity is shown as the overpotential needed to reach 0.8 mA/cm^{-2}. Data from [179].

From the two figures 2.14a and b, the activity trends are the same, but in 2.14b

the stability results are not consistent with an inverse relationship. It should be noted that in both of these analyses the metal stabilities are evaluated at a constant current and therefore at different potentials. For instance Au is evaluated at potentials around 2 V_{RHE} whereas Ru is evaluated at 1.5 V_{RHE}. These contradicting results suggest that a more in-depth understanding of the dissolution phenomena is needed before an established model can be reached.
In terms of stability analyses for non-noble metal oxides there are less studies available at this time. However, one of most active catalysts based on non-precious metals, $Ba_{0.5}Sr_{0.5}Co_{0.8}Fe_{0.2}O_{3-x}$, or in short BSCF, has been subjected to Transition Electron Microscopy, TEM, analysis before and after electrochemical tests [141]. These tests consisted of cyclic voltammetry and from the TEM images it was evident that the BSCF particles change from a crystalline phase to an amorphous one. At the same time the catalytic activity increases, which is likely due to a roughening of the surface causing more active sites to be available. The authors therefore argued that the leaching of Ba^{2+} and Sr^{2+} ions was related to the position of the O p-band center. BSCF has an O p-band center positioned relatively high compared to other catalyst materials, like $La_{0.4}Sr_{0.6}CoO_{3-\delta}$, $LaCoO_3$ and $LaMnO_3$, all of which retain crystallinity after electrochemical testing.

2.6 Conclusion

In summary, investigating catalysts for the oxygen evolution has been an active research field for more than six decades. Important progress has been made in terms of understanding the reaction and finding suitable descriptors that can aid in designing better catalysts. From theoretical analyses, scaling relations have been used to predict and describe trends in activity for a large group of oxides. Unfortunately, the scaling relations between intermediates also mean that it is complicated to surpass the performance of existing RuO_2 catalysts. Nevertheless, a large amount of work has been dedicated to optimizing Ni, Fe and Co based catalysts for use in alkaline solution and new materials are being reported frequently. The stability of new and active catalysts are not often reported in a very transparent way. This is one of the main issues addressed in this thesis. Furthermore, there is a lack of progress for identifying non-noble metal based catalysts that can work in acidic solution. The new catalysts reported in acidic solutions are instead based on Ru and Ir. It has therefore been a main goal of this project to search for a compound based on abundant elements, that can catalyse the oxygen evolution reaction in acidic environment.

Chapter 3

Experimental Methods

A variety of experimental methods have been used throughout the project and in this chapter a description of these will be given. The overall focus of the thesis is on metal oxide catalysts prepared by sputter deposition. As sample preparation technique sputter deposition has certain advantages and disadvantages which will be explained herein. In terms of sample characterization, emphasis has been put on combining the electrochemical properties with information of oxide phase determination, valency and stability. The methods of choice have been X-ray Photoelectron Spectroscopy, X-ray Diffraction, X-ray Absorption Spectroscopy, Inductively Coupled Plasma - Mass Spectrometry and Electrochemical Quartz Crystal Microbalance measurements.

3.1 Sample Preparation

As mentioned above, the samples tested for this thesis have been prepared by sputter deposition and given the large amount of time spent optimizing this technique a comprehensive introduction is justified.

3.1.1 Sputter Deposition

Sputtering is a vacuum technique utilizing bombardment of a target surface with energetic particles widely used for surface cleaning, etching, surface layer analysis and deposition. The energetic particles are typically charged Argon ions, which are created with a plasma source. When sputtering is used for

deposition, a negative bias is applied on the target material, from which the surface atoms can be knocked loose. With a sufficiently low chamber pressure the mean free path of atoms is long enough to allow for deposition on a nearby substrate. The target to substrate distance is approximately 10-15 cm in our chamber. While a suitable mean free path is desirable the pressure should still be kept high enough for the plasma to be stable and a higher pressure means a larger number of Ar ions bombarding the target. These requirements lead to a pressure range of about 1-100 mTorr (or roughly 10^{-3} to 0.1 mBar). A schematic representation of the above description can be seen in figure 3.1.

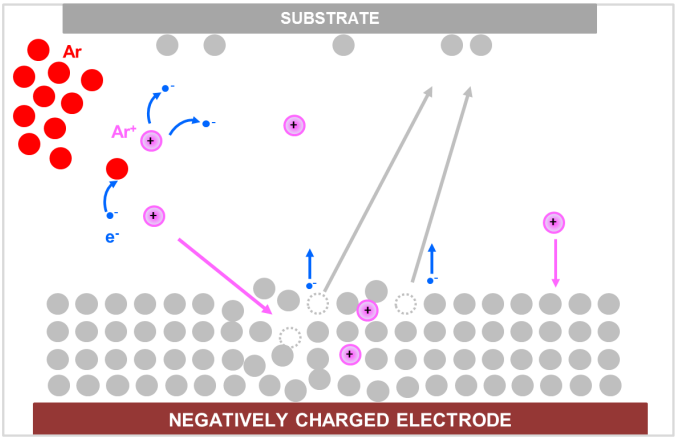

Figure 3.1: Schematic of the sputter deposition process. Ar gas, in red, is ionized in a plasma to form Ar^+, in pink. A negative bias is applied on the target material, in grey, which causes the Ar^+ ions to bombard the surface. Surface atoms from the target are then knocked loose and deposit on the substrate, solid grey. Figure from [186].

The rate of material deposited depends to a large degree on energy of the incoming Ar ions, the pressure in the chamber and the sputter yield of the target material. The energy of Ar ions and chamber pressure are both easily controlled and are important parameters in the optimization of a deposition process. The sputter yield is a material parameter and can not be manipulated. This is particularly important to realize for co-sputtering purposes where a certain film composition requires matching deposition rates from two or more targets. The difference in sputter yields can be seen in figure 3.2. In extreme cases it can vary with up to a factor of seven for pure metals, which is the case for Si and Ag.
There is a tendency for the yield to increase with increased filling of the d-shells in the transition metals. This is related to the energy transfer factor and the fact that harder collisions increase the yield while the atoms with a more open electronic structure has low yields. Fundamental studies on the sputter

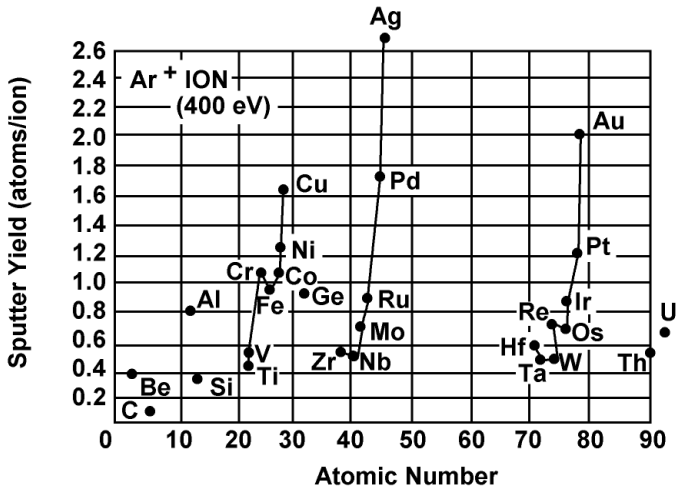

Figure 3.2: Sputter yield as function of the atomic number, from 0 to 90. Lines between points indicate 3d, 4d and 5d metal series. Figure taken from [187].

yields have not been carried out in this thesis but in practice the effect of different sputter yields is easily observed when comparing the power required for various targets to obtain desired deposition rates. For every new target a calibration of rates vs. power is carried out in order to know the thickness of the films prepared. The rate calibration is done with an in-chamber quartz crystal microbalance. In short a quartz crystal is used as deposition substrate while the change in resonant frequency is measured over time. The change in frequency is linearly related to the amount of material deposited. When the density is known, the change in frequency can be directly converted into thickness growth (Angstrom) per second. Details on how a quartz crystal microbalance works is given in section 3.4.1.

The power input and chamber pressure also affect how the sputtered particles grow on the substrate [188, 189]. The energy of incoming Ar ions affect the sputtered atoms and the energy with which they leave the target surface. In general for low energies, a few hundred electron volts, the sputtered species will be single neutral atoms while for very high energies, several thousands electron volts, clusters are formed. In our case we use from 100 to 750 eV, hence the film growth is expected to be primarily from single atoms. The energy of the sputtered atoms also depends on the chamber pressure. A higher pressure leads to more collisions and by the time the sputtered atoms hit the substrate their average energy will be lower. The mean free path of the sputtered atoms can be a useful way to estimate whether the target to substrate distance and chamber

pressure will result in useful deposition rates. The mean free path, λ, can be evaluated from the following equation, assuming the ideal gas law:

$$\lambda = \frac{kT}{\sqrt{2}\sigma P} \tag{3.1}$$

where k is the Boltzmann constant, T the Temperature, σ the cross sectional area and P the pressure. For a reasonable rate of deposition the mean free path should be in the same order of magnitude as the target to substrate distance. For $\lambda = 10$ cm the pressure should be around 10^{-3} mbar, which is in the range of pressures described above.
In practice the growth parameters can lead to stress in the films, which may detach from the substrate during testing or in case of very thin substrates, a highly strained film can cause the substrate to bend or even break. Obtaining strained films or quantification of stress/strain in the films produced have not been pursued here but it was in some instances observed as rapid film detachment. In those cases sputtering parameters different from the standard had been used and was not used again.
An important aspect that has so far been briefly touched upon is the source of the Ar ions, the plasma. A plasma is created by applying a large potential difference between a cathode and an anode in the chamber. With a sufficient energy input atoms become ionized and a large number of ions and electrons are created. Due to the high density of charged particles, the plasma will react to magnetic fields, which is exploited in magnetron sputtering systems. In such systems, which was used throughout this project, a strong magnetic field traps the electrons and concentrates the plasma close to the target material, which has a negative bias. The magnetron systems make it possible to lower the sputtering pressure significantly compared to traditional glow discharge systems, due to the confined plasma, while achieving high deposition rates.

3.1.1.1 Reactive sputter deposition

In reactive sputter deposition the parameter space is further enlarged by adding the partial pressure of a reactive gas. The reactive gas in this project is always oxygen due to the focus on preparing metal oxides. The presence of oxygen in the chamber complicates the deposition process in several ways. Oxygen will interact with the target causing surface oxidation and changes in the sputter yield. Most of the transition metals oxidise with a very negative heat of formation and the sputter yields go down. Furthermore, the deposited atoms oxidize and the density is not always easily obtained for the oxide prepared. The exact oxide phase will also be unknown until further characterization has been carried out. To explore the effects of adding oxygen a rate vs. oxygen partial pressure curve is typically made.
There is a hysteresis behavior when increasing and decreasing the oxygen partial pressure. While increasing the partial pressure more of the sputtered atoms will

oxidize until there is an excess of oxygen that is free to react with the target surface. Once that happens the sputtering yield goes down and less sputtered atoms are available, causing even more oxygen to react with the target. When decreasing the partial pressure from a high level the target will be completely passivated and since there is a low sputter yield it will take a lower partial pressure before the oxidised target surface is back to a metallic state. This type of behavior is important to realize since a high rate combined with a complete oxidation of the prepared film is often desirable. This means operating at the balance point between excess oxygen and excess sputtered atoms. For reactive co-sputtering the issue of target passivation becomes more complicated since two different materials may passivate at very different partial pressures of oxygen. In that case, obtaining the desired composition requires careful calibration and possibly using either very low rates or having incomplete oxidation of the films.

3.1.1.2 Equipment and deposition rate calibration

The sputtering equipment used throughout this thesis was a magnetron system from AJA International, with two DC power sources, two RF power sources and substrate heater. With all power sources in use up to four different materials could be sputtered simultaneously. The deposition rates were calibrated frequently using an in-chamber Quartz Crystal Microbalance. Calibration runs were made by depositing 15-20 Å three times and noting the time. For reactive sputtering it is also important to note down the time it takes for the rate to stabilize. For MnO_x the measured rates were further confirmed by film thickness measurements with a Profilometer. The Profilometer method comprises a needle scanning the surface and for a suitable edge the height can be measured down to a few nm in accuracy.

3.2 Characterization techniques

3.2.1 X-ray Photoelectron Spectroscopy

X-ray Photoelectron Spectroscopy, XPS, is a widely used method for investigating surface composition [190]. The technique is based on the ejection of electrons from a surface caused by radiation, known as the photoelectric effect. These electrons will have an energy dependent on the photon energy, $h\nu$, individual binding energy with reference to the Fermi level of the sample, E_b and work function of the spectrometer, ϕ. This can be formulated as the following equation.

$$E_k = h\nu - E_b - \phi \tag{3.2}$$

Since the electronic configuration of an element is unique the knowledge of these binding energies, E_b, allows us to identify the elemental composition of a sample.

Furthermore, electrons exhibit relatively short mean free path in solids and the range of kinetic energies observed in an XPS system is typically 10-1000 eV. The mean free path of electrons as a function of their kinetic energy can be seen in figure 3.3, which is also known as the Universal Curve. This results in an information depth of less than 2 nm and it is therefore reasonable to assume that the bulk of a sample does not contribute to the signal. The shallow depth of information, or surface sensitivity, is a distinct property of XPS and methods where electrons are measured. This is of particular importance in catalysis, which is a surface phenomenon. At the same time it also presents a challenge in electrocatalysis, where a number of unwanted changes can occur to a sample during electrochemical testing.

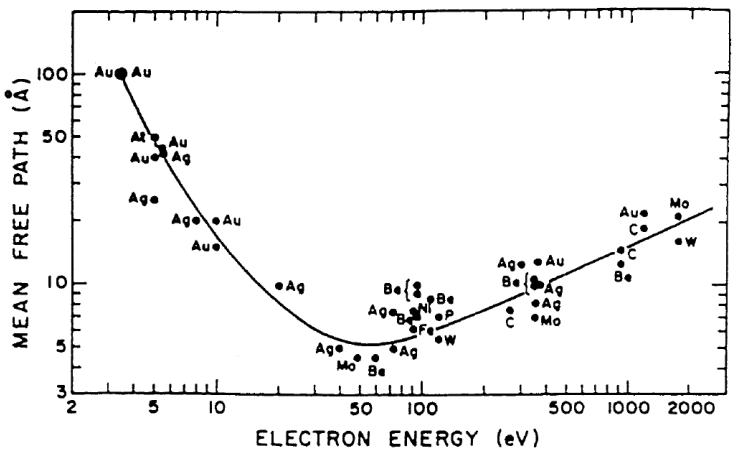

Figure 3.3: The universal curve of inelastic mean free path of electrons in a solid. The mean free path of the electrons is plotted as function of electron kinetic energy. Figure taken from [191].

With careful treatment XPS analyses of samples before and after electrochemical measurements can reveal important properties of electrocatalysts. Among the possible difficulties are unexpected dissolution of the prepared sample, interference of contaminants from the electrolyte and deposition of carbon species upon drying. In this thesis the primary uses for XPS have been to establish oxide stoichiometry of Mn oxides, to find the ratio between Mn and another metal for mixed oxides and to check for possible contamination. The oxide stoichiometry can, for most metals, be found by analysing peak shifts. However, for Mn oxides it has been reported that the peak shifts are not very significant and it is not possible to distinguish between the various oxides [192]. Instead, the Mn2p$\frac{1}{2}$ satellite structure and Mn3s multiplet splitting can be used [151,192,193]. More specifically the Mn2p$\frac{1}{2}$ satellite distance and Mn3s multiplet energy difference

are features that depend on the stoichiometry. References have been reported and compared by Gorlin *et al.* [151] and the values can be seen in table 3.1.

Sample	Reference	ΔE2p$\frac{1}{2}$ [eV]	ΔE3s [eV]
MnO	[151]	11.8	4.5
MnO	[192]	11.9	4.5
Mn_3O_4	[151]	10.0	5.1
Mn_3O_4	[192]	10.5	5.4
Mn_2O_3	[151]	6.0	6.0
Mn_2O_3	[192]	5.4	6.1
MnO_2	[151]	10.5	6.0
MnO_2	[192]	11.3	5.3

Table 3.1: Reference values for the Mn2p1/2 satellite distance and Mn3s multiplet splitting.

The XPS system used throughout the project has been a ThetaProbe Instrument from Thermo Scientific, where the base pressure was 5 x 10^{-10} mbar. The X-ray source was monochromatized $Al_{K\alpha}$ (1486.7 eV). All XPS measurements have been conducted by Kenneth Nielsen or Paolo Malacrida at CINF DTU.

3.2.2 X-ray Diffraction

X-Ray Diffraction is another routinely used technique that can provide crucial information about catalytically active samples [46]. The technique is based on the principles of Bragg's Law, which states the conditions that must be fulfilled to observe constructive interference of radiation scattered by the atoms in a crystalline specimen. In a crystalline material all the atomic positions can be described by a simple set of vectors that forms the crystal lattice. It is the interaction between the incoming radiation and a large number of crystal planes that can lead to strong constructive interference observable in X-Ray Diffractograms. This effect is illustrated in a simple schematic in figure 3.4.
The condition described by Bragg states that for a given wavelength, λ, and interplanar distance, d, constructive interference is possible at an angle θ given by:

$$n\lambda = 2d\sin\theta; \quad n = 1, 2, ... \tag{3.3}$$

Besides identifying crystalline phases, the XRD method can be used to estimate the mean size of sub-micrometer ordered domains, or crystallites, τ. This is done by using the Scherrer equation [194]:

$$\tau = \frac{K\lambda}{\beta cos\theta} \tag{3.4}$$

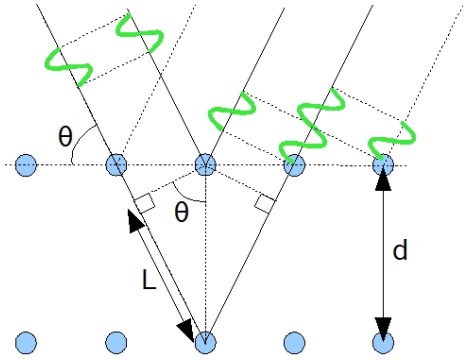

Figure 3.4: Illustration of the interaction between X-ray radiation and a crystal lattice that can lead to constructive interference. For specific angles and interplanar distances the Bragg conditions are fulfilled and this can be detected in an XRD measurement.

where K is a shape factor, with a typical value of 0.9, λ is the wavelength of the X-rays, β is the line broadening at full width half maximum (FWHM) and θ the Bragg angle as mentioned above. Another important parameter is the instrumental line broadening which should be subtracted from the measured line broadening to get β. It should also be noted that a domain size found from the Scherrer equation gives a lower bound and works best when the domains are all the same size. This is due to other factors which could contribute to the broadening. If there are a spread in the size the smaller domains could give rise to a broadening, but the larger will dominate the signal. To estimate the instrumental line broadening as function of θ a silicon reference sample was measured.
All measurements presented here were acquired with a PANalytical X'Pert Pro equipment with an X-ray wavelength of 1.54 Å for the $Cu_{K\alpha}$ line.

3.2.2.1 Glancing Angle X-Ray Diffraction

As XRD is a bulk sensitive technique it can be challenging to obtain information about thin film samples with acceptable signal to noise. Naturally, this depends on the thickness of the film, typically 10-100 nm in this project, but often the substrate will contribute with a large signal. This issue can be somewhat mitigated by using the Glancing Angle technique, GA-XRD, where the incoming X-rays are always kept at a low angle, α [195]. A schematic of this technique can be seen in figure 3.5.

By choosing a sufficiently low incoming angle the signal contribution from the substrate can be minimized due the penetration depth of the X-rays. Although useful, the higher surface selectivity comes at a cost since it puts some

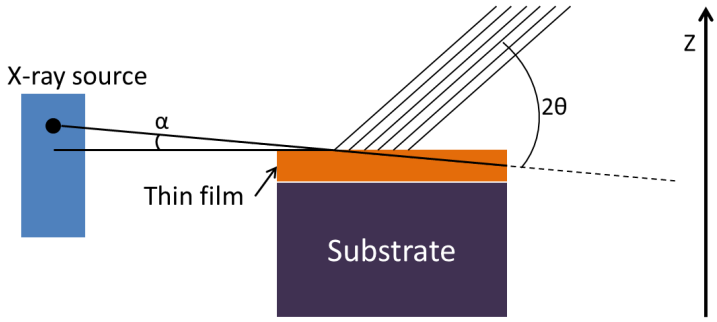

Figure 3.5: Schematic of the Glancing Angle XRD setup. This technique is also called Grazing Incidence XRD. A low incoming angle α is kept constant throughout the measurement, minimizing the signal contribution from the substrate.

constraints in the choice of sample and substrate. In general, when the films are below 100 nm setting an α of around 0.5 degrees results in high signal to noise ratios but the surface must have a low roughness. This is due to difficulties in alignment, where it must be ensured that an optimum amount of the incoming X-rays are hitting the surface of the sample instead of just below or above. An important part of this alignment procedure is therefore to adjust the height of the sample holder.

3.2.2.2 Crystalline manganese oxides

The majority of results in this project have been obtained with a highly disordered manganese oxide denoted MnO_x. This is due to the ease of preparation and less interaction with the substrate when deposition temperature is kept below 200 °C during deposition. For carbon based substrates the Mn film catalyses the formation of CO_2 in oxygen containing atmospheres, which leads to significant roughness and Mn being covered with carbon. The substrates used for EQCM measurements on the other hand could sustain a maximum temperature of 400 °C due to surface segregation of Ti forming TiO_2 at the surface. Despite these issues some time was spent on trying to identify conditions for crystalline Mn oxide deposition. The results are summarized in table 3.2.

3.2.3 X-ray Absorption Spectroscopy

The technique X-ray Absorption Spectroscopy, XAS, can be used to probe electronic structure and local geometry of matter [196]. It relies on high resolution X-rays in the range of 0.1 to 500 keV. The requirements for the radiation are: a) high X-ray flux so that good signal to noise ratio is obtained in a reasonable time, b) broad spectral range with uniform flux so a suitable spectrum can be

Oxide	p_{O_2} [mbar]	T [K]	MnO_x rate [Å/s]	Post-anneal T [K]
Mn_3O_4	$2.7 \cdot 10^{-4}$	473	0.8	na.
Mn_2O_3	$7 \cdot 10^{-4}$	473	0.8	873 (1 hour)
MnO_2	10^{-3}	473	0.1	773 (1 hour)

Table 3.2: Deposition parameters resulting in crystalline Mn oxides.

evaluated and c) high stability in energy and beam position. These requirements are all met in synchrotron sources that can deliver more than five orders of magnitude higher flux compared to laboratory sources. The energy of the photons delivered from the synchrotron is selected with monochromators.
The method is based on exciting the core electrons of atoms in a sample by absorption of photons. The photon energy required to excite a given electron depends on the energy level of the electron and the unoccupied state that can be filled. In XAS, the absorption of photons as a function of energy is used for analysis, which is in contrast to X-ray Photoelectron Spectroscopy, where the energies of photoelectrons are analysed. The absorption of photons is typically measured for a specific range corresponding to a certain "edge" indicating the core electron that is excited by the photons. The K edge corresponds to exciting the 1s, L1-3 edges correspond to 2s and 2p and M1-5 edges correspond to 3s, 3p and 3d. At the same time the K edge requires the highest photon energy while the M5 requires the lowest. X-rays can penetrate deep into samples so when transmitted X-rays or fluorescence radiation is used for analysis, XAS is a bulk sensitive technique. Transmission mode is the simplest detection method, where ion chambers before and after the sample are used to evaluate how much of the beam is absorbed. Fluorescence radiation originates from a decay of the excited state, where electrons from higher energy levels fill the empty core states and emit new photons with characteristic energies. This is shown in figure 3.6a. It is also possible to measure electron yield originating from the Auger process, in which case the technique becomes surface sensitive. This process is shown in figure 3.6b. In the Auger process, an electron from a higher energy level in an excited atom fills an empty core level and the energy difference is transferred to another electron which is released into vacuum as a photoelectron.

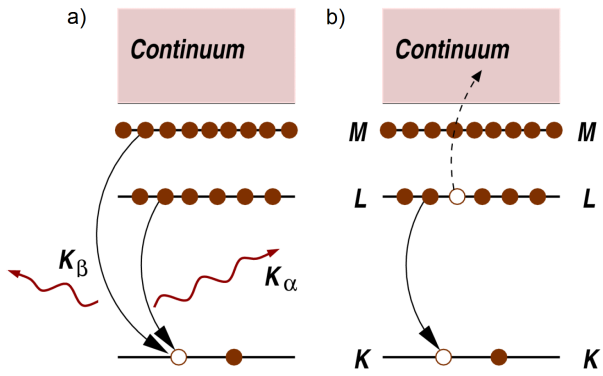

Figure 3.6: Decay phenomena for excited states in an atom. a) Fluorescence radiation, which occurs when an electron fills an empty lower state and the difference in energy is emitted as a photon. b) Auger process, where the energy difference from the decay is used to emit a photoelectron with a characteristic energy. Figure from [197].

The analysis of XAS spectra is often divided into two main categories, the X-ray Absorption Near Edge Spectroscopy region, XANES, and the Extended X-ray Absorption Fine Structure, EXAFS. These two regions are shown for a spectrum in figure 3.7.
The analyses included in this thesis encompass XANES, so EXAFS will not be treated any further. In XANES the near edge features of XAS spectra are analysed with the aim of obtaining knowledge about the valance state and coordination environment. The near edge region can be further split into pre-edge and rising edge. A common application of the XANES region is to determine valance states from the shift of the rising edge. A shift towards higher photon energies can be attributed to higher oxidation states since the core electrons are stronger bound when valence electrons are missing. However, there are multiple ways of measuring the shift and currently various experimental groups use different conventions. By comparing to measurements of reference compounds it is possible to evaluate valence states given that a robust method is used to evaluate the shift in edge energy. In this thesis, a method called "the moment method" will be used to evaluate the shift. This method is based on calculating an energy weighted quantity, E_w, with the following equation:

$$E_w = \frac{\int_{E_i}^{E_f} E \cdot I(E) dE}{\int_{E_i}^{E_f} I(E) dE} \tag{3.5}$$

where E is the photon energy, E_i the energy right before the pre-edge, E_f the energy at which features are not expected to shift significantly and $I(E)$ the normalised absorbance after background has been subtracted. E_w is therefore

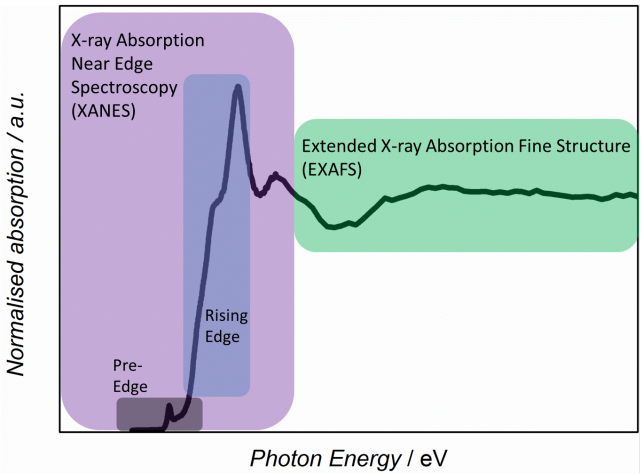

Figure 3.7: X-ray Absorption Spectrum for the Mn K-edge, exemplifying the two main regions of XAS analysis. Here the normalised absorption is plotted against the incoming photon energy. The XANES region is comprised of the pre-edge and rising edge area, whereas the EXAFS region is after the main edge.

a measure of the entire edge shift based on the range of energy defined by E_i and E_f. An edge energy can then be calculated from:

$$E_0 = 2E_w - E_f \tag{3.6}$$

For a small set of samples X-ray Absorption Spectroscopy, XAS, measurements were carried out to investigate the oxidation state of Mn. These experiments were performed at the 6-2 ES2 beamline at Stanford Synchrotron Radiation Lightsource, SSRL SLAC. Beamline scientists Tsu-Chien Weng, Dimosthenis Sokaras and Dennis Nordlund set up all the equipment and helped with the data acquisition. High energy resolution fluorescence detection was used to measure the absorption edges. The sample setup comprised a glass cell with a small and thin glassy carbon wafer attached with epoxy on one side and inlets for counter and reference electrodes. The catalytically active films were deposited on the carbon wafers and could therefore be in contact with the electrolyte while being exposed to synchrotron radiation from the back. An image of this cell can be seen in figure 3.8, together with a schematic of the beam and signal pathways.

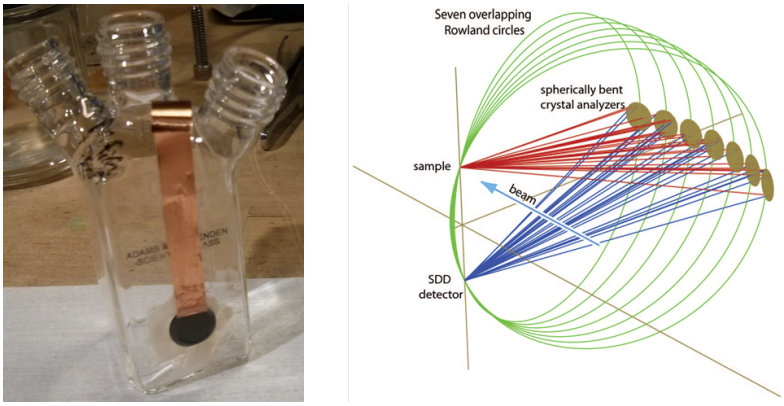

Figure 3.8: Left: Image of the glass cell used for in-situ XAS measurements. The thin films were deposited onto 200 μm thick glassy carbon wafers, which are then attached to a hole in the glass cell. A piece of copper tape is used as electrical connection to the wafer. Right: A schematic of the signal pathways for the in-situ XAS experimental set up from [198]. The beam is coming from the lower right corner and interacts with the sample as noted in the figure. Spherically bent analyzers send the signal to an SDD detector underneath the sample.

3.2.4 Scanning Electron Microscopy

In Scanning Electron Microscopy, SEM, a focused electron beam is rastered over a surface to generate a multitude of signals that can be used for analysis. The energy of the incoming electrons is typically in the range of 1-30 kV. Among the most used signals are secondary electrons, backscattered electrons, Auger electrons and characteristic X-rays [199]. An overall schematic of the signals generated can be seen in figure 3.9.
Secondary electrons are emitted from the sample surface due to electrons excited by the electron beam. The energy of these electrons varies from 10-200 eV which means that approximately one nanometer thickness of the sample contributes to the signal. The yield of these secondary electrons depends on the surface topography, since local curvature changes the amount of electrons that can escape. More specifically, for protrusion edges a larger amount of secondary electrons can escape, while the opposite holds for cavity edges. Other parameters affecting the yield include the work function of surface, incident beam energy, beam current and the density of the sample. Backscattered electrons are incident electrons which undergo elastic scattering interactions with the surface atoms. These electrons have energies close to the incident beam energy and therefore a larger interaction volume is probed. The scattering process is sensitive to the elements in the sample surface and for higher atomic numbers the back scattering signal increases. It should be noted that backscattered electrons can

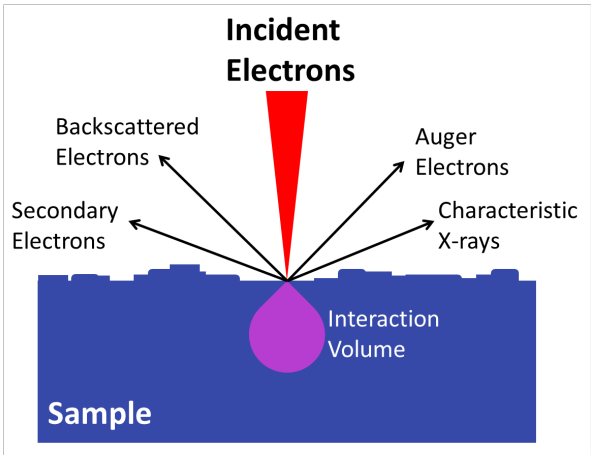

Figure 3.9: Schematic showing the SEM process and signals generated. The incident electron beam is focused down onto the sample, whereby a variety of signals are generated. Some of these are shown on the figure, including secondary electrons, backscattered electrons, Auger electrons and characteristic X-rays. The amount of secondary electrons that are able to escape the surface depends on the curvature around the beam spot and interaction volume, which give rise to contrast and topography information.

also cause secondary electrons which affect the resolution achieved in secondary electron imaging. The SEM images included in this thesis are all acquired by secondary electron detection.

3.3 Electrochemical measurements

The results in this thesis are centered around the electrochemical properties of thin films. Therefore, emphasis has been put on developing protocols and measurement procedures. In general, electrochemical measurements deals with the response of electrodes immersed in an electrolyte under the influence of applied potentials or induced currents. Specifically for this project we are interested in the response of a single electrode in a certain potential range, where the oxygen evolution reaction occurs. For this purpose a three electrode setup has been employed. An image of such a setup can be seen in figure 3.10.

The three electrodes used are: a working electrode, a counter electrode and a reference electrode. The working electrode contains the sample which response or activity is measured. Current flows between the working and the counter electrode when a suitable potential difference is applied. In the case of oxygen evolution on the working electrode (working as anode) the counter electrode will

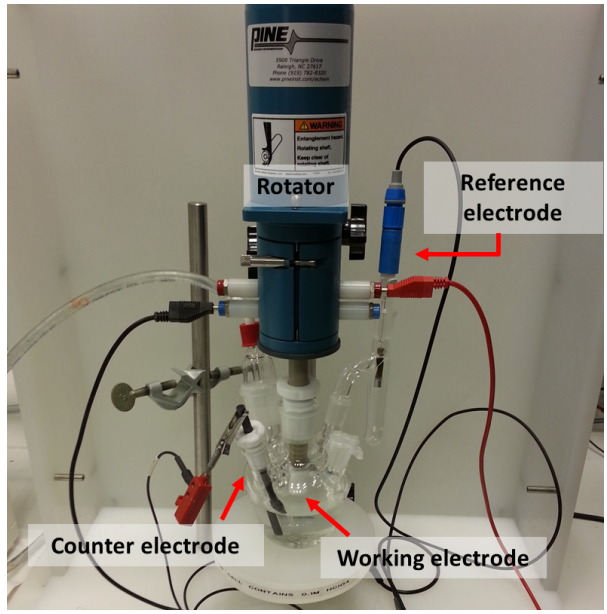

Figure 3.10: Image showing the three electrode setup in a rotating disk electrode station. The most important components are highlighted with a text label, including counter electrode (carbon rod), working electrode (attached to rotator) and reference electrode (here a $Hg/HgSO_4$ electrode). Figure taken from [186].

perform a cathodic reaction, normally hydrogen evolution. However, the potential difference between the counter and working electrode is a function of the catalytic activities of both, which makes it complicated to study one catalyst at a time. To this end, the potential applied on the working electrode is measured against a known reference electrode, composed of a redox couple in equilibrium. The potential of this reference can then be measured against a hydrogen electrode and the results can be reported using the Standard Hydrogen Electrode, SHE, or Reversible Hydrogen Electrode, RHE, scale. The standard hydrogen electrode scale is based on the consensus of a zero electrochemical potential for the hydrogen evolution reaction in equilibrium at standard conditions on a Pt electrode. For RHE the effect of pH is also taken into account, meaning that 59 mV per pH increase has to be added. Using a reference electrode makes the measurement of the working electrode independent of the catalytic activity of the counter electrode, which can then be selected more freely. Still, the counter electrode must provide sufficient surface area so that the overall reaction does not become limited by the number of sites available for the reduction reaction. Throughout this project a high surface area graphite rod has therefore been used.

3.3.1 Impedance Spectroscopy

In order to facilitate comparison between experimental groups and setups it is important to correct for the Ohmic losses. Ohmic losses come from resistance in wires, connections, sample and the electrolyte. In fact, the ionic conductivity of the electrolyte is a dominant factor and it is therefore an advantage to keep a similar distance between working and counter electrodes for a series of experiments. The magnitude of the Ohmic losses can be evaluated by impedance spectroscopy, where the impedance is measured as a function of AC current frequency. A simple equivalent circuit model of an electrochemical interface is comprised of a resistor and a constant phase element in parallel. The capacitative contribution to the impedance vanishes at high frequencies (the imaginary component is approximately zero) and the resistance can be determined as the real component of the impedance. An example of such a measurement can be seen in figure 3.11.

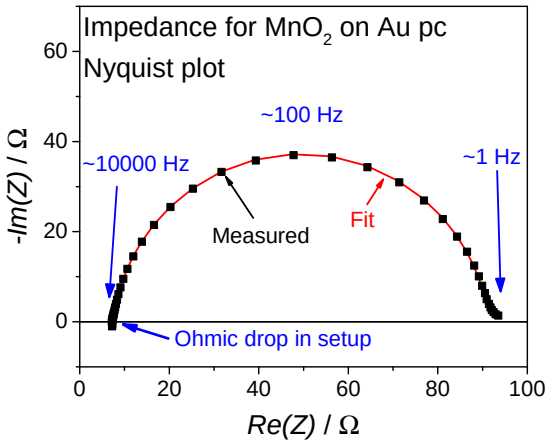

Figure 3.11: Nyquist plot of an impedance measurement for MnO_2 on a gold polycrystalline disk. The Ohmic drop in the experimental setup is found as the high frequency intercept with the 1st axis. A range of 200 kHz to 1 Hz was measured.

In practice, the Ohmic losses can be accounted for before or after measuring. The measured potential is easily corrected using Ohms law.

$$\Delta U_\Omega = j \cdot R \tag{3.7}$$

Where ΔU_Ω is the potential change due to Ohmic losses, j the measured current (not normalised) and R the resistance. It is possible to correct for 85 % of the Ohmic losses using a feature in the potentiostat. It is important to keep in mind that at high currents the remaining 15 % can actually result in rather large discrepancies between the nominally applied potential and the actual applied

potential. As an example, imagine a resistance of 40 Ω which is corrected for at 85 %. This leaves 6 Ω unaccounted for which at 10 mA corresponds to 60 mV lost. In terms of catalytic activity 60 mV can make a large difference.

3.3.2 Measuring techniques

A range of electrochemical techniques has been used extensively during this project. For determining catalytic activity cyclic voltammetry has been employed, while for most stability measurements chronoamperommetry (CA) or chronopotentiometry (CP) have been used. Cyclic voltammetry is a technique where the applied potential on the working electrode is cycled between two extremes at a constant scan rate. This is a useful technique for investigating new samples and can reveal magnitude and shifts of both irreversible and reversible redox processes, pseudo-capacitance and catalytic activity of electrodes. The results of cyclic voltammetry are typically plotted as a voltammogram, where the current (normalised to area) is a function of the potential applied on the working electrode. An example of such a voltammogram can be seen in figure 3.12.

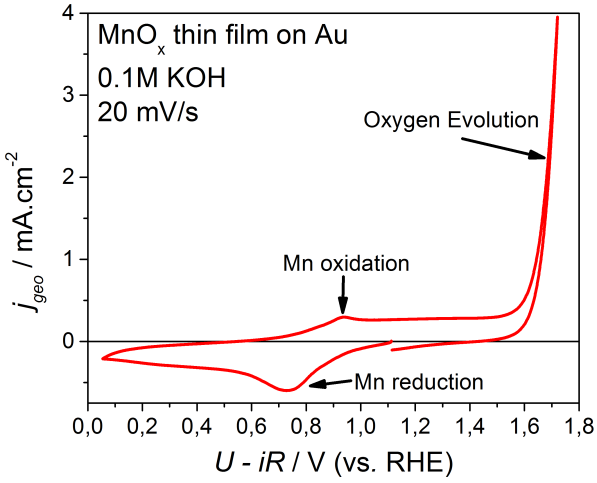

Figure 3.12: Cyclic Voltammogram of MnO_x in 0.1 M KOH, measured with 20 mV/s in the range 0.05 to 1.7 V_{RHE}. The current is normalised with the geometric area of the electrode and the potential scale has been corrected for Ohmic losses, measured with impedance spectroscopy.

From that voltammogram, the electrode can be analysed with respect to electrochemical properties. The feature around 0.9 V_{RHE} is not reversible as the oxidation and reduction occur at different potentials. If the oxidation peak can be ascribed to a specific reaction it can also be used to estimate the number

of electrochemically active metal atoms at the surface. Such an estimation is valuable due to discrepancies between geometric surface area and electrochemically accessible surface area. Another way to estimate the surface area is using the capacitive response, which is a function of the scan rate. The capacitative response is based on charging of the electrode electrolyte interface when the potential changes and is considered proportional to the number of active surface species [109]. However, for oxides there is a lack of consensus and benchmarks regarding normalisation factors and therefore attempts to normalise currents with electrochemical surface area are rarely reported.

3.4 Stability measurements

3.4.1 Electrochemical Quartz Crystal Microbalance

In order to analyse stability for electrocatalysts, it is complicated to rely on purely electrochemical current-potential measurements. In theory, a corrosion or dissolution process could occur through a well defined oxidation or reduction process that could be analysed using the amount of charged passed. However, catalyst stability is mostly relevant under conditions where a catalytic reaction takes place, in this project oxygen evolution. Therefore the dominant part of the current can usually be ascribed to this reaction. Instead, the electrochemical quartz crystal microbalance, EQCM, provides a way to monitor the mass changes that occur during an electrochemical reaction [200, 201]. The technique relies on measuring the resonant frequency of a quartz crystal which, for the right crystal orientation, changes with the amount of material present on top. An image and schematic of the QCM crystals used in this project can be seen in figure 3.13.

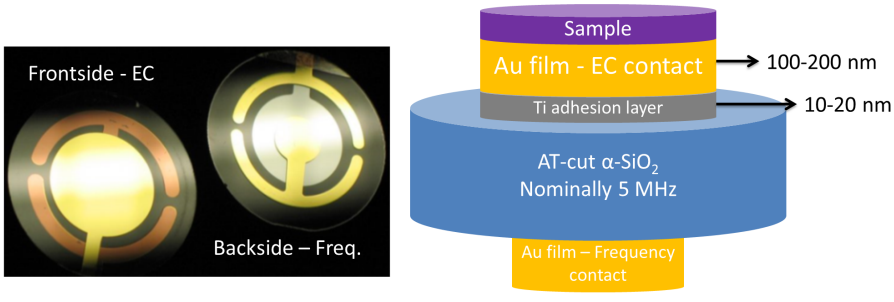

Figure 3.13: Left: Image showing the two sides of EQCM crystals. Right: A cross section schematic of the crytals is shown, indicating the layered structure that makes it possible to measure electrochemistry and resonance frequency simultaneously.

The resonance in quartz arises from the piezoelectric effect, where mechanical

stress in a crystal generates an electric potential due to a net change in dipole moment. The opposite effect is the generation of atomic displacement due to an applied electric field. This means that an oscillating potential can induce acoustic resonances with a specific frequency. This frequency can be determined with high precision. The relationship between the frequency change, Δf, and mass, Δm, is described in the Sauerbrey equation [202]:

$$\Delta f = -\frac{2f_0^2}{A\sqrt{\rho_q \mu_q}}\Delta m \tag{3.8}$$

where f_0 is the nominal frequency of the crystal, A the piezo-active area, ρ_q the density of quartz and μ_q the shear modulus of an AT-cut quartz crystal. In practice a simplified version of the equation can be used:

$$\Delta f = -C_f \cdot \Delta m \tag{3.9}$$

where C_f is a constant that can be calibrated. The crystals used for this thesis had a nominal C_f of 56.6 Hz/μg·cm^2. Calibration of C_f was carried out using silver electrodeposition [150, 203]. A clean EQCM substrate was immersed in a 0.5 M HNO_3 solution with 50 mM $AgNO_3$ and -50 μA were passed until a frequency change of 60 Hz was reached. For silver deposition it can be assumed that one electron is passed per Ag atom deposited. Therefore, the frequency change can be correlated to the mass of Ag deposited. The silver deposition was repeated 6 times and the C_f value obtained was 57 $\pm$ 1 Hz/μg·cm^2, which compared very well to the expected value.

The method is well suited for investigating mass changes for electrochemical electrodes, however, it is important to emphasize that the frequency change is measured, not the mass. Besides change of mass, there are other factors that can lead to a change in frequency. Among the most important are [200]:

- **Viscosity.** The crystal oscillations are influenced by the media in which the crystal is immersed. For liquid media the interaction with the crystal can cause a dampening, which can be expressed as the following equation [204]:

$$\Delta f = -f_0^{\frac{3}{2}}\sqrt{\frac{\eta_l \rho_l}{\pi \rho_q \mu_q}} \tag{3.10}$$

  where η is the viscosity of the liquid and the other symbols represent the same as in equation 3.8. It is clear that a higher viscosity results in a dampening in the frequency. For water there is furthermore a temperature dependence of the viscosity. As an example a change from 20 to 30 $^{\circ}$C results in a frequency change of 85 Hz. It is therefore important to maintain a stable temperature while using an EQCM setup. In our laboratory the temperature could be monitored and in short term testing it was never observed to have an impact.

- **High mass loading.** With a very high mass loading the QCM sensitivity decreases [200]. The method is considered accurate up to about 2 % of frequency change with respect to the nominal resonant frequency. This corresponds to approximately 2.4 mg, which is about four orders of magnitude higher than the typical loading for the MnO_x thin films investigated here.

- **Roughness of EQCM coating.** A high roughness of samples can in extreme cases lead to misinterpretation of the frequency changes. This is due to trapping of liquid in cavities which can be a particular problem if a rough sample is oxidised or deposited while the frequency is measured. Such a case was reported in [205] where the mass change of oxidised gold was much higher than expected due to this trapping phenomena. For the samples used here a polished substrate surface was used, which is not expected to be influenced by trapping of liquid.

- **Non-uniform samples**. With the simple Sauerbrey equation only uniform films should be evaluated as it is assumed that the film is a rigid and uniform extension of the quartz crystal.

- **Bubbles**. Finally, bubble formation can pose a problem for EQCM measurements. For a gas evolving reaction, it is important that the bubbles detach from the surface so that they are not covering a large area of the electrode. If they end up covering a large part, the frequency measurement is affected due to local viscosity effects. Furthermore, if a gas is evolved on a very rough surface it can be trapped. For the experiments carried out for this thesis, the bubbles were observed to leave the surface easily, from a macroscopic point of view.

The equipment used for EQCM measurements was a QCM200, purchased from Stanford Research Systems. The crystals were AT-cut and had a nominal resonant frequency of 5 MHz. The electrochemically active area was 1.37 cm^2, while the area sensitive to frequency measurement was 0.38 cm^2.

3.4.2 Inductively Coupled Plasma - Mass Spectrometry

In addition to knowing how an electrode is changing in mass, it is crucial to quantify the dissolved species in the electrolyte. The EQCM method can be described as blind in that respect, since it only reveals a change in the overall mass. Therefore, Inductively Coupled Plasma - Mass Spectrometry, ICP-MS, has been used in combination with the EQCM measurements.
In brief, with ICP-MS a liquid sample is analysed by injecting a small volume through a nebulizer into a plasma as aerosol droplets [206]. Travelling through the plasma the sample is desolvated, atomised and ionized. The ions are then sent into a mass spectrometer. In the Mass Spectrometer the ions are filtered

depending on their mass to charge ratio. In the system used in our laboratory a Quadrupole Mass Spectrometer is installed. The system exploits a Radio Frequency, RF, quadrupole field, created by four rods, to filter the ions. The filtered ions are finally detected and a signal can be analysed by the software. The raw data for ICP-MS is therefore a set of intensities for each mass to charge ratio, but with calibration runs of known standards the intensities can be converted into concentrations.
It is a highly sensitive technique where most elements can be analysed down to sub-ppb (part-per-billion) levels. An overview of the detection limit for all the elements can be seen in figure 3.14. In this project mainly Mn, Ti and Au have been measured, all of which have detections limits below 10 ppt (part-per-trillion). The instrument used for this project was from Thermo Fisher Scientific, the model iCAP-QC ICP-MS. For each measurement a calibration with three known concentrations was carried out.

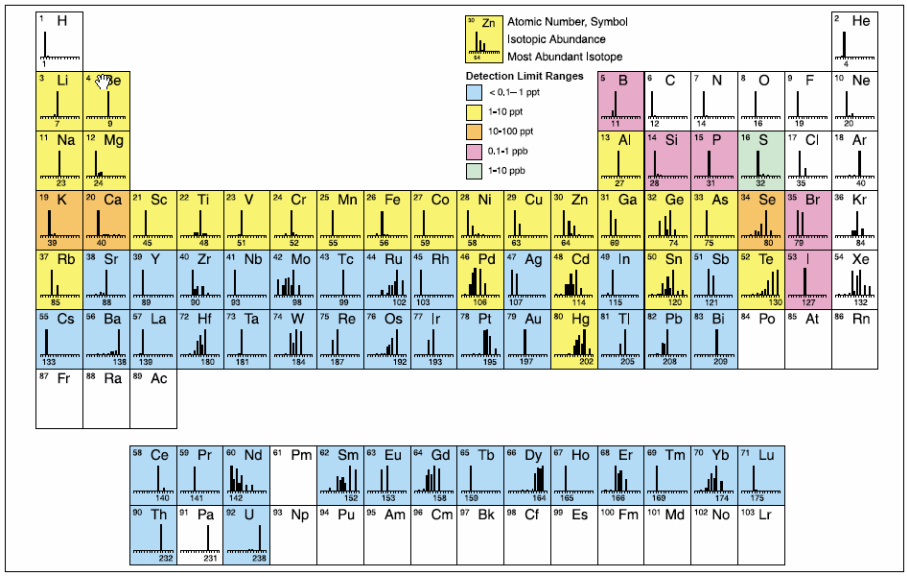

Figure 3.14: A periodic table specifying the detection limits of ICP-MS for each element in the periodic table. The different colors indicate the detection limit, while white indicate that ICP-MS is not suitable for detection. Figure taken from [206].

Chapter 4

Benchmarking the stability of OER catalysts

The development of new catalysts for the oxygen evolution could have a significant impact on the efficiency and commercialization of electrolyzers. Therefore, a lot of effort is put into identifying active mixed oxides with novel structures or stoichiometries. However, in the testing of these catalysts the stability is typically evaluated on the basis of stable electrochemical performance for a short period of time. This type of screening rules out instantaneous dissolution of the catalyst but does not ensure lifetime beyond the hours tested. In fact, for a given catalyst with a slow dissolution rate during operation there is no way to know beforehand whether the dissolution will result in better or worse performance until a significantly lower amount of active surface area is reached. To truly gauge the lifetime of a newly identified catalyst one is left with choosing between long term testing or directly measuring the rate of mass loss. Long term testing is often tedious and in this chapter it will be shown how to directly measure the rate of mass loss using short term tests [137]. The results presented here are also the basis of the appended paper I, where measurements on RuO_2 are included.

4.1 Characterization of thin films

The investigated samples are manganese oxide thin films deposited with the sputter deposition technique described in section 3.1.1. Specifically, these films are grown to be 40 nm thick, in a 5 mTorr atmosphere consisting of argon

and oxygen in a ratio of 5:1 and with a substrate temperature of 200 °C. The substrates used are quartz crystal microbalances, QCMs, which can be used to measure the mass changes of the catalyst, as described in section 3.4.1. The QCMs have a gold film on the front side which serves as the contact for electrochemical measurements. On the back side another gold film, with a smaller area, serves as contact for the frequency measurement. The overlap between these two films is sensitive to changes in frequency and therefore only this area was covered with MnO_x. TiO_2 was deposited on the remaining gold using a mask. This was done to avoid having gold in contact with the electrolyte, which could affect the electrochemical measurements. By only depositing manganese where the QCMs are sensitive the comparison between mass losses measured with EQCM and ICP-MS could be improved. The TiO_2 at the same time contributes with negligible currents and no frequency changes.

Manganese oxides exist in many valence states and therefore numerous stoichiometries can be formed, including MnO, Mn_3O_4, Mn_2O_3 and MnO_2. Furthermore, some of these oxides have several polymorphs [207]. As a first step, the deposited thin films were therefore characterized with X-ray Photoelectron Spectroscopy, XPS, and X-ray Diffraction, XRD. The data from XPS can be seen in figure 4.1 and from XRD in figure 4.2.

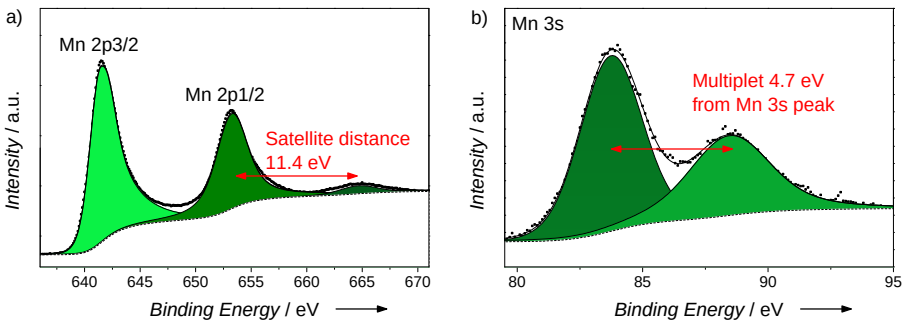

Figure 4.1: XPS spectra for a 40 nm MnO_x thin film. a) Mn2p peaks. b) Mn3s peaks. For both spectra the green areas indicate fitting peaks. The fits were used to evaluate the distance from main peak satellite, in case of Mn2p, and multiplet splitting, in the case of Mn3s.

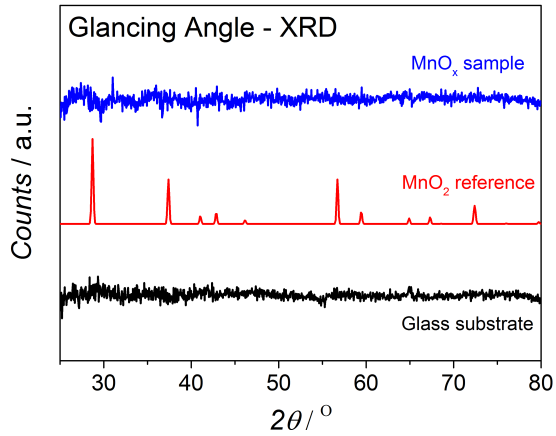

Figure 4.2: X-ray Diffraction in Glancing Angle mode used to measure on the MnO_x thin film, which is compared to an MnO_2 reference. No peaks are observed for both substrate and thin film.

For the analysis of XPS on manganese oxides several groups have shown that the oxide stoichiometry can be determined from the Mn3s and Mn2p peaks [151,192,193]. This analysis method was adopted and for the thin films described here the Mn3s multiplet splitting was determined to be 4.7 eV and the Mn2p$\frac{1}{2}$ satellite 11.4 eV away from the main peak. From comparison with literature, see table 3.1, the observed values are consistent with a Mn:O ratio of 1:2, indicating that a dioxide has formed. However, from the XRD results no peaks were identified and it was therefore concluded that the films are highly disordered or even amorphous.

4.2 Activity measurements

To ensure that the deposited films are relevant in terms of activity, they were tested with a Rotating Disk Electrode, RDE, set up. Results from these tests can be seen as a cyclic voltammogram in figure 4.3. A voltammogram for the same type of film on the EQCM substrates is also included. By comparing the two results, it is evident that the RDE test yields higher current densities. This could be due to more facile removal of oxygen formed on the catalyst when the electrode is rotated. However, the onsets of OER are very close for the two tests.

Comparison between literature results is often problematic due to different fabrication methods and testing parameters. The OER onset potential or the overpotential needed for achieving 10 mA/cm^2 are typical metrics for evaluating

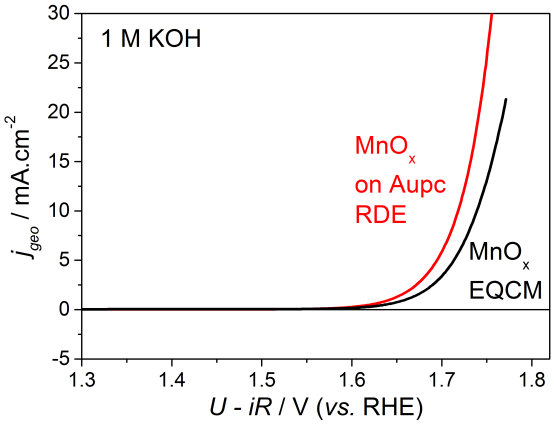

Figure 4.3: Voltammogram showing current density of MnO_x on both EQCM and glassy carbon substrates for the first anodic scan. The measurements were done with 5 mV/s in 1M KOH and the potential scale has been corrected for Ohmic losses. For the sample supported on glassy garbon, the measurement was done with a rotating disk electrode setup and the electrode was rotated at 1600 RPM.

activity [208]. The onset potential is in practice difficult to find since the true onset of most electrochemical reactions are usually masked by pseudo-capacitance, reactions with contaminants or other electrochemical processes. The overpotential needed for running 10 mA/cm^2 is a useful metric when OER catalysts are combined with suitable photoabsorbers to achieve solar water splitting [109]. However, the exact same type of material can easily be reported to have very different overpotentials due to different preparation methods, as discussed in chapter 2. Another possibility is to compare turnover frequency, TOF, which is the number of (O_2) molecules produced per second per active site. The challenge in finding a useful TOF is to evaluate how much of the catalyst that participated in the reaction. The 40 nm MnO_x thin films reported here have an estimated TOF of 0.007 s^{-1} at 400 mV overpotential, assuming a density of rutile MnO_2 and that every Mn atom can participate in the electrochemical reaction. This value is a lower bound but compares favorably to literature results, which are typically in the range of 0.002 to 0.006 s^{-1} for pure Mn oxides [209].

4.3 Stability measurements

The protocol for the stability measurements in this study was focused on utilizing the EQCM technique. For such measurements to be useful it is important to isolate frequency changes due to the actual dissolution of catalyst from changes that are due to the surroundings. For each sample the activity was

first evaluated with cyclic voltammetry and then Ohmic losses were evaluated with Electrochemical Impedance Spectroscopy, EIS. Following these two steps a stabilization period was introduced, where the electrode was kept at 1.4 V_{RHE}. This potential is well within the stability range of MnO_2 at pH 14 and almost no current is flowing [131, 138]. In this period the frequency measurement was allowed to stabilize so that effects from vibrations, temperature and cycling the potential were minimized. When the frequency changed with less than 1 Hz per 15 minutes, the actual corrosion tests were initiated. Naturally, this criterion is somewhat arbitrarily chosen but the important aspect is that drift in the frequency due to the setup or temperature is significantly lower than the changes due to dissolution. For samples that are expected to be highly stable the EQCM tests must be designed so that the drift is close to zero over extended periods. The stability tests consisted of chronoamperometry, CA, at 1.8 and 1.9 V_{RHE} or chronopotentiometry, CP, at 20 mA/cm^2. An overview of this stability protocol can be seen in figure 4.4.

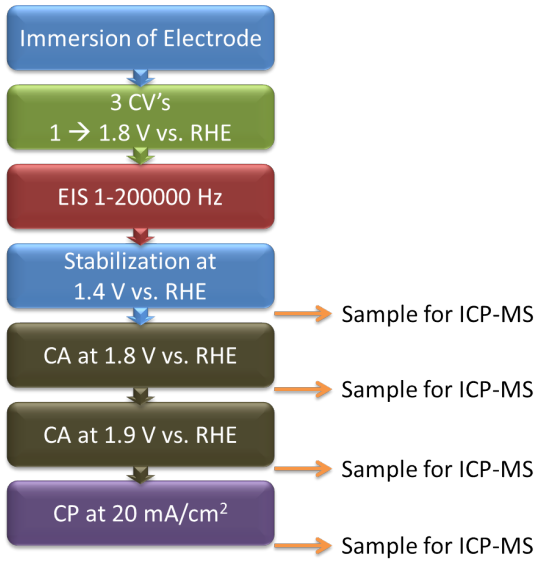

Figure 4.4: Schematic representation of the protocol for measuring the stability of thin films for oxygen evolution. This protocol is specifically designed to probe the anodic dissolution rate of MnO_x.

As mentioned above, the EQCM tests allow for simultaneously monitoring the catalytic activity, in terms of current or overpotential, and the change of mass through the resonant frequency. Such time resolved information is not easily available with any other methods. In figure 4.5a and b results of the

chronoamperometry tests can be seen for one sample. The current density decreases slowly over time which could be due to several reasons: the oxygen gas formed decreases the number of available sites, active sites are corroded away or change in film resistivity. The oxygen gas is a potential problem if the film is porous since the small pores could be filled with oxygen that is trapped. Dissolution of active sites is possible but intuitively new sites would be created after dissolution of the primary ones. Regarding change in resistivity it has been suggested that oxygen vacancies play an important role in conductivity for MnO_2 [158], and prolonged oxidation of the film could lead to oxygen incorporation and higher resistivity. It should be noted that the EIS method is not suitable for measuring local changes in film resistivity and the Ohmic loss correction does not rule out such effects. Instead in-situ characterization of the resistivity could be carried out with interdigitated array electrodes as demonstrated by Burke *et al.* [112]. However, detailed investigations of the deactivation mechanisms have not been pursued in this project, where the focus is on the mass losses.

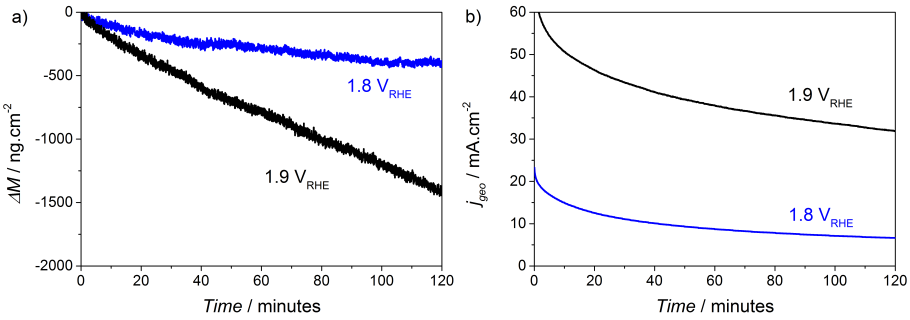

Figure 4.5: a) Mass changes based on the frequency change during the two hour tests. The frequency changes have been converted to mass changes by using the Sauerbrey equation [202]. b) Current density in two hours tests for MnO_x films at both 1.8 and 1.9 V_{RHE}. These tests were carried out in 1 M KOH.

In figure 4.5a the change of mass can be seen for two hour tests at 1.8 and 1.9 V_{RHE}. At both potentials the electrode is unstable and negative mass changes are evident. Comparing the magnitude strongly indicates that the dissolution rate is potential dependent as expected, with the faster mass loss occuring at 1.9 V_{RHE}. It is striking that the mass losses are linear and constant which allows for extrapolation to determine the lifetime of the films. In practise local thickness differences can have an impact on the actual lifetime, but as a first approach the initial dissolution rate is useful. As mentioned in the protocol description, the final step was a potentiometry test. This was carried out at 20 mA/cm^2 and the results can be seen in figure 4.6. This test shows the same story as in figure 4.5. After an initial rapid deactivation there is a slower deactivation process

approaching stable performance. However, at the same time a constant mass loss takes place at a rate consistent with the potential range being between 1.8 and 1.9 V_{RHE}.

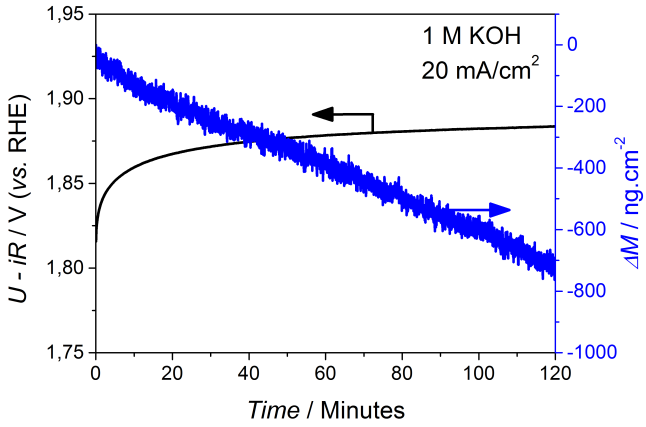

Figure 4.6: Measured potential and mass loss during a two hour chronopotentiometry test at 20 mA/cm^2 in 1 M KOH. The left side axis (data in black) shows the potential scale, corrected for Ohmic losses. The right side axis (data in blue) shows the mass losses measured with the EQCM method.

Before conducting extrapolation based on the EQCM data, it is useful to confirm which elements actually dissolved into the electrolyte. While the EQCM technique is prolific in giving time resolved information about the mass change, it is also blind to what causes these changes. With Inductively Coupled Plasma - Mass Spectrometry, ICP-MS, it is instead possible to analyse the concentrations of elements in the electrolyte. With the combination of EQCM and ICP-MS we can therefore compare the mass that left the electrode with the Mn concentration increase in the electrolyte. The pure ICP-MS results are in the form of counts registered with the mass spectrometer. The number of counts can be converted into concentration values, C_{ICP-MS} (in mass per liter), using calibration with standard solutions. However, to facilitate the comparison between EQCM and ICP-MS the concentration values are further converted to ng_{MnO_2}/cm^2, with the following equation;

$$\Delta M = C_{ICP-MS} \cdot V_{electrolyte} \cdot \frac{M_{MnO_2}}{A \cdot M_{Mn}} \tag{4.1}$$

where A is the active electrode area, M_{MnO_2} the molar mass of MnO_2, M_{Mn} the molar mass of Mn and $V_{electrolyte}$ the volume of the electrolyte solution at the time the sample was taken. In figure 4.7 a comparison between results from EQCM and ICP-MS can be seen. There are only minor discrepancies between

the two methods and the overall trend is the same.

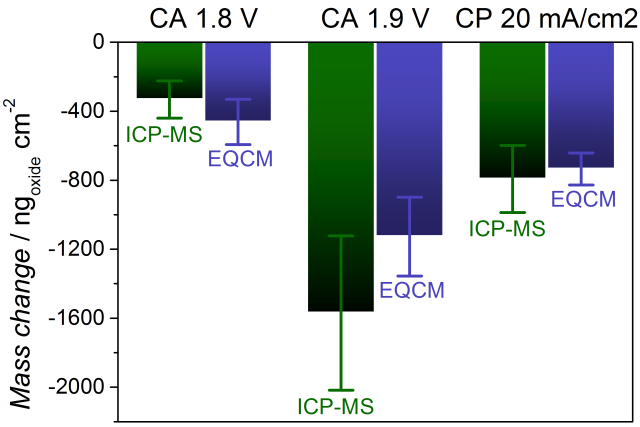

Figure 4.7: Comparison between EQCM (in blue) and ICP-MS (in green) results for the mass losses of MnO_x films. The two methods are compared with chronoamperometry (CA) at 1.8 and 1.9 V_{RHE} and chronopotentiometry (CP) at 20 mA/cm^2. The error bars indicate ± 1 standard deviation based on four independent measurements.

With the corrosion rate established as function of potential and time it is interesting to analyse the magnitude of current density that it represents. If we assume that the loss of MnO_x at the surface proceeds as the following reaction [138].

$$MnO_2 + 2H_2O \rightarrow MnO_4^- + 4H^+ + 3e^- \tag{4.2}$$

with three electrons transferred per Mn atom dissolved, a current density can be calculated from the dissolution rate. The dissolution rate is 1128 ng/cm^2 over two hours at 1.9 V_{RHE} based on the EQCM results, which corresponds to 0.5 μA/cm^2. The dissolution current is therefore more than four orders of magnitude lower than the total measured current density for the electrode. Such small currents are challenging to measure accurately with electrochemical methods. As an example the Faradaic efficiency towards oxygen evolution can be measured with rotating ring disk electrode, RRDE, systems [109,182]. However, slow processes such as the anodic MnO_4^- formation would be extremely difficult to identify since the rate corresponds to an efficiency of less than 0.001 %. In fact, even if the entire film of 40 nm dissolved in one hour the dissolution current would only be around 20 μA/cm^2 and the Faradaic efficiency would be 0.07 % which would be close to the accuracy limit of RRDE mesaurements. In table 4.1 the mass loss rates can be seen.

The dissolution rates can also be used to predict a lifetime for the thin films. At 1.9 V_{RHE} MnO_x lost 1128 ng/cm^2 over two hours and the lifetime of 40 nm

$\mathbf{MnO}_x$	$\Delta\mathbf{M}_{1.8\ \mathbf{V_{RHE}}}$	$\Delta\mathbf{M}_{1.9\ \mathbf{V_{RHE}}}$	$\Delta\mathbf{M}_{20\ \mathbf{mA/cm^2}}$
EQCM	-462 ±131	-1128 ±229	-735 ± 93
ICP-MS	-332±108	-1570 ±447	-793 ±194

Table 4.1: EQCM and ICP-MS results for MnO_x with chronoamperometry and chronopotentiometry tests. All values are in units of $[ng_{oxide}/cm^{-2}]$ and are measured over two hours.

MnO_2 is therefore 36 hours. Such a lifetime is naturally completely useless in an actual electrolyzer which should be able to run for several thousands of hours. At 1.8 V_{RHE} the dissolution rate is 462 ng/cm^2 for two hours corresponding to 87 hours which is rather long for a catalyst developer, who may want to vary a large number of parameters for a new and exciting material. The combination of EQCM and ICP-MS makes it possible to reveal the stability in short and reproducible tests that can be used to extend the understanding about materials at an early stage. For catalysts that are very stable these tests can also be used, but the level of accuracy must be kept in mind. With tests of two hours it is challenging to keep the drift of the frequency below 1 Hz. This corresponds to approximately 9 ng/cm^2 per hour. For a 40 nm film such a loss rate gives a lifetime of around 2000 hours. Using ICP-MS the detection limits can be extremely low so with this technique several years of stability could be predicted. As an example the detection limit for Mn is between 1 and 10 ppt. With a mass loss of 10 ppt or less in a 200 ml solution during 2 hours of electrochemical testing, the predicted lifetime of 40 nm would be 4100 hours. Such an example is quite idealised and assume a perfectly homogeneous film which may not hold in practise. However, it does give an impression of what can be done with short term tests. In an actual device the reaction conditions may differ substantially from idealised model investigations. Therefore, long term testing in relevant settings is necessary for establishing durability for finalized catalysts.

4.4 Conclusion

In this chapter the focus has been on developing a protocol to elucidate mass losses for OER catalysts with short term tests. To this end, manganese oxide thin films were deposited on EQCM samples and subjected to typical chronoamperometry and chronopotentiometry conditions. The activity reported here compares favourably to literature results for other Mn based catalysts. During two hour tests the catalyst shows some deactivation but more strikingly a constant loss of mass. These mass losses are measured carefully with both EQCM and ICP-MS, resulting in a good match between the methods and good reproducibility. The results show the importance of measuring mass losses instead of relying on purely electrochemical data. The mass loss rates can be used

to evaluate lifetimes and predict sudden death of similar electrodes for electrolysis. In fact, short term testing with accurate measurements of mass losses yields valuable information compared to tests where purely electrochemical data is produced. This is emphasized by the MnO_x catalyst shown here, which is predicted to last for more than two hours per nanometer at 1.8 V_{RHE} or more than 200 hours for a 100 nm thick film. Finally, these methods are not limited to the evaluation of oxygen evolution catalysts, but could be adapted to most electrochemical systems where catalysts are subjected to harsh and corrosive environments.

Chapter 5

Towards a stable and inexpensive catalyst for OER in acid

Sustainable production of hydrogen with electrolyzers has the potential to alleviate issues with fluctuating power supply from renewable sources, such as wind and solar power. As described in the introduction, Polymer Electrolyte Membrane cells, PEM, are particularly attractive due to their compact and simple design, fast start up and unmatched ionic conductivity. However, a major drawback is the extensive use of noble metal based catalysts for the oxygen electrode, the anode. For the hydrogen electrode, the search for non-precious materials has been a thriving research field for years with a large variety of interesting materials being identified as alternatives to platinum [57, 210]. This is not the case for the anode where, currently, there are no alternatives to precious metal oxides in acidic media. Furthermore, the loading of Ir constitutes a much larger issue compared to the extremely low loading of Pt used on the hydrogen electrode [41]. Most new and active catalysts that are active for OER in alkaline environment are based on Ni, Fe and Co. These transition metals are unfortunately not stable as solid phases in acidic environment [138]. Conversely, MnO_2, an intensely studied material due to its abundance and role in Photosystem II [155, 161], is stable as a solid phase in acidic pH from 1.3 to 1.7 V_{RHE} [138]. This potential range is important for water oxidation as it spans the range where an anode in an electrolyzer would operate. Although active, MnO_2 requires a significant overpotential to drive the oxygen evolution reaction

compared to Ru or Ir based catalysts, so the anodic formation of MnO_4^- above 1.7 V_{RHE} is an issue that must be taken into account. In the previous chapter the dissolution rates of MnO_x thin films were measured in alkaline environment and an unsatisfactory lifetime was predicted. In this chapter, focus will be on investigating the stability of the MnO_x films in acidic environment, together with a novel strategy for improving the stability. This strategy will first be explained on a basis of Density Functional Theory calculations and then an experimental approach will be presented. These findings are also reported as the appended paper III.

5.1 MnO_x thin films in sulfuric acid

To investigate the stability of MnO_x in acid, a test protocol similar to the one presented in chapter 4 was employed. The thin films were prepared in the same way and deposited on either quartz crystal microbalances or gold polycrystalline samples. The main difference from testing in alkaline stems from the fact that MnO_x dissolves as Mn^{2+} at potentials below 1.3 V_{RHE}. It is possible that in a real electrolyzer this could be solved by using a backup battery that can maintain the potential above a critical value at all times. However, for this early stage investigation the potentiostat is used instead of such a battery. The electrode was first immersed into the electrolyte under potential control at 1.4 V_{RHE}, using a Pt mesh as auxiliary working electrode. Then initial cyclic voltammetry, Electrochemical Impedance Spectroscopy, Ohmic drop correction and chronoamperometry techniques are started. The protocol is similar to the one presented in figure 4.4, but throughout the whole experiment the potential never drops below 1.4 V_{RHE}. The initial cyclic voltammetry is used to evaluate the activity which can be compared to the experimental studies reported in the literature, some of which are shown in figure 5.2. In figure 5.1 a first anodic scan is shown for the same type of thin film tested in both sulfuric acid and potassium hydroxide. There is a clear difference in the activity, which is much higher in alkaline solution. There is also a difference in the Tafel slope which in KOH is about 70 mV/decade and in H_2SO_4 170 mV/decade. The reason for the lower activity in acid is currently not well established in the literature. Nocera and co-workers proposed an explanation based on a disproportionation reaction which minimizes the amount of Mn^{3+} species at the surface in acidic solution [166]. Their conclusions were primarily based on analysing Tafel slope as function of the pH. However, these conclusions were for a catalyst with a Tafel slope higher than 600 mV/dec in acidic media. Takashima *et al.* had previsously reported a similar explanation based on UV-vis spectroelectrochemical detection of Mn^{3+}, which was observed to coincide with OER onset [164]. However, they tested the catalyst down to a pH of 4 and found the largest overpotential in neutral solution. The hypothesis about Mn^{3+} as the active species is in contrast to another report by Su *et al.* where MnO_2, or Mn^{4+}, was found

most stable at the surface of MnO_x at OER relevant potentials, based on DFT calculations [131]. The binding energies for MnO_2 to OER intermediates are also more favorable than the ones found for Mn_2O_3 [98]. The thermodynamic analysis from Pourbaix also shows MnO_2 as the most stable phase in both acid and alkaline under OER conditions [138].

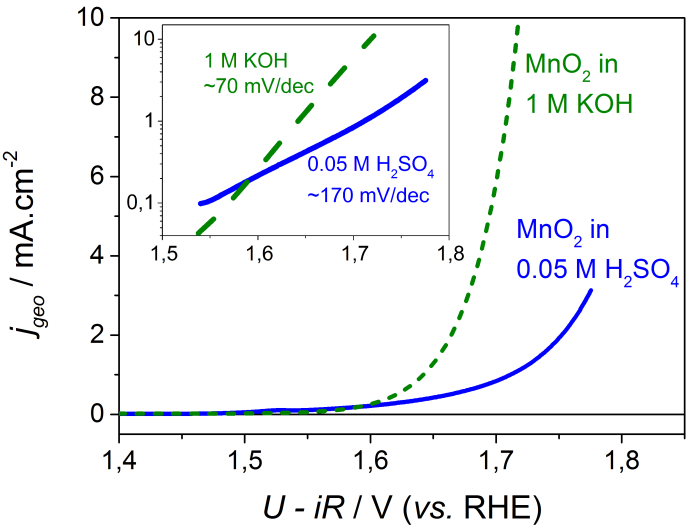

Figure 5.1: Cyclic voltammetry measurements of MnO_2 in 0.05 M H_2SO_4, blue line, and 1M KOH, dashed green line. Both measurements were taken with 5 mV/s in an RDE setup using 1600 RPM and the first anodic scan is shown. The inset shows the same data as a Tafel plot in a smaller potential range, from which the Tafel slopes can be found.

The question is how the activity of the thin films presented here compares to other reports of Mn based oxides tested in acid. The first of these reports date back to 1977 with the work done by Morita *et al.* [158] who prepared Mn oxide electrodes by thermal decomposition. More recent reports include electrodeposited thin films prepared by Huynh *et al.* [166], layered Mn-Ca oxides by Najafpour *et al.* [211] and δ-MnO_2 particles from Takashima *et al.* [164]. Due to the varying experimental conditions they will be compared on a turnover frequency, TOF, basis, taking into account an estimate of the amount of active sites contributing to the current. In figure 5.2 this comparison is shown, where a TOF range is given for each material.

The TOF_{min} is based on the total amount of Mn atoms used and gives a lower

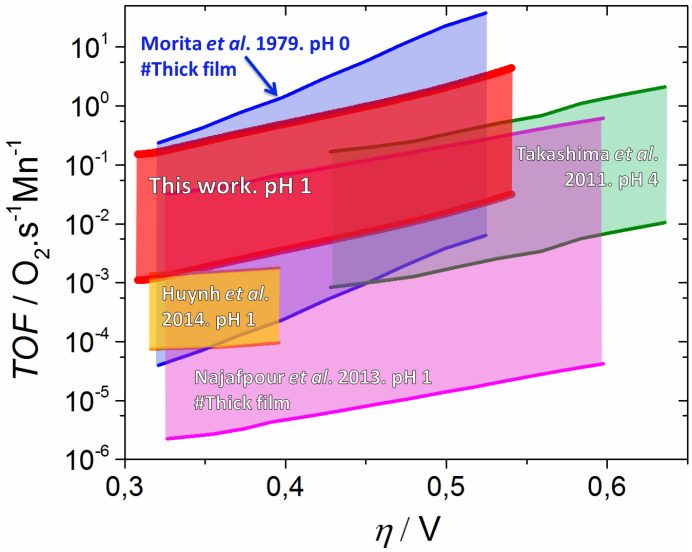

Figure 5.2: Comparison of activities achieved with MnO_x based catalysts for OER in acid on a TOF basis. The lower TOF is found from normalising with all Mn atoms in the catalyst, whereas the maximum is found from assuming a perfectly flat surface, where only the first layer participates in the reaction. The catalyst from this work is shown in red. The thick MnO_x catalyst from Morita *et al.* is in blue [158], the δ-MnO_2 catalyst from Takashima *et al.* in green [164], the electrodeposited MnO_x from Huynh *et al.* in yellow [166] and the Ca-MnO_x particles from Najafpour *et al.* in magenta [211].

limit of the turnover frequency. It was calculated with the following equation:

$$\mathrm{TOF}_{\min} = \frac{j \cdot M_{MnO_2}}{4 \cdot N_A \cdot e \cdot V_{cat} \cdot \rho_{MnO_2}} \tag{5.1}$$

where j is the current measured, M_{MnO_2} the molar mass of MnO_2, 4 electrons are transferred per O_2 molecule formed, N_A is Avogadro's constant, e is the elementary charge of an electron, V_{cat} the corresponding volume of the catalyst and ρ_{MnO_2} is the density of MnO_2. The $\mathrm{TOF}_{\max}$ is instead based on the Mn atoms of an atomically flat surface assuming that the electrodes reported in the respective papers have a roughness of 1. From the comparison in figure 5.2 the MnO_x thin film from this work stands out as the more active, except for the upper TOF limit of the electrode reported by Morita *et al.* It should be noted that the thermal decomposition method tends to yield high roughness factors [99] and in fact the same group later reported roughness factors between 50 and 100 for similar films [159]. It is likely that the roughness factor is proportional to the number of active sites available for the reaction. The stability in acid of the

MnO_x thin films used in this project will be evaluated from chronoamperometry experiments at 1.8 and 1.9 V_{RHE}, which are more anodic than the equilibrium potential of MnO_4^- formation. In 1 M KOH the dissolution rates were found to be 332 and 1570 ng/cm^2 over two hours respectively, using the results from ICP-MS. In figure 5.3 these results are compared to the rates in 0.05 M sulfuric acid.

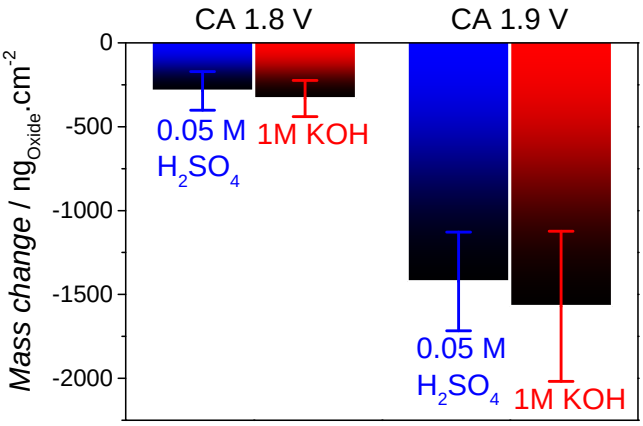

Figure 5.3: Comparison between the rates of mass loss of MnO_2 thin films in 0.05 M H_2SO_4 and 1 M KOH. The mass loss is for two hour tests at either 1.8 or 1.9 V_{RHE} and the error bars are based on at least three independent measurements.

The mass loss rates are similar in the two electrolytes and the predicted lifetimes are certainly not satisfactory for real devices, as discussed in chapter 4. However, if the MnO_2 surface could be meta-stabilized it could lead to development of inexpensive, active and stable catalysts for acidic water electrolysis. An investigation of a method for such a stabilization will be described in the next section.

5.2 A concept for improving stability of MnO_2

As mentioned in the previous chapter the anodic dissolution of MnO_2 occurs through formation of the permanganate ion, MnO_4^-, as described in equation 4.2. This process takes place at the surface of the thin film where the exposed Mn atoms can be oxidised. Interestingly, it has been reported that the sites that dissolve with the lowest energy barrier are undercoordinated sites, such as steps and kinks [212, 213]. The same conclusion can also be reached from a simple argument based on the surface formation energy. In a dissolution process an atom is removed from the surface, leaving behind a new surface structure with

a new surface formation energy. The difference in surface formation energies for initial and final state has to be considered in evaluating the probability of the process. If a kinked site or a stepped row are removed, the surface left behind has exactly same structure as before. In terms of surface formation energy there is no change either. If instead an atom from a flat terrace is removed it leaves behind a vacancy, which has a very high surface formation energy. The removal of atoms from the flat surface is therefore associated with an extra energy barrier and it is therefore likely that the undercoordinated sites are removed at lower potentials compared to flat surface sites. The activity of Mn oxides have been investigated with DFT calculations on the flat terrace sites, which matched very well with experimental results [131]. For other rutile oxides the coordinatively undersaturated sites (CUS), located on flat terraces, have been used to predict the activity [90, 98]. This leads to an interesting opportunity: if different sites are indeed responsible for activity and stability it could be possible to change the two properties independently from each other. To modify the stability the undercoordinated sites must be protected. This could be done by adding a more stable compound that would selectively block or terminate the undercoordinated sites. The prospect of selectively blocking some surface sites have been successfully carried out in numerous examples. For Ru(0001), deposited Au or Cu atoms were observed to selectively block the step edges [214, 215]. This had enormous impact on such surfaces for N_2 activation [216]. A study from Stensgaard and co-workers is particularly relevant for oxides, where it was observed that palladium would nucleate selectively on the step edges of Al_2O_3. For an MnO_2 surface this process was investigated with density functional theory, DFT, in my master thesis, which I conducted prior to this Ph.D project [217]. Here a brief description of the results will be given along with a short introduction to DFT.

5.2.1 Density Functional Theory

Density Functional Theory is a quantum mechanical theory that can be used to calculate fundamental properties of materials. Since no DFT calculations have been performed by me during this Ph.D only a short qualitative introduction will be given. The reader is referred to a book about the subject [218] and my master thesis [217]. With DFT, many-electron systems can be treated based on a functional of the electron density described with spatial coordinates. The theory originates from the idea of solving the time independent Schrödinger equation, which in principle facilitates calculating all relevant ground state information about a physical system:

$$\hat{\mathcal{H}}\Psi_n(\mathbf{R},\mathbf{r}) = \mathcal{E}_n\Psi_n(\mathbf{R},\mathbf{r}) \tag{5.2}$$

$\mathcal{E}_n$ are eigenvalues and $\Psi_n(\mathbf{R},\mathbf{r})$ are the eigenfunctions. The Hamiltonian $\hat{\mathcal{H}}$ is a complex operator which encompasses multicomponent, many body interactions

and solving the equation explicitly is practically impossible, except for very simple systems. Especially the repulsive interaction between electrons complicates the treatment of large systems. These include exchange interaction, which dictates that fermions can not occupy the same quantum state, and electronic correlation, describing the interaction between electrons. DFT relies on the Hohenberg-Kohn theorems which demonstrate that the ground state properties of a system of electrons can be uniquely determined from the electron density. In other words, if the electron density of a system is known, all ground state properties can be determined accurately. This is actually a huge advantage, since the density is a function of three spatial coordinates while treating every electron in a system with N electrons would include treating 3N coordinates. Furthermore, given a specific system of electrons, the correct electron density minimizes the energy functional. With the Kohn-Sham approach the density of electrons, and specifically exchange and correlation interactions, is approximated and can be varied slightly until a minimum in ground state energy is found. The approximation of the electron density to a high degree determines both the accuracy and the computational cost of the calculation.

5.2.2 Summary of DFT results for for MnO_2 modifications

Here a brief summary of the most important results from a previously conducted DFT study will be presented. The focus is on the concept which have been explored experimentally during the Ph.D. project. For more computational details the reader is referred to the appended paper III.
Steps and kinks of rutile MnO_2 were investigated for termination with Ti, Ge, Sn, Pt, Ru and Ir dioxides. All of these materials, except Ru, are stable at anodic potentials in acid. The question is which structure is energetically favourable. Besides the undercoordinated structures modifications of flat terrace sites and the bulk oxide were investigated. The energetics of adding the guest materials were evaluated as a termination energy, ΔE, based on the following equation:

$$\Delta E = E_{term} - E_{ref} - (E_{unit,guest} - E_{unit,ref}) \tag{5.3}$$

where E_{term} is the total energy of the terminated structure, E_{ref} the total energy of the original MnO_2 structure, $E_{unit,guest}$ the energy of a single unit of the termination material and $E_{unit,ref}$ the energy of a single unit of MnO_2 which is replaced. The energies of the single units are calculated as bulk formation energy of the rutile compound. If this termination energy, ΔE, is negative, it represents the energy gained by the system when another material is introduced. If positive, the overall system energy has increased which represents an unfavourable situation, i.e. a less stable structure.
While none of the materials exhibited favourable mixing into the bulk of MnO_2 or surface incorporation, the termination of steps was energetically favoured for

Ti and Ge which can be seen in figure 5.4. The termination energy for each material is plotted as a function of the surface formation energy of the (110) rutile surface. The trend shows that the system gains energy by terminating steps with materials that have a lower surface formation energy than MnO_2. On the other hand a less stable system is created by termination of MnO_2 with materials with a higher surface formation energy.

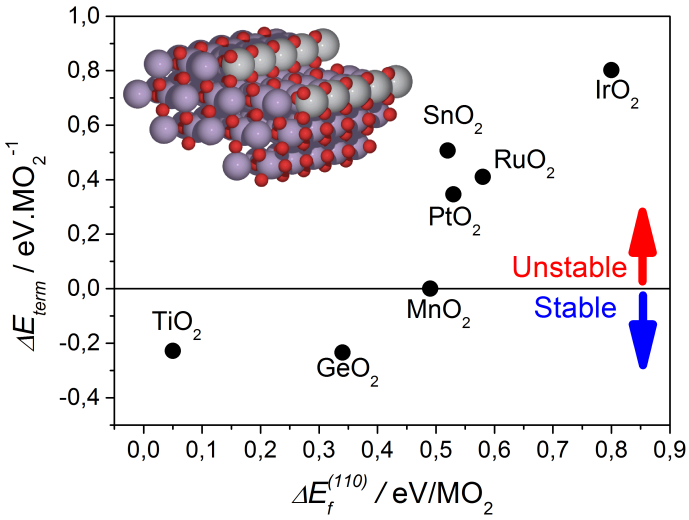

Figure 5.4: Termination energy for six different rutile metal dioxides on the steps of a rutile (120) MnO_2 surface as a function of the surface formation energy. The surface formation energies are taken from [219]. The red arrow indicates that a positive termination energy means that it will cost the system energy, whereas the blue arrow indicate an overall lowering of system energy.

The results suggest that termination of the steps with Ti and Ge is feasible. Modification of MnO_2 with TiO_2 is particularly promising as TiO_2 is abundant and has been proven a viable protection layer for other electrochemical systems [220–224]. The same type of calculations was also performed for kinked structures and again it was found that termination of Ti was favourable. These simple calculations indicate that it is feasible to terminate undercoordinated surface sites of MnO_2. In the following an experimental investigation of this concept will be presented.

5.3 Experimental validation of the concept

To investigate whether the stabilization concept could be realized experimentally, mixed Ti-MnO_2 films were prepared by sputter deposition. The deposition

parameters were the same as described earlier for the pure MnO_2 films with the exception that for the last 5 nm, Mn and Ti were co-deposited in a ratio corresponding to 4:1. The concentration value is on a total metal basis, i.e. $\frac{Ti}{Ti+Mn}$. The substrates were QCMs and Au polycrystalline samples which were kept at 200 °C during deposition. A schematic of the mixed thin film samples can be seen in figure 5.5.

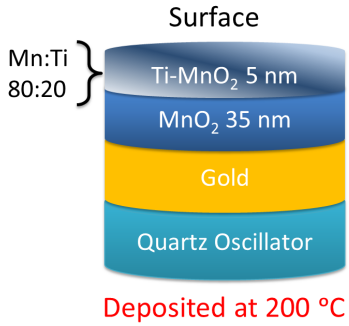

Figure 5.5: Schematic showing the layered structure of the thin film samples. The lowest layer, in teal, is a quartz oscillator which is used for the frequency measurement. A gold layer, in yellow, is deposited for electronic contact to the catalytic layer. Between the quartz and the gold a thin titanium layer is deposited for adhesion but this is not shown on the figure. On top of the gold layer a 35 nm thin MnO_2 film is deposited, shown in blue. Finally the last 5 nm consist of mixed Ti-MnO_2 deposited by co-sputtering, shown in lighter blue with a shadow line.

The deposition rates of Mn and Ti were calibrated with an in-chamber QCM to match 20 % Ti ratio and this was confirmed by X-ray Photoelectron Spectroscopy, XPS. XPS measurements were conducted before and after electrochemical test for a set of samples and Mn2p and Ti2p peaks were used for quantification. In figure 5.6a-d the XPS data can be seen for both peaks before and after testing. A simple integration of the peaks was used to obtain atomic percentage values. Both before and after test, the Mn:Ti ratios were approximately 4:1. The XPS measurements were also used to confirm that the Mn3s multiplet and Mn2p$\frac{1}{2}$ satellite positions were consistent with a MnO_2 stoichiometry, as for the pure films described in chapter 4. This was indeed the case and in this chapter the thin films will be denoted as Ti-MnO_2 and MnO_2.

The morphologies of these films were investigated with Scanning Electron Microscopy, SEM. Four different samples were used, MnO_2 and Ti-MnO_2 as prepared and after electrochemical testing. In this way, differences introduced by titanium modification could be investigated as well as from the stability tests. To facilitate comparison among the tested films, all the samples for SEM were deposited on EQCM substrates, which were then broken into smaller pieces and

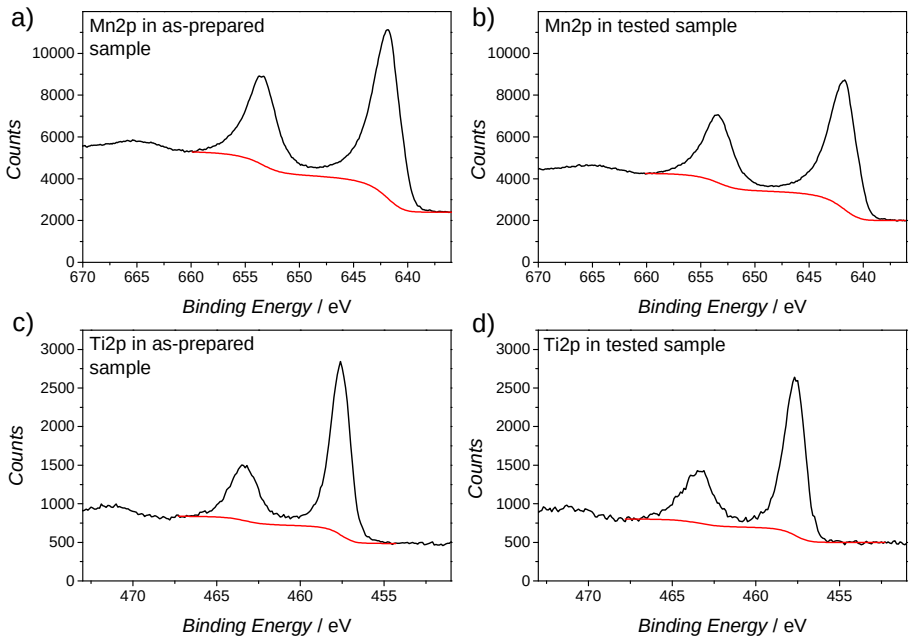

Figure 5.6: XPS measurements of the Mn2p and Ti2p peaks for Ti-MnO_2 films. a) Mn2p for the as-prepared sample. b) Mn2p for the tested sample. c) Ti2p for the as-prepared sample. d) Ti2p for the tested sample. These peaks were intergrated and used for quantification of the Ti content.

attached to aluminium stubs for the microscope stage. Since these substrates consist of a thin gold film on electronically insulating quartz it is critical to ensure that the film has optimal electronic contact to the stub. To avoid charging effects from the electron beam, silver paste was used to glue the samples to the stubs and only a small area of thin film was left visible. In figure 5.7a-d images of the surfaces can be seen.

The surface of an as-prepared MnO_2 thin film consists of small, elongated, plate-like structures in the size of approximately 10-20 nm, as shown in figure 5.7a. At the same time the structures seem densely packed and are not likely to contribute to a high roughness factor compared to electrodeposited samples or electrodes prepared by thermal decomposition [45, 151]. In figure 5.7b the surface of a tested MnO_2 film is shown and, compared to the as-prepared sample, there are only minor differences. The structures seem slightly more elongated and possibly a bit less densely packed. However, no dramatic changes has been induced from the electrochemical test. In figure 5.7c an as-prepared Ti-MnO_2 film can be seen, which again looks very similar to the pure MnO_2 film. The same plate-like features are visible. Finally, in figure 5.7d, a tested Ti-MnO_2

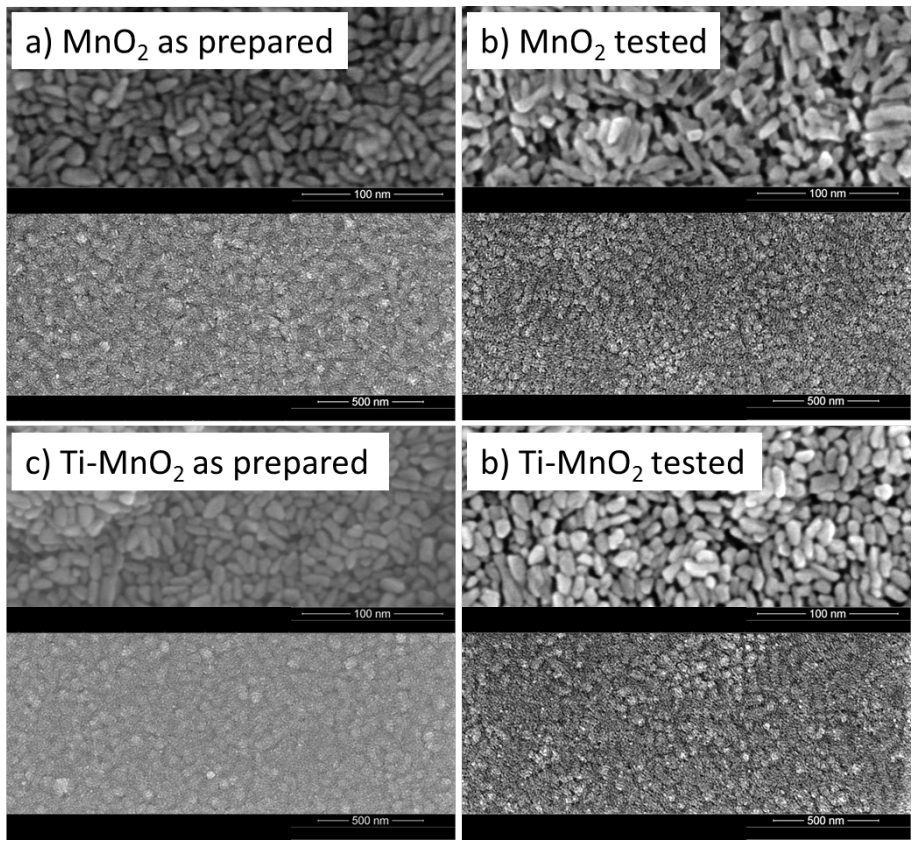

Figure 5.7: SEM micrographs of MnO_2 and Ti-MnO_2 films. a) Surface of as-prepared MnO_2. b) Surface of a tested MnO_2 film. c) Surface of as-prepared Ti-MnO_2 film. d) Surface of tested Ti-MnO_2 film. All images are taken with the FEI Helios EBS3 Microscope at DTU CEN and were acquired by Katarzyna Janik. Acceleration voltage was 3 kV and beam current 0.17 nA.

film is shown and there are no dramatic changes to observe. In fact, the tested Ti-MnO_2 surface looks similar to the as-prepared MnO_2 surface and appears slightly more dense than the surface of the tested MnO_2 in figure 5.7b. Overall, these images serve to show that: a) The thin films surfaces are not perfectly flat but consist of small nanoplates which are not likely to introduce a high roughness, b) modification with Ti does not lead to changes in surface morphology, which facilitates straighforward comparison of the electrochemical results and c) electrochemical testing of these samples does not seem to induce dramatic changes in the surface structure.

The films were subjected to the same tests as described in section 5.1. From the initial CVs it was observed that the activity was slightly lower for the mixed films. Ideally the activity could be kept at the same level, which would require an optimization of the Ti concentration and likely a fine-tuning of the temperature treatment. Optimally, the amount of Ti atoms added would match the number of undercoordinated sites since any excess of Ti is likely to lower the activity. Therefore, the current density could decrease with up to 20 % due to the Ti concentration. A deactivation is certainly observed from the CVs in figure 5.8a. However, after prolonged tests the current densities become more similar to each other as observed from the chronoamperometry test in figure 5.8b.

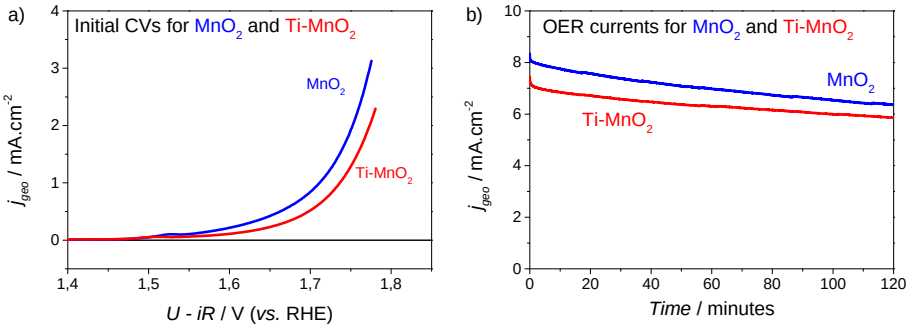

Figure 5.8: a) Cyclic voltammetry of MnO_2 and Ti-MnO_2 films at 5 mV/s. First anodic scans are shown for both. The potential scale has been corrected for Ohmic drop. b) Chronoamperometry test at 1.9 V_{RHE}. Test conducted in 0.05 M H_2SO_4. For both graphs results for the pure MnO_2 film are in blue and the Ti-MnO_2 in red.

The stability test protocol was carried out using both EQCM samples and RDE samples. For both setups, three samples with and three samples without Ti were tested. The results were then compared on basis of activity and stability. For the EQCM tests the results are summarized in figure 5.9. At 1.8 V_{RHE} the activity goes down with 18 % due to the Ti modification while the mass losses decrease with 47 %. At 1.9 V_{RHE} the activity is decreased with 10 % and the mass loss with 40 %. From these values it is clear that modification with Ti leads to a stabilizing effect for the MnO_2 surface, even though the mass losses are not completely stopped.

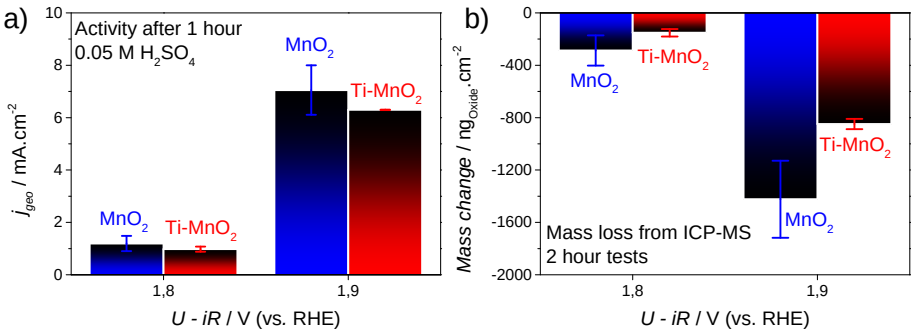

Figure 5.9: a) Activity of MnO_2 and Ti-MnO_2 supported on EQCM crystals at 1.8 and 1.9 V_{RHE} measured in 0.05 M sulfuric acid. The activity is expressed as the current density measured one hour into the test. b) Mass losses of MnO_2 and Ti-MnO_2 at 1.8 and 1.9 V_{RHE}. The mass losses here are based on ICP-MS measurements before and after each two hour test. For both graphs MnO_2 results are shown in blue and Ti-MnO_2 in red. Error bars indicate ± 1 standard deviation from three independent measurements.

The comparison in figure 5.9b is based on the ICP-MS measurements and these can be compared to the EQCM frequency measurements. In figure 5.10 the mass losses at 1.9 V_{RHE} as a function of time are shown, again based on three independent measurements for both Ti-MnO_2 and MnO_2. The mass losses start out in a similar pace but towards the end the rate of mass loss is in fact 40 % lower for the Ti modified films. It should be noted that the absolute mass loss measured with the EQCM is slightly lower than what is estimated from the ICP-MS, but the trends are the same.

Finally, the same type of experiments were carried out in a RDE setup using Au polycrystalline samples as disks. The RDE tests were conducted in a standard three electrode glass cell with rotation speed of 1600 RPM. In figure 5.11 the results of those tests can be seen. It is again evident that the mass loss decrease is more significant than the decrease in current density. It should be noted however, that both the current density and the mass loss after Ti modification are decreased by a larger percentage for the RDE tests compared to what is seen for the EQCM tests. At 1.9 V_{RHE} the current is decreased with 30 % and the mass loss 60 %. Nevertheless, there is still a significant difference between the two values with the mass loss decrease being the larger.

Without any selective termination effects a MnO_2 surface with 20 % TiO_2 is expected to have a 20 % decrease in activity towards OER combined with a 20 % slower dissolution rate. Judging from the results presented here this is not the case. For the EQCM tests the activity of Ti-MnO_2 approaches the one for pure MnO_2 after prolonged testing. At the same time, the mass losses are

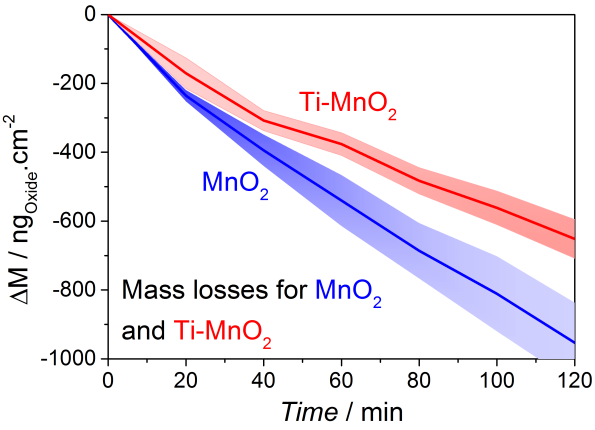

Figure 5.10: Mass change over time for MnO_2, blue, and Ti-MnO_2, red, during two hour chronoamperometry test at 1.9 V_{RHE} in 0.05 M H_2SO_4. The change in mass is based on measuring the frequency change with the EQCM. The shaded areas indicate ± 1 standard deviation from three independent measurements.

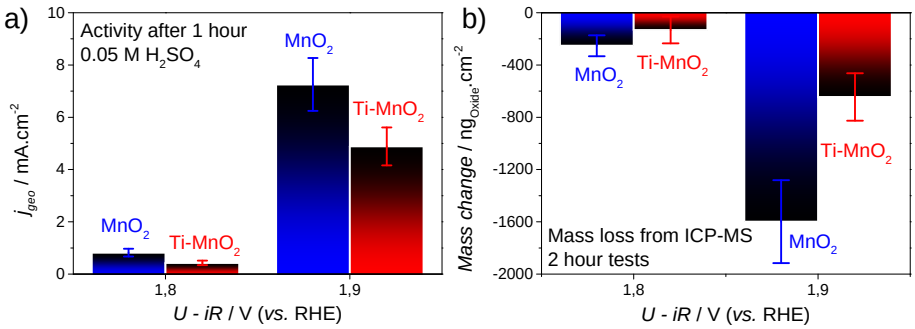

Figure 5.11: a) Activity of MnO_2 and Ti-MnO_2 supported on Au polycrystalline disks at 1.8 and 1.9 V_{RHE} measured in 0.05 M sulfuric acid. The activity is compared as the current density measured one hour into the test. b) Mass losses of MnO_2 and Ti-MnO_2 at 1.8 and 1.9 V_{RHE}. The mass losses here are based on ICP-MS measurements before and after each two hour test. For both graphs MnO_2 results are shown in blue and Ti-MnO_2 in red. Error bars indicate ± 1 standard deviation from three independent measurements.

decreased significantly more than the 20 %, indicating that a better compromise between stability and activity can be reached through the Ti modification. At the same time the XPS measurements showed that there is no enrichment of Ti in the surface after electrochemical testing. This is important since a

Ti rich surface could block the catalytic sites and over time make the surface completely inactive for oxygen evolution. These results are therefore consistent with the notion that undercoordinated sites on the MnO_2 surface are selectively terminated by Ti, causing a stabilizing effect without significantly blocking the oxygen evolution reaction. Further optimization of this concept could lead to even better performance. It is also possible that other materials could provide improved protection of the undercoordinated sites. In this study only TiO_2 was investigated experimentally, due to the earlier DFT study. However, since the MnO_2 film is not crystalline and the Ti modification still leads to a stabilized surface, it is likely that the most important criteria for successful termination is using a material with a very low surface formation energy which is also stable at highly oxidising conditions.

5.3.1 Stabilization in alkaline electrolyte

The Ti-MnO_2 films were also tested for stability in alkaline solution. As shown in figure 5.3, the mass losses for the pure MnO_2 films were very similar in acid and alkaline environment. It is therefore expected that the stabilization obtained by Ti modification works in alkaline as well. Tests confirming this notion were therefore carried out with 1 M KOH as electrolyte. The test protocol was the same as described previously, with cyclic voltammetry, stabilization at 1.4 V_{RHE} and then chronoamperometry at 1.8 and 1.9 V_{RHE}. In figure 5.12a and b the results are shown for activity and stability, respectively. The deactivation at 1.8 V_{RHE} is 47 % and at 1.9 V_{RHE} it is 30 %. These percentages are higher compared to the results for acidic electrolyte, where the corresponding deactivation was 19 and 10 % at those two potentials. It is possible that the Ti content in the samples used for alkaline measurements is slightly higher due to small changes in deposition rates over time. However, additional calibration of these rates indicated no such changes. The stability data in figure 5.12 shows that the Ti-MnO_2 exhibits significantly lower mass losses in alkaline environment compared to MnO_2. At 1.8 V_{RHE} the mass losses are 61 % lower and at 1.9 V_{RHE} the decrease is 65 %.

The measurements in alkaline therefore confirm that it is possible to obtain a more stable surface by mixing Ti into the MnO_2 film. In this case the deactivation turned out to be more significant but it was matched with a large decrease in mass loss. The results show that it is possible to obtain better balance between activity and stability and the results in alkaline adds to the generality of the concept.

At this point the results are suggesting that the concept of terminating undercoordinated sites can work. However, it is expected that through optimization of the deposition process, the deactivation could be avoided while achieving even lower mass losses. Judiciously chosen annealing treatments could induce mobility for the Ti atoms in the film. Furthermore, by varying the concentration it is possible that the number of undercoordinated sites at the surface can be

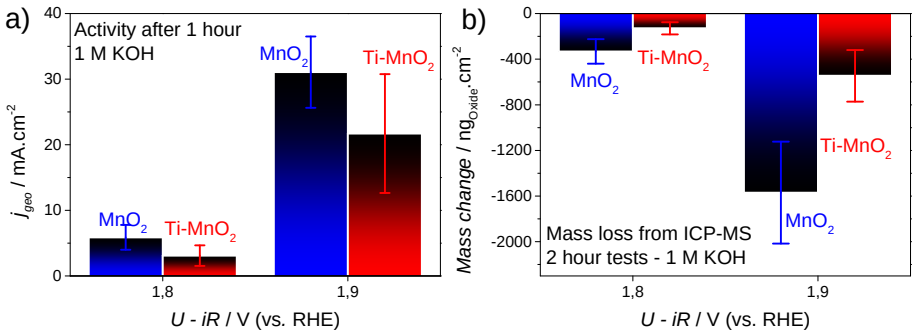

Figure 5.12: a) Activity of MnO_2 and Ti-MnO_2 supported on EQCM crystals at 1.8 and 1.9 V_{RHE} measured in 1 M KOH. The activity is compared as the current density measured one hour into the test. b) Mass losses of MnO_2 and Ti-MnO_2 at 1.8 and 1.9 V_{RHE}. The mass losses here are based on ICP-MS measurements before and after each two hour test. For both graphs MnO_2 results are shown in blue and Ti-MnO_2 in red. Error bars indicate ± 1 standard deviation from three independent measurements.

matched with a sufficient amount of Ti atoms. Another point worth discussing is the reproducibility of these experiments. So far the averaged results have been discussed and in the graphs error bars are shown based on standard deviation. In some cases these error bars are rather large, which indicates a large spread in results. This was especially true for the measurements in alkaline. At this stage it is difficult to assess the exact reason. However, both the current density measurements and mass losses are highly dependent on the electrochemical potential. As mentioned earlier, the applied potentials were corrected for Ohmic drops with a feature in the potentiostat but if the resistance of the system somehow change during a test, the current method does not accommodate for that. For just a few Ohms difference a large change in current density can be expected. In a few cases the Ohmic drop was measured before and after a two hour test and sometimes there would be a change of 1-2 Ohm, while in other instances it would be the same. These resistance changes could be a reason for the spread in current and mass losses, however, it is not likely to have a large impact on the overall results.

5.3.2 Titania overlayers for stabilized MnO_2

While most of this thesis follows a chronological order, this small section will be an exception. Initially, the stabilization predicted by the DFT calculations was investigated by depositing thin overlayers of titania, TiO_2, on top of the MnO_2 films. This is in contrast to the physical mixing of Ti and Mn obtained by co-sputtering as explained above. To indicate the difference between overlayer

TiO_2 and mixed oxides, the samples prepared with overlayers will be denoted TiO_2/MnO_2. These samples were tested with a slightly different protocol compared to what has been explained earlier; after initial cyclic voltammetry and a stabilization period at 1.4 V_{RHE}, chronoamperometry measurements were performed for one hour at 1.7, 1.75, 1.8 and 1.85 V_{RHE} subsequently. Furthermore, the stability is based solely on EQCM data, since the ICP-MS equipment had not been installed at the time. At 1.7 V_{RHE} both current and mass losses are negligible, hence, this data will not be included here. First, an overlayer thickness of nominally 1.5 Å was investigated. This thickness corresponds to approximately half a monolayer coverage assuming rutile (110) surface termination of TiO_2. Such an assumption is rather crude as these really thin layers are not very likely to be crystalline unless the conditions are met for epitaxial growth. In this case the MnO_2 film is not crystalline and epitaxial growth is not expected. Furthermore, the QCM calibration of deposition rates is made for thicker layers (15-20 Å), which means that for very thin films the uncertainty in rate is more critical. Depositing 1.5 Å is likely to result in too much TiO_2 but on the other hand with too little TiO_2 it could be difficult to measure any difference in stability. The results of depositing 1.5 Å TiO_2 on top of MnO_2 is shown in figures 5.13a and b.

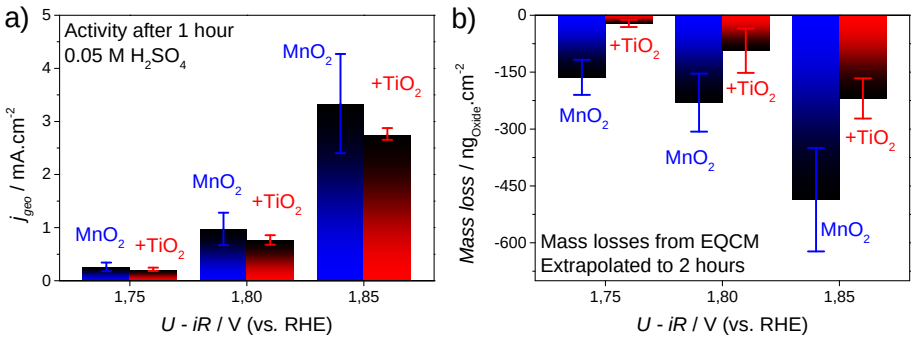

Figure 5.13: a) Activity of MnO_2 and TiO_2/MnO_2 at 1.75, 1.8 and 1.85 V_{RHE} measured in 0.05 M H_2SO_4. The activity is compared as the current density measured after one hour. b) Mass losses of MnO_2 and TiO_2/MnO_2 at 1.75, 1.8 and 1.85 V_{RHE}. The mass losses here are based on EQCM measurements of the frequency change during one hour tests. The TiO_2 layer is nominally 1.5 Å and the error bars indicate ± 1 standard deviation from 3 independent measurements.

The activity of the MnO_2 thin film has decreased upon addition of the TiO_2 overlayer. At 1.85 V_{RHE} the measured current is on average 17 % lower for TiO_2/MnO_2. In an ideal case where the MnO_2 is perfectly flat, 1.5 Å of TiO_2 is likely block a large fraction of the surface, leading to up to 50 % decrease in current density. However, the samples prepared here are not perfectly flat

as was observed with Scanning Electron Microscopy, figures 5.7a-d. It is also possible that excess TiO_2 forms particles with low adhesion to the surface. These factors complicate the evaluation of an appropriate amount of TiO_2 used to block the undercoordinated sites. However, from the stability results in figure 5.13b it is evident that the TiO_2 overlayer leads to lower mass losses. At 1.85 V_{RHE} the mass losses are on average 55 % lower. It is therefore likely that less undercoordinated sites are available for dissolution. However, since the mass loss is not zero some of these sites are still not covered, which could indicate that the mobility of TiO_2 on MnO_2 is too low at 200 °C. To test the effect of overlayer thickness two other samples were prepared; TiO_2/MnO_2 with 0.5 Å and 5 Å TiO_2. The mass losses measured for the short term tests are shown in figure 5.14.

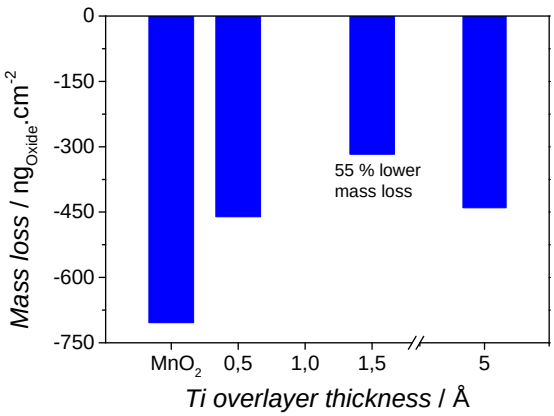

Figure 5.14: Mass losses at 1.85 V_{RHE} for MnO_2 and TiO_2/MnO_2 at 1.85 V_{RHE}, measured in 0.05 M H_2SO_4, as a function of overlayer thickness. The mass losses here are based on EQCM measurements of the frequency change during one hour tests.

A TiO_2 overlayer thickness of 0.5 Å results in lower mass losses compared to the pure MnO_2, 35 %, but the stabilization is less drastic than for 1.5 Å. Furthermore, a thicker overlayer of 5 Å only leads to a stabilization of around 37 % compared to pure MnO_2. These results indicate that there is an optimum in overlayer thickness, which is around 1.5 Å. It is especially surprising that the stabilizing effect of 5 Å is lower than for 1.5 Å but it could be explained with excess TiO_2 forming particles on the surface. Such particles would have a very different interaction with the MnO_2 surface and are not likely to selectively block undercoordinated sites. In fact, with the very low reactivity of TiO_2 particles it is possible that they will simply detach under reaction conditions. At the same time a low mobility of TiO_2 on MnO_2 could be the reason why a 0.5 Å layer is not stabilizing the surface as significantly as 1.5 Å. These three

overlayer samples were also tested for a prolonged time after the initial short term chronoamperometry. Specifically they were tested at 1.8 for 10 hours and then at 1.85 V for 8 hours, while the mass losses were evaluated with the EQCM frequency measurement. The results are shown in figure 5.15a and b, for current density and mass losses respectively.

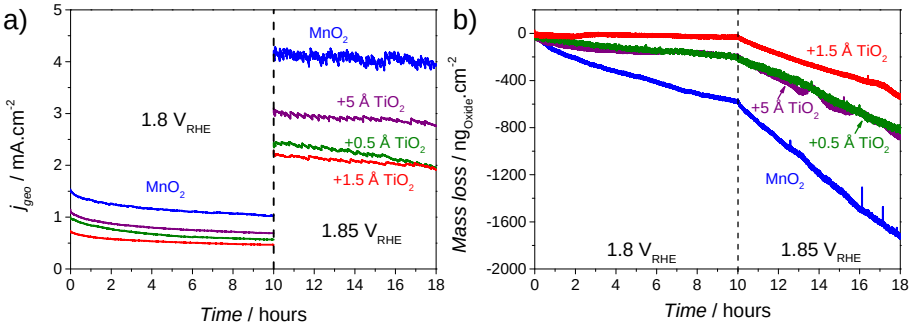

Figure 5.15: a) Current density of MnO_2 and TiO_2/MnO_2 samples at 1.8 and 1.85 V_{RHE}, measured in 0.05 M H_2SO_4. b) Mass losses of MnO_2 and TiO_2/MnO_2 at 1.8 and 1.85 V_{RHE}. The mass losses here are based on EQCM measurements of the frequency change. MnO_2 is in red, 0.5 Å TiO_2/MnO_2 in green, 1.5 Å TiO_2/MnO_2 in red and 5 Å TiO_2/MnO_2 in purple.

The activities of the TiO_2/MnO_2 are in this case significantly lower than the pure MnO_2. It should be noted that compared to the average for pure MnO_2, the sample used for long term testing had more than 30 % higher current density. Regarding the stabilizing effect of the overlayers it is again clear that the 1.5 Å thickness yields the most significant effect. After 10 hours at 1.8 V_{RHE} the 1.5 Å TiO_2/MnO_2 lost 93 % less mass compared to the pure MnO_2. After 18 hours the combined mass loss for 1.5 Å TiO_2/MnO_2 is 70 % less than what was observed for the pure MnO_2. However, the two other overlayer thicknesses, 0.5 and 5 Å, exhibited stability improvements less impressive than the 1.5 Å overlayer.

With overlayer deposition it is important that the mobility of the Ti atoms is sufficiently high so that the undercoordinated sites are blocked by incoming Ti atoms. The mobility can be tuned by changing substrate temperature. For all the samples presented here the substrate temperature was kept at 200 °C during deposition. It is possible that this is not high enough to give the titanium mobility at the surface and it is therefore an important parameter to investigate in future studies. At the same time there is a chance that the TiO_2 will simply form particles and minimize the interaction with the MnO_2 surface. In principle, the Ti atoms are sputtered off the target as single atoms or clusters consisting of very few atoms, however, if larger clusters were to form it could explain

insufficient coverage of undercoordinated sites.
For these reasons the TiO_2/MnO_2 approach was put on hold and mixed oxide films, Ti-MnO_2 were investigated instead. It would, however, be relevant to confirm the structure of the overlayers regarding particle formation and especially selective blocking of undercoordinated sites. Furthermore, varying the substrate temperature either during deposition or as an extra annealing treatment could lead to better results. Due to the time limit of my Ph.D. project these investigations were not pursued.

5.3.3 Cathodic dissolution in acid

The mixed Ti-MnO_2 films were also tested for cathodic dissolution in acid with and without titanium added to the surface. The cathodic dissolution process is different from the anodic since it is a reduction of the MnO_2 surface instead of an oxidation but it is possible that the TiO_2 can have a stabilizing effect towards that reaction as well. The dissolution reaction can be formulated as the following [138]:

$$MnO_2 + 4H^+ + 2e^- \rightarrow Mn^{2+} + 2H_2O \tag{5.4}$$

The equilibrium potential of this reduction reaction is 1.23 V at pH 0. This process is fast compared to anodic dissolution and therefore a slightly different experimental approach was followed. The MnO_2 and Ti-MnO_2 films were deposited on EQCM samples as before and the electrodes are again immersed under potential control at 1.4 V_{RHE}. Three initial potential cycles were then initiated, followed by a stabilization period at 1.4 V_{RHE}. After reaching close to zero drift in the frequency, the potential was cycled towards 1 V_{RHE} with a scan rate of 0.5 mV/s. This allowed for recording a dissolution profile, on the basis of the frequency change, as a function of applied potential. These profiles can be seen in figure 5.16 for both Ti-MnO_2 and MnO_2, based on three independent tests for each. The loss of mass observed with this experimental procedure is more drastic than what was observed for the anodic dissolution. At 1.15 V_{RHE}, 80 mV cathodic of the equilibrium potential, the pure MnO_2 films have lost 58 % of the original mass. In comparison the amount of material dissolved from the MnO_2 films after two hours at 1.9 V_{RHE}, 200 mV anodic of the MnO_4^- equilibrium potential, was approximately 7 %.
For the Ti modified films the mass loss profile is different from the MnO_2 films. At 1.15 V_{RHE} the mass loss of Ti-MnO_2 is 26 %, less than half of the mass lost in the pure films. This clearly suggests a stabilizing effect from the titanium, similar to what was observed for the anodic dissolution. The overall shift of the dissolution profile due to Ti is approximately 30 mV at 10 % of the mass dissolved and 40 mV at 90 %. For an actual electrolyzer such a potential shift is not likely to make a big difference. A battery solution will still be needed for providing potential control when the electrolyzer is not running. Nevertheless,

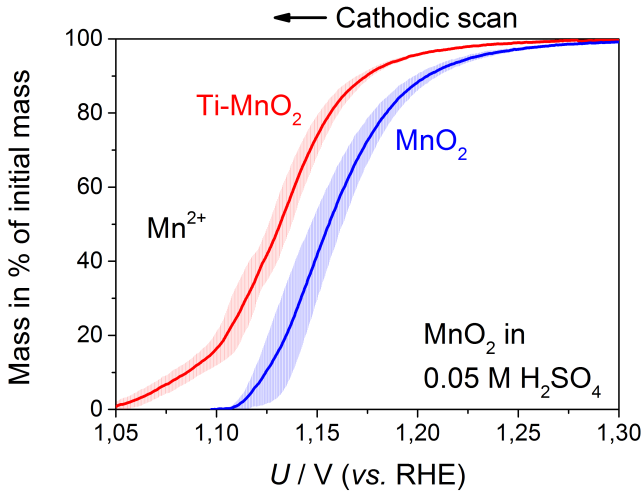

Figure 5.16: Change in mass for MnO_2, blue, and Ti-MnO_2, red, in 0.05 M H_2SO_4 when the potential is scanned cathodically from 1.4 to 1 V_{RHE} at 0.5 mV/s. The mass change is plotted as percentage of the original mass that is left on the electrode as function of the potential. The shaded areas indicate ± 1 standard deviation from three independent measurements.

it is promising that the stabilization strategy is likely to improve both cathodic and anodic stability of MnO_2.

5.4 Conclusion

In this chapter the stability and activity towards oxygen evolution of Mn oxide thin films have been characterized in acidic environment. The motivation behind this study is the lack of active non-noble metal based catalysts for OER that can work in the acidic environment of PEM cells. MnO_2 is a unique material since it is an active OER catalyst and is stable in acid in the potential region relevant for water oxidation. Regarding activity, the films are significantly less active in sulfuric acid compared to in potassium hydroxide. More specifically they suffer from a high Tafel slope of 170 mV/decade in acid compared to approximately 70 mV/decade in alkaline. Furthermore, at 400 mV overpotential the current density in acid is around half the one achieved in alkaline. However, even with this deactivation it was shown that the films prepared for this project are among the most active non-precious metal oxides for oxygen evolution, albeit still far from the performance of Ru or Ir based electrodes. The stability of the films was characterized with EQCM and ICP-MS measurements using a rigorous test protocol. The mass losses due to anodic dissolution were found to be the same

for alkaline and acid based on the two hour tests at 1.8 and 1.9 V_{RHE}. These mass loss rates yield a fairly short lifetime for the films which must be improved if they are to be used in electrolyzers. Therefore a strategy for stabilization was presented, including a short summary of a DFT study previously carried out as a master project. The concept is based on terminating undercoordinated sites that are likely to dominate in the dissolution process. TiO_2 was found to be a possible termination material, and was tested experimentally. Mixed Ti-MnO_2 films, with 20 % Ti, were prepared by co-sputtering and characterized with XPS and electrochemical tests. The mixed films exhibited slightly lower activities but also significantly lower mass losses compared to the pure MnO_2. At 1.9 V_{RHE} the mixed films sustained 10 % lower current density, while the mass losses were 40 % lower. Finally, the rate of cathodic dissolution, a very fast process, was investigated for both mixed Ti-MnO_2 and MnO_2. The introduction of Ti led to a more stable surface, which dissolved at around 25-30 mV more cathodic potentials. The results presented here serve as a first step towards inexpensive catalysts for OER in PEM cells. It is not likely that the stability improvements reached are enough to facilitate the use of Mn based catalysts but to this author's best knowledge, it is currently the first viable strategy to stabilizing an OER catalyst for use in acid. With further optimization of the preparation technique and a wider search for material combinations it could be possible to reach the goal of a catalyst that is based on abundant elements.

Chapter 6

The beneficial interaction between Au and MnO_x

The search for new electrocatalysts for the oxygen evolution reaction has long involved mixed materials benefiting from interactions rather than the addition of their individual properties. However, with the scaling relations in place it appears that further activity enhancements are highly unlikely from most standard surface structures. Even with close to optimal binding energies to intermediates, an overpotential of around 300 mV seems necessary to drive the oxygen evolution reaction at appreciable current densities. Constructing surfaces for which the scaling relations do not hold is therefore a critical challenge. In chapter 2, section 2.5.2, a few examples of beneficial combinations of materials were highlighted. In this chapter the focus will be on the interaction between Au and MnO_x, which results in large activity improvements. First, a conceptual model based on binding energies will be introduced, see appended paper II. Then an experimental approach will be presented, where the objective is a comprehensive characterization of mixed Mn-Au thin films. The experimental results obtained from this study constitute the basis for the appended paper IV.

6.1 Theoretical model of Au-MnO_x interaction

As mentioned in chapter 2, scaling relations express the linear relationship regarding binding energies for alike adsorbates. Specifically for the oxygen evolution reaction, *O, *OH and *OOH bind in a similar fashion to most surfaces and changing the binding strength to one of them necessarily changes the binding

to the two others. The scaling relations therefore implies a constant offset in binding energy between *OH and *OOH of approximately 3.2 eV for a large range of materials. Since the optimal catalyst should have an offset of 2.46 eV the scaling relations predict that the best catalysts will need $\frac{3.2-2.46\text{eV}}{2e} = 0.37$ V in overpotential to drive the reaction at high current densities [98]. To find better catalysts it is necessary to design surfaces that do not obey the scaling relations. However, an interesting starting point for such a venture is to look for materials that exhibit activity improvements beyond what is predicted from the binding energies. For this project it is particularly interesting that the activity of MnO_x based materials have been reported improve in OER activity when Au is present either as a substrate or as nanoparticles [225–227]. The same has been found for CoO_x and Ni hydroxides [228–230]. In figure 6.1 a few selected examples can be seen.

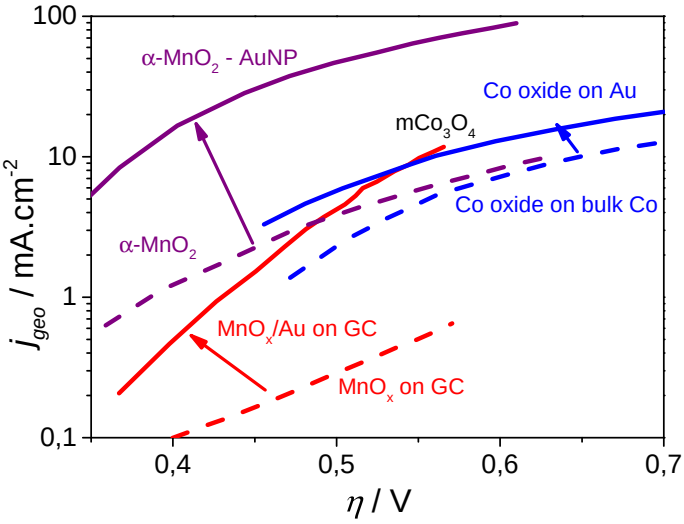

Figure 6.1: Examples from literature combined in a Tafel plot, where improvements in activity towards OER are obtained for Au-MnO_x and Au-CoO_x systems. α-MnO_2-AuNP results are from Kuo *et al.* [226] and are shown in purple. MnO_x/Au on GC is from Gorlin *et al.* [225] and are shown in red. Co oxide on Au are from Lu *et al.* [228] and are shown in blue.

The improvements for the mixed Au-MnO_x systems are significant with decreasing overpotentials ranging from 100 - 200 mV for the same current density. Currently, there is no established explanation for the activity enhancements. From the work by Kuo *et al.* it is proposed that Au facilitates the formation of more active Mn^{3+} species on the surface, which they state have a more labile Mn-O bond compared to Mn^{2+} and Mn^{4+}. This statement was supported

by ex-situ X-ray Absorption Near Edge Spectroscopy, XANES, measurements, where they observed a small shift of the Mn K-edge threshold towards lower energies when Au is present. Such an energy shift would be consistent with a small decrease of the average oxidation state of Mn. However, from DFT calculations and the Pourbaix diagram of Mn in aqueous environment, it is not expected that a high concentration of Mn^{3+} can be sustained at potentials above 1.4 V_{RHE} where MnO_2 is the most stable oxide [131, 138]. At the same time the binding energy of $^*O$ to Mn_2O_3 is too strong so that the formation of $^*OOH$ requires a large overpotential [98, 131]. On MnO_2 the binding energies are actually distributed a bit better for oxygen evolution.
For Ni and Co hydroxides supported on gold another explanation was proposed by Yeo *et al.* based on charge transfer from the transition metal to the noble metal [229, 230]. Au is a very electronegative metal and therefore it is feasible that such a charge transfer could occur. Nickel based hydroxides were studied in [230], where the authors observed that submonolayer thin films supported on Au were significantly more active than when it was supported on Pd. In their discussion it was argued that the Au facilitated oxidation of the Ni. For Co oxides, a series of noble metal substrates were tested and it was again found that using a Au substrate resulted in the highest activity [229]. The authors argued that a 4+ state of Co was important for the OER activity and that Au facilitated the oxidation of the Co sites. Similar effects could be valid for MnO_x. However, if the early oxidation to 4+ is critical it is surprising that MnO_2 is not significantly outperforming lower oxides [162]. Furthermore, the MnO_2 catalyst reported by Kuo *et al.* can still be improved with Au particles. The combined studies at this point therefore suggests that Au assumes a role beyond charge transfer.
In a study on RuO_2 doped with Ni or Co, an explanation for the improved activity has been proposed on the basis of proton transfer from $^*OOH$ at the catalytic site to a nearby proton acceptor [108]. For RuO_2 a lower overpotential could be realized if the $^*OOH$ intermediate was bound a bit stronger to the surface. If a proton acceptor is present at the surface, right next to the active catalytic site, it is possible that the $^*OOH$ intermediate would be formed with a larger probability due to instant transfer of $^*H$ and conversion into an oxygen molecule that can leave the surface. For RuO_2, oxidised Ni or Co atoms placed in a bridging position on the rutile (110) surface could function as proton acceptors [108]. Similarly to RuO_2, MnO_2 would benefit from such a proton transfer mechanism, since the $^*OOH$ step is potential determining. In figure 6.2 the possible proton transfer mechanism is illustrated schematically for MnO_2 in the presence of Au. On the illustration two scenarios are depicted, one where Au is present as a particle and one where Au is present as part of the surface. It should be noted that the illustration is purely for explanatory purposes and does not represent the actual surface for which DFT calculations were carried out.
The proton transfer mechanism was therefore investigated for a MnO_2 system based on DFT calculations. The calculations were performed by Dr. Michael

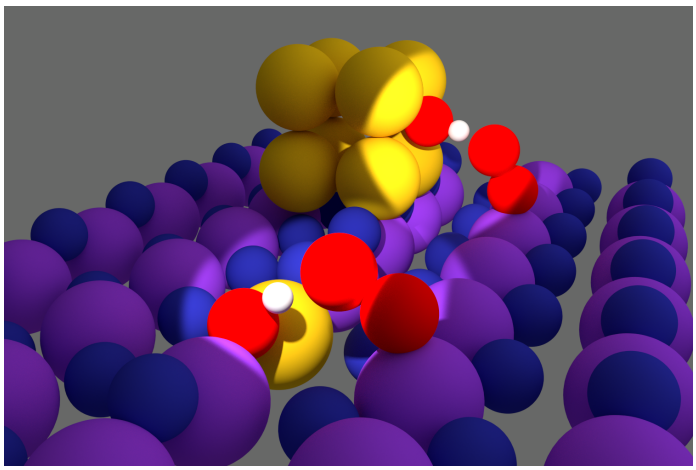

Figure 6.2: Cartoon illustrating the possible proton transfer mechanism for a rutile (110) MnO_2 surface in the presence of Au. The highlighted area in front shows an Au atom incorporated at a Bridge site, which makes the bridging oxygen available as a proton acceptor for the *OOH intermediate. The highlighted area in the back depicts another scenario where a gold nanoparticle acts as proton acceptor for the *OOH intermediate adsorbed on an active Mn site. It should be noted that this figure is an illustration and does not represent the exact surface used for calculations.

Busch at CAMd, DTU Physics. For more details the reader is referred to the appended paper II. Instead a summary of the most important conclusions will be given here. First the binding energies of *O, *OH and *OOH were calculated for both MnO_2 and Mn_2O_3, resulting in the free energy diagrams shown in figure 6.3. The binding of a hydrogen atom to the nearby Au site was modelled in a simple way, by using the Au(111) surface at a third ML coverage of *O, as reported in [89].

From the free energy diagrams it can be seen that introducing the proton transfer significantly decreases the required energy for reaching the *OOH step. This is true for both MnO_2 and Mn_2O_3. For a pure Mn_2O_3 surface the predicted overpotential would be around 1 V whereas the MnO_2 surface would give around 0.5 V. When assuming proton transfer to a gold site these values decreases to 0.2 V for Mn_2O_3 and 0.4 V for MnO_2. The reason for the drastic change of overpotential for Mn_2O_3 is that the binding of *O and *OH is close to the ideal values although a bit too strong. When the *OOH binding is stabilized, all the binding energies are very close to ideal and either the O-O bond formation or the H-transfer to a nearby Au site becomes potential determining. It should be noted that it is doubtful whether such a surface will be stable under reaction conditions, since the MnO_2 phase is expected to be the most stable phase at

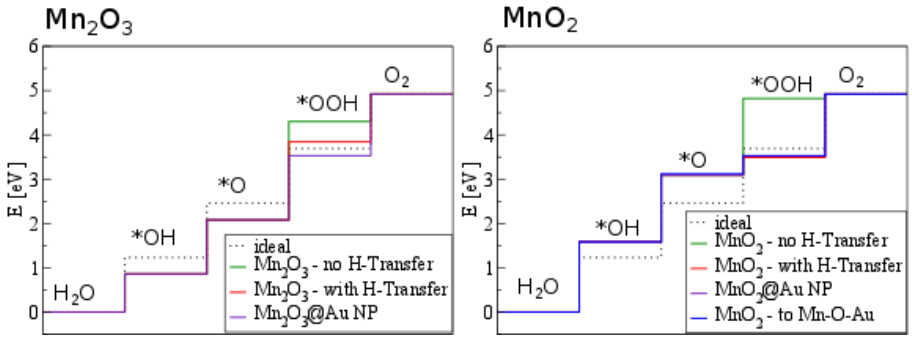

Figure 6.3: Free energy diagrams for the oxygen evolution reaction on Mn_2O_3, to the left, and MnO_2, to the right. Left: In green no H-transfer is assumed which results in a high energy for *OOH compared to *O. In red the H-transfer is included which results in a lowering of the *OOH step. In blue the results are shown for proton transfer to a nearby Au site, which indicates a further lowering of the *OOH step. Right: In green no H-transfer is included and the *OOH step is high in free energy. In red the H transfer is included, in purple a nearby Au NP is considered to facilitate H-transfer and in blue an incorporated Au atom is considered for H-transfer. Note that the red, purple and blue lines coincide and all lead to a siginificant lowering of the *OOH binding energy. For both diagrams the dotted line indicate the ideal OER catalyst, where all steps require 1.23 V to become flat.

those potentials [131]. For MnO_2 the proton transfer mechanism could in theory be possible on two neighbouring Mn sites, however, since both sites are active for OER, it is unlikely that one of the sites will be efficient as continuous proton acceptor site. Instead, it is more likely to happen with a nearby Au site, which is inactive for water oxidation at low overpotentials. At a potential of around 1.4 V_{RHE} it is thermodynamically favourable to transfer and remove protons to such a site. The predicted overpotentials for the two Mn oxides together with similar analysis for Co oxides are shown in figure 6.4 as a function of the descriptor $\Delta G_{*O} - \Delta G_{*OH}$. From this model materials on the left side of the peak, at 1.6 eV, are predicted to benefit from the proton transfer mechanism, whereas materials on the right side are not. On the right side the potential determining step is the oxidation of water to form *O, meaning that a stabilization of *OOH has minimum impact on the activity.

In summary, these DFT calculations provide a possible explanation for the activity enhancement. In terms of absolute decrease in overpotential it is difficult to directly compare to experimentally measured values. This is due to an unknown fraction of Mn sites with Au neighbours as well as an often unknown roughness factor. On the other hand the DFT calculations are not accurate enough to fully predict absolute values of overpotential, although the trends described are expected to be robust.

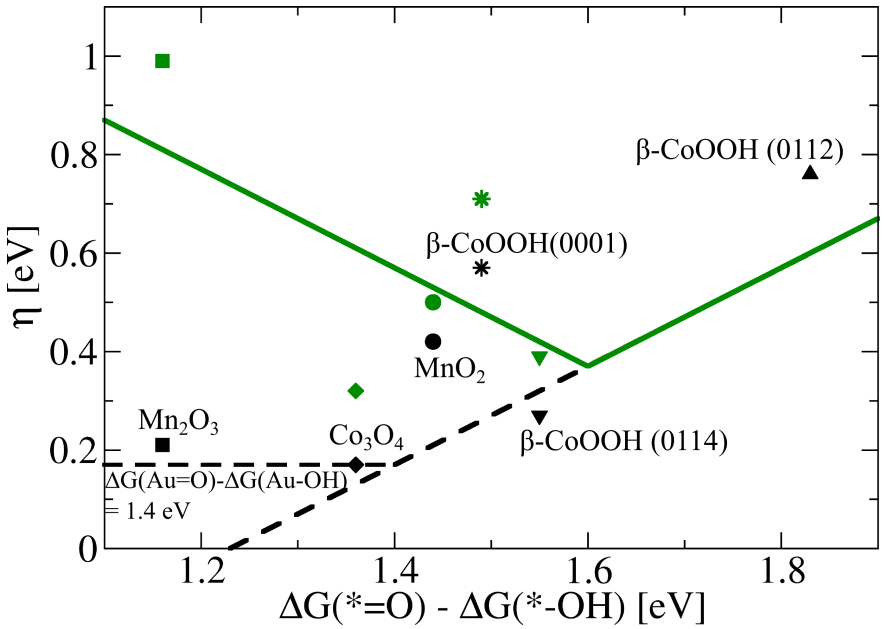

Figure 6.4: Volcano shaped activity plot for OER. The predicted overpotential is plotted as function of the calculated difference in free energy for the $^*O$ and $^*OOH$ steps. The solid green lines are based on scaling relations from [98]. The green points indicate calculations for specific oxides when proton transfer is not included in the analysis. Black points indicate the predicted overpotential for each surface when proton transfer is included. The dashed sloped line indicate how the scaling relations would predict overpotential if the $^*OOH$ binding energy could be optimized independently from the other intermediates. The horizontal dashed line indicate the potential where proton transfer to Au can be expected and at the same time a lower bound of the overpotential that can be expected from including such a transfer mechanism with Au.

6.2 Experimental investigation of Au-MnO_x catalysts

To understand the interaction between Au and Mn our approach was to maximise the number of neighbouring Mn-Au sites in catalytically active thin films. To this end, mixed Au-MnO_x thin films were prepared with a co-sputtering deposition procedure. The thickness of the films was again nominally 40 nm and glassy carbon disks were used as substrates. Adhesion to the glassy carbon was found to be enhanced by a sputter cleaning procedure of the carbon surface prior to deposition. This was done for 10 minutes in the sputter chamber with a 50 W

RF plasma and a bias on the substrate holder. After the cleaning substrate, Mn and Au were co-sputtered with rates calibrated by the in chamber QCM. The sputter deposition was carried out differently than for the films in chapter 4 and 5, where a slow rate of MnO_x deposition was used. The Au sputter yield is high compared to that of Mn in the presence of oxygen, so the argon to oxygen ratio was changed from 25:5 to 25:3. This ensured a higher rate of MnO_x, which could then be matched with the Au rate. Furthermore, with a low overall deposition rate there would be a greater chance of the Au forming large domains due to high mobility of Au atoms. The substrate temperature during deposition was kept at 200 °C. The focus of this study will be on comparing two different Au concentrations (30 and 50 % on a total metal basis) in MnO_x with pure MnO_x films.

6.2.1 Characterization

The prepared thin films were characterized to investigate any differences due to the changed preparation procedure and Au modification. First X-ray Photoelectron Spectroscopy was used to quantify the Mn:Au ratio in the films and to get an initial estimation of the Mn:O stoichiometry. The stoichiometry can be evaluated with the $Mn2p\frac{1}{2}$ satellite distance and Mn3s multiplet splitting, as explained in section 3.2.1. In figure 6.5a and b the Mn2p and Mn3s spectra can be seen for the MnO_x films prepared with a lower oxygen partial pressure. For the pure MnO_x film the distance between the $Mn2p\frac{1}{2}$ peak and its satellite is found to be 10.1 eV. The distance between the two peaks in the Mn3s spectrum is 5.4 eV. These values match with reference values for the Mn_3O_4 oxide as seen in table 3.1. The Au concentrations were found from integrating the Mn2p and Au4d peaks, shown in figures 6.5a and c. The Au concentrations are reported on a total metal basis, i.e. $\frac{Au}{Au+Mn}$.
In order to investigate the structure of the mixed films, Glancing Angle X-ray Diffraction experiments were carried out. For these measurements the films were deposited with double thickness, to increase signal from the films, on SiO_2 windows. The resulting diffractograms can be seen in figure 6.6a and b, for pure MnO_x and Au modified films respectively.
The pure MnO_x film matches well with a Mn_3O_4 structure based on nine observed peaks. From this point the pure Mn oxide films will therefore be denoted Mn_3O_4. This Mn:O stoichiometry is consistent with a lower amount of oxygen available during deposition and is in contrast to the disordered MnO_2 prepared at higher oxygen flow used previously. Interestingly, the ratios of peak heights do not match the powder standard reference, which indicates preferential growth of some planes, which is not unusual for thin films. However, from 6.6b, where the results from mixed films are shown, the Mn_3O_4 phase vanishes upon introduction of Au. Instead, the four most pronounced Au peaks are observed. For both concentrations the peaks are broad which indicates small Au domains located in the Mn_3O_4 film. The peaks are slightly broader in the film with 30 %

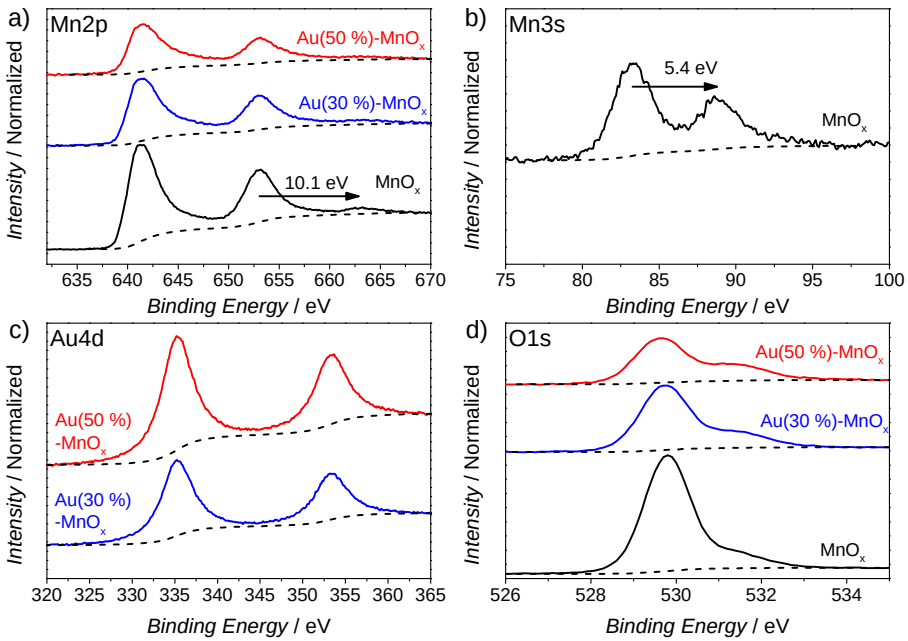

Figure 6.5: XPS spectra for the three films. a) Mn2p region. An arrow indicates the distance for the Mn2p$\frac{1}{2}$ satellite. b) Mn3s region. An arrow indicates the distance between the two peaks. c) Au4d region. d) O1s region. For all the spectra pure MnO_x is shown in black, Au(30 %)-MnO_x in blue and Au(50 %)-MnO_x in red.

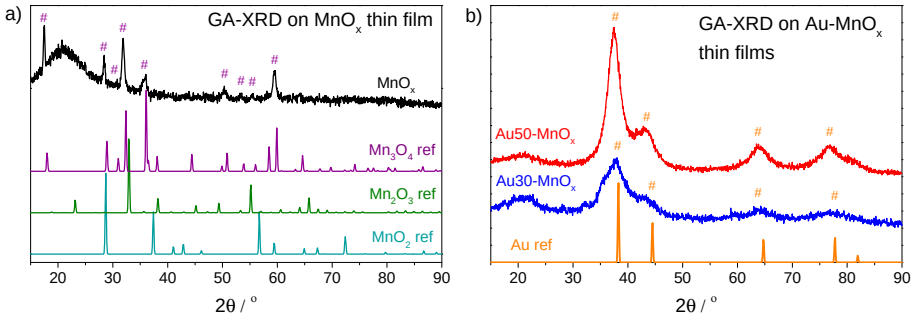

Figure 6.6: X-ray diffractograms. a) Pure MnO_x films (in black) together with references from literature. Mn_3O_4 reference (purple) is from [231], Mn_2O_3 (green) is from [232] and MnO_2 (teal) is from [233]. b) Au(30 %)-MnO_x (blue) film and Au(50 %)-MnO_x (red) together with an Au reference (orange) from [234].

Au. With the Scherrer equation it is possible to evaluate domain size based on the peak broadening, as explained in chapter 3. This analysis indicates that 30 % Au in the film results in Au domains of about 2 nm in size. At 50 % the domains reach 3 nm. So despite the co-sputtering method there are clearly particle formation taking place under deposition conditions. However, these nanosized Au domains are still expected to be dispersed into the Mn_3O_4 matrix, yielding a high density of Mn-Au sites. Due to the lack of Mn oxide peaks for the mixed films, they will be denoted Au-MnO_x from this point.

Scanning Electron Microscopy was employed to get an overview of the surface morphology. The images shown in this section are taken with secondary electron detection so that the contrast stems from surface morphology. In figure 6.7a and b the surface of a pure Mn_3O_4 film can be seen with two magnifications. The micrographs indicate that the surface consists of pyramid shaped features in the size range of 10 to 20 nm. At the same time these features are quite densely packed and the surface does not appear porous. It should also be noted that the surface of this film looks significantly different from the MnO_2 films shown in figure 5.7 in chapter 5, where the features were rounded and less densely packed.

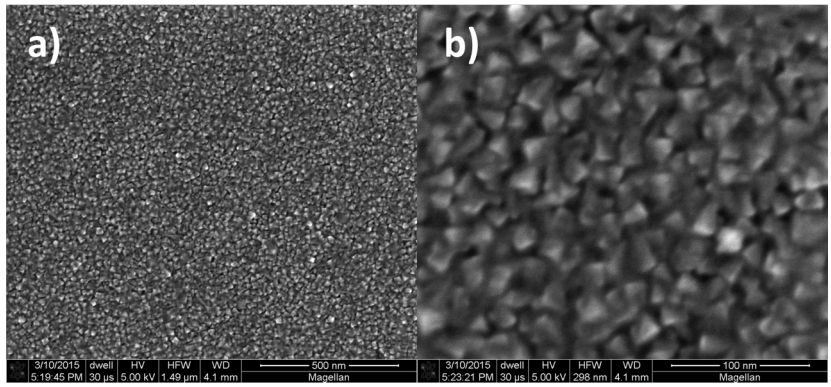

Figure 6.7: Scanning Electron Micrographs for pure Mn_3O_4 film. a) Overview image of the surface. b) Close-up revealing the surface structure.

In figure 6.8a and b images of a modified film with approximately 30 % Au are shown. The features for this surface are more rounded, almost spherical, with small bright spots. These roundish domains are also in the order of 10 to 20 nm. The surface is again quite densely packed but it looks like the introduced Au has stopped the MnO_x domains in growing in the same way as it was observed for the Mn_3O_4 film. This would also be consistent with the XRD results, where the mixed films only show peaks for Au. The surface for 50 % Au shows similar features and a slightly more porous structure, see figure 6.9a and b. It is tempting to interpret the bright spots in the images as gold particles, but this

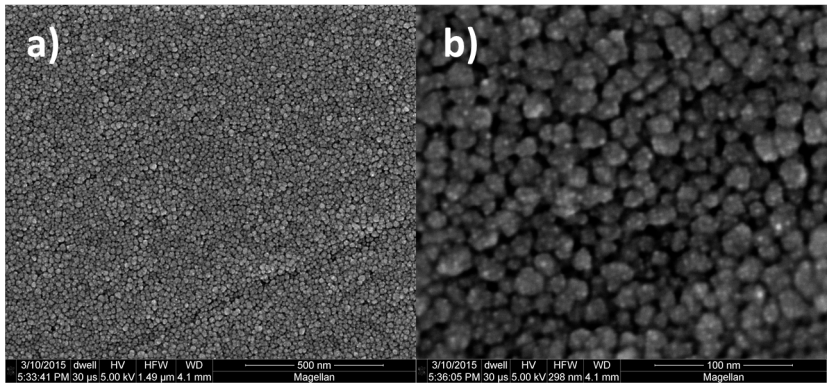

Figure 6.8: Scanning Electron Micrographs for pure Au(30%)-MnO_x film. a) Overview image of the surface. b) Close-up revealing the surface structure.

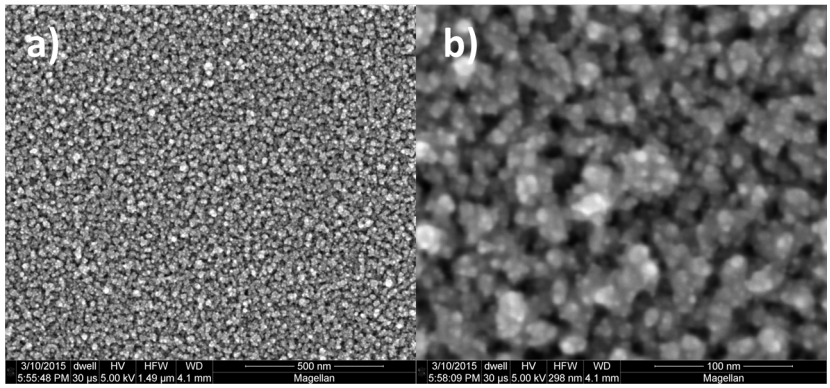

Figure 6.9: Scanning Electron Micrographs for pure Au(50%)-MnO_x film. a) Overview image of the surface. b) Close-up revealing the surface structure.

is not a straightforward analysis since the bright spots could also be caused by charging effects due to areas with low electronic conductivity.

6.2.2 Electrochemical characterization

The activities of these thin films were measured with cyclic voltammetry in 1 M KOH. A scan rate of 20 mV/s was used and for each type of sample three independent measurements were performed. The results of those measurements can be seen in figure 6.10, where the first anodic scans for the three types of films are shown.

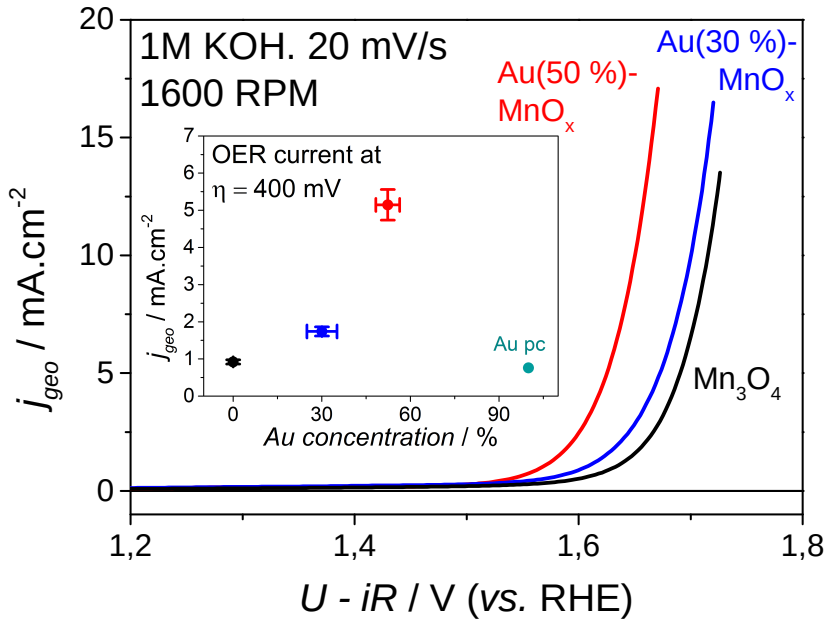

Figure 6.10: First anodic scan of Mn_3O_4 (black), Au(30%)-MnO_x (blue) and Au(50%)-MnO_x (red) films. Measurements were done in 1M KOH, with 1600 RPM and at 20 mV/s. The potential scale has been corrected for Ohmic drop. The inset shows current density of the films at an overpotential of 400 mV as function of the Au concentration. The activity of a gold polycrystalline disk is also shown in teal. Error bars are ±1 standard deviation from three independent measurements.

The inset of figure 6.10 shows a comparison of the current density at 400 mV overpotential for the films. Both Au concentrations lead to an increase in current density. However, 30 % Au lead to a 1.9 times improvement in current density while at 50 % the improvement is a factor of 5.5 over the pure Mn_3O_4. Another metric often used in comparing OER catalysts is the overpotential needed to reach 10 mA/cm^2. For the 50 % Au film the overpotential for reaching that current density is 65 mV lower than for the pure Mn_3O_4. Since the SEM images indicated a slight difference in porosity for the films, with the more active sample looking less densely packed, it is interesting to analyse the electrochemically active surface area. Double layer capacitance has been reported to be proportional to this area [109]. For these films the double layer capacitance could be approximated at 1.3 V_{RHE} where no other electrochemical process is expected to occur. The positive and negative currents measured for the second cycle at 1.3 V_{RHE} were therefore used as an evaluation of the pseudo capacitance. With this method the capacitances for the Au modified films were found to be slightly

higher than for the pure Mn_3O_4 film. The increase in capacitance over the pure Mn oxide film is plotted in figure 6.11 together with the improvement in current density at 400 mV overpotential. Assuming an increase in capacitance is proportional to an increase of the OER active sites, the increase in capacitance is not enough to explain the activity improvement observed for 30 or 50 % gold.

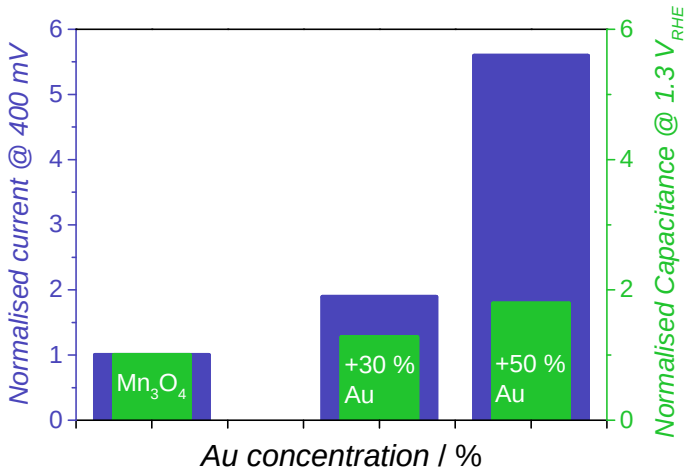

Figure 6.11: Current density increase (in blue) and pseudo capacitance increase (in green) for the thin films as function of gold concentration. Both scales are normalised to the value obtained for Mn_3O_4.

With such an improvement in activity it is interesting to further analyse the differences in behavior for these films. Especially the changes of Mn and Au under reaction conditions are of interest. Such a study can be done with in situ X-ray Absorption Near Edge Spectroscopy, XANES.

6.2.3 In situ X-ray Absorption Near Edge Spectroscopy

The three types of films, Mn_3O_4, Au(30%)-MnO_x and Au(50%)-MnO_x, were investigated with XAS. Specifically, the Mn K-edge and Au L3-Edge were investigated at the Stanford Synchrotron Radiation Lightsource using a setup with high energy resolution fluorescence detection which allowed for in-situ measurements. This detection method is a bulk sensitive technique and gives information about the average state of all Mn and Au atoms in the sample. The great advantage is that this setup allows for studying the Mn and Au atoms in the films while working as oxygen evolution catalysts. As mentioned in section 3.2.3, the measurements were carried out in collaboration with Prof. Thomas Jaramillo's group at Stanford University Chemical Engineering and in particular with Linsey Seitz and beam scientists Dimosthenis Sokaras, Tsu-Chien Weng and Dennis

Nordlund.
One of the hypotheses brought forward regarding Au and Mn oxide interactions is a possible change in Mn oxidation state. Kuo *et al.* suggested that upon Au modification the Mn oxidation state decreases and a higher concentration of Mn^{3+} species can exist at the surface [226]. This was concluded from ex-situ XAS measurements. With this in-situ study differences in the Mn oxidation state can be documented for catalytically active films while the reaction takes place in the same environment as the activity measurements.
XAS mesaurements for the three films were made for both dry conditions and immersed in 1 M KOH. The measurements with electrolyte were further carried out at open circuit, 0.8, 1.0, 1.2, 1.4 and 1.65 V_{RHE}. It should be noted that the results presented here have been processed and normalised to have an edge jump of unity after linear backgrounds are subtracted. In figure 6.12 results from the dry measurements are shown for the Mn K-edge of all three films.

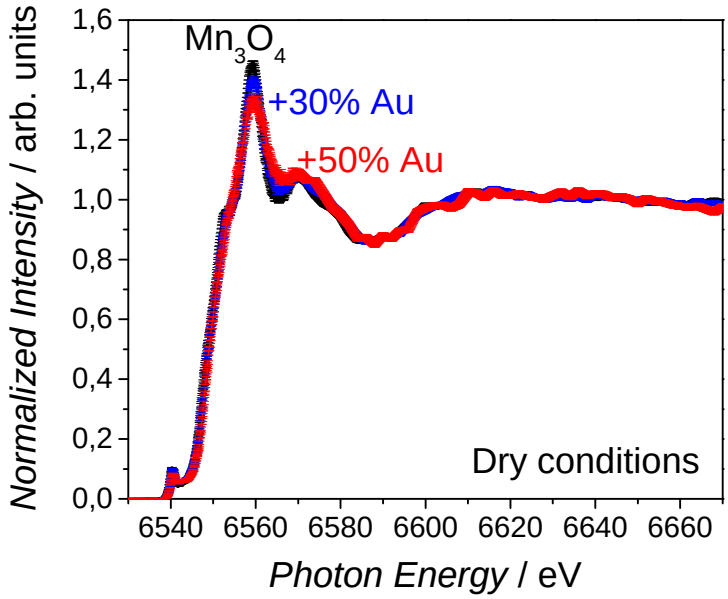

Figure 6.12: Mn K-edge XAS of the three Mn oxide films under dry conditions. Mn_3O_4 in black, Au(30%)-MnO_x in blue and Au(50%)-MnO_x in red. Error bars are based on standard deviations from Poisson statistics on several scans.

The overall features are very similar. The differences are mainly a slightly lower white line (the highest peak) for the films containing gold, which can be due to fewer Mn atoms. Fewer Mn atoms yield a slightly lower signal to noise ratio. Besides this small difference the single pre-edge and shoulder around 6552 eV are close to identical for the films. The shoulder feature has been reported

for Mn atoms in a formal 2+ state, which is consistent with the Mn_3O_4 phase, comprising both 2+ and 3+ [156,235]. From a qualitative point of view, the edge can be analysed by looking at the overall position of the edge. When a feature or the whole edge moves towards higher photon energies it is indicative of an oxidation of the Mn atoms, consistent with more tightly bound core electrons. In the following, only the XANES section of the results will be shown, to highlight the changes in the edge profile as function of applied potential.
When introducing the electrolyte and applying a potential, changes in these features are observed. For the pure Mn_3O_4 film, XAS spectra following the gradual increase in electrochemical potential can be seen in figure 6.13. The edge is shifting towards higher photon energies when the potential is increased, as indicated with the arrow. At the same time the shoulder at 6552 eV seems to decrease slightly and with a closer look an extra pre-edge around 6543 eV can be observed for the highest potential. These small changes and shift of the edge indicates an average oxidation of the Mn atoms present in the sample, which is certainly expected from the anodic potential applied.

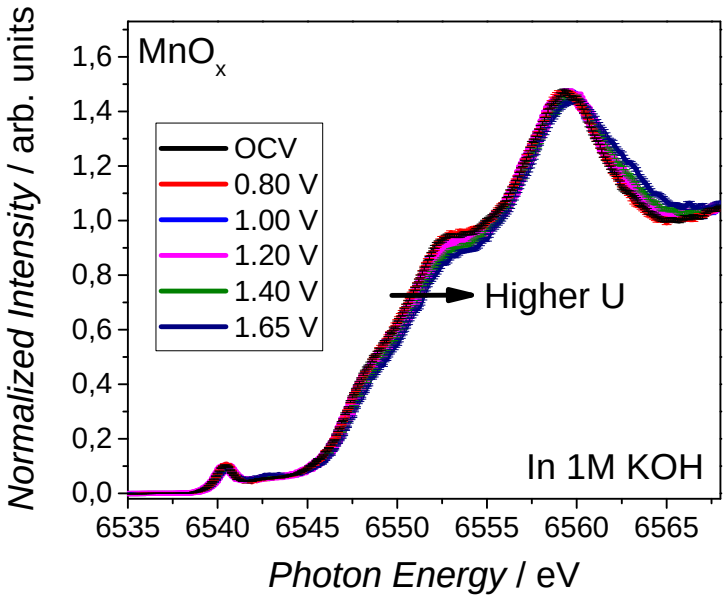

Figure 6.13: Mn K-edge XAS of the Mn_3O_4 film under potential control in 1M KOH. Error bars are based on standard deviations from Poisson statistics on several scans.

The spectra obtained from the Au(30%)-MnO_x sample can be seen in figure 6.14 and from the Au(50%)-MnO_x in figure 6.15. From both sets of spectra a very clear shift of the entire edge can be seen.

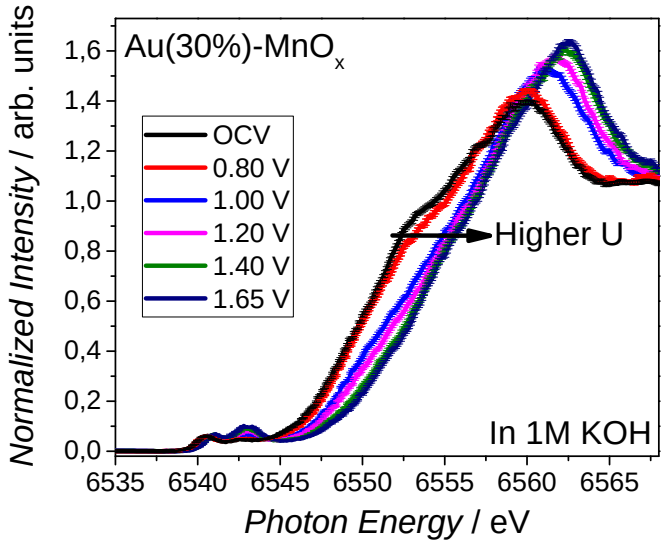

Figure 6.14: Mn K-edge XAS of the Au(30%)-MnO_x film under potential control in 1M KOH.

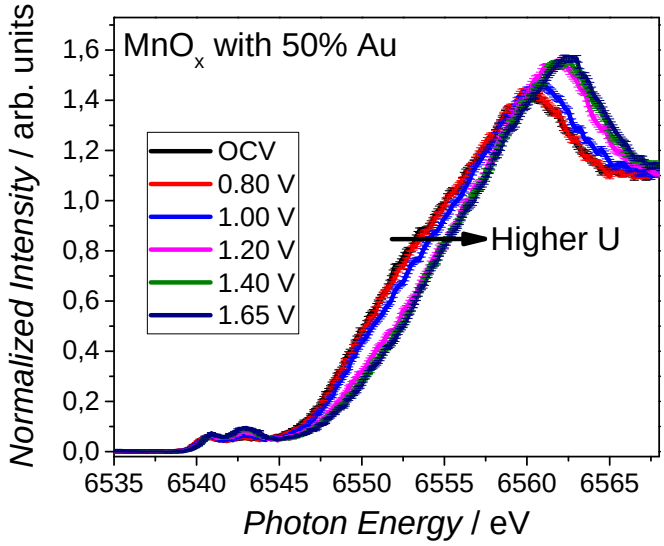

Figure 6.15: Mn K-edge XAS of the Au(50%)-MnO_x film under potential control in 1M KOH.

In figures 6.14 and 6.15 the shoulder feature at 6552 eV completely disappears and a splitting of the pre-edge is observed already from an electrochemical potential of 1.0 V_{RHE}. To highlight the differences between the pure Mn_3O_4 and the Au modified films the spectra taken at 1.65 V_{RHE} are compared in figure 6.16.

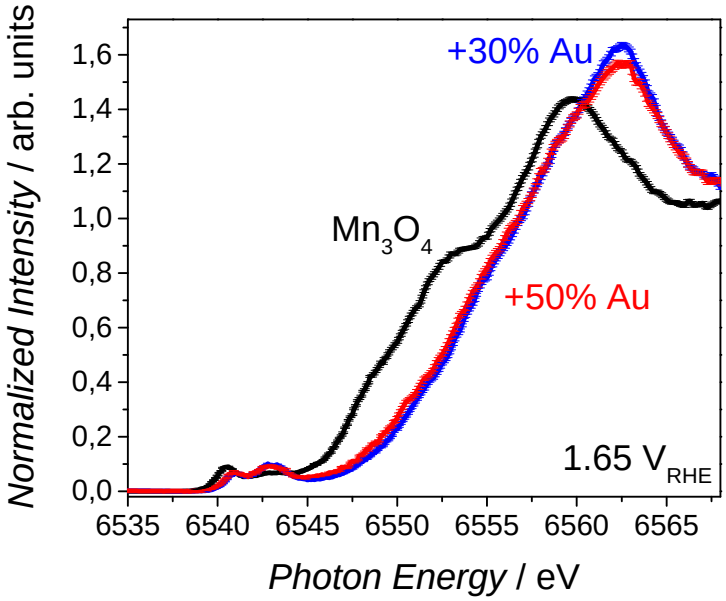

Figure 6.16: Mn K-edge XAS of the three Mn oxide films at 1.65 V_{RHE} in 1M KOH. Mn_3O_4 in black, Au(30%)-MnO_x in blue and Au(50%)-MnO_x in red.

The splitting of the pre-edge has been reported to follow oxidation of Mn and is only visible for average oxidation state of 3 or higher [235]. From this qualitative analysis of the XAS features it seems that the Au modification leads to higher oxidation state of Mn under anodic polarisation of the electrode. This finding is in contrast to the report from Kuo *et al.* [226]. However, the spectra can also be quantified. This is often done by selecting a rather arbitrary point on the XAS spectrum to measure the edge shift. By using reference measurements the shift can then be related to an oxidation state [156, 236, 237]. A problem associated with using a single point of reference for the edge shift is that the edge features depend on structure as well as oxidation state. Unless the structures of samples used for comparison are well defined, two compounds with the same nominal oxidation state could be evaluated differently using a single reference point [237]. Instead it is possible to evaluate the overall shift of a spectrum by using a first moment method as described in section 3.2.3 [238, 239]. The edge shift was calculated for all the spectra of Mn_3O_4 and Au-MnO_x. The results

are plotted as function of applied potential on the working electrode in figure 6.17.

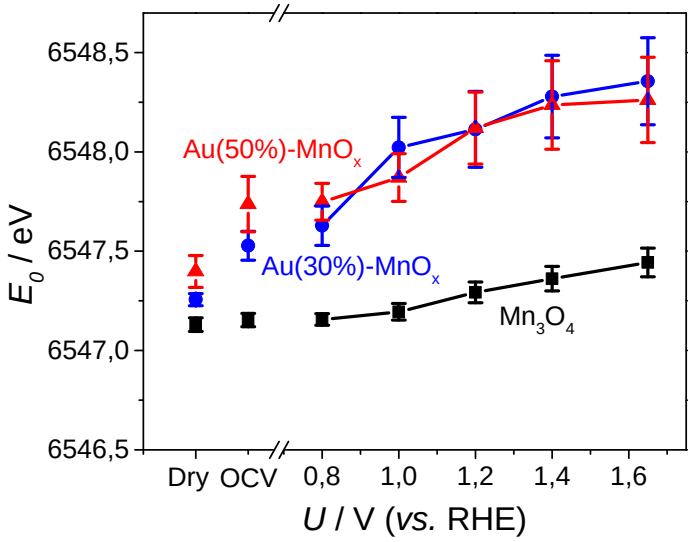

Figure 6.17: Overall edge position for the Mn K-edge of the Mn_3O_4 (purple), Au(30%)-MnO_x (wine red) and Au(50%)-MnO_x (green) as function of the applied potential. Note that the first two points are Dry and OCV conditions followed by the actual potential scale. The error bars here are based on varying the integral range from equation 3.5.

For the pure Mn_3O_4 there is very little edge shift observed before 1.2 V_{RHE}. Even at the highest potential the total shift is around 0.3 eV. For comparison the edge shift observed when going from +3 at around 6546.9 eV to +4 at around 6549.1 eV is 2.2 eV for reference crystalline Mn oxides [237]. For the mixed films there seem to be a shift already at OCV and again at 1.0 V_{RHE}. At the final potential, 1.65 V_{RHE}, the spectrum for 30 % Au has shifted 0.7 eV compared to the spectrum for dry conditions. The edge shifts found with this experimental configuration take into account all Mn atoms in the thin films. This is important to realize, since only the atoms in contact with the electrolyte are likely to oxidise due to the anodic potential. Thus, only a small fraction of the Mn atoms are in fact changing their oxidation state and it is not meaningful to assign a specific oxidation state to the catalytically active surface species. Still there is a significant increase in oxidation state observed due to the Au modification.

6.2.3.1 Au L3-Edge

As mentioned above, the Au L3-edge was also investigated in-situ for the samples containing gold. It is interesting to see if there are differences for the two concentrations since the differences in capacitance and Mn oxidation under reaction conditions are small but the differences in activity are rather large. From XRD measurements the size of gold domains was different for the two concentrations, 2 nm at 30 % and 3 nm at 50 %. In this size range Au nanoparticles have been reported to change reactivity quite drastically due to the increased ratio of undercoordinated sites vs. flat terraces [240, 241]. So even though the size estimation from XRD is not completely accurate there is certainly a difference which is interesting in terms of reactivity. It is therefore important to check if these domains change oxidation state upon anodic polarisation. Spectra obtained for in-situ measurements can be seen in figures 6.18 at OCV, 6.19 at 1.20 V_{RHE} and 6.20 at 1.65 V_{RHE} for the two Au concentrations. Up to 1.20 V_{RHE} the Au edge for the two samples looks very similar and any differences are within the error margin, as seen on figure 6.18. However, at 1.20 V_{RHE} a small difference in the main edge feature is observed, see figure 6.19. The white line is slightly higher for 30 % Au compared to the 50 %. At 1.65 V_{RHE} this difference is very clear and the white line feature for the 30 % sample is significantly higher than for the 50 %. A higher white line is related to Au in a 3+ state [242, 243].

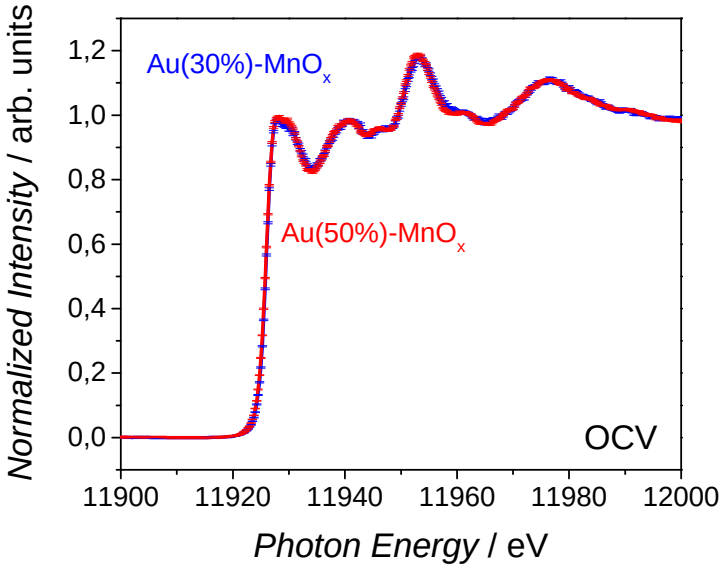

Figure 6.18: Au L3-edge for Au(30%)-MnO_x (blue) and Au(50%)-MnO_x (red) at OCV conditions. Error bars are based on standard deviations from Poisson statistics on several scans.

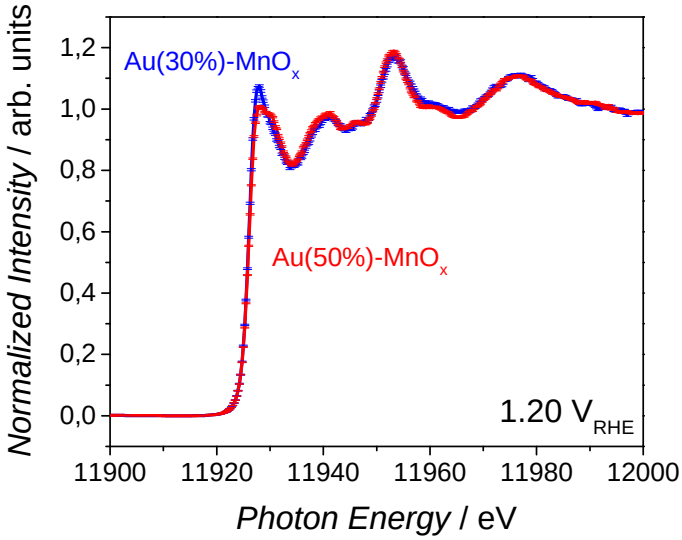

Figure 6.19: Au L3-edge for Au(30%)-MnO_x (blue) and Au(50%)-MnO_x (red) at 1.20 V_{RHE}.

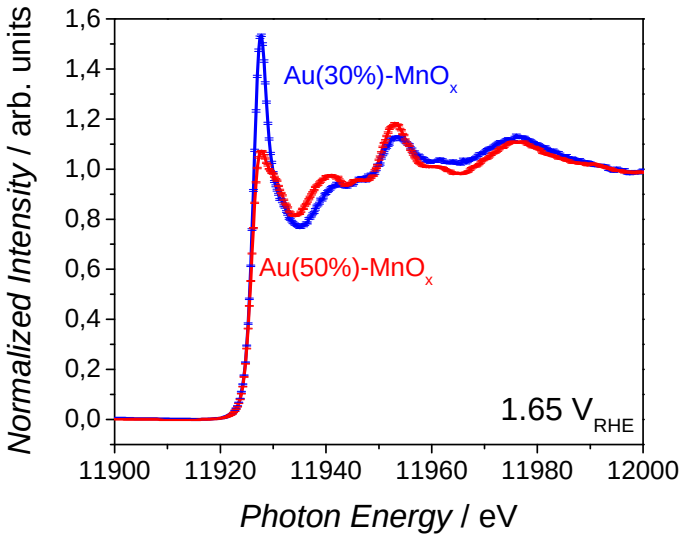

Figure 6.20: Au L3-edge for Au(30%)-MnO_x (blue) and Au(50%)-MnO_x (red) at 1.65 V_{RHE}.

From the Pourbaix diagram of gold in aqueous solutions, the surface is expected to oxidise to a +3 state at 1.46 V_{RHE} [138]. However, since the reactivity for small Au nanoparticles can be drastically increased it is perhaps not surprising that the Au(30%)-MnO_x show some oxidation already at 1.2 V_{RHE}. In conclusion, a distinct difference between the two Au concentrations is observed: the Au atoms in the lower concentration film are on average more oxidised than the Au atoms in the higher concentration film.

6.2.3.2 Discussion

Throughout the experimental part of this chapter, several characterization methods have been employed with the aim of studying Mn-Au interaction. From XPS the concentrations of Au were found to be 30 % and 50 % while the Mn oxide film matched a Mn_3O_4 stoichiometry. Glancing Angle XRD confirmed the Mn_3O_4 phase of the pure Mn oxide film, however, the mixed films only showed peaks for small gold domains. The size of these domains could be estimated from the XRD peak broadening, which indicated 2 nm for 30 % and 3 nm for 50 %. Surface morphology was assessed with SEM, indicating a slightly more open and less densely packed structure. This porosity was also in line with electrochemical evaluation of the surface area. Judging from capacitance measurements the mixed gold films had capacitances up to 80 % higher than the pure Mn oxide. However, the increased capacitance was not sufficient to explain the increase in activity, which was up to 5.5 times higher than Mn_3O_4 for the films with 50 % gold. From literature reports, it was suggested that Mn^{3+} states were promoted by gold interactions, which was thought to improve the activity. However, the in-situ XANES spectra presented here are in strong contrast to that conclusion. Instead, the mixed films were significantly more oxidised compared to the Mn_3O_4. Finally, the Au L3-edge spectra indicated that the Au atoms for 30 % concentration were on average more oxidised than the gold in a 50 % concentration, a difference that was observed already at 1.2 V_{RHE}.

From the combined set of experiments, it can be concluded that a beneficial interaction between Mn and Au for OER catalysis is observed for co-sputtered thin films. The results further indicate that the interaction depends on the size of the Au domains. For small domains, roughly 2 nm, the activity enhancement is low and can almost be explained by increase in surface area. These small domains also oxidise under reaction conditions which can be interpreted as detrimental for obtaining a high OER activity. On the other hand for larger domains, 3 nm, the particles show only little oxidation. It would be interesting to combine these findings with the theoretical model explained in section 6.1. In this model it was suggested that Au sites act as proton acceptors, but it was assumed that these sites would exhibit the properties of bulk gold. While the experiments done so far can not directly confirm the theoretical concept at this stage it is interesting to note that binding energies for the larger particles are expected to be more similar to bulk gold compared to the smaller particles.

This is due to a larger fraction of undercoordinated sites as the particle size decrease [241]. For Au it has further been shown that the (211) surface exhibits stronger binding to *O, *OH and *OOH, which would also be consistent with earlier oxidation of the Au atoms on the surface [133]. However, a more systematic study is needed, which due to time constraints have not been part of the thesis work. As future work, it is expected that investigations into size effects could result in a more detailed model. Such a study could encompass a combination of DFT calculations on Au nanoparticles and experimental characterization of a larger set of thin films with varied gold domain sizes.

Another possibility that has not been discussed so far is whether the increased gold content could significantly increase electronic conductivity of the thin films. At this stage experiments have not been carried out to pursue this option. A way to find out would be to investigate thinner films where conductivity is not expected to play an important role or alternatively follow a procedure similar to the Ti-MnO_2 films reported in chapter 5, where only the top 5 nm is modified. It should also be noted that the beneficial interaction between Au and Mn has been reported for other systems where conductivity enhancements are less likely to play a role. As example, MnO_x nanoparticles deposited onto Au nanoparticles exhibited great enhancement in activity for OER [225].

6.3 Conclusion

To sum up, this chapter encompassed interactions between gold and manganese oxide from both a theoretical and experimental point of view. The theoretical model was briefly introduced and was based on a bifunctional surface, where active Mn sites could benefit from neighbouring proton accepting Au sites. The proton acceptor scheme is beneficial due to a selective stabilization of the *OOH binding, which is normally too weak on Mn oxides. It was shown, from a thermodynamic analysis, that including the proton acceptor pathway results in a significant lowering of the predicted overpotential, with 100 mV decrease for MnO_2. From the experimental studies on mixed films, an enhancement of up to 5.5 times the activity of pure Mn_3O_4 could be reported. This activity enhancement was measured for a high concentration of Au, 50 %, which consisted of 3 nm Au domains dispersed in the Mn oxide films. For a lower concentration, 30 %, the activity enhancement was more modest at approximately 2 times the activity of Mn_3O_4. The activity enhancements could not be explained by higher porosity or increase in surface area judging from capacitance measurements. The films were also characterized with XPS, GA-XRD and SEM for structural and compositional analyses. Furthermore an in-situ study of the Mn K-edge revealed that Mn atoms oxidise at an earlier potential when Au is nearby, which is in contrast to previously reported ex-situ studies in the literature [225, 226]. The measurements on Au L3-edge at the same time showed that the Au domain size had an impact on the Au oxidation. For the lower Au concentration, with

smaller domains, oxidation features were observed already at 1.2 V_{RHE}. The XAS study therefore indicates that Mn oxidation state is not the critical parameter and instead the properties of nearby Au sites could be more important. Such a notion is in line with Au sites playing an active role in the reaction mechanism such as suggested in the thermodynamics analysis. In conclusion, the experimental findings have shown important properties of the Mn-Au system, which can guide further design into improved Mn based catalysts for OER. More experiments are needed for a comprehensive understanding of the activity enhancements.

Chapter 7

Conclusion and outlook

7.1 Conclusion

The overall aim of this thesis has been to investigate and improve the performance of an abundant catalytic material for oxygen evolution, MnO_x. The work was motivated by the important role of electrolyzers in the future energy infrastructure, where intermittent renewable sources must be exploited to their full potential. To do so, energy storage and carbon neutral fuels production are key issues, which can be alleviated with electrolysis. Electrolyzers based on Polymer Electrolyte Membrane cells are particularly promising but are acidic in nature and therefore limits the catalysts choice to noble metal based materials. Thus, a renewed research effort into identifying materials for oxygen evolution based on abundant elements is highly relevant.

Finding and characterizing catalysts for electrolysis is not a new research field and a literature review was dedicated to bring the present thesis into the relevant context. In the past decades a big emphasis has been put on understanding the oxygen evolution reaction and on finding descriptors that could predict the optimal material properties. In more recent years many new catalysts have been reported for alkaline solutions, however, for acidic electrolytes very little progress has been made for materials not based on noble metals. Furthermore, rigorous stability tests were not often carried out. These shortcomings were therefore addressed in this thesis.

In chapter 4 the aim was therefore to establish stability tests based on mass loss analysis. From short term electrochemical characterization there are no guarantees that a stable performance indicate material stability. Instead, it was shown

that mass loss analysis, even in the short term, can be used to predict lifetimes. The established procedure was based on EQCM measurements combined with ICP-MS analysis of the electrolyte. These two methods complement each other, since the former gives information about the electrode mass and the latter gives information about which elements are in the electrolyte. Specifically for MnO_x thin films the rates of mass loss were established at potentials anodic of the dissolution potential and lifetimes were calculated.
MnO_x is a unique material for oxygen evolution. In contrast to NiO_x and CoO_x, it has a stable phase in acidic environment in the range of 1.3 to 1.7 V_{RHE} and it is therefore possible to use this material in acidic electrolyzers. However, as it was established in chapter 4, the anodic dissolution constitutes a problem for long term stability. In chapter 5 the focus has been on investigating a strategy for stabilizing MnO_2 surfaces. This could be done by selectively blocking sites responsible for the dissolution process. It is likely that undercoordinated sites are dominant in that process and from theoretical calculations it was found that Ti atoms segregate to such sites. At the same time, according to current understanding, the flat terrace sites are most important for the OER activity. Experimentally, co-sputtered thin films of Ti-MnO_2 were prepared and found to exhibit a better compromise between stability and activity than pure MnO_2. As mentioned above, the catalytic performance of MnO_x electrodes can not match noble metal based electrodes at this stage. To that end, it has been reported that MnO_x electrodes mixed with Au exhibit remarkable activity enhancements. While gold is not an ideal activity promoter from a practical point of view, it is important to understand the beneficial interactions. In chapter 6 the interactions between gold and manganese oxides were investigated with a conceptual as well as experimental approach. It was shown that activity enhancements could be explained by introducing a Au proton acceptor site next to OER active Mn sites. The experimental approach encompassed mixed thin films, which were characterized thoroughly. The activity towards OER could be increased more than five fold by incorporating Au domains of approximately 3 nm, whereas 2 nm domains lead to modest enhancements. These thin films were found to behave differently under reaction conditions by characterization with in-situ XANES. Importantly, these measurements show that Mn atoms are more oxidised in the presence of gold. It is important to combine the conceptual understanding with experimental observations and the findings presented here provide a step in that direction.

7.2 Outlook

As mentioned in chapter 5 and 6, important progress was made regarding both stabilization of MnO_x and understanding the activity enhancements observed. However, it is also evident that both stability and activity must be improved further in order for MnO_x to be a practical electrode material for PEM elec-

trolyzers.

The strategy for stabilizing the MnO_2 surface is still in its infancy and several directions for optimization can be undertaken. It would be of great importance to establish and observe how the Ti atoms are located on the MnO_2 surface. Such a characterization could be done with cross-sectional Transmission Electron Microscopy imaging. Atomic resolution of the mixed Ti-MnO_2 layer could provide a lot of insight. It would be challenging to distinguish Ti from Mn, especially if the Ti is located as single atoms on the surface. Another possible route is to image the surface with Scanning Tunnelling Microscopy under UHV while depositing small quantities of Ti onto MnO_2. This requires very flat and well defined surfaces which are difficult to prepare using the sputter deposition technique. It may instead be possible with annealing treatments for a Mn single crystal and slow evaporation of Ti. Given that deposition and annealing parameters can be utilized to block all the undercoordinated sites of MnO_2 with Ti, it would be highly relevant to further develop the concept. For commercial electrolyzers the catalyst material must be applied with a very high surface area. Therefore, it would be important to prepare nanoparticulate Ti-MnO_2 with high activity on a geometric basis combined with optimal long term stability. Finally, it is possible that other stability promoting materials could be even more suited for blocking the undercoordinated sites. Tantalum, niobium and zirconium are among the most stable materials in acidic environment and the reason they have not been included here is that they do not form rutile dioxides. In a larger screening study it could be interesting to mix these materials into the surface layers of MnO_2.
Regarding the Mn-Au interactions, it would be interesting to investigate the Au size dependence in greater detail. The sputter deposition could be tuned to deliver Au domains in different sizes. Alternatively, size selected Au clusters could be added to a MnO_2 surface, with the cluster source available in our laboratory. Ideally, such studies should be combined with more detailed DFT calculations so that the properties of gold clusters could be related to observed activities. In the end, the ultimate goal would be to use the understanding of Mn-Au interactions to propose and design Mn oxides modified with another abundant element or compound.

Bibliography

[1] Worldmapper, "www.worldmapper.org," 2015. Checked 2015-07-30.

[2] OSQAR, "Is there a link between energy use and standard of living?." http://osqar.suncor.com/2010/12/is-there-a-link-between-energy-use-and-standard-of-living.html, 2010. [Checked 2015-07-30].

[3] British Petroleum, "BP Statistical Review of World Energy June 2015," tech. rep., 2015.

[4] United States Census Bureau, "International data base, world population." http://www.census.gov/population/international/data/worldpop/table_population.php, 2015. [2015-07-30].

[5] U.S. Energy Information Administration, "International Energy Outlook 2014," tech. rep., 2014.

[6] Energinet.dk, "2013 was a record-setting year for Danish wind power." http://www.energinet.dk/EN/El/Nyheder/Sider/2013-var-et-rekordaar-for-dansk-vindkraft.aspx, 2014. [Checked 30/7-2015].

[7] GWEC, "2014 marked a record year for global wind power." http://www.gwec.net/global-figures/wind-energy-global-status/, 2015. [Checked 2015-07-30].

[8] U.S. Energy Information Administration, "International Energy Outlook 2001," tech. rep., EIA, 2001.

[9] U.S. Energy Information Administration, "International Energy Outlook 2004," tech. rep., EIA, 2004.

[10] British Petroleum, "BP Statistical Review of World Energy 2002," tech. rep., 2002.

[11] British Petroleum, "BP Statistical Review of World Energy 2004," tech. rep., 2004.

[12] British Petroleum, "BP Statistical Review of World Energy 2005," tech. rep., 2005.

[13] British Petroleum, "BP Statistical Review of World Energy 2007," tech. rep., 2007.

[14] British Petroleum, "BP Statistical Review of World Energy 2009," tech. rep., 2009.

[15] British Petroleum, "BP Statistical Review of World Energy 2011," tech. rep., 2011.

[16] British Petroleum, "BP Statistical Review of World Energy 2013," tech. rep., 2013.

[17] W. Zittel, J. Zerhusen, and M. Zerta, "Fossil and Nuclear Fuels - the Supply - Outlook," no. March, pp. 1–41, 2013.

[18] J. D. Hughes, "Drilling Deeper: A reality check on U.S. government forecasts for a lasting tight oil & shale gas boom," tech. rep., Post Carbon Institute, 2014.

[19] R. D. Vidic, S. L. Brantley, J. M. Vandenbossche, D. Yoxtheimer, and J. D. Abad, "Impact of shale gas development on regional water quality.," *Science*, vol. 340, p. 1235009, 2013.

[20] C. A. Hall, R. Powers, and W. Schoenberg, "Peak Oil, EROI, Investments and the Economy in an Uncertain Future," in *Biofuels, Solar and Wind as Renewable Energy Systems: Benefits and Risks*, pp. 109–132, 2008.

[21] D. J. Murphy and C. A. Hall, "Year in review-EROI or energy return on (energy) invested," *Annals of the New York Academy of Sciences*, vol. 1185, pp. 102–118, 2010.

[22] G.-R. Walther, E. Post, P. Convey, A. Menzel, C. Parmesan, T. J. C. Beebee, J.-M. Fromentin, O. Hoegh-Guldberg, and F. Bairlein, "Ecological responses to recent climate change.," *Nature*, vol. 416, no. 6879, pp. 389–395, 2002.

[23] C. Parmesan, C. Parmesan, G. Yohe, and G. Yohe, "A globally coherent fingerprint of climate change impacts across natural systems.," *Nature*, vol. 421, no. 6918, pp. 37–42, 2003.

[24] C. D. Thomas, C. D. Thomas, A. Cameron, A. Cameron, R. E. Green, R. E. Green, M. Bakkenes, M. Bakkenes, L. J. Beaumont, L. J. Beaumont, Y. C. Collingham, Y. C. Collingham, B. F. N. Erasmus, B. F. N. Erasmus, M. F. De Siqueira, M. F. De Siqueira, A. Grainger, A. Grainger, L. Hannah, L. Hannah, L. Hughes, L. Hughes, B. Huntley, B. Huntley, A. S. Van Jaarsveld, A. S. Van Jaarsveld, G. F. Midgley, G. F. Midgley, L. Miles, L. Miles, M. a. Ortega-Huerta, M. a. Ortega-Huerta, a. T. Peterson, a. T. Peterson, O. L. Phillips, O. L. Phillips, S. E. Williams, and S. E. Williams, "Extinction risk from climate change.," *Nature*, vol. 427, no. 6970, pp. 145–8, 2004.

[25] M. Meinshausen, N. Meinshausen, W. Hare, S. C. B. Raper, K. Frieler, R. Knutti, D. J. Frame, and M. R. Allen, "Greenhouse-gas emission targets for limiting global warming to 2 degrees C.," *Nature*, vol. 458, no. 7242, pp. 1158–1162, 2009.

[26] International Energy Agency, "Energy and climate change," tech. rep., International Energy Agency, 2015.

[27] International Energy Agency, "Tracking Clean Energy Progress 2015," tech. rep., International Energy Agency, 2015.

[28] R. F. Service, "Solar energy. Is it time to shoot for the sun?," *Science*, vol. 309, no. 5734, pp. 548–551, 2005.

[29] Energinet.dk, "Wind turbines reached record level in 2014." http://energinet.dk/EN/El/Nyheder/Sider/Vindmoeller-slog-rekord-i-2014.aspx, 2015. [Checked 30/7-2015].

[30] EMD International A/S, "Elforbrug og vindmølleproduktion." http://www.emd.dk/el/, 2015. [Checked 2015-07-30].

[31] International Energy Agency, "Smart Grids in Distribution Networks: Roadmap Development and Implementation," tech. rep., 2015.

[32] International Energy Agency, "Technology Roadmap: Hydrogen and Fuel Cells," tech. rep., International Energy Agency, 2015.

[33] International Energy Agency, "Technology Roadmap, Energy storage," tech. rep., International Energy Agency, 2014.

[34] B. Decourt, B. Lajoie, R. Debarre, and O. Soupa, "Hydrogen-Based Energy Conversion," tech. rep., SBS Energy Institute, 2014.

[35] A. Ursua, L. Gandia, and P. Sanchis, "Hydrogen Production From Water Electrolysis: Current Status and Future Trends," *Proceedings of the IEEE*, vol. 100, no. 2, pp. 410 –426, 2012.

[36] W. Sheng, H. A. Gasteiger, and Y. Shao-Horn, "Hydrogen Oxidation and Evolution Reaction Kinetics on Platinum: Acid vs Alkaline Electrolytes," *Journal of The Electrochemical Society*, vol. 157, no. 11, p. B1529, 2010.

[37] J. Larminie and A. Dicks, "Proton Exchange Membrane Fuel Cells," in *Fuel Cell Systems Explained*, ch. 4, pp. 67–119, Wiley, 2nd ed., 2003.

[38] M. Carmo, D. L. Fritz, J. Mergel, and D. Stolten, "A comprehensive review on PEM water electrolysis," *International Journal of Hydrogen Energy*, vol. 38, no. 12, pp. 4901–4934, 2013.

[39] K. E. Ayers, E. B. Anderson, C. Capuano, B. Carter, L. Dalton, G. Hanlon, J. Manco, and M. Niedzwiecki, "Research Advances towards Low Cost, High Efficiency PEM Electrolysis," vol. 33, no. 1, pp. 3–15, 2010.

[40] E. A. Paoli, F. Masini, R. Frydendal, D. Deiana, C. Schlaup, M. Malizia, T. W. Hansen, S. Horch, I. E. L. Stephens, and I. Chorkendorff, "Oxygen evolution on well-characterized mass-selected Ru and RuO_2 nanoparticles," *Chemical Science*, vol. 6, pp. 190–196, Sept. 2014.

[41] M. K. Debe, S. M. Hendricks, G. D. Vernstrom, M. Meyers, M. Brostrom, M. Stephens, Q. Chan, J. Willey, M. Hamden, C. K. Mittelsteadt, C. B. Capuano, K. E. Ayers, and E. B. Anderson, "Initial Performance and Durability of Ultra-Low Loaded NSTF Electrodes for PEM Electrolyzers," *Journal of The Electrochemical Society*, vol. 159, no. 6, p. K165, 2012.

[42] J. R. Varcoe, P. Atanassov, D. R. Dekel, A. M. Herring, M. a. Hickner, P. a. Kohl, A. R. Kucernak, W. E. Mustain, K. Nijmeijer, K. Scott, T. Xu, and L. Zhuang, "Anion-exchange membranes in electrochemical energy systems," *Energy Environ. Sci.*, vol. 7, pp. 3135–3191, Aug. 2014.

[43] M. Ni, M. K. H. Leung, and D. Y. C. Leung, "Technological development of hydrogen production by solid oxide electrolyzer cell (SOEC)," *International Journal of Hydrogen Energy*, vol. 33, no. 9, pp. 2337–2354, 2008.

[44] M. A. Laguna-Bercero, "Recent advances in high temperature electrolysis using solid oxide fuel cells: A review," *Journal of Power Sources*, vol. 203, pp. 4–16, 2012.

[45] S. Trasatti, "Electrocatalysis: Understanding the success of DSA®," *Technology*, vol. 45, pp. 2377–2385, May 2000.

[46] I. Chorkendorff and H. Niemantsverdriet, "X-ray Diffraction," in *Concepts of Modern Catalysis and Kinetics*, ch. 4, pp. 131–134, Wiley-VCH, 2nd ed., 2007.

[47] P. Sabatier, "Hydrogenation and dehydrogenation for catalysis," *BERICHTE DER DEUTSCHEN CHEMISCHEN GESELLSCHAFT*, vol. 44, pp. 1984–2001, 1911.

[48] R. Parsons, "The rate of Electrolytic Hydrogen Evolution and the Heat of Adsorption of Hydrogen," *Transactions of the Faraday Society*, vol. 54, pp. 1053–1063, 1958.

[49] J. K. Nørskov, T. Bligaard, J. Rossmeisl, and C. H. Christensen, "Towards the computational design of solid catalysts.," *Nature chemistry*, vol. 1, no. 1, pp. 37–46, 2009.

[50] J. Larminie and A. Dicks, "Efficiency and Open Circuit Voltage," in *Fuel Cell Systems Explained*, ch. 2, pp. 25–43, Wiley, 2nd ed., 2003.

[51] S. Trasatti, "Reaction mechanism and rate determining steps," in *Handbook of Fuel Cells Vol. 2* (W. Vielstich, H. A. Gasteiger, and A. Lamm, eds.), ch. 9, pp. 79–87, Wiley-VCH, 2003.

[52] E. Skúlason, G. S. Karlberg, J. Rossmeisl, T. Bligaard, J. Greeley, H. Jónsson, and J. K. Nørskov, "Density functional theory calculations for the hydrogen evolution reaction in an electrochemical double layer on the Pt(111) electrode.," *Physical chemistry chemical physics : PCCP*, vol. 9, pp. 3241–50, July 2007.

[53] N. M. Markovic, B. N. Grgur, and P. N. Ross, "Temperature-Dependent Hydrogen Electrochemistry on Platinum Low-Index Single-Crystal Surfaces in Acid Solutions," *Journal of Physical Chemistry B*, vol. 101, no. 20, p. 3719, 1997.

[54] K. Kunimatsu, T. Senzaki, M. Tsushima, and M. Osawa, "A combined surface-enhanced infrared and electrochemical kinetics study of hydrogen adsorption and evolution on a Pt electrode," *Chemical Physics Letters*, vol. 401, no. 4-6, pp. 451–454, 2005.

[55] T. F. Jaramillo, K. P. Jørgensen, J. Bonde, J. H. Nielsen, S. Horch, and I. Chorkendorff, "Identification of active edge sites for electrochemical H_2 evolution from MoS_2 nanocatalysts.," *Science*, vol. 317, no. 5834, pp. 100–102, 2007.

[56] M. T. M. Koper, "Thermodynamic theory of multi-electron transfer reactions: Implications for electrocatalysis," *Journal of Electroanalytical Chemistry*, vol. 660, pp. 254–260, Sept. 2011.

[57] J. D. Benck, T. R. Hellstern, J. Kibsgaard, P. Chakthranont, and T. F. Jaramillo, "Catalyzing the Hydrogen Evolution Reaction (HER) with Molybdenum Sulfide Nanomaterials," *ACS Catalysis*, vol. 4, pp. 3957–3971, 2014.

[58] K. C. Neyerlin, W. Gu, J. Jorne, and H. a. Gasteiger, "Study of the Exchange Current Density for the Hydrogen Oxidation and Evolution Reactions," *Journal of The Electrochemical Society*, vol. 154, no. 7, p. B631, 2007.

[59] L. Chen, D. Guay, and A. Lasia, "Kinetics of the Hydrogen Evolution Reaction on RuO_2 and IrO_2 Oxide Electrodes in H_2SO_4 Solution: An AC Impedance Study," *Journal of The Electrochemical Society*, vol. 143, no. 11, p. 3576, 1996.

[60] E. J. Popczun, C. G. Read, C. W. Roske, N. S. Lewis, and R. E. Schaak, "Highly Active Electrocatalysis of the Hydrogen Evolution Reaction by Cobalt Phosphide Nanoparticles.," *Angewandte Chemie (International ed. in English)*, pp. 1–5, Apr. 2014.

[61] Z.-Y. Li, Z.-l. Liu, J.-C. Liang, C.-W. Xu, and X. Lu, "Facile synthesis of Pd–Mn_3O_4/C as high-efficient electrocatalyst for oxygen evolution reaction," *J. Mater. Chem. A*, vol. 2, pp. 18236–18240, Sept. 2014.

[62] L. Feng, H. Vrubel, M. Bensimon, and X. Hu, "Easily-prepared dinickel phosphide (Ni_2P) nanoparticles as an efficient and robust electrocatalyst for hydrogen evolution.," *Physical chemistry chemical physics : PCCP*, vol. 16, no. 13, pp. 5917–21, 2014.

[63] W. Chen, C.-H. Wang, K. Sasaki, N. Marinkovic, W. Xu, J. T. Muckerman, Y. Zhu, and R. R. Adzic, "Highly Active and Durable Nanostructured Molybdenum Carbide Electrocatalysts for Hydrogen Production," *Energy & Environmental Science*, vol. 6, no. 3, pp. 943–951, 2013.

[64] J. Kibsgaard, T. F. Jaramillo, and F. Besenbacher, "Building an appropriate active-site motif into a hydrogen-evolution catalyst with thiomolybdate $[Mo_3S_{13}]^{2-}$ clusters.," *Nature chemistry*, vol. 6, no. 3, pp. 248–53, 2014.

[65] X. Chen, L. Liu, P. Y. Yu, and S. S. Mao, "Increasing solar absorption for photocatalysis with black hydrogenated titanium dioxide nanocrystals.," *Science*, vol. 331, pp. 746–50, Feb. 2011.

[66] A. K. M. S. Huq and A. J. Rosenberg, "Electrochemical Behavior of Nickel Compounds," *Journal of The Electrochemical Society*, vol. 111, no. 3, pp. 270–278, 1964.

[67] N. Pentland, J. O. Bockris, and E. Sheldon, "Hydrogen Evolution Reaction on Copper, Gold, Molybdenum, Palladium, Rhodium, and Iron," *Journal of The Electrochemical Society*, vol. 104, no. 3, p. 182, 1957.

[68] A. Belanger and A. K. Vijh, "Hydrogen Evolution Reaction on Vanadium, Chromium, Manganese, Cobalt," *Journal of The Electrochemical Society*, vol. 121, no. 2, p. 225, 1974.

[69] A. K. Vijh, "Electrolytic hydrogen evolution reaction on aluminum in acidic solutions," *The Journal of Physical Chemistry*, vol. 72, no. 4, pp. 1148–1156, 1968.

[70] W. Sheng, A. P. Bivens, M. Myint, Z. Zhuang, R. V. Forest, Q. Fang, J. G. Chen, and Y. Yan, "Non-precious metal electrocatalysts with high activity for hydrogen oxidation reaction in alkaline electrolytes," *Energy & Environmental Science*, vol. 7, no. 5, p. 1719, 2014.

[71] J. R. Mckone, B. F. Sadtler, C. A. Werlang, N. S. Lewis, and H. B. Gray, "Ni-Mo Nanopowders for Efficient Electrochemical Hydrogen Evolution," *ACS Catalysis*, vol. 3, pp. 166–169, 2013.

[72] C. Chen, Y. Kang, Z. Huo, Z. Zhu, W. Huang, H. L. Xin, J. D. Snyder, D. Li, J. A. Herron, M. Mavrikakis, M. Chi, K. L. More, Y. Li, N. M. Markovic, G. A. Somorjai, P. Yang, and V. R. Stamenkovic, "Highly crystalline multimetallic nanoframes with three-dimensional electrocatalytic surfaces.," *Science*, vol. 343, no. 6177, pp. 1339–43, 2014.

[73] W. Sheng, M. Myint, J. G. Chen, and Y. Yan, "Correlating the hydrogen evolution reaction activity in alkaline electrolytes with the hydrogen binding energy on monometallic surfaces," *Energy & Environmental Science*, vol. 6, no. 5, pp. 1509–1512, 2013.

[74] E. Fabbri, A. Habereder, K. Waltar, R. Kotz, and T. Schmidt, "Developments and perspectives of oxide-based catalysts for the oxygen evolution reaction," *Catalysis Science & Technology*, vol. 4, pp. 3800–3821, 2014.

[75] I. Katsounaros, S. Cherevko, A. R. Zeradjanin, and K. J. J. Mayrhofer, "Oxygen electrochemistry as a cornerstone for sustainable energy conversion.," *Angewandte Chemie (International ed. in English)*, vol. 53, pp. 102–21, Jan. 2014.

[76] A. Hickling and S. Hill, "Oxygen overvoltage. Part I. The influence of electrode material, current density, and time in aqueous solution," *Discussions of the Faraday Society*, vol. 1, pp. 236–246, 1947.

[77] P. Ruetschi and P. Delahay, "Influence of Electrode Material on Oxygen Overvoltage - a Theoretical Analysis," *Journal of Chemical Physics*, vol. 23, no. 3, pp. 556–560, 1955.

[78] J. O. Bockris and A. K. M. S. Huq, "The mechanism of the electrolytic evolution of oxygen on platinum," *Proceedings of the Royal Society of London. Series A, Mathematical and Physical Sciences*, vol. 237, no. 1209, pp. 277–296, 1956.

[79] E. R. S. Winter, "Exchange reactions of oxides. Part IX," *Journal of the Chemical Society A: Inorganic, Physical, Theoretical*, p. 2889, 1968.

[80] G. K. Boreskov, "The Catalysis of Isotopic Exchange in Molecular Oxygen," *Advances in Catalysis*, vol. 15, no. C, pp. 285–339, 1965.

[81] K. Klier, "Oxidation-reduction potentials and their relation to the catalytic activity of transition metal oxides," *Journal of Catalysis*, vol. 8, no. 1, pp. 14–21, 1967.

[82] S. Trasatti, "ELECTROCATALYSIS BY OXIDES – ATTEMPT AT A UNIFYING APPROACH," *Journal of Electroanalytical Chemistry*, vol. 111, pp. 125–131, 1980.

[83] J. O. M. Bockris and T. Otagawa, "The Electrocatalysis of Oxygen Evolution on Perovskites," *Journal of The Electrochemical Society*, vol. 131, no. 2, p. 290, 1984.

[84] H. B. Beer, "The Invention and Industrial Development of Metal Anodes 1," *Journal of The Electrochemical Society*, vol. 127, no. 8, pp. 303–307, 1980.

[85] L.-A. Naslund, C. M. Sanchez-Sanchez, A. S. Ingason, J. Backstrom, E. Herrero, J. Rosen, and S. Holmin, "The Role of TiO_2 Doping on RuO_2 -Coated Electrodes for the Water Oxidation Reaction," *The Journal of Physical Chemistry C*, vol. 117, no. 12, pp. 6126–6135, 2013.

[86] C. Comninellis and G. P. Vercesi, "Characterization of DSA type oxygen evolving electrodes: Choice of a coating," *Journal of Applied Electrochemistry*, vol. 21, pp. 335–345, 1991.

[87] B. Hammer, L. B. Hansen, and J. Nørskov, "Improved adsorption energetics within density-functional theory using revised Perdew-Burke-Ernzerhof functionals," *Physical Review B*, vol. 59, pp. 7413–7421, Mar. 1999.

[88] J. K. Nørskov, J. Rossmeisl, A. Logadottir, L. Lindqvist, J. R. Kitchin, T. Bligaard, and H. Jónsson, "Origin of the Overpotential for Oxygen Reduction at a Fuel-Cell Cathode," *The Journal of Physical Chemistry B*, vol. 108, pp. 17886–17892, Nov. 2004.

[89] J. Rossmeisl, A. Logadottir, and J. K. Nørskov, "Electrolysis of water on (oxidized) metal surfaces," *Chemical Physics*, vol. 319, pp. 178–184, Dec. 2005.

[90] J. Rossmeisl, Z.-W. Qu, H. Zhu, G.-J. Kroes, and J. K. Nørskov, "Electrolysis of water on oxide surfaces," *Journal of Electroanalytical Chemistry*, vol. 607, pp. 83–89, Sept. 2007.

[91] V. Tripković, E. Skúlason, S. Siahrostami, J. K. Nørskov, and J. Rossmeisl, "The oxygen reduction reaction mechanism on Pt(111) from density functional theory calculations," *Electrochimica Acta*, vol. 55, pp. 7975–7981, Nov. 2010.

[92] T. Bligaard, J. Nørskov, S. Dahl, J. Matthiesen, C. Christensen, and J. Sehested, "The Brønsted–Evans–Polanyi relation and the volcano curve in heterogeneous catalysis," *Journal of Catalysis*, vol. 224, pp. 206–217, May 2004.

[93] A. Vojvodic, F. Calle-Vallejo, W. Guo, S. Wang, A. Toftelund, F. Studt, J. I. Martinez, J. Shen, I. C. Man, J. Rossmeisl, T. Bligaard, J. K. Norskov, and F. Abild-Pedersen, "On the behavior of Brønsted-Evans-Polanyi relations for transition metal oxides.," *The Journal of chemical physics*, vol. 134, p. 244509, June 2011.

[94] I. C. Man, *Theoretical study of electro-catalysts for oxygen evolution*. PhD thesis, Technical University of Denmark, 2011.

[95] E. M. Fernández, P. G. Moses, A. Toftelund, H. A. Hansen, J. I. Martínez, F. Abild-Pedersen, J. Kleis, B. Hinnemann, J. Rossmeisl, T. Bligaard, and J. K. Nørskov, "Scaling relationships for adsorption energies on transition metal oxide, sulfide, and nitride surfaces.," *Angewandte Chemie (International ed. in English)*, vol. 47, pp. 4683–6, Jan. 2008.

[96] F. Calle-Vallejo, J. I. Martínez, J. M. García-Lastra, J. Rossmeisl, and M. T. M. Koper, "Physical and chemical nature of the scaling relations between adsorption energies of atoms on metal surfaces," *Physical Review Letters*, vol. 108, no. 11, pp. 1–5, 2012.

[97] F. Abild-Pedersen, J. Greeley, F. Studt, J. Rossmeisl, T. Munter, P. Moses, E. Skúlason, T. Bligaard, and J. Nørskov, "Scaling Properties of Adsorption Energies for Hydrogen-Containing Molecules on Transition-Metal Surfaces," *Physical Review Letters*, vol. 99, p. 016105, July 2007.

[98] I. C. Man, H.-Y. Su, F. Calle-Vallejo, H. A. Hansen, J. I. Martínez, N. G. Inoglu, J. Kitchin, T. F. Jaramillo, J. K. Nørskov, and J. Rossmeisl, "Universality in Oxygen Evolution Electrocatalysis on Oxide Surfaces," *ChemCatChem*, vol. 3, pp. 1159–1165, July 2011.

[99] G. Lodi, E. Sivieri, A. D. Battisti, and S. Trasatti, "Ruthenium dioxide-based film electrodes. III. Effect of chemical composition and surface morphology on oxygen evolution in acid solutions," *Journal of Applied Electrochemistry*, vol. 8, pp. 135–143, 1978.

[100] T. Reier, M. Oezaslan, and P. Strasser, "Electrocatalytic Oxygen Evolution Reaction (OER) on Ru, Ir, and Pt Catalysts: A Comparative Study of Nanoparticles and Bulk Materials," *ACS Catalysis*, vol. 2, pp. 1765–1772, Aug. 2012.

[101] Y. Lee, J. Suntivich, K. May, E. E. Perry, and Y. Shao-Horn, "Synthesis and activities of rutile IrO_2 and RuO_2 nanoparticles for oxygen evolution

in acid and alkaline solutions," *The Journal of Physical Chemistry Letters*, vol. 3, pp. 399–404, 2012.

[102] P. C. K. Vesborg and T. F. Jaramillo, "Addressing the terawatt challenge: scalability in the supply of chemical elements for renewable energy," *RSC Advances*, vol. 2, no. 21, p. 7933, 2012.

[103] J. Sedlak, R. J. Lawrance, and J. Enos, "Advances in oxygen evolution catalysis in solid polymer electrolyte water electrolysis," *International Journal of Hydrogen Energy*, vol. 6, no. 2, pp. 159–165, 1981.

[104] K. Juodkazis, J. Juodkazyte, R. Vilkauskaite, B. Sebeka, and V. Jasulaitiene, "Oxygen evolution on composite ruthenium and nickel oxides electrode," *CHEMIJA*, vol. 19, no. 1, pp. 1–6, 2008.

[105] K. Macounová, J. Jirkovský, M. V. Makarova, J. Franc, and P. Krtil, "Oxygen evolution on $Ru_{1-x}Ni_xO_{2-y}$ nanocrystalline electrodes," *Journal of Solid State Electrochemistry*, vol. 13, pp. 959–965, Aug. 2009.

[106] R. Forgie, G. Bugosh, K. C. Neyerlin, Z. Liu, and P. Strasser, "Bimetallic Ru Electrocatalysts for the OER and Electrolytic Water Splitting in Acidic Media," *Electrochemical and Solid-State Letters*, vol. 13, no. 4, pp. B36–B39, 2010.

[107] V. Petrykin, K. Macounová, M. Okube, S. Mukerjee, and P. Krtil, "Local structure of Co doped RuO_2 nanocrystalline electrocatalytic materials for chlorine and oxygen evolution," *Catalysis Today*, vol. 202, pp. 63–69, Mar. 2013.

[108] N. B. Halck, V. Petrykin, P. Krtil, and J. Rossmeisl, "Beyond the volcano limitations in electrocatalysis - oxygen evolution reaction.," *Physical chemistry chemical physics : PCCP*, vol. 16, pp. 13682–13688, Mar. 2014.

[109] C. C. L. McCrory, S. Jung, J. C. Peters, and T. F. Jaramillo, "Benchmarking heterogeneous electrocatalysts for the oxygen evolution reaction.," *Journal of the American Chemical Society*, vol. 135, pp. 16977–87, Nov. 2013.

[110] C. C. L. McCrory, S. Jung, I. M. Ferrer, S. Chatman, J. C. Peters, and T. F. Jaramillo, "Benchmarking HER and OER Electrocatalysts for Solar Water Splitting Devices," *Journal of the American Chemical Society*, vol. 137, pp. 4347–4357, 2015.

[111] A. R. Zeradjanin, A. a. Topalov, Q. Van Overmeere, S. Cherevko, X. Chen, E. Ventosa, W. Schuhmann, and K. J. J. Mayrhofer, "Rational design of the electrode morphology for oxygen evolution – enhancing the performance for catalytic water oxidation," *RSC Advances*, vol. 4, no. 19, p. 9579, 2014.

[112] M. S. Burke, M. G. Kast, L. Trotochaud, A. M. Smith, and S. W. Boettcher, "Cobalt-iron (oxy)hydroxide oxygen evolution electrocatalysts: The role of structure and composition on activity, stability, and mechanism," *Journal of the American Chemical Society*, p. 150220163913001, 2015.

[113] M. D. Macia, J. M. Campina, E. Herrero, and J. M. Feliu, "On the kinetics of oxygen reduction on platinum stepped surfaces in acidic media," *Journal of Electroanalytical Chemistry*, vol. 564, no. 1-2, pp. 141–150, 2004.

[114] J. Zhang, M. B. Vukmirovic, Y. Xu, M. Mavrikakis, and R. R. Adzic, "Controlling the catalytic activity of platinum-monolayer electrocatalysts for oxygen reduction with different substrates," *Angewandte Chemie - International Edition*, vol. 44, no. 14, pp. 2132–2135, 2005.

[115] A. B. Anderson, J. Roques, S. Mukerjee, V. S. Murthi, N. M. Markovic, and V. Stamenkovic, "Activation energies for oxygen reduction on platinum alloys: Theory and experiment," *Journal of Physical Chemistry B*, vol. 109, no. 3, pp. 1198–1203, 2005.

[116] D. S. Strmcnik, P. Rebec, M. Gaberscek, D. Tripkovic, V. Stamenkovic, C. Lucas, and N. M. Markovic, "Relationship between the Surface Coverage of Spectator Species and the Rate of Electrocatalytic Reactions," *Journal of Physical Chemistry C*, vol. 111, pp. 18672–18678, 2007.

[117] V. R. Stamenkovic, B. Fowler, B. S. Mun, G. Wang, P. N. Ross, C. a. Lucas, and N. M. Marković, "Improved oxygen reduction activity on $Pt_3Ni(111)$ via increased surface site availability.," *Science*, vol. 315, no. 5811, pp. 493–497, 2007.

[118] I. E. L. Stephens, A. S. Bondarenko, F. J. Perez-Alonso, F. Calle-Vallejo, L. Bech, T. P. Johansson, A. K. Jepsen, R. Frydendal, B. P. Knudsen, J. Rossmeisl, and I. Chorkendorff, "Tuning the activity of Pt(111) for oxygen electroreduction by subsurface alloying," *Journal of the American Chemical Society*, vol. 133, no. 14, pp. 5485–5491, 2011.

[119] I. E. L. Stephens, A. S. Bondarenko, L. Bech, and I. Chorkendorff, "Oxygen Electroreduction Activity and X-Ray Photoelectron Spectroscopy of Platinum and Early Transition Metal Alloys," *ChemCatChem*, vol. 4, pp. 341–349, Mar. 2012.

[120] M. B. Vukmirovic, R. L. Sabatini, and R. R. Adzic, "Growth of RuO_2 by electrochemical and gas-phase oxidation of an Ru(0001) surface," *Surface Science*, vol. 572, pp. 269–276, Nov. 2004.

[121] P. Castelli and S. Trasatti, "SINGLE CRYSTALS AS MODEL ELECTROCATALYSTS OXYGEN evolution on $RuO_2(110)$," *Journal of Electroanalytical Chemistry*, vol. 210, pp. 189–194, 1986.

[122] K. Stoerzinger, L. Qiao, M. D. Biegalski, and Y. Shao-Horn, "Orientation-Dependent Oxygen Evolution Activities of Rutile IrO_2 and RuO_2," *The Journal of Physical Chemistry Letters*, vol. 5, pp. 1636–1641, 2014.

[123] M. Watanabe, H. Sei, and P. Stonehart, "The influence of platinum crystallite size on the electroreduction of oxygen," *Journal of Electroanalytical Chemistry and Interfacial Electrochemistry*, vol. 261, no. 2, pp. 375–387, 1989.

[124] F. J. Perez-Alonso, C. F. Elkjær, S. S. Shim, B. L. Abrams, I. E. L. Stephens, and I. Chorkendorff, "Identical locations transmission electron microscopy study of Pt/C electrocatalyst degradation during oxygen reduction reaction," *Journal of Power Sources*, vol. 196, pp. 6085–6091, Aug. 2011.

[125] M. Nesselberger, S. Ashton, J. C. Meier, I. Katsounaros, K. J. J. Mayrhofer, and M. Arenz, "The Particle Size Effect on the Oxygen Reduction Reaction Activity of Pt Catalysts: Influence of Electrolyte and Relation to Single Crystal Models," *Journal of the American Chemical Society*, vol. 133, no. 43, pp. 17428–17433, 2011.

[126] G. A. Tritsaris, J. Greeley, J. Rossmeisl, and J. K. Nørskov, "Atomic-scale modeling of particle size effects for the oxygen reduction reaction on Pt," *Catalysis Letters*, vol. 141, no. 7, pp. 909–913, 2011.

[127] F. J. Perez-Alonso, D. N. McCarthy, A. Nierhoff, P. Hernandez-Fernandez, C. Strebel, I. E. L. Stephens, J. H. Nielsen, and I. Chorkendorff, "The effect of size on the oxygen electroreduction activity of mass-selected platinum nanoparticles.," *Angewandte Chemie (International ed. in English)*, vol. 51, pp. 4641–3, May 2012.

[128] P. Hernandez-Fernandez, F. Masini, D. N. McCarthy, C. E. Strebel, D. Friebel, D. Deiana, P. Malacrida, A. Nierhoff, A. Bodin, A. M. Wise, J. H. Nielsen, T. W. Hansen, A. Nilsson, I. E. L. Stephens, and I. Chorkendorff, "Mass-selected nanoparticles of Pt_xY as model catalysts for oxygen electroreduction," *Nature Chemistry*, vol. 6, no. 8, pp. 732–738, 2014.

[129] M. Nesselberger, M. Roefzaad, R. F. Hamou, P. U. Biedermann, F. F. Schweinberger, S. Kunz, K. Schloegl, G. K. H. Wiberg, S. Ashton, U. Heiz, K. J. J. Mayrhofer, and M. Arenz, "The effect of particle proximity on the oxygen reduction rate of size-selected platinum clusters.," *Nature materials*, vol. 12, no. 10, pp. 919–24, 2013.

[130] J. Jakub, H. Hoffmannova, M. Klementova, and P. Krtil, "Particle Size Dependence of the Electrocatalytic Activity of Nanocrystalline RuO_2 Electrodes," *Journal of The Electrochemical Society*, vol. 153, no. 6, p. E111, 2006.

[131] H.-Y. Su, Y. Gorlin, I. C. Man, F. Calle-Vallejo, J. K. Nørskov, F. Jaramillo, and J. Rossmeisl, "Identifying active surface phases for metal oxide electrocatalysts: a study of manganese oxide bi-functional catalysts for oxygen reduction and water oxidation catalysis.," *Physical chemistry chemical physics*, vol. 14, pp. 14010–14022, Oct. 2012.

[132] M. Bajdich, M. García-Mota, A. Vojvodic, J. K. Nørskov, and A. T. Bell, "Theoretical investigation of the activity of cobalt oxides for the electrochemical oxidation of water.," *Journal of the American Chemical Society*, vol. 135, pp. 13521–13530, Sept. 2013.

[133] J. Greeley, J. Rossmeisl, A. Hellman, and J. K. Nørskov, "Theoretical Trends in Particle Size Effects for the Oxygen Reduction Reaction," *Zeitschrift für Physikalische Chemie*, vol. 221, no. 9-10, pp. 1209–1220, 2007.

[134] H. N. Nong, L. Gan, E. Willinger, D. Teschner, and P. Strasser, "IrO_x core-shell nanocatalysts for cost- and energy-efficient electrochemical water splitting," *Chemical Science*, vol. 5, pp. 2955–2963, 2014.

[135] H. N. Nong, H.-S. Oh, T. Reier, E. Willinger, M.-G. Willinger, V. Petkov, D. Teschner, and P. Strasser, "Oxide-Supported $IrNiO_x$ Core-Shell Particles as Efficient, Cost-Effective, and Stable Catalysts for Electrochemical Water Splitting," *Angewandte Chemie International Edition*, vol. 54, pp. 2975–2979, 2015.

[136] H.-S. Oh, H. N. Nong, T. Reier, M. Gliech, and P. Strasser, "Oxide-supported Ir nanodendrites with high activity and durability for the oxygen evolution reaction in acid PEM water electrolyzers," *Chemical Science*, vol. 6, pp. 3321–3328, 2015.

[137] R. Frydendal, E. A. Paoli, B. P. Knudsen, B. Wickman, P. Malacrida, I. E. L. Stephens, and I. Chorkendorff, "Benchmarking the Stability of Oxygen Evolution Reaction Catalysts: The Importance of Monitoring Mass Losses," *ChemElectroChem*, vol. 1, pp. 2075–2081, Oct. 2014.

[138] M. Pourbaix, "Atlas of Electrochemical Equilibria in Aqueous Solutions," 1966.

[139] J. Suntivich, K. J. May, H. A. Gasteiger, J. B. Goodenough, and Y. Shao-Horn, "A Perovskite Oxide Optimized for Oxygen Evolution Catalysis from Molecular Orbital Principles," *Science*, vol. 334, pp. 1383–1385, Dec. 2011.

[140] A. Grimaud, K. J. May, C. E. Carlton, Y.-L. Lee, M. Risch, W. T. Hong, J. Zhou, and Y. Shao-Horn, "Double perovskites as a family of highly active catalysts for oxygen evolution in alkaline solution.," *Nature Communications*, vol. 4, p. 2439, Jan. 2013.

[141] K. J. May, C. E. Carlton, K. a. Stoerzinger, M. Risch, J. Suntivich, Y.-L. Lee, A. Grimaud, and Y. Shao-Horn, "Influence of Oxygen Evolution during Water Oxidation on the Surface of Perovskite Oxide Catalysts," *The Journal of Physical Chemistry Letters*, vol. 3, pp. 3264–3270, Nov. 2012.

[142] R. L. Doyle, I. J. Godwin, M. P. Brandon, and M. E. G. Lyons, "Redox and electrochemical water splitting catalytic properties of hydrated metal oxide modified electrodes.," *Physical chemistry chemical physics : PCCP*, vol. 15, pp. 13737–83, Sept. 2013.

[143] M. Gong, Y. Li, H. Wang, Y. Liang, J. Z. Wu, J. Zhou, J. Wang, T. Regier, F. Wei, and H. Dai, "An advanced Ni-Fe layered double hydroxide electrocatalyst for water oxidation.," *Journal of the American Chemical Society*, vol. 135, pp. 8452–5, June 2013.

[144] R. D. L. Smith, M. S. Prévot, R. D. Fagan, Z. Zhang, P. a. Sedach, M. K. J. Siu, S. Trudel, and C. P. Berlinguette, "Photochemical route for accessing amorphous metal oxide materials for water oxidation catalysis.," *Science*, vol. 340, pp. 60–63, Apr. 2013.

[145] X. Yu, M. Zhang, W. Yuan, and G. Shi, "A high-performance three-dimensional Ni–Fe layered double hydroxide/graphene electrode for water oxidation," *J. Mater. Chem. A*, vol. 3, pp. 6921–6928, 2015.

[146] F. Song and X. Hu, "Exfoliation of layered double hydroxides for enhanced oxygen evolution catalysis," *Nature Communications*, vol. 5, pp. 1–9, July 2014.

[147] L. Trotochaud, S. L. Young, J. K. Ranney, and S. W. Boettcher, "Nickel-iron oxyhydroxide oxygen-evolution electrocatalysts: the role of intentional and incidental iron incorporation.," *Journal of the American Chemical Society*, vol. 136, pp. 6744–53, May 2014.

[148] D. Friebel, M. W. Louie, M. Bajdich, K. E. Sanwald, Y. Cai, A. M. Wise, M.-J. Cheng, D. Sokaras, T.-C. Weng, R. Alonso-Mori, R. C. Davis, J. R. Bargar, J. K. Nørskov, A. Nilsson, and A. T. Bell, "Identification of Highly Active Fe Sites in (Ni,Fe)OOH for Electrocatalytic Water Splitting," *Journal of the American Chemical Society*, vol. 137, no. 3, pp. 1305–1313, 2015.

[149] B. M. Hunter, J. D. Blakemore, M. Deimund, H. B. Gray, J. R. Winkler, and A. M. Muller, "Highly Active Mixed-Metal Nanosheet Water Oxidation Catalysts Made by Pulsed-Laser Ablation in Liquids," *Journal of the American Chemical Society*, vol. 136, pp. 13118–13121, 2014.

[150] L. Trotochaud, J. K. Ranney, K. N. Williams, and S. W. Boettcher, "Solution-cast metal oxide thin film electrocatalysts for oxygen evolution.,"

Journal of the American Chemical Society, vol. 134, pp. 17253–17261, Oct. 2012.

[151] Y. Gorlin and T. F. Jaramillo, "A bifunctional nonprecious metal catalyst for oxygen reduction and water oxidation.," *Journal of the American Chemical Society*, vol. 132, pp. 13612–13614, Oct. 2010.

[152] J. Blakemore, H. Gray, J. Winkler, and A. Muller, "Co_3O_4 nanoparticle water-oxidation catalysts made by pulsed-laser ablation in liquids," *ACS Catalysis*, vol. 3, pp. 2497–2500, 2013.

[153] A. Bergmann, I. Zaharieva, H. Dau, and P. Strasser, "Electrochemical water splitting by layered and 3D cross-linked manganese oxides: correlating structural motifs and catalytic activity," *Energy & Environmental Science*, vol. 6, no. 9, p. 2745, 2013.

[154] I. Zaharieva, P. Chernev, M. Risch, K. Klingan, M. Kohlhoff, A. Fischer, and H. Dau, "Electrosynthesis, functional, and structural characterization of a water-oxidizing manganese oxide," *Energy & Environmental Science*, vol. 5, no. 5, p. 7081, 2012.

[155] M. Wiechen, I. Zaharieva, H. Dau, and P. Kurz, "Layered manganese oxides for water-oxidation: alkaline earth cations influence catalytic activity in a photosystem II-like fashion," *Chemical Science*, vol. 3, no. 7, pp. 2330–2339, 2012.

[156] F. Jiao and H. Frei, "Nanostructured manganese oxide clusters supported on mesoporous silica as efficient oxygen-evolving catalysts.," *Chemical Communications*, vol. 46, pp. 2920–2922, May 2010.

[157] M. M. Najafpour, F. Rahimi, M. Amini, S. Nayeri, and M. Bagherzadeh, "A very simple method to synthesize nano-sized manganese oxide: an efficient catalyst for water oxidation and epoxidation of olefins.," *Dalton transactions*, vol. 41, pp. 11026–31, Aug. 2012.

[158] M. Morita, C. Iwakura, and H. Tamura, "The anodic characteristics of manganese dioxide electrodes prepared by thermal decomposition of manganese nitrate," *Electrochimica Acta*, vol. 22, pp. 325–328, Apr. 1977.

[159] M. Morita, C. Iwakura, and H. Tamura, "THE ANODIC CHARACTERISTICS OF MODIFIED OXIDE ELECTRODE: Ti / RuO_x / MnO_x," *Electrochimica Acta*, vol. 23, pp. 331–335, 1978.

[160] M. Morita, C. Iwakura, and H. Tamura, "The anodic characteristics of massive manganese oxide electrode," *Electrochimica Acta*, vol. 24, no. 4, pp. 357–362, 1979.

[161] H. Dau, C. Limberg, T. Reier, M. Risch, S. Roggan, and P. Strasser, "The Mechanism of Water Oxidation: From Electrolysis via Homogeneous to Biological Catalysis," *ChemCatChem*, vol. 2, no. 7, pp. 724–761, 2010.

[162] D. M. Robinson, Y. B. Go, M. Mui, G. Gardner, Z. Zhang, D. Mastrogiovanni, E. Garfunkel, J. Li, M. Greenblatt, and G. C. Dismukes, "Photochemical water oxidation by crystalline polymorphs of manganese oxides: structural requirements for catalysis.," *Journal of the American Chemical Society*, vol. 135, pp. 3494–501, Mar. 2013.

[163] A. Ramírez, P. Hillebrand, D. Stellmach, M. M. May, P. Bogdanoff, and S. Fiechter, "Evaluation of MnO_x , Mn_2O_3 , and Mn_3O_4 Electrodeposited Films for the Oxygen Evolution Reaction of Water," *The Journal of Physical Chemistry C*, 2014.

[164] T. Takashima, K. Hashimoto, and R. Nakamura, "Mechanisms of pH-Dependent Activity for Water Oxidation to Molecular Oxygen by MnO_2 Electrocatalysts," *Journal of the American Chemical Society*, vol. 134, pp. 1519–1527, Jan. 2011.

[165] T. Takashima, K. Hashimoto, and R. Nakamura, "Inhibition of charge disproportionation of MnO_2 electrocatalysts for efficient water oxidation under neutral conditions.," *Journal of the American Chemical Society*, 2012.

[166] M. Huynh, D. Bediako, and D. Nocera, "A Functionally Stable Manganese Oxide Oxygen Evolution Catalyst in Acid," *Journal of the American Chemical Society*, vol. 136, pp. 6002–6010, 2014.

[167] K. L. Pickrahn, S. W. Park, Y. Gorlin, H.-B.-R. Lee, T. F. Jaramillo, and S. F. Bent, "Active MnO_x Electrocatalysts Prepared by Atomic Layer Deposition for Oxygen Evolution and Oxygen Reduction Reactions," *Advanced Energy Materials*, vol. 2, pp. 1269–1277, June 2012.

[168] K. Mette, A. Bergmann, J.-P. Tessonnier, M. Hävecker, L. Yao, T. Ressler, R. Schlögl, P. Strasser, and M. Behrens, "Nanostructured Manganese Oxide Supported on Carbon Nanotubes for Electrocatalytic Water Splitting," *ChemCatChem*, vol. 4, pp. 851–862, June 2012.

[169] V. R. Stamenkovic, B. S. Mun, K. J. J. Mayrhofer, P. N. Ross, and N. M. Markovic, "Effect of surface composition on electronic structure, stability, and electrocatalytic properties of Pt-transition metal alloys: Pt-skin versus Pt-skeleton surfaces," *Journal of the American Chemical Society*, vol. 128, no. 27, pp. 8813–8819, 2006.

[170] J. Zhang, K. Sasaki, E. Sutter, and R. R. Adzic, "Stabilization of platinum oxygen-reduction electrocatalysts using gold clusters.," *Science*, vol. 315, pp. 220–222, Jan. 2007.

[171] K. J. Mayrhofer, J. C. Meier, S. J. Ashton, G. K. Wiberg, F. Kraus, M. Hanzlik, and M. Arenz, "Fuel cell catalyst degradation on the nanoscale," *Electrochemistry Communications*, vol. 10, pp. 1144–1147, Aug. 2008.

[172] B. Wickman, H. Gronbeck, P. Hanarp, and B. Kasemo, "Corrosion Induced Degradation of Pt/C Model Electrodes Measured with Electrochemical Quartz Crystal Microbalance," *Journal of The Electrochemical Society*, vol. 157, no. 4, pp. B592–B598, 2010.

[173] A. Topalov, I. Katsounaros, M. Auinger, S. Cherevko, J. C. Meier, S. O. Klemm, and K. J. J. Mayrhofer, "Dissolution of platinum: limits for the deployment of electrochemical energy conversion?," *Angewandte Chemie (International ed. in English)*, vol. 51, pp. 12613–5, Dec. 2012.

[174] A. S. Bandarenka, E. Ventosa, A. Maljusch, J. Masa, and W. Schuhmann, "Techniques and methodologies in modern electrocatalysis: evaluation of activity, selectivity and stability of catalytic materials.," *The Analyst*, vol. 139, pp. 1274–91, Mar. 2014.

[175] A. Ohma, K. Shinohara, A. Iiyama, T. Yoshida, and A. Daimaru, "Membrane and catalyst performance targets for automotive fuel cells by FCCJ membrane, catalyst, MEA WG," *ECS Transactions*, vol. 41, no. 1, pp. 775–784, 2011.

[176] M. Escudero-Escribano, A. Verdaguer-Casadevall, P. Malacrida, U. Grønbjerg, B. P. Knudsen, A. K. Jepsen, J. Rossmeisl, I. E. L. Stephens, and I. Chorkendorff, "Pt_5Gd as a highly active and stable catalyst for oxygen electroreduction," *Journal of the American Chemical Society*, pp. 1–4, 2012.

[177] P. Malacrida, M. Escudero-Escribano, A. Verdaguer-Casadevall, I. E. L. Stephens, and I. Chorkendorff, "Enhanced activity and stability of Pt–La and Pt–Ce alloys for oxygen electroreduction: the elucidation of the active surface phase," *Journal of Materials Chemistry A*, vol. 2, no. 12, p. 4234, 2014.

[178] S. Cherevko, A. a. Topalov, A. R. Zeradjanin, I. Katsounaros, and K. J. J. Mayrhofer, "Gold dissolution: towards understanding of noble metal corrosion," *RSC Advances*, vol. 3, pp. 16516–16527, 2013.

[179] S. Cherevko, A. R. Zeradjanin, A. A. Topalov, N. Kulyk, and J. J. Mayrhofer, "Dissolution of noble metals during oxygen evolution in acidic media," *ChemCatChem*, vol. 6, no. 8, pp. 2219–2223, 2014.

[180] S. Cherevko, T. Reier, A. R. Zeradjanin, Z. Pawolek, P. Strasser, and K. J. Mayrhofer, "Stability of nanostructured iridium oxide electrocatalysts during oxygen evolution reaction in acidic environment," *Electrochemistry Communications*, vol. 48, pp. 81–85, 2014.

[181] R. Kotz, S. Stucki, D. Scherson, and D. M. Kolb, "IN-SITU IDENTIFICATION OF RuO_4 AS THE CORROSION PRODUCT DURING OXYGEN EVOLUTION ON RUTHENIUM IN ACID MEDIA," *Journal of Electroanalytical Chemistry*, vol. 172, pp. 211–219, 1984.

[182] M. Vukovic, "Rotating Ring-Disc Electrode Study of the Enhanced Oxygen Evolution on an Activated Ruthenium Electrode," *J. Chem. Soc., Faraday Trans*, vol. 86, no. 22, pp. 3743–3746, 1990.

[183] N. Danilovic, R. Subbaraman, K.-C. C. Chang, S. H. Chang, Y. J. Kang, J. D. Snyder, A. P. Paulikas, D. Strmcnik, Y.-T. T. Kim, D. J. Myers, V. R. Stamenkovic, and N. M. Markovic, "Activity-Stability Trends for the Oxygen Evolution Reaction on Monometallic Oxides in Acidic Environments," *The Journal of Physical Chemistry Letters*, vol. 5, pp. 2474–2478, June 2014.

[184] N. Danilovic, R. Subbaraman, K. C. Chang, S. H. Chang, Y. Kang, J. Snyder, A. P. Paulikas, D. Strmcnik, Y. T. Kim, D. Myers, V. R. Stamenkovic, and N. M. Markovic, "Using Surface Segregation To Design Stable Ru-Ir Oxides for the Oxygen Evolution Reaction in Acidic Environments," *Angewandte Chemie International Edition*, vol. 53, pp. 14016–14021, Oct. 2014.

[185] S. H. Chang, N. Danilovic, K.-C. Chang, R. Subbaraman, A. P. Paulikas, D. D. Fong, M. J. Highland, P. M. Baldo, V. R. Stamenkovic, J. W. Freeland, J. a. Eastman, and N. M. Markovic, "Functional links between stability and reactivity of strontium ruthenate single crystals during oxygen evolution.," *Nature Communications*, vol. 5, no. May, p. 4191, 2014.

[186] E. A. Paoli, *Activity and Stability of RuOx Based Electrocatalysts for the Oxygen Evolution Reaction*. PhD thesis, Technical University of Denmark, 2014.

[187] K. Wasa, M. Kitabatake, and H. Adachi, "Sputtering Phenomena," in *Thin Film Materials Technology*, ch. 3, pp. 71–114, William Andrew Publishing - Springer, 1st ed., 2004.

[188] J. A. Thornton, "High Rate Thick Film Growth," *Annual Review of Materials Science*, vol. 7, pp. 239–260, Aug. 1977.

[189] A. Anders, "A structure zone diagram including plasma-based deposition and ion etching," *Thin Solid Films*, vol. 518, pp. 4087–4090, May 2010.

[190] I. Chorkendorff and H. Niemantsverdriet, "X-ray Photoelectron Spectroscopy," in *Concepts of Modern Catalysis and Kinetics*, pp. 134–139, Wiley-VCH, 2nd ed., 2007.

[191] G. A. Somorjai, *Chemistry in Two Dimensions: surfaces*. Ithaca: Cornell University Press, 1981.

[192] V. Di Castro and G. Polzonetti, "XPS study of MnO oxidation," *Journal of Electron Spectroscopy and Related Phenomena*, vol. 48, pp. 117–123, Jan. 1989.

[193] Y. Gorlin and T. F. Jaramillo, "Investigation of Surface Oxidation Processes on Manganese Oxide Electrocatalysts Using Electrochemical Methods and Ex Situ X-ray Photoelectron Spectroscopy," *Journal of the Electrochemical Society*, vol. 159, pp. H782–H786, Aug. 2012.

[194] A. Langford, J.I. and Wilson, "Scherrer after Sixty Years: A Survey and Some New Results in the Determination of Crystallite Size," *Journal of Applied Crystallography*, vol. 11, pp. 102–113, 1978.

[195] B. van Brussel and J. T. M. D. Hosson, "Glancing angle x-ray diffraction: A different," *Applied physics letters*, vol. 64, no. 12, pp. 1585–1587, 1994.

[196] I. Chorkendorff and H. Niemantsverdriet, "Extended X-ray Absorption Fine Structure," in *Concepts of Modern Catalysis and Kinetics*, ch. 4, pp. 139–143, Wiley-VCH, 2nd ed., 2007.

[197] M. Newville, "Fundamentals of XAFS," tech. rep., University of Chicago, 2004.

[198] D. Sokaras, T. C. Weng, D. Nordlund, R. Alonso-Mori, P. Velikov, D. Wenger, a. Garachtchenko, M. George, V. Borzenets, B. Johnson, T. Rabedeau, and U. Bergmann, "A seven-crystal Johann-type hard x-ray spectrometer at the Stanford Synchrotron Radiation Lightsource," *Review of Scientific Instruments*, vol. 84, no. 5, 2013.

[199] D. Brandon and W. D. Kaplan, "Scanning Electron Microscopy," in *Microstructural Characterization of Materials*, ch. 5, pp. 261–286, Wiley, 2nd ed., 2008.

[200] D. A. Buttry and M. D. Ward, "Measurement of interfacial processes at electrode surfaces with the electrochemical quartz crystal microbalance," *Chemical Reviews*, vol. 92, pp. 1355–1379, Sept. 1992.

[201] M. Vukovic, "Electrochemical quartz crystal microbalance study of electrodeposited ruthenium," *Journal of Electroanalytical Chemistry*, vol. 474, pp. 167–173, 1999.

[202] G. Sauerbrey, "Verwendung von Schwingquarzen zur Wägung dünner Schichten und zur Mikrowägung," *Zeitschrift für Physik A Hadrons and Nuclei*, vol. 155, pp. 206–222, 1959.

[203] C. Gabrielli, M. Keddam, and R. Torresi, "Calibration of the electrochemical quartz crystal microbalance," *Journal of The Electrochemical Society*, vol. 138, no. 9, pp. 2657–2660, 1991.

[204] K. Keiji Kanazawa and J. G. Gordon, "The oscillation frequency of a quartz resonator in contact with liquid," *Analytica Chimica Acta*, vol. 175, no. C, pp. 99–105, 1985.

[205] R. Schumacher, G. Borges, and K. Kanazawa, "The quartz microbalance: A sensitive tool to probe surface reconstructions on gold electrodes in liquid," 1985.

[206] Perkin-Elmer, ""The 30 Minute Guide to ICP-MS"," tech. rep., 2011.

[207] D. M. Robinson, Y. B. Go, M. Mui, G. Gardner, Z. Zhang, D. Mastrogiovanni, E. Garfunkel, J. Li, M. Greenblatt, and G. C. Dismukes, "Photochemical Water Oxidation by Crystalline Polymorphs of Manganese Oxides: Structural Requirements for Catalysis.," *Journal of the American Chemical Society*, vol. 135, pp. 3494–3501, Feb. 2013.

[208] M. G. Walter, E. L. Warren, J. R. McKone, S. W. Boettcher, Q. Mi, E. A. Santori, and N. S. Lewis, "Solar water splitting cells.," *Chemical reviews*, vol. 110, pp. 6446–6473, Nov. 2010.

[209] Y. Gorlin, B. Lassalle-Kaiser, J. D. Benck, S. Gul, S. M. Webb, V. K. Yachandra, J. Yano, and T. F. Jaramillo, "In situ X-ray absorption spectroscopy investigation of a bifunctional manganese oxide catalyst with high activity for electrochemical water oxidation and oxygen reduction.," *Journal of the American Chemical Society*, vol. 135, pp. 8525–8534, June 2013.

[210] P. C. K. Vesborg, B. Seger, and I. Chorkendorff, "Recent Development in Hydrogen Evolution Reaction Catalysts and Their Practical Implementation," *The Journal of Physical Chemistry Letters*, pp. 951–957, Mar. 2015.

[211] M. M. Najafpour, K. C. Leonard, F.-R. F. Fan, M. A. Tabrizi, A. J. Bard, C. K. King'ondu, S. L. Suib, B. Haghighi, and S. I. Allakhverdiev, "Nano-size layered manganese-calcium oxide as an efficient and biomimetic catalyst for water oxidation under acidic conditions: comparable to platinum.," *Dalton transactions*, vol. 42, pp. 5085–91, Apr. 2013.

[212] R. Jinnouchi, E. Toyoda, T. Hatanaka, and Y. Morimoto, "First Principles Calculations on Site-Dependent Dissolution Potentials of Supported and Unsupported Pt Particles," *Journal of Physical Chemistry C*, vol. 114, no. 3, pp. 17557–17568, 2010.

[213] J. Greeley, "Structural effects on trends in the deposition and dissolution of metal-supported metal adstructures," *Electrochimica Acta*, vol. 55, pp. 5545–5550, Aug. 2010.

[214] G. Pötschke, J. Schröder, C. Günther, R. Hwang, and R. Behm, "A STM investigation of the nucleation and growth of thin Cu and Au films on Ru(0001)," *Surface Science Letters*, vol. 251-252, no. 0001, p. A346, 1991.

[215] J. Schroder, C. Gunther, R. Q. Hwang, and R. J. Behm, "A comparative STM study of the growth of thin Au films on clean and oxygen-precovered Ru(0001) surfaces," *Ultramicroscopy*, vol. 42-44, no. Part A, pp. 475–482, 1992.

[216] S. Dahl, a. Logadottir, R. Egeberg, J. Larsen, I. Chorkendorff, E. Törnqvist, and J. Nørskov, "Role of Steps in N_2 Activation on Ru(0001)," *Physical Review Letters*, vol. 83, no. 9, pp. 1814–1817, 1999.

[217] R. Frydendal, "Stability and activity of new mixed oxide catalysts for the Oxygen Evolution Reaction under acidic conditions," Master's thesis, Technical University of Denmark, 2012.

[218] J. Kohanoff, *Electronic Structure Calculations for Solids and Molecules*. CAMBRIDGE, 1st ed., 2006.

[219] D. J. Mowbray, J. I. Martínez, J. Rossmeisl, K. S. Thygesen, K. W. Jacobsen, and J. K. Nørskov, "Trends in Metal Oxide Stability for Nanorods , Nanotubes , and Surfaces," *The Journal of Physical Chemistry C*, vol. 115, pp. 2244–2252, 2011.

[220] B. Seger, T. Pedersen, A. Laursen, P. Vesborg, O. Hansen, and I. Chorkendorff, "Using TiO_2 as a Conductive Protective Layer for Photocathodic H_2 Evolution," *Journal of the American Chemical Society*, vol. 135, pp. 1057–1064, 2013.

[221] B. Seger, D. S. Tilley, T. Pedersen, P. C. K. Vesborg, O. Hansen, M. Grätzel, and I. Chorkendorff, "Silicon protected with atomic layer deposited TiO_2: durability studies of photocathodic H_2 evolution," *RSC Advances*, vol. 3, no. 48, pp. 25902–25907, 2013.

[222] B. Seger, S. D. Tilley, T. Pedersen, P. C. K. Vesborg, O. Hansen, M. Grätzel, and I. Chorkendorff, "Silicon protected with atomic layer deposited TiO_2: conducting versus tunnelling through TiO_2," *Journal of Materials Chemistry A*, vol. 1, no. 47, pp. 15089–15094, 2013.

[223] M. F. Lichterman, A. I. Carim, M. T. McDowell, S. Hu, H. B. Gray, B. S. Brunschwig, and N. S. Lewis, "Stabilization of n-cadmium telluride photoanodes for water oxidation to O_2(g) in aqueous alkaline electrolytes using amorphous TiO_2 films formed by atomic-layer deposition," *Energy & Environmental Science*, vol. 7, no. 10, pp. 3334–3337, 2014.

[224] N. C. Strandwitz, D. J. Comstock, R. L. Grimm, A. C. Nichols-Nielander, J. Elam, and N. S. Lewis, "Photoelectrochemical Behavior of n-type Si(100) Electrodes Coated with Thin Films of Manganese Oxide Grown by Atomic Layer Deposition," *The Journal of Physical Chemistry C*, vol. 117, pp. 4931–4936, Mar. 2013.

[225] Y. Gorlin, C.-J. Chung, J. D. Benck, D. Nordlund, L. Seitz, T.-C. Weng, D. Sokaras, B. M. Clemens, and T. F. Jaramillo, "Understanding Interactions between Manganese Oxide and Gold That Lead to Enhanced Activity for Electrocatalytic Water Oxidation.," *Journal of the American Chemical Society*, vol. 136, pp. 4920–4926, Mar. 2014.

[226] C.-h. Kuo, W. Li, L. Pahalagedara, A. M. El-Sawy, D. Kriz, N. Genz, C. Guild, T. Ressler, S. L. Suib, and J. He, "Understanding the Role of Gold Nanoparticles in Enhancing the Catalytic Activity of Manganese Oxides in Water Oxidation Reactions," *Angewandte Chemie International Edition*, vol. 127, pp. 2375–2380, Oct. 2014.

[227] M. S. El-Deab, M. I. Awad, A. M. Mohammad, and T. Ohsaka, "Enhanced water electrolysis: Electrocatalytic generation of oxygen gas at manganese oxide nanorods modified electrodes," *Electrochemistry Communications*, vol. 9, pp. 2082–2087, Aug. 2007.

[228] X. Lu, Y. H. Ng, and C. Zhao, "Gold nanoparticles embedded within mesoporous cobalt oxide enhance electrochemical oxygen evolution.," *ChemSusChem*, vol. 7, pp. 82–86, Jan. 2014.

[229] B. S. Yeo and A. T. Bell, "Enhanced activity of gold-supported cobalt oxide for the electrochemical evolution of oxygen.," *Journal of the American Chemical Society*, vol. 133, pp. 5587–5593, Apr. 2011.

[230] B. S. Yeo and A. T. Bell, "In Situ Raman Study of Nickel Oxide and Gold-Supported Nickel Oxide Catalysts for the Electrochemical Evolution of Oxygen," *The Journal of Physical Chemistry C*, vol. 116, no. 15, pp. 8394–8400, 2012.

[231] D. Jarosch and U. Wien, "Crystal Structure Refinement and Reflectance Measurements of Hausmannite, Mn_3O_4," *Mineralogy and Petrology*, vol. 37, pp. 15–23, 1987.

[232] S. Geller, "Structure of α-Mn_2O_3, $(Mn_{0.983}Fe_{0.017})_2O_3$ and $(Mn_{0.37}Fe_{0.63})_2O_3$ and relation to magnetic ordering," *Acta Crystallographica Section B Structural Crystallography and Crystal Chemistry*, vol. 27, no. 4, pp. 821–828, 1971.

[233] W. H. Baur, "Rutile-type compounds. V. Refinement of MnO_2 and MgF_2," *Acta Crystallographica Section B Structural Crystallography and Crystal Chemistry*, vol. 32, no. 7, pp. 2200–2204, 1976.

[234] W. P. Davey, "Precision measurements of the lattice constants of twelve common metals," *Physical Review*, vol. 25, no. 6, pp. 753–761, 1925.

[235] F. Farges, "Ab initio and experimental pre-edge investigations of the Mn K-edge XANES in oxide-type materials," *Physical Review B - Condensed Matter and Materials Physics*, vol. 71, no. 15, pp. 1–14, 2005.

[236] S. J. A. Figueroa, F. G. Requejo, E. J. Lede, L. Lamaita, M. A. Peluso, and J. E. Sambeth, "XANES study of electronic and structural nature of Mn-sites in manganese oxides with catalytic properties," *Catalysis Today*, vol. 107-108, pp. 849–855, 2005.

[237] A. Manceau, M. A. Marcus, and S. Grangeon, "Determination of Mn valence states in mixed-valent manganates by XANES spectroscopy," *American Mineralogist*, vol. 97, no. 5-6, pp. 816–827, 2012.

[238] H. Visser, E. Anxolabéhère-Mallart, U. Bergmann, P. Glatzel, J. H. Robblee, S. P. Cramer, J. J. Girerd, K. Sauer, M. P. Klein, and V. K. Yachandra, "Mn K-edge XANES and Kbeta XES studies of two Mn-oxo binuclear complexes: investigation of three different oxidation states relevant to the oxygen-evolving complex of photosystem II.," *Journal of the American Chemical Society*, vol. 123, no. 29, pp. 7031–7039, 2001.

[239] T. C. Weng, W. Y. Hsieh, E. S. Uffelman, S. W. Gordon-Wylie, T. J. Collins, V. L. Pecoraro, and J. E. Penner-Hahn, "XANES evidence against a manganyl species in the S_3 state of the oxygen-evolving complex," *Journal of the American Chemical Society*, vol. 126, no. 26, pp. 8070–8071, 2004.

[240] M. Haruta, "When gold is not noble: Catalysis by nanoparticles," *Chemical Record*, vol. 3, no. 2, pp. 75–87, 2003.

[241] S. H. Brodersen, U. Grønbjerg, B. Hvolbæk, and J. Schiøtz, "Understanding the catalytic activity of gold nanoparticles through multi-scale simulations," *Journal of Catalysis*, vol. 284, no. 1, pp. 34–41, 2011.

[242] P. Haider, J. D. Grunwaldt, R. Seidel, and A. Baiker, "Gold supported on Cu-Mg-Al and Cu-Ce mixed oxides: An in situ XANES study on the state

of Au during aerobic alcohol oxidation," *Journal of Catalysis*, vol. 250, no. 2, pp. 313–323, 2007.

[243] Y. Konishi, T. Tsukiyama, N. Saitoh, T. Nomura, S. Nagamine, Y. Takahashi, and T. Uruga, "Direct determination of oxidation state of gold deposits in metal-reducing bacterium Shewanella algae using X-ray absorption near-edge structure spectroscopy (XANES).," *Journal of bioscience and bioengineering*, vol. 103, no. 6, pp. 568–571, 2007.

Paper I

Benchmarking the Stability of Oxygen Evolution Reaction Catalysts: The Importance of Monitoring Mass Losses
Rasmus Frydendal, Elisa A. Paoli, Brian P. Knudsen, Björn Wickman, Paolo Malacrida, Ifan E.L. Stephens, Ib Chorkendorff
ChemElectroChem, 2014, *DOI* : 10.1002/*celc*.201402262

ChemPubSoc Europe

DOI: 10.1002/celc.201402262

Benchmarking the Stability of Oxygen Evolution Reaction Catalysts: The Importance of Monitoring Mass Losses

Rasmus Frydendal,[a] Elisa A. Paoli,[a] Brian P. Knudsen,[a] Björn Wickman,[a, b] Paolo Malacrida,[a] Ifan E. L. Stephens,*[a] and Ib Chorkendorff*[a]

Because of the rising need for energy storage, potentially facilitated by electrolyzers, improvements to the catalysis of the oxygen evolution reaction (OER) become increasingly relevant. Standardized protocols have been developed for determining critical figures of merit, such as the electrochemical surface area, mass activity and specific activity. Even so, when new and more active catalysts are reported, the catalyst stability tends to play a minor role. In this work, we monitor corrosion on RuO_2 and MnO_x by combining the electrochemical quartz crystal microbalance (EQCM) with inductively coupled plasma mass spectrometry (ICP–MS). We show that a meaningful estimation of the stability cannot be achieved based on purely electrochemical tests. On the catalysts tested, the anodic dissolution current was four orders of magnitude lower than the total current. We propose that even if long-term testing cannot be replaced, a useful evaluation of the stability can be achieved with short-term tests by using EQCM or ICP–MS.

1. Introduction

Water electrolysis is set to play a key role in the provision of solar fuels, as a sustainable substitute for fossil fuels.[1] Polymer electrolyte membrane (PEM) electrolysers are particularly well-suited towards the localised storage of renewables such as wind or solar, which are inherently intermittent. It turns out that the majority of the efficiency losses on these devices can be traced back to the oxygen evolution reaction (OER).[2,3] Consequently, it is critical that the OER catalyst has a sufficiently high activity, to minimise these losses, and that this activity is stable over the whole lifetime of the catalyst. This is particularly challenging, not only because the anode operates at inherently oxidising potentials, but also as a result of the acidic electrolyte of PEM electrolysers. At present, only IrO_x and RuO_x based materials show reasonable activity and stability under such conditions.[4,5] The best-performing catalysts in acidic media are shown in the Tafel plot in Figure 1 a, which provides an overview of the current state of the art, clearly dominated by oxide catalysts based on the scarce elements Ru and Ir. However, should PEM electrolysis make a true impact to the global energy landscape, it will need to be scaled up to the terawatt level;[6] consequently, the loading of the precious metals required to catalyse the OER should be decreased drastically or eliminated altogether.[7,8] In principle, the proton-con-

[a] R. Frydendal, E. A. Paoli, B. P. Knudsen, Dr. B. Wickman, Dr. P. Malacrida, Prof. I. E. L. Stephens, Prof. I. Chorkendorff
Center for Individual Nanoparticle Functionality
Department of Physics, Technical Univ. of Denmark
DK-2800 Kongens Lyngby (Denmark)
E-mail: ifan.stephens@fysik.dtu.dk
ibchork@fysik.dtu.dk

[b] Dr. B. Wickman
Department of Applied Physics
Chalmers University of Technology
SE-41296 Göteborg (Sweden)

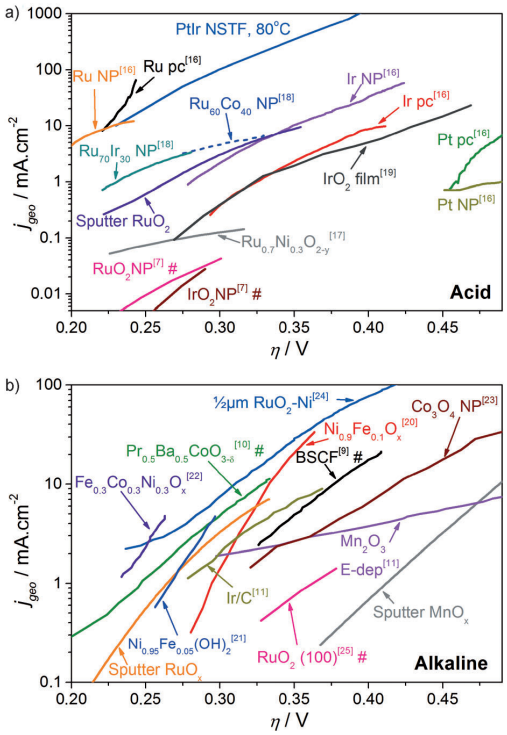

Figure 1. Overview of the state of the art for the oxygen evolution reaction: a) In acid media. Data adapted from: Present work for sputtered RuO_2,[16] for Ru, Ir and Pt polycrystalline (pc) and nanoparticles (NP),[17] for $Ru_{0.7}Ni_{0.3}O_{2-y}$ nanocrystals,[18] for RuCo and RuIr NP,[19] for IrO_2 film and[7] for RuO_2 and IrO_2 NP (# normalised to oxide area). b) In alkaline media. Data adapted from: Present work for sputtered MnO_x, from this group for sputtered RuO_x,[20] for $Ni_{0.9}Fe_{0.1}O_x$,[21] For $Ni_{0.95}Fe_{0.05}(OH)_2$,[22] for $Fe_{0.3}Co_{0.3}Ni_{0.3}O_x$,[9] for $Ba_{0.5}Sr_{0.5}Co_{0.8}Fe_{0.2}$ (# normalised to oxide area),[10] for $Pr_{0.5}Ba_{0.5}CoO_{3-\delta}$ (# normalised to oxide area),[11] for Ir/C and Mn_2O_3 E-dep,[23] for Co_3O_4 NP,[24] for RuO_2-Ni and[25] for RuO_2 (100) (normalised to oxide area).

ducting polymers used in PEM electrolysers could be replaced by hydroxide-conducting membranes; indeed, several materials have recently been discovered in alkaline electrolytes with a catalytic activity at least as high as that of RuO_x and IrO_x.[9–12] In Figure 1b, the best-performing OER catalysts in alkaline media are shown in a unified Tafel plot (it should be noted that in this plot the activity of some of the catalysts has been reported as a current density normalised according to the microscopic surface area, denoted by the symbol # in the plot, whereas other catalysts have been normalised according to the geometric surface area). It is clear from the plot that the most active catalysts are primarily based on Ni or Co. Even so, the use of alkaline polymeric membranes comes at the cost of increased overpotential for hydrogen evolution, and lower membrane conductivity and stability.[13–15]

Regardless of the pH of the electrolyte, robust OER catalyst benchmarks are required that allow a straightforward comparison of catalyst performance between different experimental groups.[4,7] Critical parameters include: 1) the geometric activity, that is, the current normalised according to the geometric or projected area, 2) the mass activity, that is, the current per unit mass precious metals, 3) the specific activity, the current normalised according to the microscopic area, and 4) the stability of the catalyst.

In a commercial device, it is essential that the geometric activity is maximised, to minimise overpotentials. Moreover, should precious metal oxides be employed, a high geometric activity should not be reliant on significant loadings of scarce elements, that is, the mass activity should also be maximised. Both the geometric activity and mass activity can be maximised by employing materials with a high specific activity and a high surface area. However, to judge whether a material is intrinsically active for a reaction, knowledge of the specific activity becomes important. This metric, in turn, is dependent on an accurate knowledge of the electrochemically active surface area, which is challenging to measure on oxides. Alternatively, the catalyst activity can be assessed using smooth thin films, where the microscopic surface area is as close as possible to the geometric surface area.[20,26,27]

The procedures for assessing the stability of OER catalysts are not well established in the literature; this is in contrast to the reverse of the OER, the oxygen reduction reaction (ORR), where detailed tests for assessing the catalyst stability have been developed to simulate the conditions required for automotive applications[28]. Thus far, most researchers have assessed the stability under OER conditions for a limited number of hours, by performing chronopotentiometry at a constant current density or chronoamperometry at a constant potential. However, it remains questionable whether such measurements can provide the basis upon which one could judge the long-term performance of a catalyst in a real device over the required lifetime, that is, a number of years.

A number of methods exist to monitor catalyst corrosion.[29] Microscopic techniques, such as scanning tunneling microscopy[30,31] and transmission electron microscopy,[32–35] can monitor changes in the electrode morphology and structure. On the other hand, macroscopic techniques can be applied to determine the corrosion rates; these include the rotating ring disk electrode (RRDE; for example, for monitoring the anodic dissolution of RuO_2[36,37]), the quartz crystal microbalance,[38] and inductively coupled plasma mass spectrometry (ICP–MS).[39–41] Nonetheless, as of yet, no standardized protocols for assessing the stability under OER conditions have emerged.

Herein, we present guidelines for establishing the stability of OER electrocatalysts. By combining standard RDE tests with electrochemical quartz crystal microbalance[42] (EQCM) measurements and inductively coupled plasma mass spectrometry (ICP–MS), we provide a detailed description of corrosion processes that take place in parallel to the OER. The catalysts investigated are RuO_2 and MnO_x. RuO_2 is an extensively studied material with a high activity in acidic electrolyte.[16,43–45] However, the stability of RuO_2 is limited at high overpotentials. MnO_x has been proposed as a more abundant and inexpensive alternative to RuO_2;[46–49] not only is it active for the OER, but also for the ORR, opening up possibilities for its use in regenerative fuel cells.[50] Manganese can form numerous oxides and many of these have been reported active for OER in alkaline and neutral electrolytes.[51] However, as for ruthenium dioxide, the stability can be an issue at high overpotentials.

Experimental Section

Preparation of Thin Films

Thin MnO_x and RuO_2 films were prepared by reactive sputter deposition on Au polycrystals and EQCM crystals. The deposition rates were calibrated with an in-chamber QCM. Prior to deposition, the samples were sonicated in acetone, isopropanol, and then Millipore water (18.2 MΩ). RuO_2 films were deposited at 300 °C and 3 mTorr with a power of 50 W using an argon and oxygen flow at a ratio of 5:2, with a metallic Ru target. MnO_x films were deposited at 200 °C, 5 mTorr, and 140 W with an argon and oxygen flow at a ratio of 5:1, and a metallic Mn target. The EQCM crystals were purchased from Stanford Research Systems (QCM200) and consist of a gold film deposited onto AT-cut quartz with a titanium layer in between for improved adhesion. The top electrode, functioning as working electrode for the electrochemical measurements, has a geometrical surface area of 1.37 cm^2. The bottom electrode is smaller, 0.38 cm^2, and the QCM is sensitive only in the overlapping region of the top and bottom electrodes. This means that approximately 28% of the electrochemically active layer is sensitive to the QCM measurement. The frequency change is converted to mass change using the Sauerbrey equation, as explained below. In this equation, a homogeneous mass change across the electrode is assumed. Because of the semiconducting nature of manganese oxides, we used a mask to confine the MnO_x area to where the QCM is sensitive (the central 0.38 cm^2 of the top electrode). This was done to diminish effects of local potential differences, for example, caused by gradients in film thickness. The remaining part of the gold film was covered with TiO_2, which introduced negligible currents and no frequency change during the stability tests. As RuO_2 is expected to be a metallic conductor, all of the gold film was covered with RuO_2. The Au polycrystalline electrodes (0.196 cm^2) used in RDE tests were polished prior to deposition with 0.25 μm diamond paste, then plasma cleaned in argon and annealed to 700 °C in two consecutive cycles. The targets for sputtering had a 99.95% purity and were purchased from AJA International.

Electrochemical Tests

The electrochemical tests on RuO_2 were performed in a glass cell with 0.05 M N_2-saturated H_2SO_4 (Merck Suprapur 96%, diluted with 18.2 MΩ Millipore water) at room temperature. The tests on MnO_x were performed in a two-compartment Teflon cell with 1 M N_2-saturated KOH (Merck Suprapur 99.995, diluted with 18.2 MΩ Millipore water) at room temperature. For the tests in sulfuric acid, a Hg/$HgSO_4$ reference electrode was used, whereas for the tests in KOH, a Hg/HgO in 20 wt% KOH reference electrode was used. The reference-electrode potentials were measured with respect to a reversible hydrogen electrode (RHE) by bubbling 1 bar hydrogen over a clean Pt surface in the same electrolyte. In both electrolytes, graphite rods were used as counter electrodes. All the data is presented using the RHE scale and corrected for Ohmic losses, found from the fitted high-frequency intercept measured using electrochemical impedance spectroscopy over the range of 1–200 000 Hz at a DC potential of 10 mV. The Ohmic drop for tests in 0.05 M H_2SO_4 was in the range of 15–18 Ω, whereas the tests in 1 M KOH comprised an Ohmic drop in the range of 3–5 Ω. For chronoamperometry measurements, the Ohmic drop was compensated at 85% using the Bio-Logic software EC-lab method MIR. Mass changes from EQCM measurements were calculated using the Sauerbrey equation with $C_f = (56.6 \pm 2.8)$ Hz cm^2 μg^{-1};[52] this value was calibrated by the electrodeposition of silver onto the Au-coated quartz crystal, repeated six times.[53] Each stability test performed by both EQCM and ICP–MS was repeated four times.

Since gold is not expected to be stable at high oxidative potentials,[40] we did not perform reference measurements with the bare EQCM crystals. Instead, the gold was coated by the catalyst thin film, as described above, and we measured the amount of gold in the electrolyte after OER tests. Based on two-hour tests at 1.9 V_{RHE} for three MnO_x samples, the increase of gold was less than 9 ng cm^{-2} or equivalent to less than 0.6 Hz. We therefore assumed that Au is sufficiently masked from the electrolyte.

At high current densities, gas formation on the electrode affects the frequency measurement; however, since the electrode was oriented vertically, the bubbles moved upwards and did not accumulate on the active area. While the bubble formation could cause some noise in the measurement, it would not have an effect on the trends observed over two-hour experiments.

Characterisation Methods

ICP–MS experiments were performed with equipment from Thermo Fisher Scientific, model iCAP-QC ICP-MS. Samples were taken out of the electrolyte before and after each measurement using a pipette. For tests in 0.05 M H_2SO_4, the samples were analysed without further dilution, whereas for 1 M KOH, the samples were diluted to 0.1 M to protect the ICP–MS components. For the quantitative analysis, calibration tests were performed using diluted solutions of Mn or Ru, made from standards with 1000 μg_{metal} mL^{-1} purchased from SCP Science. Calibrations were made with at least three concentrations. These were prepared in the range of 0.1 to 10 μg L^{-1} since the concentrations of Mn and Ru in the investigated electrolytes are all within that range. The calibration curves obtained could all be fitted to a linear curve with an R^2 of 0.99 or better. To calculate the total mass loss with ICP–MS, the volume of the electrolyte was measured for each experiment. For measurements with the two-compartment Teflon cell, only the volume of the compartment containing the working electrode was used. It was confirmed with a separate ICP–MS test that the amount of metal in the reference-electrode compartment was negligible. The thin films were evaluated by X-ray photoelectron spectroscopy using a Theta Probe instrument (Thermo Scientific) where the base pressure was 5×10^{-10} mbar. The X-ray source was monochromatized $Al_{K\alpha}$ (1486.7 eV). Furthermore, the thin films were analysed by X-ray diffraction (XRD) using a PANanalytical X'pert PRO equipment with an X-ray wavelength of 1.54 Å for the $Cu_{K\alpha}$ line.

2. Results and Discussion

To determine the structure of the two oxides, we performed glancing-angle XRD measurements. In Figure 2a, the diffractograms for RuO_2 and MnO_x are shown, together with literature references and a measurement for the glass substrate. For the RuO_2 film, the diffractogram obtained was consistent with a rutile RuO_2 structure,[54] whereas for MnO_x, no significant peaks were found, indicating that the film is amorphous. To

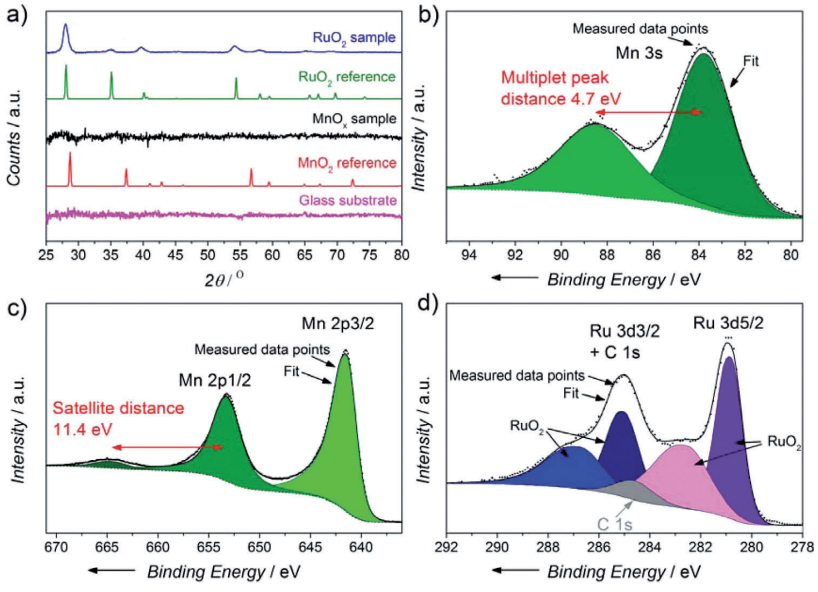

Figure 2. a) XRD diffractograms for RuO_2, MnO_x and the substrate, together with literature references. The literature data for RuO_2 is from Ref. [54] and that for MnO_2 from Ref. [59]. b) XPS spectra of the Mn 3s region for a 40 nm MnOx on EQCM sample. The red arrow indicates the difference in binding energy for the Mn 3s multiplet splitting. c) XPS spectra of the Mn 2p region for a 40 nm MnO_x on EQCM sample. The red arrow indicates the distance from the Mn 2p1/2 peak to its corresponding satellite. d) XPS spectra of the Ru 3d core level region for a 40 nm RuO_2 on EQCM sample.

further characterise the composition, XPS analyses were carried out. The results can be seen in Figure 2b–d for MnO_x and RuO_2, respectively. The MnO_x film was evaluated using the Mn 3 s multiplet splitting and Mn $2p_{1/2}$ distance between the main peak and its satellite.[55,56] The former was found to be 4.7 eV and the latter 11.4 eV, suggesting that the stoichiometry is consistent with MnO_2, which is also the most stable surface for Mn under OER conditions.[57] The RuO_2 film was evaluated based on the position and area of the Ru 3d lines, which matched with RuO_2 literature references.[58]

The electrochemical results are described in experimental order to ensure ease of reproducibility. As a first step, the activity of each sample was evaluated by using standard cyclic voltammetry at 5 mV s^{-1}. Representative results can be seen in Figure 3 for both RDE and EQCM setups. A useful figure of merit is the overpotential needed to sustain 10 mA cm^{-2}.[3] For RuO_2 in 0.05 M H_2SO_4 it is (354 ± 8) mV whereas for MnO_x it is (494 ± 6) mV, using the results from the RDE setup, based on two independent measurements for each oxide. These overpotentials are comparable to earlier reports in the literature, even though the films are only 40 nm thick and deposited onto smooth substrates, likely resulting in lower surface areas compared to samples made by electrodeposition or thermally prepared oxides. The activity obtained in the EQCM setup is slightly lower at high overpotentials for both samples; this discrepancy could result from a less facile bubble removal, compared to the rotating disk. However, the onsets of OER are the same in the two setups. Next, the Ohmic loss was evaluated by using impedance spectroscopy, followed by a stabilisation period during which the measured resonance frequency for the EQCM settled at a constant level. We observed that the frequency reading became stable after approximately 30 to 60 min, presumably due to temperature equilibration or equipment vibrations from cell assembly. Our criterion for establishing the stability was that the frequency would change less than 1 Hz over 15 min, which corresponds to a lower change than for any subsequent OER test. In the case of the RuO_2, the films were stabilised at 1.23 V_{RHE} whereas the MnO_x films were

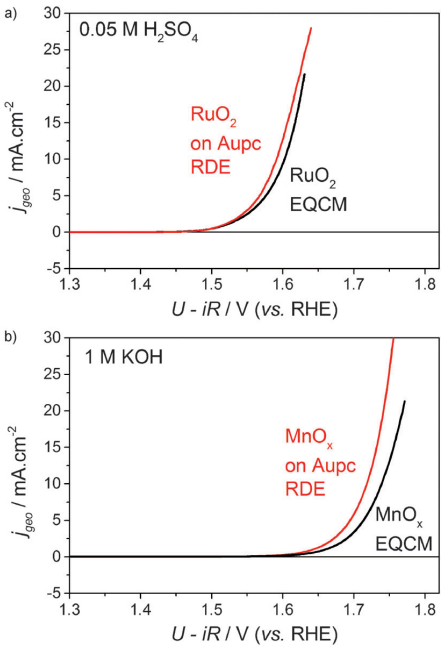

Figure 3. Cyclic voltammetry curves at room temperature for: a) 40 nm RuO_2 in 0.05 M N_2-saturated H_2SO_4. b) 40 nm MnO_x in 1 M N_2-saturated KOH. The scan rate was 5 mV s^{-1} and 1600 RPM (revolutions per minute) were used in the RDE tests. The current was normalised to the geometric area. The first anodic sweeps are shown.

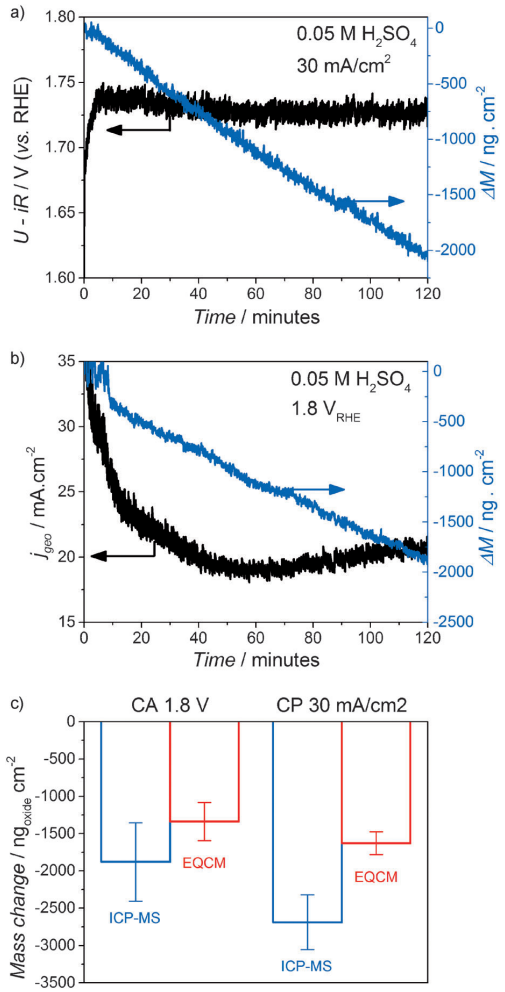

Figure 4. a) Chronopotentiometry at 30 mA cm^{-2} for 40 nm RuO_2 by using EQCM in 0.05 M N_2-saturated H_2SO_4 at room temperature. The black line indicates the measured potential and the blue line indicates the change in mass based on in situ resonance frequency measurements. b) Chronoamperometry at 1.8 V_{RHE} for 40 nm RuO_2 by using EQCM in 0.05 M N_2-saturated H_2SO_4 at room temperature. c) Comparison of the mass change found from EQCM and ICP–MS based on four separate experiments. The mass loss from the ICP–MS measurements was adjusted to the equivalent RuO_2 mass (rather than the Ru mass) for more direct comparison to EQCM measurements.

stabilised at 1.4 V_{RHE}; in both cases these potentials were chosen on the basis that the dioxide phases would be stable.[59] After the initial period of cycling, impedance measurement and stabilisation, samples for ICP–MS analysis were taken. From four measurements on each catalyst we found an average of (123 ± 60) $ng_{oxide}\,cm^{-2}$ RuO_2 and (472 ± 240) $ng_{oxide}\,cm^{-2}$ MnO_2 present in the solution prior to further testing. These results indicate that the initial cyclic voltammetry induces mass losses for both materials, these losses being more significant for MnO_x. During subsequent corrosion measurements, to assess the amount of Ru or Mn dissolved during the test, the initial amount of dissolved Ru or Mn at the start of the measurement was subtracted from the final amount.

Once the frequency had stabilised, first chronoamperometry, CA, and then chronopotentiometry, CP, measurements were started. For RuO_2, we measured CA at 1.8 V_{RHE} and CP at 30 $mA\,cm^{-2}$. These parameters were chosen to ensure that the potential was positive of the reversible potential for RuO_4 formation, 1.39 V_{RHE},[60] under standard conditions. For MnO_x, potentials at 1.8 and 1.9 V_{RHE} and a current density of 20 $mA\,cm^{-2}$ were chosen to be positive of the potential for MnO_4^- formation.[60] All stability tests were carried out for 2 h. We have observed that longer term tests tend to yield a poorer reproducibility; this could be a result of thickness gradients giving rise to local conductivity issues, exposed substrate, redeposition of dissolved species or precipitation. It should also be noted that corrosion mechanisms are highly dependent on the material.[39] The degradation of some materials may actually be accelerated by potential cycling (as shown by Mayrhofer and co-workers to be the case for Pt, by combining cyclic voltammetry with online ICP measurements[61]). Consequently, to study the resistance to corrosion of such materials, potentiodynamic—rather than potentiostatic—tests would be necessary.

2.1. Stability of RuO_2

In the case of RuO_2, the results from chronopotentiometry and chronoamperometry can be seen in Figure 4 a,b. Chronopotentiometry, as a technique, should correspond to the performance for a constant hydrogen production load on an electrolyser. The extra overpotential needed to sustain the hydrogen production is directly correlated to energy loss. In Figure 4 a, it can be seen that RuO_2 can maintain a stable performance, which changes only slightly during 2 h. However, looking at the mass change associated with the test, it is clear that there is a constant mass loss. This mass loss is equivalent to 4.8 monolayers (ML) per hour assuming the density and lattice parameters of (110) RuO_2 layers.[54] Figure 4 b shows the results of the chronoamperometry measurement. The potential is held constant throughout the measurement; since the current depends exponentially on the potential, any deactivation shows up more clearly than in a chronopotentiometry measurement. A constant potential at 1.8 V_{RHE} yields a mass loss equivalent of 4.4 ML per hour. With this rate, it would take approximately 29 h to corrode all of the 40 nm film. Assuming that the corrosion proceeds in accordance to $RuO_2 + 2H_2O \rightarrow RuO_{4(aq)} + 4H^+ + 4e^-$,[36] a dissolution rate of 4 ML per hour would be equivalent to 0.6 $\mu A\,cm^{-2}$, that is, more than four orders of magnitude lower than the oxygen evolution current density. In principle, the transient formation of RuO_4[36] could be detected with a rotating ring disk electrode setup; however, the necessary current sensitivity would be unrealistic. We also analysed the solution by ICP–MS after the electrochemical tests; Figure 4 c compares the EQCM and ICP–MS results. The mass losses found from the ICP–MS measurements shown in Figure 4 c are converted to RuO_2 equivalent since ICP–MS is only sensitive towards single elements and not the initial oxides. Comparing the two methods, there are differences for

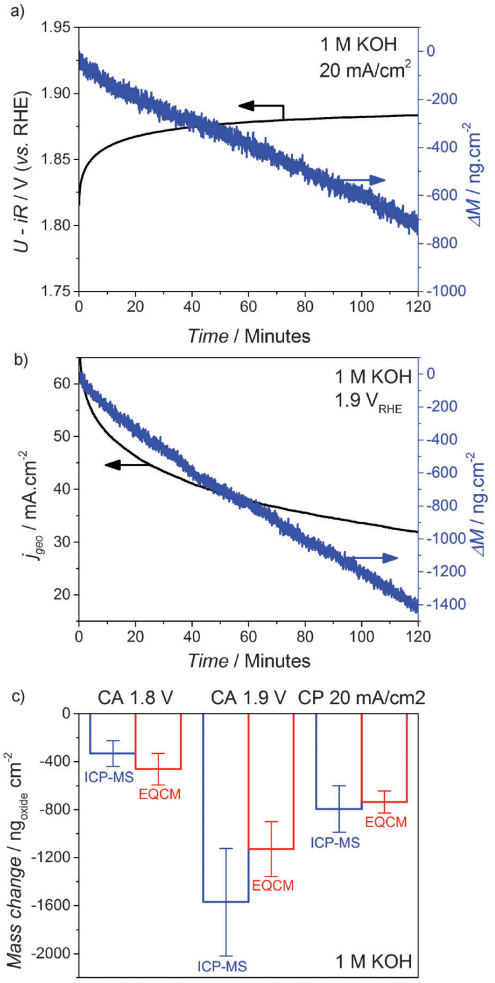

Figure 5. a) Chronopotentiometry at 20 $mA\,cm^{-2}$ for 40 nm MnO_x by using EQCM in 1 M N_2-saturated KOH at room temperature. The black line indicates the measured potential and the blue line indicates the change in mass based on in situ resonance frequency measurements. b) Chronoamperometry at 1.9 V_{RHE} for 40 nm MnO_x by using EQCM in 1 M N_2-saturated KOH at room temperature. c) Comparison of the mass change found from EQCM and ICP–MS based on four separate experiments. The mass loss from the ICP–MS measurements was adjusted to the equivalent MnO_2 mass (rather than the Mn mass), for more direct comparison to EQCM measurements.

both tests. The losses evaluated by ICP–MS are higher than what is seen from the EQCM method. This could be due to the fact that EQCM is only sensitive to about 28% of the catalytically active area, as descibed in the experimental section. We assume a homogeneous mass loss across the electrode but an inhomogenous current distribution could result in a wrong estimation. On the other hand, ICP–MS is sensitive to losses from the entire electrode area, which is likely to give a more accurate evaluation.

2.2. Stability of MnO_x

Chronopotentiometry and chronoamperometry tests were also carried out for MnO_x in alkaline solution, 1 M KOH, as shown on Figure 5 a,b. Compared to the results for RuO_2, the chronopotentiometry test results in a larger increase of potential during the two hours. The graph in Figure 5 a also shows the importance of choosing an axis length spanning only the relevant data range so the change is easily spotted. However, on the basis of the chronoamperometry measurement in Figure 5 b, the deactivation is even clearer because of the exponential behaviour of the current density as a function of the overpotential. However, in both measurements, a constant mass loss takes place in parallel with the oxygen evolution current. At 1.9 V_{RHE}, the loss of 1128 ng cm^{-2} is equivalent to about 3.9 ML per hour, assuming the density and lattice parameters of rutile (110) MnO_2 layers,[59] while a constant current at 20 mA cm^{-2} leads to a loss of about 2.6 ML per hour.[1] Assuming that the losses are due to anodic dissolution, that is, $MnO_2 + 2H_2O \rightarrow MnO_4^-{}_{(aq)} + 4H^+ + 3e^-$,[60] this rate would be equivalent to a current density of 0.35 μA cm^{-2}, more than four orders of magnitude lower than the total current.[2] The mass losses were also evaluated by ICP–MS after each measurement, as shown in Figure 5 c. We note that the error bars are rather large. Nonetheless, the two methods show an overall agreement. Extrapolating the data here, the time required to completely corrode a 40 nm-thick MnO_x film would be approximately 36 h at a constant potential of 1.9 V_{RHE}. From another perspective, a confirmation of stability for a given catalyst would require that a specific lifetime can be ensured. As an example, a lifetime of five years for a 40 nm film corresponds to a maximum of 0.02 Å dissolved material in a two-hour test. This rate for a RuO_2 catalyst on a 1 cm^2 electrode in 100 mL of electrolyte results in a less than 2 ppt concentration in the ICP–MS analysis. Such concentrations approach the limit of detection, that is, 0.4 ppt for Ru,[62] which complicates meaningful extrapolation. Therefore, a comprehensive lifetime evaluation should be accompanied by a long-term test. In Table 1, the relevant stability metrics and standard deviations are listed together with the OER activity of the thin films.

Table 1. Stability metrics from EQCM and ICP–MS.

Sample[a]	$\eta_{10\ mA\ cm^{-2}}$ [mV] from RDE		$\Delta M_{1.8\ V(RHE)}$ 2 h [$ng_{oxide}\ cm^{-2}$]	$\Delta M_{1.9\ V(RHE)}$ 2 h [$ng_{oxide}\ cm^{-2}$]	$\Delta M_{30\ mA\ cm^{-2}}$ 2 h [$ng_{oxide}\ cm^{-2}$]	$\Delta M_{20\ mA\ cm^{-2}}$ 2 h [$ng_{oxide}\ cm^{-2}$]
RuO_2	360 ± 8	EQCM	−1464 ± 13/	–	−1566 ± 110/	–
		ICP-MS	−1915 ± 69		−2624 ± 346	
MnO_x	490 ± 6	EQCM	−462 ± 131/	−1128 ± 229/	–	−735 ± 93/
		ICP-MS	−332 ± 108	−1570 ± 447		−793 ± 194

[a] For both oxides the measured mass losses are shown with corresponding standard deviation from four independent measurements. The overpotentials listed here are from RDE tests based on two independent measurements. Mass losses from EQCM are calculated from the frequency change using the Sauerbrey equation. Values for ICP–MS are corrected to the corresponding dioxide masses.

From these measurements, it is clear that solely examining current or potential changes for a small number of hours is insufficient to establish the long-term performance of an OER catalyst in an electrolyser. On the contrary, the anodic dissolution of a catalyst may actually manifest itself over a short-term measurement as an improvement in current density or decreased overpotential, due to an increased surface area.[34] OER conditions may lead to an increase in the microscopic surface area, a decrease in the catalyst surface area and a structural change to a more stable phase; without prior knowledge, it is not possible to determine which of these processes would predominate. Therefore, we emphasise that explicit analyses of mass changes are needed to quantify the stability of these catalysts.

3. Conclusions

In conclusion, we have shown that the stability of catalysts for the oxygen evolution reaction can be assessed by means of short-term tests based on a combination of EQCM and ICP–MS. It is clear that it is not possible to even roughly estimate the long-term performance of a catalyst on the basis of short-term chronopotentiometry or chronoamperometry measurements alone. Benchmarking and standardising research efforts are still at an early stage for this reaction. Nonetheless, when a new catalyst is discovered, rigorous and transparent criteria should be applied to establish whether or not the material is stable. While the end goal should be to test catalysts over the long term in actual devices, the quantification of mass losses using well-defined electrodes combined with EQCM and ICP–MS provides a less-time-consuming, albeit meaningful, alternative. Finally, although we have focused on the oxygen evolu-

[1] *We assumed a MnO_2 composition on the basis of our XPS analysis. Although the XRD experiments suggested that the films are amorphous, we take the view that the rutile (110) plane provides a reasonable approximation of the surface termination. Should we have chosen a different structure, the interplanar distance would always be between 2–4 Å, varying the loss in monolayers by less than a factor of two. The exact surface termination will not change our overall conclusions.*

[2] *It is conceivable that MnO_2 dissolves via a two-electron process to MnO_4^{2-},[60] which would lead to a corrosion current density of 0.26 μA cm^{-2}, rather than 0.35 μA cm^{-2}. Regardless, this will not change the picture presented herein, as the anodic current would still be negligible in comparison to the overall dissolution current.*

tion reaction, the findings of this report are general and could be applied to many other electrochemical reactions, including hydrogen evolution, oxygen reduction and CO_2 reduction.

Acknowledgements

The authors gratefully acknowledge financial support from the Danish Ministry of Science's UNIK initiative, Catalysis for Sustainable Energy. The Center for Individual Nanoparticle Functionality is supported by the Danish National Research Foundation (DNRF54). B.W. thanks Formas (project number 219-2011-959) for financial support.

Keywords: corrosion · electrochemistry · heterogeneous catalysis · thin films · water splitting

[1] J. Greeley, N. M. Markovic, *Energy Environ. Sci.* **2012**, *5*, 9246.
[2] A. Marshall, B. Børresen, G. Hagen, M. Tsypkin, R. Tunold, *Energy* **2007**, *32*, 431 – 436.
[3] M. G. Walter, E. L. Warren, J. R. McKone, S. W. Boettcher, Q. Mi, E. A. Santori, N. S. Lewis, *Chem. Rev.* **2010**, *110*, 6446 – 6473.
[4] C. C. L. McCrory, S. Jung, J. C. Peters, T. F. Jaramillo, *J. Am. Chem. Soc.* **2013**, *135*, 16977 – 16987.
[5] S. Trasatti, *J. Electroanal. Chem.* **1980**, *111*, 125 – 131.
[6] R. Smalley, *MRS Bull.* **2005**, *30*, 00.
[7] Y. Lee, J. Suntivich, K. May, E. E. Perry, Y. Shao-Horn, *J. Phys. Chem. Lett.* **2012**, *3*, 399 – 404.
[8] P. C. K. Vesborg, T. F. Jaramillo, *RSC Adv.* **2012**, *2*, 7933.
[9] J. Suntivich, K. J. May, H. A. Gasteiger, J. B. Goodenough, Y. Shao-Horn, *Science* **2011**, *334*, 1383 – 1385.
[10] A. Grimaud, K. J. May, C. E. Carlton, Y.-L. Lee, M. Risch, W. T. Hong, J. Zhou, Y. Shao-Horn, *Nat. Commun.* **2013**, *4*, 2439.
[11] Y. Gorlin, T. F. Jaramillo, *J. Am. Chem. Soc.* **2010**, *132*, 13612 – 13614.
[12] M. Gong, Y. Li, H. Wang, Y. Liang, J. Z. Wu, J. Zhou, J. Wang, T. Regier, F. Wei, H. Dai, *J. Am. Chem. Soc.* **2013**, *135*, 8452 – 8455.
[13] W. Sheng, H. A. Gasteiger, Y. Shao-Horn, J. E. Soc, P. B-b, *J. Electrochem. Soc.* **2010**, *157*, B1529.
[14] K. Ayers, L. Dalton, E. Anderson, *ECS Trans.* **2012**, *41*, 27 – 38.
[15] M. Piana, M. Boccia, A. Filpi, E. Flammia, H. A. Miller, M. Orsini, F. Salusti, S. Santiccioli, F. Ciardelli, A. Pucci, *J. Power Sources* **2010**, *195*, 5875 – 5881.
[16] T. Reier, M. Oezaslan, P. Strasser, *ACS Catal.* **2012**, *2*, 1765 – 1772.
[17] K. Macounová, J. Jirkovský, M. V. Makarova, J. Franc, P. Krtil, *J. Solid State Electrochem.* **2009**, *13*, 959 – 965.
[18] R. Forgie, G. Bugosh, K. C. Neyerlin, Z. Liu, P. Strasser, *Electrochem. Solid-State Lett.* **2010**, *13*, B36.
[19] M. Vuković, *J. Appl. Electrochem.* **1987**, *17*, 737 – 745.
[20] L. Trotochaud, J. K. Ranney, K. N. Williams, S. W. Boettcher, *J. Am. Chem. Soc.* **2012**, *134*, 17253 – 17261.
[21] L. Trotochaud, S. L. Young, J. K. Ranney, S. W. Boettcher, *J. Am. Chem. Soc.* **2014**, *136*, 6744 – 6753.
[22] R. D. L. Smith, M. S. Prévot, R. D. Fagan, Z. Zhang, P. A. Sedach, M. K. J. Siu, S. Trudel, C. P. Berlinguette, *Science* **2013**, *340*, 60 – 63.
[23] J. Blakemore, H. Gray, J. Winkler, A. Müller, *ACS Catal.* **2013**, *3*, 2497 – 2500.
[24] K. Juodkazis, J. Juodkazytė, R. Vilkauskaitė, B. Šebeka, V. Jasulaitienė, *CHEMIJA* **2008**, *19*, 1 – 6.
[25] K. Stoerzinger, L. Qiao, M. D. Biegalski, Y. Shao-Horn, *J. Phys. Chem. Lett.* **2014**, *5*, 1636 – 1641.
[26] R. Subbaraman, D. Tripkovic, K.-C. Chang, D. Strmcnik, A. P. Paulikas, P. Hirunsit, M. Chan, J. Greeley, V. Stamenkovic, N. M. Markovic, *Nat. Mater.* **2012**, *11*, 550 – 557.
[27] M. Risch, K. A. Stoerzinger, S. Maruyama, W. T. Hong, I. Takeuchi, Y. Shao-Horn, *J. Am. Chem. Soc.* **2014**, *136*, 5229 – 5232.
[28] A. Ohma, K. Shinohara, A. Iiyama, T. Yoshida, A. Daimaru, *ECS Trans.* **2011**, *41*, 775 – 784.
[29] A. S. Bandarenka, E. Ventosa, A. Maljusch, J. Masa, W. Schuhmann, *Analyst* **2014**, *139*, 1274 – 1291.
[30] L. Tang, B. Han, K. Persson, C. Friesen, T. He, K. Sieradzki, G. Ceder, *J. Am. Chem. Soc.* **2009**, *132*, 596 – 600.
[31] M. Wakisaka, S. Asizawa, H. Uchida, M. Watanabe, *Phys. Chem. Chem. Phys.* **2010**, *12*, 4184 – 4190.
[32] K. J. J. Mayrhofer, J. C. Meier, S. J. Ashton, G. K. H. Wiberg, F. Kraus, M. Hanzlik, M. Arenz, *Electrochem. Commun.* **2008**, *10*, 1144 – 1147.
[33] F. J. Perez-Alonso, C. F. Elkjær, S. S. Shim, B. L. Abrams, I. E. L. L. Stephens, I. Chorkendorff, *J. Power Sources* **2011**, *196*, 6085 – 6091.
[34] K. J. May, C. E. Carlton, K. A. Stoerzinger, M. Risch, J. Suntivich, Y.-L. Lee, A. Grimaud, Y. Shao-Horn, *J. Phys. Chem. Lett.* **2012**, *3*, 3264 – 3270.
[35] J. C. Meier, I. Katsounaros, C. Galeano, H. J. Bongard, A. A. Topalov, A. Kostka, A. Karschin, F. Schüth, K. J. J. Mayrhofer, *Energy Environ. Sci.* **2012**, *5*, 9319.
[36] M. Vuković, *J. Chem. Soc. Faraday Trans.* **1990**, *86*, 3743 – 3746.
[37] N. Danilovic, R. Subbaraman, K.-C. Chang, S. H. Chang, Y. Kang, J. D. Snyder, A. P. Paulikas, D. Strmcnik, Y.-T. Kim, D. J. Myers, V. R. Stamenkovic, N. M. Markovic, *J. Phys. Chem. Lett.* **2014**, *5*, 2427 – 2478.
[38] B. Wickman, H. Grönbeck, P. Hanarp, B. Kasemo, *J. Electrochem. Soc.* **2010**, *157*, B592 – B598.
[39] S. Cherevko, A. R. Zeradjanin, A. A. Topalov, N. Kulyk, J. J. Mayrhofer, *ChemCatChem* **2014**, DOI: 10.1002/cctc.201.
[40] S. Cherevko, A. a. Topalov, A. R. Zeradjanin, I. Katsounaros, K. J. J. Mayrhofer, *RSC Adv.* **2013**, *3*, 16516 – 16527.
[41] L. Xing, M. A. Hossain, M. Tian, D. Beauchemin, K. T. Adjemian, G. Jerkiewicz, *Electrocatalysis* **2014**, *5*, 96 – 112.
[42] D. A. Buttry, M. D. Ward, *Chem. Rev.* **1992**, *92*, 1355 – 1379.
[43] G. Lodi, E. Sivieri, A. De Battisti, S. Trasatti, *J. Appl. Electrochem.* **1978**, *8*, 135 – 143.
[44] H. Over, *Chem. Rev.* **2012**, *112*, 3356 – 3426.
[45] E. A. Paoli, F. Masini, R. Frydendal, D. Deiana, C. Schlaup, M. Malizia, T. W. Hansen, S. Horch, I. E. L Stephens, I. Chorkendorff, *Chem. Sci.* **2014**, DOI: 10.1039/C4SC02685C.
[46] H. Dau, C. Limberg, T. Reier, M. Risch, S. Roggan, P. Strasser, *ChemCatChem* **2010**, *2*, 724 – 761.
[47] Y. Gorlin, T. F. Jaramillo, *J. Electrochem. Soc.* **2012**, *159*, H782 – H786.
[48] K. L. Pickrahn, S. W. Park, Y. Gorlin, H.-B.-R. Lee, T. F. Jaramillo, S. F. Bent, *Adv. Energy Mater.* **2012**, *2*, 1269 – 1277.
[49] K. Mette, A. Bergmann, J.-P. Tessonnier, M. Hävecker, L. Yao, T. Ressler, R. Schlögl, P. Strasser, M. Behrens, *ChemCatChem* **2012**, *4*, 851 – 862.
[50] J. W. Desmond Ng, Y. Gorlin, T. Hatsukade, T. F. Jaramillo, *Adv. Energy Mater.* **2013**, *3*, 1545 – 1550.
[51] D. M. Robinson, Y. B. Go, M. Mui, G. Gardner, Z. Zhang, D. Mastrogiovanni, E. Garfunkel, J. Li, M. Greenblatt, G. C. Dismukes, *J. Am. Chem. Soc.* **2013**, *135*, 3494 – 3501.
[52] G. Sauerbrey, *Z. Phys.* **1959**, *155*, 206 – 222.
[53] C. Gabrielli, M. Keddam, R. Torresi, *J. Electrochem. Soc.* **1991**, *138*, 2657 – 2660.
[54] C. Boman, *Acta Chem. Scand.* **1970**, *24*, 116 – 122.
[55] Y. Gorlin, B. Lassalle-Kaiser, J. D. Benck, S. Gul, S. M. Webb, V. K. Yachandra, J. Yano, T. F. Jaramillo, *J. Am. Chem. Soc.* **2013**, *135*, 8525 – 8534.
[56] V. Di Castro, G. Polzonetti, *J. Electron Spectrosc. Relat. Phenom.* **1989**, *48*, 117 – 123.
[57] H.-Y. Su, Y. Gorlin, I. C. Man, F. Calle-Vallejo, J. K. Nørskov, T. F. Jaramillo, J. Rossmeisl, F. Jaramillo, *Phys. Chem. Chem. Phys.* **2012**, *14*, 14010 – 14022.
[58] R. Kötz, H. J. Lewerenz, S. Stucki, *J. Electrochem. Soc.* **1983**, *130*, 825 – 829.
[59] W. H. Baur, *Acta Crystallogr. Sect. B* **1976**, *32*, 2200 – 2204.
[60] M. Pourbaix, *Atlas of Electrochemical Equilibria in Aqueous Solutions*, Pergamon Press, Oxford, **1966**.
[61] A. Topalov, I. Katsounaros, M. Auinger, S. Cherevko, J. C. Meier, S. O. Klemm, K. J. J. Mayrhofer, *Angew. Chem. Int. Ed.* **2012**, *51*, 12613 – 12615; *Angew. Chem.* **2012**, *124*, 12782 – 12784.
[62] *ICP Application Note for iCAP-QC*, Thermo Fisher Scientific, **2012**.

Received: July 31, 2014
Published online on ■■ ■■, 2014

ARTICLES

R. Frydendal, E. A. Paoli, B. P. Knudsen, B. Wickman, P. Malacrida, I. E. L. Stephens, I. Chorkendorff**

■■ – ■■

Benchmarking the Stability of Oxygen Evolution Reaction Catalysts: The Importance of Monitoring Mass Losses

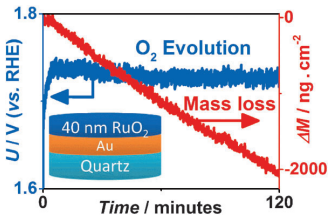

Quantifying stability: It is shown that short-term electrochemical measurements are inadequate to establish oxygen evolution catalyst stability. Independent measurements of mass losses are essential.

Paper II

Enhancing Activity for the Oxygen Evolution Reaction: the Beneficial Interaction of Au with Mn and Co Oxides
Rasmus Frydendal, Michael Busch, Niels Halck-Brendtsen, Elisa A. Paoli, Peter Krtil, Ib Chorkendorff, Jan Rossmeisl
ChemCatChem, 2014, *DOI* : 10.1002/*cctc*.201402756

ChemPubSoc Europe

DOI: 10.1002/cctc.201402756

Enhancing Activity for the Oxygen Evolution Reaction: The Beneficial Interaction of Gold with Manganese and Cobalt Oxides

Rasmus Frydendal,[a] Michael Busch,[b] Niels B. Halck,[b] Elisa A. Paoli,[a] Petr Krtil,[c] Ib Chorkendorff,[a] and Jan Rossmeisl*[b]

Electrochemical production of hydrogen, facilitated in electrolyzers, holds great promise for energy storage and solar fuel production. A bottleneck in the process is the catalysis of the oxygen evolution reaction, involving the transfer of four electrons. The challenge is that the binding energies of all reaction intermediates cannot be optimized individually. However, experimental investigations have shown that drastic improvements can be realized for manganese and cobalt-based oxides if gold is added to the surface or used as substrate. We propose an explanation for these enhancements based on a hydrogen acceptor concept. This concept comprises a stabilization of an *–OOH intermediate, which effectively lowers the potential needed for breaking bonds to the surface. On this basis, we investigate the interactions between the oxides and gold by using DFT calculations. The results suggest that the oxygen evolution reaction overpotential decreases by 100–300 mV for manganese oxides and 100 mV for cobalt oxides.

Introduction

The sustainable production of hydrogen is a promising route for intermittent energy sources such as wind and solar power.[1] The electrochemical splitting of water is facilitated in electrolyzers, in which hydrogen is evolved at the cathode and oxygen at the anode. The overall efficiency of such cells is severely hindered by losses at the anode,[2,3] at which the complicated oxygen evolution reaction (OER) introduces a large overpotential. This process has been the focus of many studies, both theoretical[4–10] and experimental,[11–17] but despite the keen attention, the state-of-the-art OER catalysts still exhibit large overpotentials. In OER, four electrons and protons are removed from two water molecules. The proton and electron most difficult to remove determine the overpotential. The four reaction steps are shown in Equations (1)–(4).

$$*-OH_2 \rightarrow *-OH + H^+ + e^- \quad (1)$$

$$*-OH \rightarrow *=O + H^+ + e^- \quad (2)$$

$$*=O + H_2O \rightarrow *-OOH + H^+ + e^- \quad (3)$$

$$*-OOH \rightarrow * + O_2 + H^+ + e^- \quad (4)$$

in which * represents an active surface site. This reaction pathway is valid for acidic solutions but changing to an alkaline environment does not change the thermodynamic analysis presented herein. The potential-determining step indicates the potential needed to have all steps downhill in free energy. From a thermodynamic point of view, the potential for removing protons and electrons is given by differences in free energy between reaction intermediates.[18] Therefore, minimizing the overpotential is firstly a matter of binding the reaction intermediates with the right strength to the catalyst surface, making the largest free energy difference for any oxidation step as small as possible. Unfortunately, the binding energies of the different intermediates cannot be varied independently from each other; in general binding energies of similar intermediates scale with each other.[19–21] This phenomenon has been established for reaction intermediates such as SH_x, NH_x, and OH_x on a variety of surfaces including metals, sulfides, nitrides, and oxides and is known as scaling relations. The two OER intermediates *–OH and *–OOH therefore interact in a similar way with any catalyst surface, which limits the activity of even the best performing catalysts. For the OER (proceeding via *–OH and *–OOH intermediates), a minimal overpotential of 0.3–0.4 V is needed owing to a constant difference in free energy of 3.2 eV for the $2e^-/H^+$ oxidation from *–OH to *–OOH.[9,10] The minimum overpotential can be found from the energy difference of 3.2 eV by dividing with two elementary charges and subtracting the equilibrium potential for oxygen

[a] R. Frydendal, E. A. Paoli, Prof. I. Chorkendorff
Center for Individual Nanoparticle Functionality
Department of Physics
Technical University of Denmark
DK-2800 Kongens Lyngby (Denmark)

[b] Dr. M. Busch, N. B. Halck, Prof. J. Rossmeisl
Center for Atomic-Scale Materials Design
Department of Physics
Technical University of Denmark
DK-2800 Kgs. Lyngby (Denmark)
E-mail: jross@fysik.dtu.dk

[c] Dr. P. Krtil
Department of Electrocatalysis
J. Heyrovský Institute of Physical Chemistry
Academy of Sciences of the Czech Republic
Dolejškova 3, 18223 Prague (Czech Republic)

Supporting information for this article is available on the WWW under http://dx.doi.org/10.1002/cctc.201402756.

evolution at standard conditions of 1.23 V.[9] Thus, the two proton–electron transfers both proceed at 1.6 V, equivalent to an overpotential of 0.37 V. By changing from one catalyst to another and thereby changing the binding strength, there is little hope to break this fundamental limitation for OER. For catalyst surfaces that bind too strongly (which is the situation on Mn, Co, Ir, and Ru oxides), the overpotential originates from breaking a bond between the intermediates and the surface [Eq. (3)].

For surfaces that bind too weakly, such as NiO or TiO_2, the overpotential is related to bonds forming to the surface [Eqs. (1) or (2)]. This simple relationship between catalytic activity and binding of intermediates illustrates the Sabatier principle.[22] For the OER a suitable descriptor for the activity is the reaction energy of the second step [Eq. (2)], $\Delta G_{*=O} - \Delta G_{*-OH}$. Through the linear scaling relation between *–OH and *–OOH, this single descriptor can describe the potential-determining step for both strong and weak binding catalysts towards the OER.[10]

For catalyst surfaces on which reaction (3) is potential-determining, the activity could be enhanced by stabilizing the *–OOH intermediate relative to *=O and *–OH, as reaction (3) would then require a lower potential. A strategy and example on this concept have recently been demonstrated for mixtures with RuO_2 and either Co or Ni.[23] The idea is to introduce a hydrogen acceptor on the RuO_2 surface, in this case an oxygen atom, near Co or Ni so that *–OOH forms a strong hydrogen bond to this acceptor or even donates the hydrogen, forming $*–OH_{acceptor}$ and O_2 on the surface rather than the *–OOH intermediate. Experimentally, several studies have reported activities that oxides based on Ru–Co or Ru–Ni mixtures are more active than pure RuO_2.[24–26]

Decoupling the *–OOH binding energy from the *–OH binding makes it possible to tune the catalytic properties by varying the hydrogen acceptor. Reaction (3) is therefore changed into reaction (5):

$$*{=}O + H_2O + *{=}O_{acceptor} \rightarrow *{-}O_2 + *{-}OH_{acceptor} + H^+ + e^- \quad (5)$$

In this case the thermodynamic restrictions owing to the linear scaling relationships between *–OH and *–OOH binding no longer hold, that is, formally the OER may proceed at potentials closer to the thermodynamic limit.[23] The desirable property of the acceptor site is a suitable potential at which $*{=}O_{acceptor} \rightarrow *{-}OH_{acceptor}$ can proceed and regenerate. For oxygen evolution, the optimal potential for this hydrogen acceptor process would be near 1.23 V.

Manganese and cobalt oxides have been studied extensively in recent years[6–8,13,27–31] as alternatives to the commonly used Ru or Ir-based catalysts.[11] Besides being abundant and benign elements, they have been proven active in the OER[32–35] and, in the case of MnO_x, also in the oxygen reduction reaction.[36,37] It has recently been shown that the activity of MnO_x nanoparticles towards oxygen evolution can be drastically increased in the presence of Au.[38] From those results, a combination of MnO_x and Au nanoparticles showed a 20-fold increase in turnover frequency at 400 mV overpotential. The enhanced activity was also obtained by adding Au as $H[AuCl_4]$ to the electrolyte. A similar effect was found earlier by El-Deab, Mohammad et al. by using Au as substrate for nano-MnOOH, reducing the overpotential by more than 200 mV compared to that found on Pt or glassy carbon substrates.[39,40]

Similarly, for CoO_x it has been found that depositing 0.4 monolayers of CoO_x on Au results in a higher activity than pure CoO_x.[41] It was even shown that Au-supported CoO_x was more active than Pt, Pd, and Cu-supported CoO_x. From those results the authors suggested that the effect of the metal support was related to the electronegativity affecting the binding to oxygen.[41] Another interpretation could be that the metal support was directly involved in the OER mechanism, as the effect was most pronounced for submonolayer films. Furthermore, in a recent study Au nanoparticles embedded in mesoporous Co_3O_4 were found to enhance the activity towards OER.[30] In Figure 1, the experimental observations from[30,38,41] have been summarized in a Tafel plot. For MnO_x nanoparticles, the decrease in overpotential due to presence of Au varied from 100 to 150 mV, whereas for CoO_x the decrease varied from 20 to 100 mV.

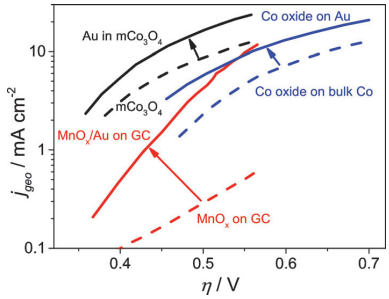

Figure 1. Experimental data summarized in a Tafel plot, showing recent reports of OER activity enhancements due to the presence of Au. For MnO_x/Au and MnO_x the data is taken from Ref. [38]. For CoO_x on Au and on bulk Co the data is from Ref. [41], and for Au in mesoporous (m-) Co_3O_4 and Co_3O_4 the data is from Ref. [30].

In this work we propose an explanation for these activity enhancements on the basis of the recently proposed hydrogen transfer from *OOH to an adjacent acceptor site.[23] By using DFT, the binding energies to the OER intermediates have been calculated on both rutile MnO_2 and Mn_2O_3 and the effect of Au interaction is explored. These two oxides are chosen due to their stability at OER relevant potentials.[27,42] Data for CoO_x are taken from Ref. [43].

Results and discussion

First, we focus on MnO_x and later extend the conceptual understanding to CoO_x. Water oxidation on pure Mn_2O_3 (and Co_3O_4) via *–OOH is thermodynamically limited by the formation of the *–OOH intermediate, as seen in the free energy diagram in Figure 2a. The free energy diagrams in Figure 2 are all shown at 0 V and depict the energy levels for each reaction

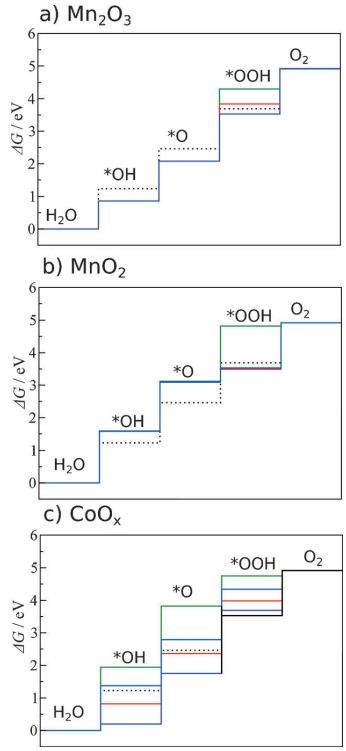

Figure 2. Free energy diagrams for the OER at zero applied potential. a) Mn_2O_3 without H transfer (——), with H transfer (——), and with H transfer to an adjacent Au=O site (——). b) Rutile MnO_2 without H transfer (——), with H transfer (——), with H transfer to an adjacent Au=O acceptor (——), and with H transfer to an Mn–O–Au site (——); blue and purple lines coincide. c) CoOOH (0112) (——), (0114) (——), and (0001) (——) surfaces, Co_3O_4 (——), and Co_3O_4 with H transfer to a Au=O acceptor (——). CoOOH data are taken from Ref. [43]. •••••: Energy levels for an ideal catalyst.

step [Eqs. (1)–(4)] with and without the hydrogen transfer mechanism. The overpotential for Mn_2O_3 is estimated to be 1.0 V, rendering this oxide inert for water oxidation. The overpotential is lowered significantly with a rutile-type MnO_2 catalyst, the surface Mn atoms of which are more oxidized. This weakens the Mn=O bond so that it breaks more easily on formation of the Mn–OOH intermediate, thus, the related overpotential decreases (see Figure 2b). Even in this case the formation of Mn–OOH remains potential-determining but the critical Mn=O intermediate is significantly destabilized, lowering the potential required to form the O–O bond to 1.7 eV. This corresponds to an overpotential of 0.5 V.

In both cases a stabilization of the *–OOH would result in a decrease of overpotential. Such an effect may be obtained by a hydrogen transfer from *–OOH to an adjacent acceptor site.[23] The hydrogen transfer could occur either to a Au=O acceptor site at an adjacent nanoparticle or, assuming the possibility of incorporating Au into the surface, to a Mn–O–Au site. Notably, the *–OH binding energy for a Au nanoparticle is modelled by the binding energy to Au(111). A visualization of these effects can be seen in Figure 3, with the hydrogen transfer to a nearby Au nanoparticle shown at the top and the incorporated Au site at the bottom. Additionally, the possibility of hydrogen transfer to a Mn=O unit needs to be considered. The latter situation may also be present in pure MnO_2.

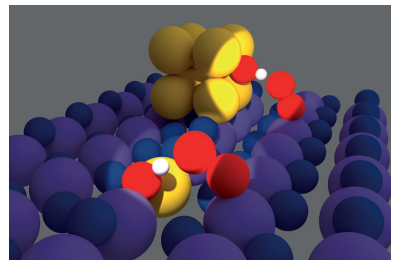

Figure 3. Model showing two different pathways for hydrogen transfer during OER on a rutile (110) MnO_2 surface. ●: Au, ●: Mn, ●: lattice O, ●: reacting O, and ○: H atoms. In the first pathway (upper highlight), the hydrogen transfer is facilitated by an adjacent Au nanoparticle. In the second pathway (lower highlight), the Mn–O–Au site functions as hydrogen acceptor, requiring Au to be incorporated into the MnO_2. A similar situation is possible for Co_3O_4 or the (0114) facet of β-CoOOH, which both benefit from Au=O as hydrogen acceptor.

Including hydrogen transfer to an adjacent Mn=O site on MnO_2 in the reaction mechanism results in the free energy diagram shown in Figure 2b (——). There is a clear stabilization of the Mn–OOH binding, the energy of which becomes 3.5 eV. At this point, only 0.3 eV is required to facilitate O–O bond formation. Correspondingly, the oxidation of water to a hydroxide [Eq. (1)] becomes potential-determining, resulting in a decrease in the overall overpotential to only 0.4 V. Although the assumed hydrogen transfer is thermodynamically favorable, it would likely be blocked under the reaction conditions as the required adjacent Mn=O sites are involved in the OER and thus unavailable.

This is in contrast to the case with Au=O and Mn–O–Au sites, which are both inactive for water oxidation[39] but show favorable energetics as hydrogen acceptors. The cost for recovery of Au=O species, assuming an *=O coverage of 1/3 at a face-centered cubic (111) surface was reported to be 1.4 eV.[4] In fact, there is likely a variety of different sites available on Au nanoparticles that could act as hydrogen acceptors, however, treating a full Au nanoparticle is outside the scope of this investigation. Correspondingly, the binding energy of the *–OOH species decreases to 3.5 eV, rendering the initial formation of *–OH [Eq. (2)] potential-determining. Again the overpotential is lowered to 0.4 V. Incorporation of Au into the MnO_2 lattice, depicted in the lower highlight in Figure 3, can result in the formation of a Mn–O–Au site. In such a configuration the Au is located in a bridging position.[10] Assuming hydrogen transfer to a Mn–O–Au site again renders the oxidation of water to Mn–OH potential-determining by lowering the binding energy of Mn–OOH to 3.5 eV. Therefore, reaction (1) determines the theoretical overpotential, which becomes 0.4 V.

In the case of Mn_2O_3 the binding to all the intermediates are stronger, resulting in a close to ideal binding of the *O and *OH intermediates. Upon assuming hydrogen transfer to an adjacent Au=O site at a Au nanoparticle, the overpotential is lowered to only 0.2 V. Here the recovery of the hydrogen acceptor unit and the O–O bond formation step require approximately the same potentials. Further improvements are only possible with a more ideal hydrogen acceptor. This analysis is summarized in Figure 4, which includes the volcano plot showing the activity dependence based on a single descriptor, $\Delta G_{*=O} - \Delta G_{*-OH}$. This volcano arises from limitations of the scaling relations that result in an overpotential of 0.3–0.4 V at the peak, as described in the Introduction. Pure Mn_2O_3 is predicted to be less active than pure MnO_2, but with Au as hydrogen acceptor the order shifts as more ideal binding energies are available for reactions (1) and (2) on Mn_2O_3.

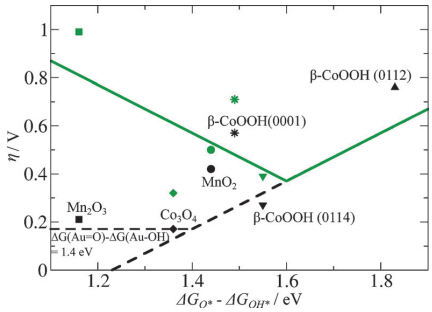

Figure 4. The theoretical volcano plot obtained for OER proceeding via *–OH and *–OOH (——) by using the difference in binding free energies between the *=O and the *–OH, established in Ref. [10] as a descriptor for the theoretical overpotential in [V]. **-----**: Potential of a Au=O hydrogen acceptor that is also the lower limit for overpotentials obtained from interaction with such a site. *: Theoretical overpotential without a hydrogen acceptor, *: overpotential including the hydrogen acceptor. Mn_2O_3 (■/■), MnO_2 (●/●), and Co_3O_4 (◆/◆) are placed on the strong binding branch of the volcano. For β-CoOOH only the (0114) facet (▼/▼) is on the strong binding, for which an effect of Au interaction can be expected.

Thermodynamically it is expected that MnO_2 is the most stable phase at OER-relevant potentials, at which a Mn_2O_3 surface would be oxidized.[27,42] For Mn_2O_3, reaction (3) is potential-determining and essentially corresponds to a reduction of the active site. However, as the binding energy to *–OOH is so weak, the lowest potential path for OER on Mn_2O_3 is through an oxidation to MnO_2. In the presence of Au (hydrogen acceptors), the lowest potential would instead occur in the OER on the Mn_2O_3 site itself. This suggests that during OER the Mn_2O_3 sites near Au could exist simply because they can perform the reduction of the catalytic site. This reducing effect agrees with the indication from ex situ X-ray absorption spectroscopy that a lower oxidation state of Mn forms in the vicinity of the Au.[38] It also indicates that a very small subset of improved sites are responsible for the overall increase in current, meaning that these special sites must be very active. Unfortunately, it is difficult to assess the quantity of sites with improved catalytic activity due to the presence of Au, which complicates estimations of the real decrease in overpotential.

Extending the concept to CoO_x, Co_3O_4 binds the intermediates similarly to MnO_2, which results in a very similar reaction profile. Due to some scatter in the binding energies, the overpotential for the reaction proceeding via Co–OOH becomes only 0.3 eV.[10] This is lowered to 0.2 V on assuming a hydrogen transfer to Au=O. Under OER conditions the most stable phase for CoO_x is β-CoOOH and the most active of the facets is (0114).[43] Despite significant structural differences between these cobalt oxides and hydroxides, the redox potentials for the different oxidation steps are very similar, that is, an overpotential of 0.40 V is found on assuming a Co–OOH intermediate. This is lowered to 0.3 V when considering the possibility of hydrogen transfer to Au=O. Similar results are also found for the (0001) facet. In case of (0112) the oxidation of water to *O is potential-determining. Correspondingly, no improvements can be achieved by stabilizing the *OOH intermediate.

Similar to CoO_x and MnO_x, improvements from using a Au support have also been reported for nickel oxides.[44] For NiO and NiO_2, which lie on the weak binding side of the volcano plot, reaction (2) is potential-determining. Thus, stabilization of the Ni–OOH intermediate through a hydrogen acceptor no longer results in a lower overpotential. Instead, an improvement could originate from the same property of Au, that is, the oxidation potential at which a Au site forms Au=O. Alternatively, Au can act as an electron sea so that reaction (2) can proceed at a lower potential. This would be similar to the effect of doping in, for example, TiO_2.[45]

Conclusions

We propose that hydrogen transfer to an adjacent site significantly improves catalytic activity in the oxygen evolution reaction (OER) on Mn and Co oxides. Such an effect can explain the beneficial interactions between Au and the oxides reported experimentally. The absolute values of potentials described here may not be directly transferable to the experimental conditions, however, the trends indicate enhancements in overpotential in the order of 100 mV for MnO_2 and 300 mV for Mn_2O_3. For both Co_3O_4 and CoOOH the enhancement is approximately 100 mV. These trends are qualitatively consistent with the experimental results. As an unknown fraction of the total amount of sites is affected by the addition of Au it is complicated to compare these results directly to experimental work. It is likely that, since a small subset of sites is improved, the experimental enhancement is dampened in comparison to what the theoretical calculations suggest. Potentially, the OER sites on Mn and Co oxides close to Au approach the thermodynamic limit for OER just like the special sites that have an increased OER activity due to the Ni and Co incorporation on Ni and Co-modified RuO_2.[23] Therefore, a huge challenge remains in increasing the density of these special catalytic sites and stabilizing the surface.

Computational Data

All MnO_x were modeled by using periodic boundary conditions. The calculations were performed with the GPAW[46,47] DFT code (version 0.9.0.8965) at the generalized gradient approximation level of theory. DFT using the revised Perdew–Burke–Ernerhof functional[48] in combination with a finite difference grid (grid spacing: 0.15 Å) and 2×2×1 k point set were employed. For the Au doped system the k point set was reduced to 2×1×1 owing to a larger unit cell and a set containing only the gamma point was used for the considered molecules. The inner electrons were approximated by projector augmented wavefunctions[49] (version 0.9.9672). Spin was treated explicitly by assuming a high spin electron configuration with ferromagnetic coupling between the Mn ions. A similar procedure has been employed for a number of systems.[6,8,14] Geometries were relaxed by using the Broyden–Fletcher–Goldfarb–Shanno algorithm as implemented into ASE 3.6.0.[50] Convergence of the structure was assumed complete if the forces were below 0.05 eV Å^{-1}. Zero-point energies and entropy effects were included by adding constant corrections as described previously.[10] All adsorption energies were calculated by following the procedure described by Man et al. under standard conditions (pH 0 and $T = 283.15$ K).[10]

MnO_2 was modeled by using a 2×1 unit cell for the non-Au-doped case and a 3×1 unit cell for the Au-doped case of the (110) surface combined with a 2 monolayer (ML)-thick slab. In agreement with previous work[27] the surface was assumed to be fully oxidized, that is, all surface manganese atoms had a formal oxidation state of +5. The slab was terminated on the "bulk" side by *–OH species to model the bulk +4 oxidation state. Convergence of the slab was ensured by comparison with a 3 ML slab. No significant differences were found.

The Mn_2O_3 model was constructed by employing a slightly simplified Mn_2O_3 unit cell similar to that used by Su et al. containing 2 Mn_2O_3 units.[27] The 2 ML slab was cut in the (110) direction and terminated such that all "bulk" manganese atoms were in a formal oxidation state of +3. Again, no differences with the results obtained on a 3 ML Mn_2O_3 slab were found.

All binding energies used are shown in the Supporting Information with the zero-point energy and entropy corrections. From the calculated free energies, predictions of overpotentials were made by using a previously reported method.[4,5,18] The basis of this method was to set the reference potential to that of the standard hydrogen electrode and model the electrode potential (U) by shifting the energy levels by $-eU$. The lowest theoretical overpotential was then the difference between U, with all steps downhill in energy, and the equilibrium of water oxidation, 1.23 V.

Acknowledgements

The authors gratefully acknowledge financial support from the Danish Ministry of Science's UNIK initiative, Catalysis for Sustainable Energy. The Center for Individual Nanoparticle Functionality is supported by the Danish National Research Foundation (DNRF54).

Keywords: cobalt · electrocatalysis · gold · manganese · density functional calculations

[1] J. Greeley, N. M. Markovic, *Energy Environ. Sci.* **2012**, *5*, 9246 – 9256.
[2] A. Marshall, B. Børresen, G. Hagen, M. Tsypkin, R. Tunold, *Energy* **2007**, *32*, 431 – 436.
[3] M. G. Walter, E. L. Warren, J. R. McKone, S. W. Boettcher, Q. Mi, E. A. Santori, N. S. Lewis, *Chem. Rev.* **2010**, *110*, 6446 – 6473.
[4] J. Rossmeisl, A. Logadottir, J. K. Nørskov, *Chem. Phys.* **2005**, *319*, 178 – 184.
[5] J. Rossmeisl, Z.-W. Qu, H. Zhu, G.-J. Kroes, J. K. Nørskov, *J. Electroanal. Chem.* **2007**, *607*, 83 – 89.
[6] M. Busch, E. Ahlberg, I. Panas, *Phys. Chem. Chem. Phys.* **2011**, *13*, 15069 – 15076.
[7] M. Busch, E. Ahlberg, I. Panas, *J. Phys. Chem. C* **2013**, *117*, 288 – 292.
[8] M. Busch, E. Ahlberg, I. Panas, *Catal. Today* **2013**, *202*, 114 – 119.
[9] M. T. M. Koper, *J. Electroanal. Chem.* **2011**, *660*, 254 – 260.
[10] I. C. Man, H.-Y. Su, F. Calle-Vallejo, H. A. Hansen, J. I. Martínez, N. G. Inoglu, J. Kitchin, T. F. Jaramillo, J. K. Nørskov, J. Rossmeisl, *ChemCatChem* **2011**, *3*, 1159 – 1165.
[11] S. Trasatti, *J. Electroanal. Chem.* **1980**, *111*, 125 – 131.
[12] R. Subbaraman, D. Tripkovic, K.-C. Chang, D. Strmcnik, A. P. Paulikas, P. Hirunsit, M. Chan, J. Greeley, V. Stamenkovic, N. M. Markovic, *Nat. Mater.* **2012**, *11*, 550 – 557.
[13] A. Grimaud, K. J. May, C. E. Carlton, Y.-L. Lee, M. Risch, W. T. Hong, J. Zhou, Y. Shao-Horn, *Nat. Commun.* **2013**, *4*, 2439.
[14] P. Steegstra, M. Busch, I. Panas, E. Ahlberg, *J. Phys. Chem. C* **2013**, *117*, 20975 – 20981.
[15] T. Reier, M. Oezaslan, P. Strasser, *ACS Catal.* **2012**, *2*, 1765 – 1772.
[16] H. Dau, C. Limberg, T. Reier, M. Risch, S. Roggan, P. Strasser, *ChemCatChem* **2010**, *2*, 724 – 761.
[17] J. Suntivich, K. J. May, H. A. Gasteiger, J. B. Goodenough, Y. Shao-horn, *Science* **2011**, *334*, 1383 – 1385.
[18] J. K. Nørskov, J. Rossmeisl, A. Logadottir, L. Lindqvist, J. R. Kitchin, T. Bligaard, H. Jónsson, *J. Phys. Chem. B* **2004**, *108*, 17886 – 17892.
[19] E. M. Fernández, P. G. Moses, A. Toftelund, H. A. Hansen, J. I. Martínez, F. Abild-Pedersen, J. Kleis, B. Hinnemann, J. Rossmeisl, T. Bligaard, J. K. Nørskov, *Angew. Chem. Int. Ed.* **2008**, *47*, 4683 – 4686; *Angew. Chem.* **2008**, *120*, 4761 – 4764.
[20] F. Abild-Pedersen, J. Greeley, F. Studt, J. Rossmeisl, T. Munter, P. Moses, E. Skúlason, T. Bligaard, J. Nørskov, *Phys. Rev. Lett.* **2007**, *99*, 016105.
[21] H. A. Hansen, I. C. Man, F. Studt, F. Abild-Pedersen, T. Bligaard, J. Rossmeisl, *Phys. Chem. Chem. Phys.* **2010**, *12*, 283 – 290.
[22] P. Sabatier, *Ber. Dtsch. Chem. Ges.* **1911**, *44*, 1984 – 2001.
[23] N. B. Halck, V. Petrykin, P. Krtil, J. Rossmeisl, *Phys. Chem. Chem. Phys.* **2014**, *16*, 13682 – 13688.
[24] R. Forgie, G. Bugosh, K. C. Neyerlin, Z. Liu, P. Strasser, *Electrochem. Solid-State Lett.* **2010**, *13*, B36 – B39.
[25] K. Macounová, J. Jirkovský, M. V. Makarova, J. Franc, P. Krtil, *J. Solid State Electrochem.* **2009**, *13*, 959 – 965.
[26] K. Juodkazis, J. Juodkazytė, R. Vilkauskaitė, B. Šebeka, V. Jasulaitienė, *Chemija* **2008**, *19*, 1 – 6.
[27] H.-Y. Su, Y. Gorlin, I. C. Man, F. Calle-Vallejo, J. K. Nørskov, T. F. Jaramillo, J. Rossmeisl, *Phys. Chem. Chem. Phys.* **2012**, *14*, 14010 – 14022.
[28] M. M. Najafpour, T. Ehrenberg, M. Wiechen, P. Kurz, *Angew. Chem. Int. Ed.* **2010**, *49*, 2233 – 2237; *Angew. Chem.* **2010**, *122*, 2281 – 2285.
[29] J. Blakemore, H. Gray, J. Winkler, A. Müller, *ACS Catal.* **2013**, *3*, 2497 – 2500.
[30] X. Lu, Y. H. Ng, C. Zhao, *ChemSusChem* **2014**, *7*, 82 – 86.
[31] F. Jiao, H. Frei, *Angew. Chem. Int. Ed.* **2009**, *48*, 1841 – 1844; *Angew. Chem.* **2009**, *121*, 1873 – 1876.
[32] M. Wiechen, I. Zaharieva, H. Dau, P. Kurz, *Chem. Sci.* **2012**, *3*, 2330 – 2339.
[33] K. Mette, A. Bergmann, J.-P. Tessonnier, M. Hävecker, L. Yao, T. Ressler, R. Schlögl, P. Strasser, M. Behrens, *ChemCatChem* **2012**, *4*, 851 – 862.
[34] D. M. Robinson, Y. B. Go, M. Mui, G. Gardner, Z. Zhang, D. Mastrogiovanni, E. Garfunkel, J. Li, M. Greenblatt, G. C. Dismukes, *J. Am. Chem. Soc.* **2013**, *135*, 3494 – 3501.
[35] M. Huynh, D. Bediako, D. Nocera, *J. Am. Chem. Soc.* **2014**, *136*, 6002 – 6010.
[36] Y. Gorlin, T. F. Jaramillo, *J. Am. Chem. Soc.* **2010**, *132*, 13612 – 13614.
[37] Y. Gorlin, C. Chung, D. Nordlund, *ACS Catal.* **2012**, *2*, 2687 – 2694.
[38] Y. Gorlin, C.-J. Chung, J. D. Benck, D. Nordlund, L. Seitz, T.-C. Weng, D. Sokaras, B. M. Clemens, T. F. Jaramillo, *J. Am. Chem. Soc.* **2014**, *136*, 4920 – 4926.

[39] M. S. El-Deab, M. I. Awad, A. M. Mohammad, T. Ohsaka, *Electrochem. Commun.* **2007**, *9*, 2082 – 2087.
[40] A. M. Mohammad, M. I. Awad, M. S. El-Deab, T. Okajima, T. Ohsaka, *Electrochim. Acta* **2008**, *53*, 4351 – 4358.
[41] B. S. Yeo, A. T. Bell, *J. Am. Chem. Soc.* **2011**, *133*, 5587 – 5593.
[42] M. Pourbaix, *Atlas of Electrochemical Equilibria in Aqueous Solutions*, Pergamon Press, **1966**.
[43] M. Bajdich, M. García-Mota, A. Vojvodic, J. K. Nørskov, A. T. Bell, *J. Am. Chem. Soc.* **2013**, *135*, 13521 – 13530.
[44] B. S. Yeo, A. T. Bell, *J. Phys. Chem. C* **2012**, *116*, 8394 – 8400.
[45] M. García-Mota, A. Vojvodic, H. Metiu, I. C. Man, H.-Y. Su, J. Rossmeisl, J. K. Nørskov, *ChemCatChem* **2011**, *3*, 1607 – 1611.
[46] J. Mortensen, L. Hansen, K. Jacobsen, *Phys. Rev. B* **2005**, *71*, 1 – 11.
[47] J. Enkovaara, C. Rostgaard, J. J. Mortensen, J. Chen, M. Dułak, L. Ferrighi, J. Gavnholt, C. Glinsvad, V. Haikola, H. A. Hansen, H. H. Kristoffersen, et al., *J. Phys. Condens. Matter* **2010**, *22*, 253202.
[48] B. Hammer, L. B. Hansen, J. K. No, J. Nørskov, *Phys. Rev. B* **1999**, *59*, 7413 – 7421.
[49] P. E. Blöchl, *Phys. Rev. B* **1994**, *50*, 17953 – 17979.
[50] S. Bahn, K. Jacobsen, *Comput. Sci. Eng.* **2002**, *4*, 56 – 66.

Received: September 21, 2014
Published online on ■■ ■■, 0000

Beyond the scaling relations: Enhancing the activity of electrocatalysts for the oxygen evolution reaction is complicated owing to non-optimal binding energies of the intermediates. We present a strategy to circumvent this problem by introducing gold as a hydrogen acceptor on catalytically active surfaces. This leads to lower theoretical overpotentials for manganese and cobalt oxides.

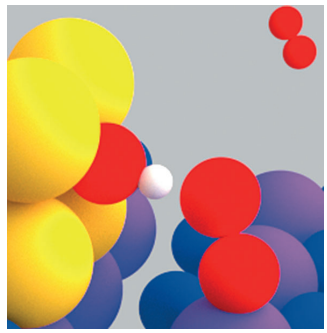

*R. Frydendal, M. Busch, N. B. Halck, E. A. Paoli, P. Krtil, I. Chorkendorff, J. Rossmeisl**

■■ – ■■

Enhancing Activity for the Oxygen Evolution Reaction: The Beneficial Interaction of Gold with Manganese and Cobalt Oxides

Paper III

Toward an active and stable catalyst for oxygen evolution in acidic media: Ti-stabilized MnO_2
Rasmus Frydendal, Elisa A. Paoli, Ib Chorkendorff, Jan Rossmeisl, Ifan E.L. Stephens
Accepted for publication in Advanced Energy Materials

Toward an active and stable catalyst for oxygen evolution in acidic media: Ti-stabilized MnO_2

Rasmus Frydendal,[a] Elisa A. Paoli,[a] Ib Chorkendorff,[a] Jan Rossmeisl,[b,c,] Ifan E.L. Stephens[a,]**

[a] *Center for Individual Nanoparticle Functionality, Department of Physics, Building 312, Technical University of Denmark, DK-2800 Kgs. Lyngby, Denmark*

[b] *Center for Atomic-scale Materials Design, Department of Physics, Building 307, Technical University of Denmark, DK-2800 Kgs. Lyngby, Denmark*

[c] *Department of Chemistry, University of Copenhagen, Universitetsparken 5, DK-2100, København Ø, Denmark*

Keywords: Electrochemistry, Catalysis, Oxygen Evolution, Density Functional Theory, Corrosion

Abstract

Catalysts are required for the oxygen evolution reaction, which are abundant, active and stable in acid. MnO_2 is a promising candidate material for this purpose. However, it dissolves at high overpotentials. Using first principles calculations, we develop a strategy to mitigate this problem by decorating under-coordinated surface sites of MnO_2 with a stable oxide. TiO_2 stands out as the most promising of the different oxides in the simulations. We experimentally verify this prediction by testing sputter-deposited thin films of MnO_2 and Ti-MnO_2. We perform a combination of electrochemical measurements, quartz crystal microbalance and inductively coupled plasma – mass spectrometry measurements and X-ray photoelectron spectroscopy. Small amounts of TiO_2 incorporated into MnO_2 lead to a moderate improvement in stability, with only a small decrease in activity. This study opens up the possibility of engineering surface properties of catalysts so that active and abundant non-precious metal oxides can be used in acid electrolytes.

1. Introduction

The wider uptake of intermittent sources of renewable energy, such of wind and solar, requires efficient and scalable means of storing the energy. Electrochemical devices such as electrolysers, photoelectrolysers and metal air-batteries are ideally suited towards this purpose.[1–4] Unfortunately, it turns out that the efficiencies of these technologies are severely limited by the sluggish kinetics of the oxygen evolution electrode.[5] Furthermore, the choice of electrolyte, acid or alkaline, has a significant impact on the materials available as catalysts.[6–8] This is exemplified by the case of Proton Exchange Membrane (PEM) electrolyzers, which are well suited for localized hydrogen production, due to their superior efficiency at high current densities, ability to manage fluctuating power inputs, and fast start up times.[9,10] A major drawback of the technology is that the acidic nature of the electrolyte severely limits the number of available electrode materials.[11,12] Copious amounts of precious metal oxides are required to catalyze the oxygen evolution reaction (OER), in particular Ir.[9,13–15] We recently estimated that in order for PEM electrolyzers to be scaled up to the terawatt level (i.e. to make a serious impact to the global energy challenge), ten years of the annual Ir production would be needed, solely for the oxygen electrode.[5,16][9] Similar scale up limitations hold for devices for photo-catalytic water splitting.[6] One alternative would be to switch to hydroxide conducting polymer electrolytes; under alkaline conditions, catalysts based on Ni, Fe and Co catalyze the OER on par, or even better, than the noble metal oxides.[17–24] However, despite their promise, hydroxide conducting polymeric electrolytes are still in their technological infancy: they are less stable and slightly less conductive than their proton conducting counterparts, and impose greater overpotentials at the hydrogen electrode.[25–27] It turns out that Ni, Fe and Co are unstable towards dissolution in acid.[11,28] In fact, even the noble metals and their oxides corrode under OER conditions.[29–32] A number of non-precious metal oxides, such as TiO_2, SnO_2, Ta_2O_5 and Nb_2O_5, are stable in acid, but inactive towards the OER.[14] As a consequence, it has long been recognized that there is a great need to finding stable and active materials, based on non-precious metals, for water-oxidation in acid; even so, to date, no obvious solutions or even strategies have been put forward.[33]

MnO_2 presents an interesting example, as it shows some compromise between being active and stable in both alkaline and acidic media.[34–43] In particular, the Pourbaix diagram of Mn reveals

that it is stable, in the form of MnO_2, at pH 0 to 14 from 1.3-1.7 V_{RHE},[28,44] a highly relevant range for OER. There are few reports of MnO_x catalysts used for OER in low pH. In Figure 1, a comparison of these catalysts and a RuO_2 thin film is shown, using a turnover frequency basis, TOF. Due to differences in thickness and preparation techniques, a direct comparison is complicated. The upper limit, TOF_{max}, is found by assuming that only the surface participates in the reaction, whereas TOF_{min} is found by assuming all of the catalytic material can contribute. Although these assumptions are crude, it is evident that the MnO_2 film in this work has a significantly higher activity than the other MnO_x references, with the exception of the Morita *et al.* catalyst. However, their catalyst is prepared by thermal composition and likely had a high roughness factor.[45] See more details in the supplementary information.

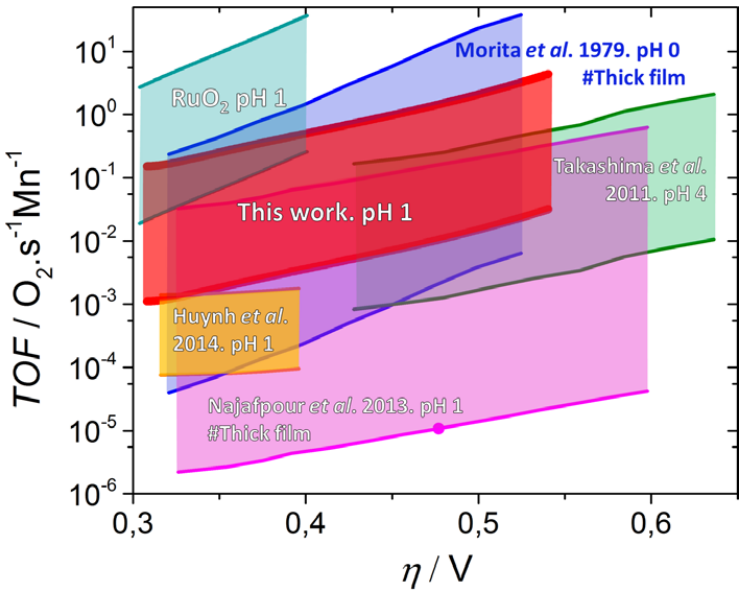

Figure 1. Comparison of the MnO_x-based catalysts reported in the literature, based on both TOF_{max} and TOF_{min}. Data from Morita *et al*. is shown in blue,[46] from Takashima *et al*. in green,[47] Huynh *et al*. in yellow [35] and Najafpour *et al*. in magenta.[48] A benchmark RuO_2 catalyst from [32] is shown in teal. The catalyst reported in this work is shown in red (measured with 5 mV/s, 1600 RPM and 0.05 M H_2SO_4).

Recently, Nocera and co-workers reported the activity and stability of a novel MnO_x based OER catalyst, from pH 1 to 13.[35] They demonstrated that at pH as low as 1, MnO_2 can catalyze oxygen evolution within the range of its bulk thermodynamic stability, as shown in Figure 1. However, in order to utilize MnO_2 in PEM electrolyzers, it will be essential to stabilize the surface at potentials positive of the standard dissolution potential, 1.7 V_{RHE}.[28]

Consequently, a key challenge, which has not been addressed thus far, is the development of active and stable catalysts for the OER in acid, which are free of precious metals. Herein, we develop a strategy to address this challenge. We employ density functional theory (DFT) calculations to investigate the feasibility of meta-stabilizing an oxide OER catalyst. Based on our calculations, we synthesize the oxides in the form of sputtered thin films. We test their catalytic activity and stability using our recently developed method,[32] combining electrochemical techniques, quartz crystal microbalance (QCM) and inductively coupled plasma mass spectrometry (ICP-MS).

2. Results and Discussion

2.1 Theoretical calculations

The anodic dissolution of MnO_2 in acid proceeds through the formation of the higher oxide MnO_4^- as described in Equation (1):

$$\mathrm{MnO_2 + 2H_2O \rightarrow MnO_4^- + 4H^+ + 3e^-} \qquad \text{Equation (1)}$$

The dissolution will proceed via the surface, where a variety of different sites will be present. The sites that dissolve at the lowest overpotential can be identified by invoking a simple argument, based on the cost in terms of surface energy. Terrace atoms are less prone to dissolution, as their removal would leave behind vacancies, which inherently have a high surface energy. On the other hand, removal of a stepped row or a kink site leads to the same surface structure; hence, no cost in surface energy is associated with the process. Therefore, the dissolution of under-coordinated sites is favored over the dissolution of terrace sites. DFT models describing the dissolution of metal surfaces yielded similar results.[49,50] According to our present understanding, the coordinatively unsaturated (CUS)

sites marked in Figure 2a, which are located on the terraces, are the active sites for oxygen evolution on MnO_2.[44] DFT calculations suggest this to be the case for RuO_2 and other rutile oxides.[13,14,51] It follows that a viable approach for stabilizing such a surface would be to selectively block the under-coordinated sites with a compound that is stable at highly anodic potentials; in principle, this should not come at the cost of catalytic activity, as we expect these sites to be inactive.

The notion that the undercoordinated sites could be selectively blocked is supported by numerous reports in the literature. For Ru(0001) surfaces Behm and coworkers observed that Au or Cu would selectively adsorb on step edges from which larger islands could grow.[52,53] Interestingly, the same phenomena was observed for Ru growth on Au(111).[54] Specifically for N_2 activation on Ru, selectively blocked step edges had enormous impact on the activity.[55] Selective adsorption has also been observed for Sulphur deposition on Ni(111) and for Oxygen on Ruthenium.[56,57] A relevant example for oxides was reported by Stensgaard and co-workers, who showed that Pd nucleates preferentially on the step edges of Al_2O_3.[58] Finally, for electrochemical systems Bi and Te have been reported to decorate steps of Pt(775) [59] and Cu bind the strongest to Pt steps and kinks.[60]

Herein, using DFT, we simulate several MnO_2 structures with different guest oxides placed at the undercoordinated sites, with the configurations shown in Figure 2b and c. The guest oxides, in their bulk form, have more positive dissolution potentials than any MnO_2 compounds. Our approach allows us to elucidate trends in surface segregation on MnO_2, and to predict whether heteroatoms may stabilize the surface of the catalyst. The calculations are performed at the Generalized Gradient Approximation (GGA) level, with an RPBE functional[61]. Similar calculations have previously been reported to be sufficient for finding bulk properties of oxides,[62] surface stability and activity of Mn oxides,[44] trends in overpotential for OER catalysts [13,14,51,63] and dissolution phenomena.[50,64]

The structures used for the model are shown in Figure 2b and 2c. As a first order approach, we will define the energy of termination as the stability of the guest material versus its own bulk structure using Equation (2):

$$\Delta E = E_{\mathrm{term}} - E_{\mathrm{ref}} - (E_{\mathrm{unit,guest}} - E_{\mathrm{unit,ref}}) \qquad \text{Equation (2)}$$

Where ΔE is the termination energy, E_{term} the total energy of the terminated structure, E_{ref} the energy of the original MnO_2 structure, $E_{\mathrm{unit,guest}}$ the energy of a unit cell of the guest oxide in its bulk form, and $E_{\mathrm{unit,MnO_2}}$ the energy of a unit cell of the MnO_2 in its bulk form, which is substituted. The energies are reported in eV/MO_2 units, with M being a transition metal.

A negative ΔE suggests there is a favorable driving force for the guest material to segregate to the under-coordinated sites. An oxide with a very negative $E_{\mathrm{unit,guest}}$ is very stable in its pure bulk form. Consequently, it should be unfavorable to terminate the MnO_2 with an oxide that is more stable in the bulk form.

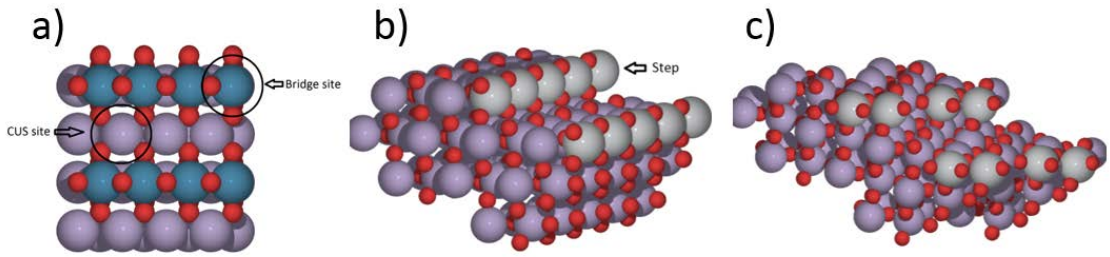

Figure 2: a) A top view of the rutile (110) surface. Two types of metal sites are available. The CUS sites are shown with purple spheres and the Bridge sites with dark green spheres**. b)** A stepped rutile MnO_2 structure based on the (120) surface used to calculate termination energies. Here the slab is repeated 5 times in the x direction and 2 times in y. **c)** Kinked rutile MnO_2 structure based on the (120) surface used to calculate termination energies. Here the slab is repeated 2 times in the x direction and 2 times in y. In all three figures, the purple spheres represent manganese, red spheres oxygen and grey spheres a terminated step or kink.

A (120) MnO_2 surface was terminated with TiO_2, GeO_2, SnO_2, PtO_2, RuO_2 and IrO_2 at the step site. The results are summarized in Figure 3, where the termination energy is plotted as function of the (110) surface formation energy of the guest oxides. The plot shows that the two quantities are correlated:

surfaces with more positive values of the (110) surface formation energies have positive termination energies, i.e. PtO_2, SnO_2, RuO_2 and IrO_2. Other factors influencing the termination energy are the lattice mismatch between the MnO_2 and the guest oxide. It turns out that all compounds plotted in Figure 3, apart from SnO_2, exhibit calculated lattice parameters, *a*, ranging from 4.5 Å to 4.725, comparable to the 4.499 Å of MnO_2. Of all the oxides, the lattice parameters of GeO_2 are closest to matching the lattice parameters of MnO_2; this could explain why this compound has the most negative termination energy. On the other hand, SnO_2 has the largest value of *a*, which would make its incorporation into MnO_2 less favorable, leading to an anomalously positive termination energy. The calculated lattice constants are all listed in the Supporting Information in Table S1. Out of the six guest materials, TiO_2 and GeO_2 stand out as the only materials exhibiting negative termination energies.

To further investigate the termination we modeled kinked (120) MnO_2 surfaces. The kinked structures were made twice as large as the stepped structures but repeated with a shift of roughly one lattice constant in the direction orthogonal to the step edge. When further repeated the stepped edge now contains kinks, as seen in Figure 2c, where the grey spheres indicate the exposed edges. Due to a difference in oxygen coordination for the resulting kinked structure, two Mn atoms are replaced with Ti, forming the kink as shown in Figure 2c. This resulted in an average oxygen coordination of two for each Ti, which is consistent with the stepped surface model. The resulting termination energy for Ti is -0.3 eV/$Atom_{Ti}$, indicating that there is a driving force for this oxide to be located at the kink sites. Since it is more negative than for the stepped surface, the kinks are more likely to be occupied by Ti than the step sites. We also simulated an Ir-terminated (120) MnO_2 kink surface; its stability was +0.1 eV $(MO_2)^{-1}$, i.e. it is unstable. Consequently, the data for the kink-terminated Ir and Ti surfaces seem to be consistent with the equivalent data for the stepped surfaces.

In order to explore the possibility that the guest oxide, in particular TiO_2, could form undesired structures with MnO_2, we also simulated the incorporation of Ti into the bulk of MnO_2, the substitution of Ti into the (110) surfaces of MnO_2 and the formation of separate MnO_2 and TiO_2 phases. It turned out that none of these undesired structures were stable, as described in the

Supporting Information. In summary, we predict that decorating the surface of MnO_2 with Ti or Ge could stabilize these oxides against anodic dissolution.

The scarcity of Ge makes it less attractive for large scale energy applications.[16] On the other hand, Ti is abundant and, in the form of TiO_2, stable against dissolution up until 2.1 V at pH 0.[28] On this account, Ti is often used to stabilize materials against anodic dissolution. The most well-known example of this, is the dimensionally stabilized anodes used for chlorine evolution, where Ti reduces the corrosion of RuO_2 electrodes.[65,66] Moreover, several laboratories, including our own, have recently demonstrated that layers of TiO_2 can stabilize photoelectrodes against corrosion[67–72].

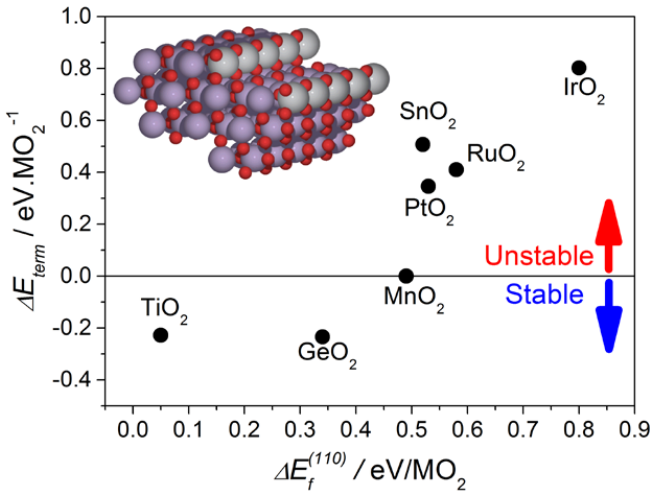

Figure 3. Termination energies for a rutile (120) MnO_2 surface where TiO_2, GeO_2, PtO_2, RuO_2, SnO_2 or IrO_2 are covering the steps. The termination energy is plotted as function of the surface formation energy of the guest dioxides, taken from ref.[62] Both bridge and CUS steps were modelled; however, there were only minor differences, up to 0.1 eV between the two types of sites. Consequently, for clarity, we have only plotted the data for the bridge sites.

To summarize our theoretical findings: undercoordinated sites are the most prone to dissolution. There is a thermodynamic driving force for TiO_2 to selectively segregate to the undercoordinated sites, due to its favorable surface formation energy. This should lead to an overall stabilization of the

surface, since TiO_2 is stable in acid up to more than 2.1 V_{RHE}.[28] At the same time the terrace sites, critical for the activity towards the oxygen evolution reaction, are less likely to be occupied by TiO_2. For the remainder of this paper, we shall experimentally verify the theoretical prediction that TiO_2 decorated MnO_2 should exhibit improved stability, relative to MnO_2, without compromising the OER activity.

2.2 Experimental results

Several options exist for the experimental realization of the theoretically predicted catalyst; we chose to do so by sputter-depositing thin films of mixed Mn and Ti oxides. We adapted the deposition methods from our previous study on pure oxides.[32] The films had a nominal total thickness of 40 nm (based on the average deposition rates-see Experimental Methods section). The upper 5 nm of the Ti modified samples contain 20 % TiO_2. The mixed oxide layers were obtained by simultaneous co-sputtering of Mn and Ti targets. We anticipate that this should form a mixed film with high dispersion of Ti in MnO_2. Although we cannot rule out phase separation, we find this possibility unlikely, given that the mobility of the material would be low at the deposition temperature of 200 °C. Figure 5a shows a schematic of the prepared thin films. The procedure we employ is based on our earlier study where we tested the activity and stability of pure oxides.[32]

Grazing Angle X-Ray Diffraction, GA-XRD, and X-ray Photoelectron Spectroscopy, XPS, were used to establish the structure and composition. From GA-XRD, no peaks were found, indicating that the films are highly disordered and possibly amorphous (Figure S1). However, from XPS analysis the oxidation state of the Mn was consistent with MnO_2 spectra in literature. The XPS spectra of the Mn3s and Mn2p½ can be seen in Figure S2a and b, and the analysis of the oxidation state is based on the multiplet splitting of the Mn3s and the distance for the satellite feature of the Mn 2p½.[73,74] Furthermore, the ratio Mn:Ti in the surface was found to be 80:20, based on the Mn2p and Ti2p (Figure S2c) peaks, which is in good agreement with the measured deposition rates.

The samples were also characterized with Scanning Electron Microscopy, SEM, in order to elucidate surface morphology and possible surface changes from electrochemical testing. In Figure 4a

micrographs of as prepared MnO_2 film can be seen, indicating that the surface consists of densely packed structures with a size range of 10-20 nm. In Figure 4b a MnO_2 film after electrochemical test is shown, which besides appearing slightly less dense, looks very similar to the as prepared sample. In Figure 4c and 4d the surfaces of two Ti-MnO_2 films are shown, one as prepared and one after electrochemical test respectively. These two films look exactly like the pure MnO_2 counterparts and we therefore conclude that no significant reconstruction is taking place for the two types of thin films during the stability tests and that the introduced Ti is not changing the overall morphology.

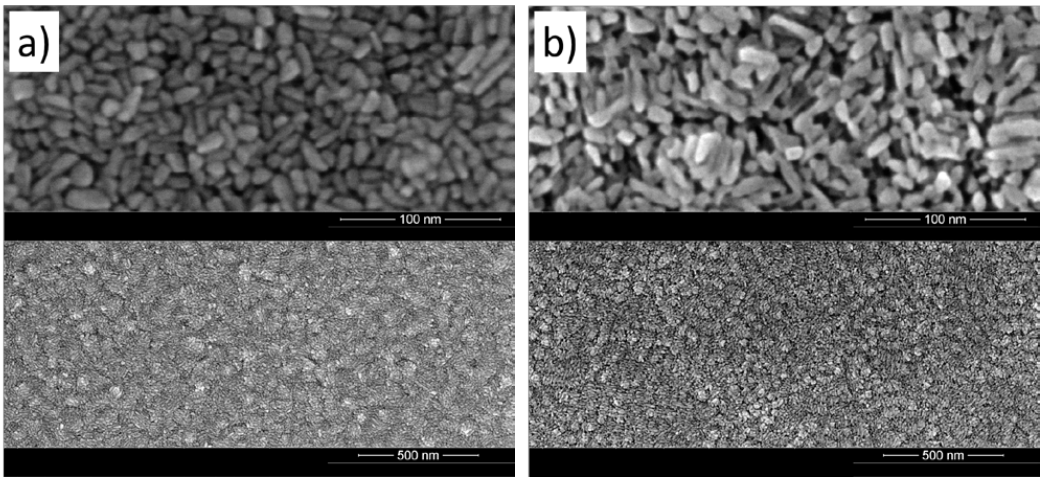

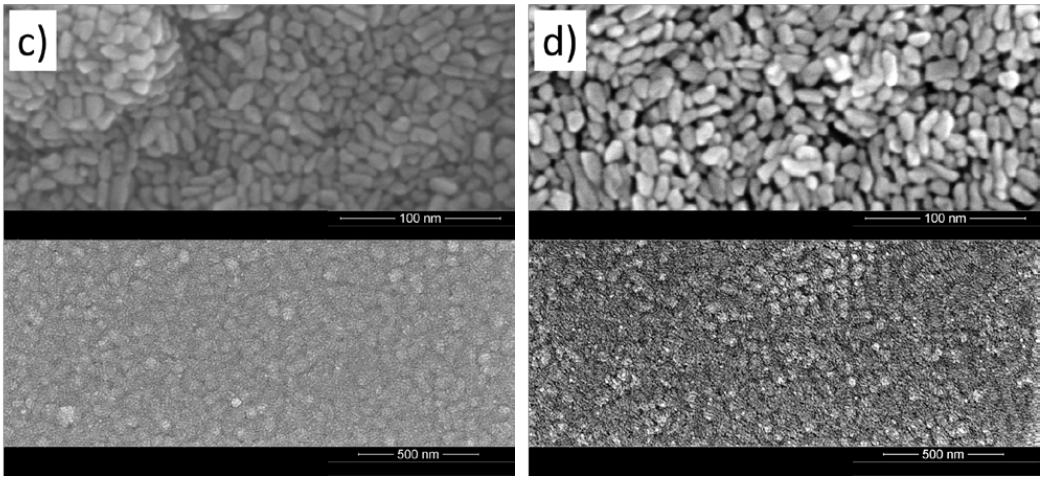

Figure 4. SEM images showing the surface morphology of the samples. a) A pure MnO_2 film as prepared. b) A pure MnO_2 after electrochemical testing at both 1.8 and 1.9 V_{RHE}. c) Ti-MnO_2 film as prepared. d) Ti-MnO_2 film after electrochemical testing at both 1.8 and 1.9 V_{RHE}. Each graph has a scale bar indicated in the bottom. All four images were acquired with an acceleration voltage of 3 kV.

We previously reported the catalytic activity of the pure MnO_2 films in 1 M KOH;[32] which we found to exhibit comparable activity to the best performing manganese-based OER catalysts reported in literature.[34,42,46,75,76] Several manganese-based catalysts were recently compared by Gorlin *et al.* on the basis of turnover frequencies (TOF), which were in the order of 0.002 to 0.006 s^{-1} at an overpotential of 0.4 V.[77] In comparison, the MnO_2 reported here exhibit an initial TOF_{min} of 0.007 s^{-1} when using the same normalization procedure (see Supporting Information for details). Figure 5b shows the initial activity of the unmodified MnO_2 thin film, tested in 1M KOH and 0.05 M H_2SO_4.

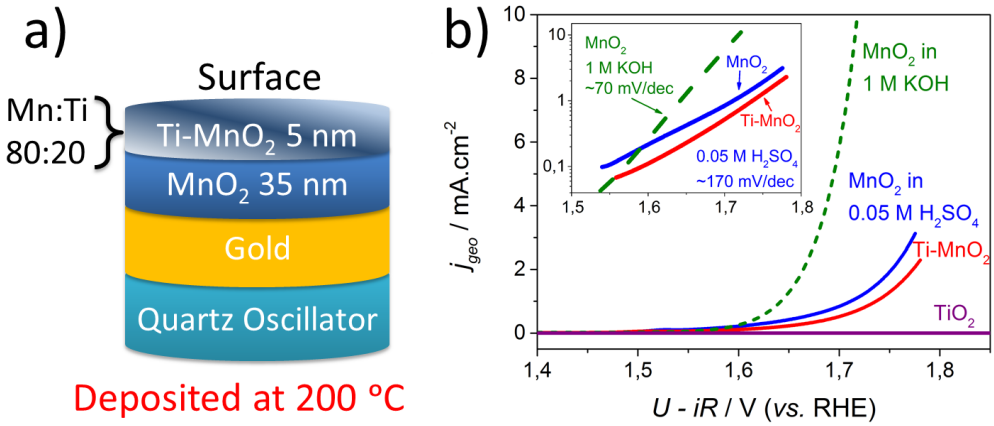

Figure 5. a) A schematic showing the layered thin film structure, deposited onto a gold-coated quartz crystal oscillator. The thicknesses shown are based on deposition rates measured with an in-chamber QCM. For the unmodified MnO_2 samples the thin film structure is the same except for the top layer being without Ti, making it 40 nm thick MnO_2. **b)** Initial OER activity of the MnO_2 thin films measured with a RDE setup. The activity of the unmodified MnO_2 measured in 1M KOH solution and in 0.05 M H_2SO_4 are shown in green and blue, respectively; while the Ti modified MnO_2 is shown in red. A pure TiO_2 film was measured, as is shown in purple. The results shown here are the first scan to anodic potentials, the rotation speed was 1600 RPM and scan rate 5 mV/s. In the inset, the Tafel plots of the unmodified films in alkaline and acid media are illustrated.

It is striking that the OER activity in acid media drops by a factor of two relative to alkaline, to a TOF_{min} of 0.0035 ± 0.001 s^{-1} at 0.4 V overpotential. There is also a difference in Tafel slope, from 70 mV/dec in 1 M KOH to 170 mV/dec in 0.05 M H_2SO_4. This Tafel slope is nonetheless considerably lower (i.e. steeper) than reported in recent literature in acid.[35,36] Moreover, to the best of our knowledge the activity we report is the highest reported for a non-precious metal oxide in acid on a TOF basis; see Figure 1 for direct comparison to literature references. The figure also shows that the MnO_2 has a turnover frequency only 20-40 times lower than the state-of-the-art RuO_2 thin film.

The samples were tested at constant potential for two hours at 1.8 V_{RHE} and subsequently at 1.9 V_{RHE}. Before and after each potential step, aliquots of electrolyte were sampled for ICP-MS analysis. To compare the activity of modified and unmodified MnO_2, we used the current obtained after one hour

at constant potential. It is critical for the stabilization strategy that the OER activity of the modified catalyst does not decrease significantly. The activity of the catalysts supported on the gold-coated quartz crystal microbalances is plotted on Figure 6a. The TiO_2-modified samples exhibit an 11% lower current density at 1.9 V_{RHE}. This is less than expected from the 20 % TiO_2 content. Over time, the loss of Mn could lead to an enrichment of Ti in the surface, which would be detrimental to the activity. We ruled out this possibility, by measuring the Mn:Ti ratio of a tested sample with XPS, which again showed about 20 % of Ti at the surface, see Figure S2d. Since the ratio between Mn and Ti, for the 1 nm depth probed by XPS, is constant throughout the test it is likely that the role of the Ti is to block dissolution only when located at the undercoordinated sites. Figure 6b shows the corresponding mass losses of manganese evaluated with ICP-MS; at 1.9 V_{RHE} the TiO_2 addition leads to 40 % lower losses. This value is four times as high as the loss in OER current, indicating that a better compromise between activity and stability can be achieved by modifying MnO_2 with TiO_2. It should also be noted that RuO_2 thin films prepared and characterized with the same methods exhibit mass losses that are roughly six times higher than MnO_2 at 1.8 V_{RHE}.[32] The findings for EQCM substrates were further validated by RDE tests, combined with ICP analysis, of the catalyst films supported on polycrystalline gold disks, see Supporting Information.

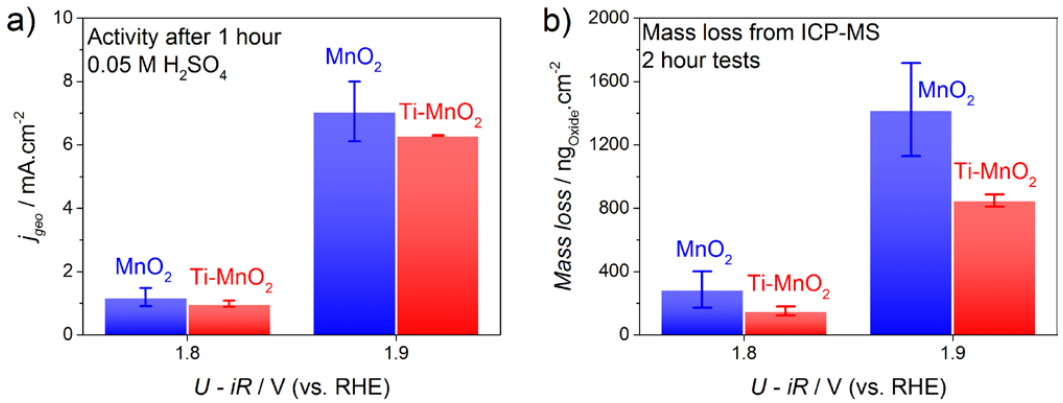

Figure 6. a) OER current after 1-hour of the chronoamperometry tests at 1.8 and 1.9 V_{RHE}. **b)** Mass loss for MnO_2 and TiO_2-modified MnO_2 based on ICP-MS analysis. The amount of Mn measured in the electrolyte is then corrected for volume of electrolyte and converted into corresponding MnO_2 weight. Blue bars show the MnO_2 while the red bars show TiO_2-modified

MnO_2. Both the currents and mass losses shown are averages for three independent measurements with the EQCM setup and the error bars are ±1 standard deviation.

Time resolved measurements of the corrosion were obtained with the electrochemical quartz crystal microbalances when the catalyst was subjected to the testing procedure described above. The time resolved change in mass can be seen in Figure 7. The mass losses during the first 20 minutes are similar between the pure MnO_2 and the Ti-MnO_2. However, the slope progressively diverges between the two samples: by the last 20 minutes of the experiment, the slope of the Ti-MnO_2 is 40% less steep than the MnO_2 sample, indicating a lower rate of mass loss. In other words; since the slopes are significantly different toward the end of the test, it indicates that fewer undercoordinated sites are now available for MnO_4^- formation. It is likely that at the beginning, a small fraction of the undercoordinated sites have not been successfully covered with TiO_2, therefore, MnO_2 can corrode away until a front of TiO_2 is reached. If it was the case that TiO_2 simply prevent the electrolyte from being in contact with the MnO_2, then the oxygen evolution activity would decrease by the same proportion as the corrosion rate. However, this is not the case, as we see a 40 % lower mass losses, but only 10 % lower OER current. These results substantiate the notion that the TiO_2 can stabilize MnO_2.

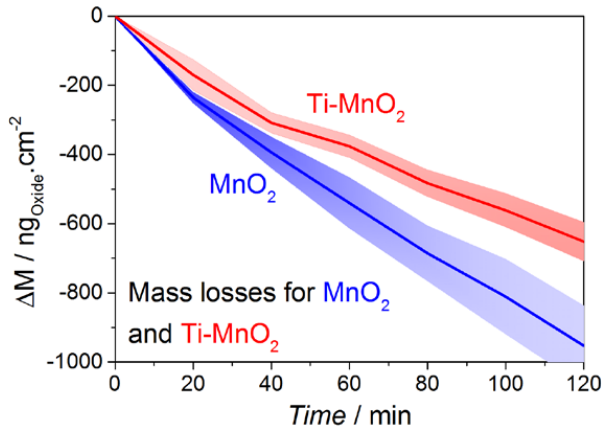

Figure 7. Change in mass during the experiment based on the resonant frequency of the quartz oscillator. The frequency measurements have been converted into mass changes using the Sauerbrey equation.[78] The blue line shows the MnO_2 while the red line shows the TiO_2-

modified MnO_2. The graphs are based on averaging the results for three independent measurements and points are taken for each 20 minutes passed. The error bars are evaluated at each 20-minute point, representing ±1 standard deviation, and are shown as faded areas following the lines.

3. Discussion

Our experimental results confirm the theoretical prediction that Ti can stabilize MnO_2 based catalysts under OER conditions. We note that there are significant differences between the experiments and the DFT model. In the modelled structures, Ti is confined to the surface, whereas Ti is also in the bulk of our thin films. Even so, we anticipate that upon application of anodic potentials, in acid, the local surface configuration would resemble the modelled structure: surface MnO_2 would corrode until it reaches a front consisting of undercoordinated TiO_2; this, in turn, would provide kinetic stability against further dissolution of MnO_2 from the terraces. Such an oxide would be somewhat analogous to the acid-leached, dealloyed "Pt-skeleton" type structures formed on the bimetallic Pt-alloy catalysts used for oxygen reduction.[79–82]

We have used the mass losses to predict the lifetime of the thin film catalysts.[32] Here we will assume the 40 nm thin films to have the bulk density of rutile MnO_2. At 1.8 V_{RHE}, pure MnO_2 can then be expected to last 140 hours, a relatively long time when compared to a 40 nm RuO_2 film which can last for 29 hours at the same potential. With the Ti modification the predicted lifetime increases to 265 hours at 1.8 V_{RHE}. At 1.9 V_{RHE} with increased driving force towards MnO_4^- formation, the lifetimes are shorter; 28 hours for the pure MnO_2 and 47 hours after Ti modification. The stabilization method needs to further optimized before practical deployment of this catalyst in electrolysers.

In order to realize a more stable structure on the basis of the concept we propose, the, TiO_2 would need to be added in a highly controlled fashion, only blocking the under-coordinated sites. This would, in principle, lead to more a pronounced stabilization. Such a structure could be established by developing appropriate annealing treatments to the catalyst,[83] and by optimizing the Ti:Mn ratio during deposition.

The next step would be to characterize the Ti-MnO_2 layer with microscopic techniques such as Transmission Electron Microscopy and Scanning Tunneling Microscopy, with a focus on identifying the exact location of Ti in the MnO_2 structure. It would be of great interest to combine a very accurate characterisation with optimization of the deposition technique. To that end, STM studies of the surface while depositing low amounts of Ti would be particularly fruitful.[84,85] These studies are outside the scope of the current study, where we develop and experimentally prove a key concept for stabilizing non-precious metal oxygen evolution catalysts.

The activity of the catalyst could, in principle, be improved beyond what we reported herein. For instance, in alkaline solution, when the surface of MnO_x is in intimate contact with Au, its activity is increased by an order of magnitude.[75,77,86,87] Should this phenomenon be exploited in acid, ideally using an element more abundant than Au, it would boost the efficiency of electrolysis with Mn-based catalysts.

4. Conclusion

The search for non-precious OER catalysts for acidic media calls for new strategies for stabilizing oxide surfaces, without compromising catalytic activity. Herein, we demonstrate such a strategy, by selectively terminating under-coordinated sites on MnO_2. Using DFT-based simulations, we showed that the termination energy correlates with the surface formation energy of the guest oxides in their pure form. Consequently, the termination of under-coordinated sites on MnO_2 is favorable for guest oxides with lower surface formation energies than MnO_2. Our calculations predicted that GeO_2- and TiO_2-terminated MnO_2 should improve the stability of MnO_2.

Based on this theoretical insight, we tested the OER activity and stability of sputter-deposited thin films of pure MnO_2 and Ti-MnO_2 in 0.05 M H_2SO_4. The thin films exhibit unprecedented activity for non-noble metal oxides in acidic solution. Using ICP-MS and EQCM measurements, we showed that the mass losses could be moderately decreased by incorporating Ti into the catalyst, with only a small drop in catalytic activity towards OER. Therefore, the experimental results shown here support the DFT-based model, which suggested that a more optimal balance between stability and activity could

be achieved by engineering the surface properties of MnO_2. This approach is general, and could be used to stabilize all kinds of catalysts, including metals, against corrosion in electrochemical devices. Further development of this work could lead to stable, active and abundant materials to catalyze oxygen evolution in PEM electrolysers and photoelectrolysers for water splitting.

5. Experimental Section

Computational details

The calculations in this work are done with the GPAW code and the revised Perdew-Burke-Ernzerhof exchange and correlation approximation.[61,88,89] Optimal positions for the termination atoms were found by relaxing structures with a Broyden-Fletcher-Goldfarb-Shanno algorithm until a maximum force of 0.05 eV/Å was obtained. All systems were optimized with (4,4,6) Monkhorst-Pack type k-points sampling and the effect of grid spacing converged at 0.15 Å. Between slabs 10 Å of vacuum was introduced in the *z* direction while in *x* and *y* the slab could be repeated. Periodic boundary conditions have been implemented throughout. Four kinds of rutile MnO_2 systems were investigated. A bulk MnO_2 slab (2x2x1 repeated unit cells), a flat (110) MnO_2 surface (4 layers in z-direction, 4 surface metal atoms), a stepped (120) MnO_2 surface (tilted (110) surface) and a (120) MnO_2 surface with introduced kinks. MnO_2 lattice constants were optimized in this setup to be a=4.499 Å and c=2.909 Å. For the surface structures, the bottom layer was fixed in order to have a bulk structure unaffected by surface changes. Notably, the termination energies are not calculated as Gibbs free energies with entropy contributions, since the comparison is between solid states only and no chemical reactions are modeled. Furthermore, on a rutile (110) surface, two different metal sites will be present, one being the coordinately unsaturated site (CUS) and the other the Bridge site, see Figure 1a.[14] We modelled steps and kinks as CUS and Bridge and found that the overall trend remained the same so the results shown here are for the Bridge terminated structures. All the calculated values are listed in Table S1.

Sample preparation

We prepared thin film samples of MnO_2 and TiO_2-modified MnO_2 using reactive sputter deposition.[32] For the unmodified samples, 40 nm thick films (nominally) of MnO_2 were deposited onto the substrates using a power of 140 W in a 5 mTorr Ar/O_2 mixture with a ratio of 5/1. For the TiO_2 modified samples, a 35 nm MnO_2 film was grown first, onto which a 5 nm thick mixed oxide layer was added. The mixed layer was prepared by co-sputtering manganese and titanium and the rates were calibrated with an in-chamber Quartz Crystal Microbalance. The power used for manganese was kept at 140 W while titanium was sputtered at 150 W. According to the calibration performed with an in-chamber QCM, the TiO_2 rate was 20 % of the total deposition rate. All depositions were carried out with a substrate temperature of 200 ^{o}C. Prior to deposition, the EQCM crystals were cleaned in an ultrasonic bath first in acetone, then isopropanol and finally Millipore water (18.2 MΩ). The gold polycrystalline disks were polished with a 0.25 µm diamond paste, sonicated in isopropanol and water, then plasma cleaned and annealed to 700 ^{o}C in two consecutive cycles. After electrochemical tests, the remaining MnO_2 film was removed by scanning the working electrode towards 0 V_{RHE}.

The Electrochemical Quartz Crystal Microbalance crystals were purchased from Stanford Research Systems and the gold polycrystalline disks from Pine Instruments. The electrochemically active area on the EQCM samples is nominally 1.37 cm^2 but only 0.38 cm^2 in the center is sensitive to the frequency measurement. Therefore, we applied a mask of TiO_2 on the non-sensitive area and deposited the MnO_2 catalyst in the sensitive area only. Frequency measurements have been converted to mass changes by using the Sauerbrey equation.[32,78]

Electrochemical tests

The samples were tested in 0.05 M H_2SO_4, Merck Suprapur. In the BioLogic software package, EC-Lab, a test protocol was designed including the following procedure: the electrode is inserted under potential control at 1.4 V_{RHE}, cyclic voltammetry (CV) is performed to evaluate activity, electrochemical impedance spectroscopy (EIS) is used to evaluate the Ohmic losses, the Ohmic drop is compensated at 85 %, the electrode is held at 1.4 V vs RHE to stabilize, chronoamperometry is performed (CA) at 1.8 V vs. RHE and finally CA is performed at 1.9 V vs. RHE. The electrochemical tests

in acid took place in a glass cell with an $Hg/HgSO_4$ reference electrode and a carbon counter electrode. Nitrogen gas was bubbled into the electrolyte throughout the experiments. The reference electrode potential was measured against a reversible hydrogen electrode (RHE) in the same electrolyte solution using a Pt mesh and bubbling hydrogen. The data is presented using the RHE scale and corrected for Ohmic losses, measured with electrochemical impedance spectroscopy (EIS) in the range of 1-200000 Hz at a DC potential of 10 mV.[90] The Ohmic drop for the Rotating Disk Electrode tests was in the order of 30-40 Ω and for the EQCM tests 20-25 Ω.

Characterization Methods

Inductively Coupled Plasma-Mass Spectrometry (ICP-MS) measurements were conducted with a Thermo Fischer Scientific iCAP-QC. Samples of the electrolyte solution were taken out prior to and after each chronoamperometry experiment using a pipette. For quantitative analysis, the signal of Mn was calibrated standard solutions bought from SCP Science. The calibrations were made with pure 0.05 M H_2SO_4, 1 µg/L and 10 µg/L, matching the range of concentrations of Mn found after stability tests. The volume of electrolyte used was measured after each test in order to report absolute mass losses. The volume varied from 267 to 324 ml for the EQCM tests and from 121 to 152 ml for the RDE tests. It should also be noted that the amount of Mn found from ICP-MS in the electrolyte is converted to MnO_2 mass to ease the comparison to EQCM results.

The modified and unmodified MnO_2 films were characterized with X-ray Photoelectron Spectroscopy (XPS) using a Theta Probe instrument (Thermo Fischer Scientific). The base pressure was 5×10^{-10} mbar and the X-ray source monochromatized $Al_{K\alpha}$ (1486.7 eV). Glancing Angle X-ray Diffraction analysis was acquired with a PANanalytical X'pert PRO equipment having an X-ray wavelength of 1.54 Å for the $Cu_{K\alpha}$ line.

Scanning Electron Microscopy analyses were carried out on a FEI Helios EBS3 Microscope at DTU Center for Electron Nanoscopy. All images were acquired in Secondary Electrons mode with an acceleration voltage of 3 kV and a current of 0.17 nA.

Corresponding authors

ifan@fysik.dtu.dk

jan.rossmeisl@chem.ku.dk

Acknowledgments

Katarzyna Janik, DTU CEN, is acknowledged for providing Scanning Electron Microscopy images.

The authors gratefully acknowledge financial support from the Danish Ministry of Science's UNIK initiative, Catalysis for Sustainable Energy. The Center for Individual Nanoparticle Functionality is supported by the Danish National Research Foundation (DNRF54) and the Danish Council for Strategic Research's project MEDLYS (10-093906).

References

[1] J. Greeley, N. M. Markovic, *Energy Environ. Sci.* **2012**, *5*, 9246.
[2] H. A. Gasteiger, N. M. Markovic, *Science* **2009**, *324*, 48.
[3] N. S. Lewis, D. G. Nocera, *Proc. Natl. Acad. Sci. U. S. A.* **2006**, *103*, 15729.
[4] K. Maeda, K. Domen, *J. Phys. Chem. Lett.* **2010**, *1*, 2655.
[5] E. A. Paoli, F. Masini, R. Frydendal, D. Deiana, C. Schlaup, M. Malizia, T. W. Hansen, S. Horch, I. E. L. Stephens, I. Chorkendorff, *Chem. Sci.* **2014**, 36.
[6] B. Seger, I. E. Castelli, P. C. K. Vesborg, K. W. Jacobsen, O. Hansen, I. Chorkendorff, *Energy Environ. Sci.* **2014**, *7*, 2397.
[7] J. R. Mckone, N. S. Lewis, H. B. Gray, *Chem. Mater.* **2014**, *26*, 407.
[8] J. D. Benck, T. R. Hellstern, J. Kibsgaard, P. Chakthranont, T. F. Jaramillo, *ACS Catal.* **2014**.
[9] M. K. Debe, S. M. Hendricks, G. D. Vernstrom, M. Meyers, M. Brostrom, M. Stephens, Q. Chan, J. Willey, M. Hamden, C. K. Mittelsteadt, C. B. Capuano, K. E. Ayers, E. B. Anderson, *J. Electrochem. Soc.* **2012**, *159*, K165.
[10] K. E. Ayers, E. B. Anderson, C. Capuano, B. Carter, L. Dalton, G. Hanlon, J. Manco, M. Niedzwiecki, **2010**, *33*, 3.
[11] C. C. L. McCrory, S. Jung, J. C. Peters, T. F. Jaramillo, *J. Am. Chem. Soc.* **2013**, *135*, 16977.
[12] E. Fabbri, A. Habereder, K. Waltar, R. Kotz, T. Schmidt, *Catal. Sci. Technol.* **2014**, *4*, 3800.
[13] J. Rossmeisl, Z.-W. Qu, H. Zhu, G.-J. Kroes, J. K. Nørskov, *J. Electroanal. Chem.* **2007**, *607*, 83.
[14] I. C. Man, H.-Y. Su, F. Calle-Vallejo, H. A. Hansen, J. I. Martínez, N. G. Inoglu, J. Kitchin, T. F. Jaramillo, J. K. Nørskov, J. Rossmeisl, *ChemCatChem* **2011**, *3*, 1159.
[15] H. N. Nong, L. Gan, E. Willinger, D. Teschner, P. Strasser, *Chem. Sci.* **2014**, *5*, 2955.
[16] P. C. K. Vesborg, T. F. Jaramillo, *RSC Adv.* **2012**, *2*, 7933.
[17] A. Grimaud, K. J. May, C. E. Carlton, Y.-L. Lee, M. Risch, W. T. Hong, J. Zhou, Y. Shao-Horn, *Nat. Commun.* **2013**, *4*, 2439.
[18] L. Trotochaud, S. L. Young, J. K. Ranney, S. W. Boettcher, *J. Am. Chem. Soc.* **2014**, *136*, 6744.
[19] R. D. L. Smith, M. S. Prévot, R. D. Fagan, Z. Zhang, P. a Sedach, M. K. J. Siu, S. Trudel, C. P. Berlinguette, *Science* **2013**, *340*, 60.
[20] M. Gong, Y. Li, H. Wang, Y. Liang, J. Z. Wu, J. Zhou, J. Wang, T. Regier, F. Wei, H. Dai, *J. Am. Chem. Soc.* **2013**, *135*, 8452.
[21] J. Rosen, G. S. Hutchings, F. Jiao, *J. Am. Chem. Soc.* **2013**, *135*, 4516.
[22] F. Jiao, H. Frei, *Angew. Chemie* **2009**, *48*, 1841.
[23] J. Suntivich, H. A. Gasteiger, N. Yabuuchi, H. Nakanishi, J. B. Goodenough, Y. Shao-Horn, *Nat. Chem.* **2011**, *3*, 546.

[24] W. T. Hong, M. Risch, K. A. Stoerzinger, A. Grimaud, J. Suntivich, Y. Shao-Horn, *Energy Environ. Sci.* **2015**, DOI 10.1039/C4EE03869J.

[25] S. Kotrel, S. Bräuninger, in *Handb. Heterog. Catal. (eds G. Ertl, H. Knoezinger, F. Scheuth, J. Weitkamp)*, **2008**, pp. 1936–1958.

[26] J. R. Varcoe, P. Atanassov, D. R. Dekel, A. M. Herring, M. a. Hickner, P. a. Kohl, A. R. Kucernak, W. E. Mustain, K. Nijmeijer, K. Scott, T. Xu, L. Zhuang, *Energy Environ. Sci.* **2014**, *7*, 3135.

[27] J. Durst, a. Siebel, C. Simon, F. Hasché, J. Herranz, H. a. Gasteiger, *Energy Environ. Sci.* **2014**, *7*, 2255.

[28] M. Pourbaix, *Atlas of Electrochemical Equilibria in Aqueous Solutions*, Pergamon Press, **1966**.

[29] S. Cherevko, A. a. Topalov, A. R. Zeradjanin, I. Katsounaros, K. J. J. Mayrhofer, *RSC Adv.* **2013**, *3*, 16516.

[30] S. Cherevko, A. R. Zeradjanin, A. A. Topalov, N. Kulyk, J. J. Mayrhofer, *ChemCatChem* **2014**, *6*, 2219.

[31] N. Danilovic, R. Subbaraman, K.-C. C. Chang, S. H. Chang, Y. J. Kang, J. D. Snyder, A. P. Paulikas, D. Strmcnik, Y.-T. T. Kim, D. J. Myers, V. R. Stamenkovic, N. M. Markovic, *J. Phys. Chem. Lett.* **2014**, 140624200848001.

[32] R. Frydendal, E. A. Paoli, B. P. Knudsen, B. Wickman, P. Malacrida, I. E. L. Stephens, I. Chorkendorff, *ChemElectroChem* **2014**, *1*, 2075.

[33] I. Katsounaros, S. Cherevko, A. R. Zeradjanin, K. J. J. Mayrhofer, *Angew. Chem. Int. Ed. Engl.* **2014**, *53*, 102.

[34] Y. Gorlin, T. F. Jaramillo, *J. Am. Chem. Soc.* **2010**, *132*, 13612.

[35] M. Huynh, D. Bediako, D. Nocera, *J. Am. Chem. Soc.* **2014**, *136*, 6002.

[36] T. Takashima, K. Hashimoto, R. Nakamura, *J. Am. Chem. Soc.* **2012**, DOI 10.1021/ja306499n.

[37] D. M. Robinson, Y. B. Go, M. Mui, G. Gardner, Z. Zhang, D. Mastrogiovanni, E. Garfunkel, J. Li, M. Greenblatt, G. C. Dismukes, *J. Am. Chem. Soc.* **2013**, *135*, 3494.

[38] M. M. Najafpour, F. Rahimi, M. Amini, S. Nayeri, M. Bagherzadeh, *Dalton Trans.* **2012**, *41*, 11026.

[39] M. Wiechen, I. Zaharieva, H. Dau, P. Kurz, *Chem. Sci.* **2012**, *3*, 2330.

[40] M. Khan, E. Suljoti, A. Singh, S. a. Bonke, T. Brandenburg, K. Atak, R. Golnak, L. Spiccia, E. F. Aziz, *J. Mater. Chem. A* **2014**, *2*, 18199.

[41] M. M. Najafpour, T. Ehrenberg, M. Wiechen, P. Kurz, O. Catalysts, *Angew. Chem. Int. Ed. Engl.* **2010**, *49*, 2233.

[42] K. L. Pickrahn, S. W. Park, Y. Gorlin, H.-B.-R. Lee, T. F. Jaramillo, S. F. Bent, *Adv. Energy Mater.* **2012**, *2*, 1269.

[43] M. Morita, C. Iwakura, H. Tamura, *Electrochim. Acta* **1979**, *24*, 357.

[44] H.-Y. Su, Y. Gorlin, I. C. Man, F. Calle-Vallejo, J. K. Nørskov, T. F. Jaramillo, J. Rossmeisl, *Phys. Chem. Chem. Phys.* **2012**, *14*, 14010.

[45] G. Lodi, E. Sivieri, A. De Battisti, S. Trasatti, *J. Appl. Electrochem.* **1978**, *8*, 135.

[46] M. Morita, C. Iwakura, H. Tamura, *Electrochim. Acta* **1977**, *22*, 325.

[47] T. Takashima, K. Hashimoto, R. Nakamura, *J. Am. Chem. Soc.* **2011**, *134*, 1519.

[48] M. M. Najafpour, K. C. Leonard, F.-R. F. Fan, M. A. Tabrizi, A. J. Bard, C. K. King'ondu, S. L. Suib, B. Haghighi, S. I. Allakhverdiev, *Dalton Trans.* **2013**, *42*, 5085.

[49] R. Jinnouchi, E. Toyoda, T. Hatanaka, Y. Morimoto, *Society* **2010**, 17557.

[50] J. Greeley, *Electrochim. Acta* **2010**, *55*, 5545.

[51] N. B. Halck, V. Petrykin, P. Krtil, J. Rossmeisl, *Phys. Chem. Chem. Phys.* **2014**, *16*, 13682.

[52] G. Pötschke, J. Schröder, C. Günther, R. Q. Hwang, R. J. Behm, *Surf. Sci. Lett.* **1991**, *251-252*, A346.

[53] J. Schroder, C. Gunther, R. Q. Hwang, R. J. Behm, *Ultramicroscopy* **1992**, *42-44*, 475.

[54] S. Strbac, R. J. Behm, a. Crown, a. Wieckowski, *Surf. Sci.* **2002**, *517*, 207.

[55] S. Dahl, a. Logadottir, R. Egeberg, J. Larsen, I. Chorkendorff, E. Törnqvist, J. Nørskov, *Phys. Rev. Lett.* **1999**, *83*, 1814.

[56] L. Ruan, I. Stensgaard, F. Besenbacher, E. Laegsgaard, *J. Vac. Sci. Technol. B* **1994**, *12*, 1772.

[57] T. Zambelli, J. Wintterlin, J. Trost, G. Ertl, *Science (80-.).* **1996**, *273*, 1688.

[58] K. Hansen, T. Worren, S. Stempel, E. Lægsgaard, M. Bäumer, H.-J. Freund, F. Besenbacher, I. Stensgaard, *Phys. Rev. Lett.* **1999**, *83*, 4120.

[59] E. Herrero, V. Climent, J. M. Feliu, *Electrochem. commun.* **2000**, *2*, 636.

[60] P. Strasser, S. Koh, J. Greeley, *Phys. Chem. Chem. Phys.* **2008**, *10*, 3670683.

[61] B. Hammer, L. B. Hansen, J. Nørskov, *Phys. Rev. B* **1999**, *59*, 7413.

[62] D. J. Mowbray, J. I. Martínez, J. Rossmeisl, K. S. Thygesen, K. W. Jacobsen, J. K. Nørskov, *Differences* **2011**, 2244.

[63] J. Rossmeisl, A. Logadottir, J. K. Nørskov, *Chem. Phys.* **2005**, *319*, 178.
[64] J. Greeley, J. Norskov, J. K. Nørskov, *Electrochim. Acta* **2007**, *52*, 5829.
[65] H. B. Beer, *J. Electrochem. Soc.* **1980**, *127*, 303.
[66] S. Trasatti, *Technology* **2000**, *45*, 2377.
[67] B. Seger, T. Pedersen, A. Laursen, P. Vesborg, O. Hansen, I. Chorkendorff, *J. Am. Chem. Soc.* **2013**, *135*, 1057.
[68] B. Seger, D. S. Tilley, T. Pedersen, P. C. K. Vesborg, O. Hansen, M. Grätzel, I. Chorkendorff, *RSC Adv.* **2013**, *3*, 25902.
[69] S. Hu, M. R. Shaner, J. a Beardslee, M. Lichterman, B. S. Brunschwig, N. S. Lewis, *Science* **2014**, *344*, 1005.
[70] B. Seger, S. D. Tilley, T. Pedersen, P. C. K. Vesborg, O. Hansen, M. Grätzel, I. Chorkendorff, *J. Mater. Chem. A* **2013**, *1*, 15089.
[71] M. F. Lichterman, A. I. Carim, M. T. McDowell, S. Hu, H. B. Gray, B. S. Brunschwig, N. S. Lewis, *Energy Environ. Sci.* **2014**, *7*, 3334.
[72] N. C. Strandwitz, D. J. Comstock, R. L. Grimm, A. C. Nichols-Nielander, J. Elam, N. S. Lewis, *J. Phys. Chem. C* **2013**, *117*, 4931.
[73] Y. Gorlin, B. Lassalle-Kaiser, J. D. Benck, S. Gul, S. M. Webb, V. K. Yachandra, J. Yano, T. F. Jaramillo, *J. Am. Chem. Soc.* **2013**, *135*, 8525.
[74] V. Di Castro, G. Polzonetti, *J. Electron Spectros. Relat. Phenomena* **1989**, *48*, 117.
[75] M. S. El-Deab, M. I. Awad, A. M. Mohammad, T. Ohsaka, *Electrochem. commun.* **2007**, *9*, 2082.
[76] L. Trotochaud, J. K. Ranney, K. N. Williams, S. W. Boettcher, *J. Am. Chem. Soc.* **2012**, *134*, 17253.
[77] Y. Gorlin, C.-J. Chung, J. D. Benck, D. Nordlund, L. Seitz, T.-C. Weng, D. Sokaras, B. M. Clemens, T. F. Jaramillo, *J. Am. Chem. Soc.* **2014**, *136*, 4920.
[78] G. Sauerbrey, *Zeitschrift für Phys. A Hadron. Nucl.* **1959**, *155*, 206.
[79] V. R. Stamenkovic, B. S. Mun, K. J. J. Mayrhofer, P. N. Ross, N. M. Markovic, *J. Am. Chem. Soc.* **2006**, *128*, 8813.
[80] C. Cui, L. Gan, M. Heggen, S. Rudi, P. Strasser, *Nat. Mater.* **2013**, *12*, 765.
[81] L.-J. Wan, T. Moriyama, M. Ito, H. Uchida, M. Watanabe, *Chem. Commun. (Camb).* **2002**, 58.
[82] P. Hernandez-Fernandez, F. Masini, D. N. McCarthy, C. E. Strebel, D. Friebel, D. Deiana, P. Malacrida, A. Nierhoff, A. Bodin, A. M. Wise, J. H. Nielsen, T. W. Hansen, A. Nilsson, I. E. L. Stephens, I. Chorkendorff, *Nat. Chem.* **2014**, *6*, 732.
[83] N. Danilovic, R. Subbaraman, K. C. Chang, S. H. Chang, Y. Kang, J. Snyder, A. P. Paulikas, D. Strmcnik, Y. T. Kim, D. Myers, V. R. Stamenkovic, N. M. Markovic, *Angew. Chemie Int. Ed.* **2014**, *53*, 14016.
[84] T. F. Jaramillo, K. P. Jørgensen, J. Bonde, J. H. Nielsen, S. Horch, I. Chorkendorff, *Science (80-.).* **2007**, *317*, 100.
[85] F. Besenbacher, *Science (80-.).* **1998**, *279*, 1913.
[86] R. Frydendal, M. Busch, N. B. Halck, E. a. Paoli, P. Krtil, I. Chorkendorff, J. Rossmeisl, *ChemCatChem* **2015**, *7*, 149.
[87] C. Kuo, W. Li, L. Pahalagedara, A. M. El-Sawy, D. Kriz, N. Genz, C. Guild, T. Ressler, S. L. Suib, J. He, *Angew. Chemie Int. Ed.* **2014**, *127*, 2375.
[88] J. Mortensen, L. Hansen, K. Jacobsen, *Phys. Rev. B* **2005**, *71*, 1.
[89] J. Enkovaara, C. Rostgaard, J. J. Mortensen, J. Chen, M. Dułak, L. Ferrighi, J. Gavnholt, C. Glinsvad, V. Haikola, H. a Hansen, H. H. Kristoffersen, M. Kuisma, a H. Larsen, L. Lehtovaara, M. Ljungberg, O. Lopez-Acevedo, P. G. Moses, J. Ojanen, T. Olsen, V. Petzold, N. a Romero, J. Stausholm-Møller, M. Strange, G. a Tritsaris, M. Vanin, M. Walter, B. Hammer, H. Häkkinen, G. K. H. Madsen, R. M. Nieminen, J. K. Nørskov, M. Puska, T. T. Rantala, J. Schiøtz, K. S. Thygesen, K. W. Jacobsen, *J. Phys. Condens. Matter* **2010**, *22*, 253202.
[90] V. Čolić, J. Tymoczko, A. Maljusch, A. Ganassin, W. Schuhmann, A. S. Bandarenka, *ChemElectroChem* **2015**, *2*, 143.

Supporting Information

Towards an active and stable catalyst for oxygen evolution in acidic media: Ti-stabilised MnO_2

Rasmus Frydendal,[a] Elisa A. Paoli,[a] Ib Chorkendorff,[a] Jan Rossmeisl,[b,c,] Ifan E.L. Stephens[a,]**

[a] Center for Individual Nanoparticle Functionality, Department of Physics, Building 312, Technical University of Denmark, DK-2800 Kgs. Lyngby, Denmark

[b] Center for Atomic-scale Materials Design, Department of Physics, Building 307, Technical University of Denmark, DK-2800 Kgs. Lyngby, Denmark

[c] Department of Chemistry, University of Copenhagen, Universitetsparken 5, DK-2100, København Ø, Denmark

Glancing Angle X-ray Diffraction of MnO_x catalyst

X-ray diffraction was performed on a PANalytical X'PERT Pro equipment, using the $Cu_{k\alpha}$ line of 1.54 Å wavelength. To maximize the surface to bulk signal we used the glancing angle mode at 0.5 º which still did not result in any peaks coming from MnO_2 or other crystalline Mn oxide phases.

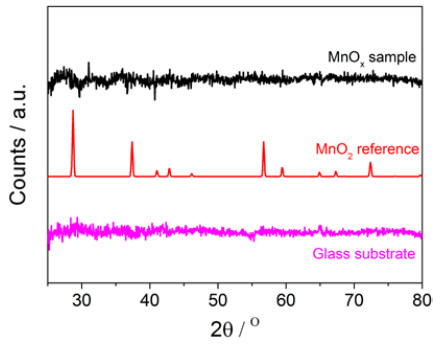

Figure S1. X-ray diffraction results for the MnO_2 film prepared by reactive sputter deposition at 200 C in 5 mTorr Ar:O_2, ratio 5:1. No peaks are coming from the films indicating an amorphous phase.

X-ray Photoelectron Spectroscopy

X-ray Photoelectron Spectroscopy measurements were carried out to estimate the oxide stoichiometry for the MnO_x catalyst and to confirm the Mn:Ti ratio. In Figure S2a the Mn3s spectra can be seen for a Ti-MnO_2 catalyst, together with the energy difference for the Mn3s multiplet, 4.7 eV. In Figure S2b the Mn2p peak for the same sample is shown, with indication of the energy difference between the Mn2p½ and its satellite. These two energy differences are consistent with MnO_2 spectra in the literature.[1,2] In Figure S2c the Ti2p peak is shown for a Ti-MnO_2 sample as prepared and in Figure S2d for a tested Ti-MnO2 sample. These spectra were used to evaluate the Mn:Ti ratio which was found to be 80:20 both before and after the stability tests described in the main text.

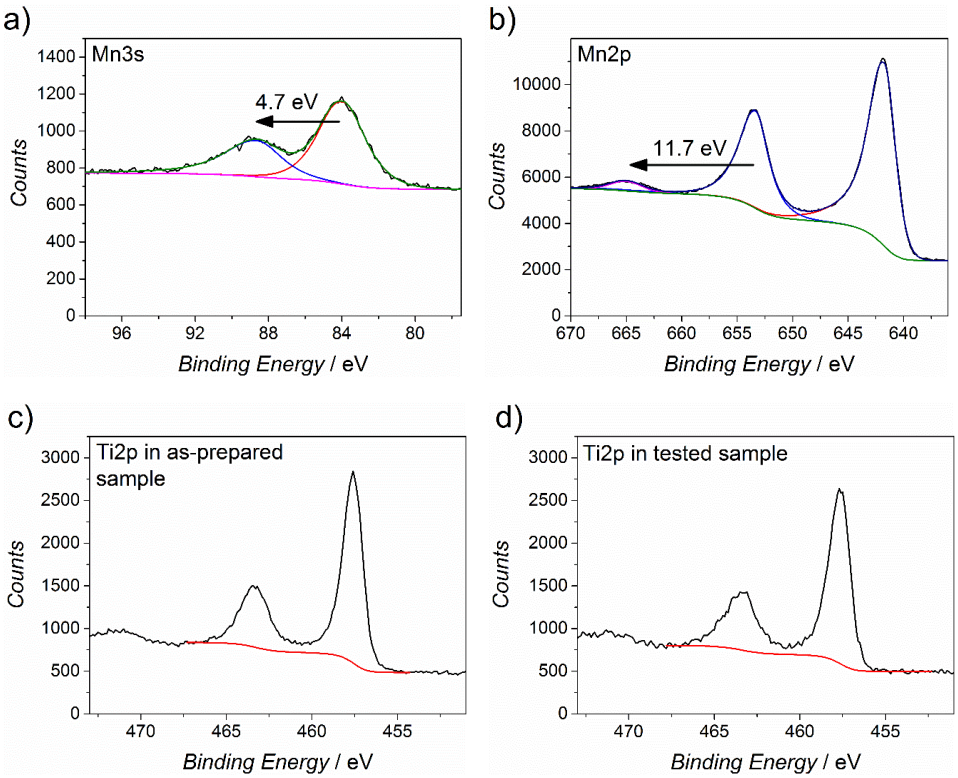

Figure S2. **a)** Mn3s spectrum where the distance for the multiplet is indicated. **b)** Mn2p spectrum where the distance for the Mn2p½ satellite is indicated. **c)** Ti2p spectrum used for evaluation of the Mn:Ti ratio. **d)** Ti2p spectrum for a sample tested two hours both at 1.8 V_{RHE} and 2 hours at 1.9 V_{RHE}.

Activity over time for EQCM experiments

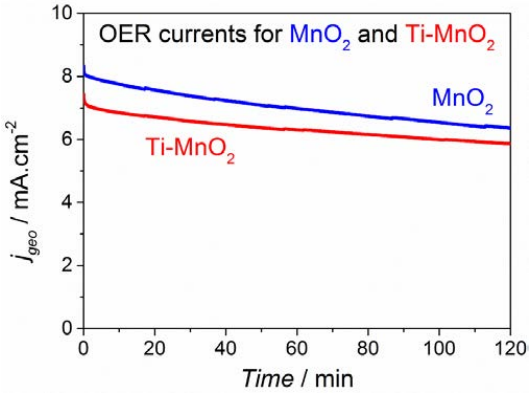

Figure S3. Chronoamperometry results for the MnO_2 and Ti-MnO_2 catalysts tested in 0.05 M H_2SO_4 at 1.9 V_{RHE}. 85 % ohmic drop compensation was applied.

ICP-MS results for RDE experiments

To support the tests done with the EQCM system, we also performed Rotating Disk Electrode, RDE, experiments with the same catalyst films supported by gold polycrystalline disks. The test conditions were nominally the same as for the EQCM measurements; 0.05 M H_2SO_4, 2 hours at 1.8 and 1.9 V_{RHE}; aliquots of electrolyte were taken before and after each test. Furthermore, for the RDE tests, a rotation speed of 1600 RPM was used. The results can be seen in Figure S4a and S4b. After one hour 1t 1.9 V, the Ti-MnO2 sample has a current density 30 % lower current density than MnO_2. However, there decrease in mass loss of 60 %. These results again support the finding that a better compromise between stability and activity can be obtained by the incorporation of Ti into MnO_2.

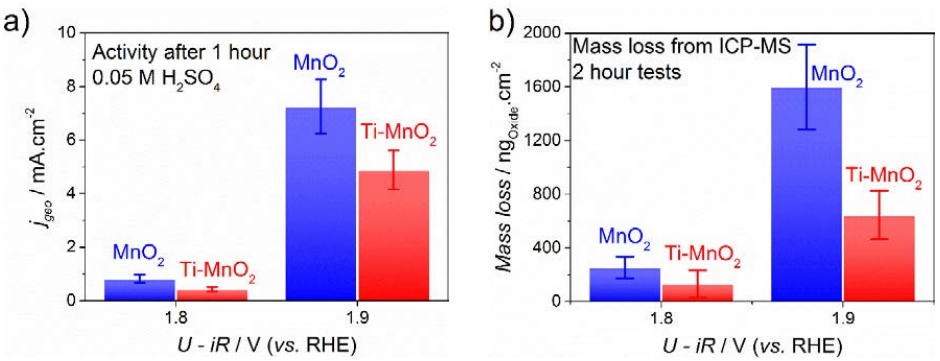

Figure S4. a) The activity of MnO_2 and Ti-MnO_2 after one hour at each potential, measured with an RDE setup. b) The mass losses for MnO_2 and Ti-MnO_2 after 2 hours at each potential, evaluated with ICP-MS. The error bars shown here are ±1 standard deviation from three independent measurements.

Calculations of Turnover Frequencies (TOF)

We compare the activities of literature references on the basis of turnover frequency. The definition we will use is the number of O_2 molecules produced per Mn atom per second. Due to the differences in catalyst loading it is challenging to find meaningful ways of normalization; and therefore an upper and lower limit will be presented.

The upper limit, $\mathrm{TOF}_{\max}$, constitutes the case where the surface is perfectly smooth and only surface atoms take part in the reaction. With this assumption, the number of Mn atoms per cm^2 is the same for all references and the geometric current density can be used directly to obtain the $\mathrm{TOF}_{\max}$ by multiplying j_{geo} with 1.545 $\frac{cm^2}{s\ mA}$.

For the lower limit, $\mathrm{TOF}_{\min}$, we instead assume that all the Mn atoms within the bulk of the electrode are available for the reaction:

$$\mathrm{TOF}_{\min} = \frac{j(C \cdot s^{-1}) \cdot M_{MnO_2}(g \cdot mol^{-1})}{4(e) \cdot N_A(mol^{-1}) \cdot 1.602 \cdot 10^{-19}(C \cdot e^{-1}) \cdot V_{film}(cm^3) \cdot \rho_{MnO2}(g \cdot cm^{-3})}$$

Where j is the absolute current drawn, M_{MnO2} the molar mass of MnO_2, N_A the Avogadro's constant, V_{film} the volume of catalyst used and ρ_{MnO_2} the density of MnO_2.

As this equation indicates, we assume the thin films reported in the current paper to have the density and molar mass of rutile MnO_2. While it is amorphous, the XPS results are consistent with a dioxide stoichiometry. Other possible oxide stoichiometries include MnO, Mn_3O_4 and Mn_2O_3. Using the densities and molar weights of these compounds leads to a maximum error of around 50 %.

The TOF for literature references has been calculated based on the information given below:

β-MnO_2 - α-Mn_2O_3/Morita[3]

From the description of the electrode preparation 10^{-5} moles/cm^2 Mn is loaded onto the substrate by thermal decomposition of a nitrate precursor. Activity data is taken from figure 2 in [3] where Pt is used as substrate and the catalyst is tested in 1N H_2SO_4 by anodic polarization. The original potential scale used is Hg/$HgSO_4$ in 1N H_2SO_4. In order to show the data using the RHE scale the standard redox potential of 0.674 V vs. RHE has been added. This results in a $\mathrm{TOF}_{\min}$ of 0.00026 s^{-1} per mA/cm^2.

$Ca_{0.16}Mn_2(H_2O)_2$/Najafpour[4]

The authors report dropcasting a solution consisting of 2.5 mg catalyst in 750 ml water with Nafion. 40 µl of this solution is used for a 3 mm Glassy Carbon electrode. Prior to drop casting, the solution is sonicated to give a good dispersion and this should give 1.89 mg/cm^2 of the $Ca_{0.16}Mn_2(H_2O)_2$ catalyst powder. The number of Mn atoms was then estimated by assuming a molar weight of 152.4 g/mol. These assumptions lead to a $\mathrm{TOF}_{\min}$ of 0.0001 s^{-1} per mA/cm^2. Activity data was digitized from Figure 7 in [4] where the catalyst is tested in 0.1 M $HClO_4$ with a linear sweep.

Electrodeposited MnO_2/Huynh et al.[5]

The amount of catalyst loaded onto 1 cm^2 of substrate was estimated from the reported deposition charge. The standard amount encompassed 6 mC of charge. From [6] the overall deposition reaction is described with two electrons per MnO_2 unit. Using this assumption a $\mathrm{TOF_{min}}$ of 0.0833 s^{-1} per mA/cm^2 can be estimated. The activity results used for comparison is taken from Figure 1 in [5] where the catalyst was measured at steady state (60-90 seconds at each potential) in diluted phosphoric acid mixed with KNO_3 and KOH (pH 2.5).

δ-MnO_2/Takashima[7]

The electrodes in this work were prepared by spray deposition using a 0.5 mM colloidal solution of δ-MnO_2. In total, 6 ml of this solution was sprayed onto a 3x3 cm FTO substrate resulting in a loading of 3.33 x 10^{-7} mol/cm^2. Assuming that this quantity is representative for Mn atoms the $\mathrm{TOF_{min}}$ is 0.0077 s^{-1} per mA/cm^2. Activity data is taken from figure 6a in [7] where the catalyst is tested with cyclic voltammetry in aqueous Na_2SO_4 mixed with H_2SO_4 and NaOH resulting in a pH of 4. The original data is shown on an SHE scale. In order to compare on the RHE scale, we have converted it by adding 59 mV per pH value.

These estimations are summarized in Figure 1. Morita *et al.* prepared their catalyst using thermal decomposition[3], a method typically resulting in surfaces with a very high roughness.[8] Consequently, the actual TOF for the catalyst reported by Morita *et al.* would likely be orders of magnitude lower than the $\mathrm{TOF_{max}}$; on this basis our thin film catalyst is the most active.

DFT calculations on bulk and planar MnO_2

The mixing of Ti or Ir into the bulk of rutile MnO_2 was investigated by evaluating 3 concentrations, 25, 50 and 75 %. The calculation parameters used are as described in the main text. The stabilities of the mixed oxides are evaluated similarly to the termination energy:

$$\Delta E_{bulk\ mix} = E_{mix} - E_{ref} - (x \cdot E_{unit,guest} - x \cdot E_{unit,ref})$$

Here $\Delta E_{bulk\ mix}$ is the energy of formation for the mixed oxide, E_{mix} the total energy of the mixed structure, E_{ref} the energy of the original MnO_2 structure, $E_{unit,guest}$ the energy of a unit cell of the guest material, $E_{unit,MnO2}$ the energy of a unit cell of the MnO_2 and x the amount of substituted atoms, which is substituted. Surface incorporation was also investigated for 25 and 50 % surface sites substituted. It is seen in Table S1 that none of the concentrations results in negative energy of formation for bulk mixtures or surface incorporation. This is also consistent with results from the materials project database where the only stable mixed oxide with Mn and Ti is a perovskite type, $TiMnO_3$, while for Mn and Ir no stable mixed oxide are found.[9,10]

Calculated values

The values calculated with DFT can be seen below in Table S1.

Termination material	Step termination [eV/MO_2]	Kink termination [eV/MO_2]	Bulk mixing $Mn_{0.75}X_{0.25}O_2$ [eV/MO_2]	Surface $Mn_{0.75}X_{0.25}O_2$ [eV/MO_2]	Lattice parameter *a* [Å]	Lattice parameter *c* [Å]
MnO_2	-	-	-	-	4,499	2,902
TiO_2	-0.23	-0.35	0.01	0.1	4,708	2,958

GeO_2	-0.21				4,500	2,932
SnO_2	0.54		0.2	0.1	4,852	3,265
PtO_2	0.37		0.1	0	4,725	3,182
RuO_2	0.41		0.04	0	4,662	3,185
IrO_2	0.82	0.13	0.1	0.1	4,658	3,166

References

[1] V. Di Castro, G. Polzonetti, *J. Electron Spectros. Relat. Phenomena* **1989**, *48*, 117.

[2] Y. Gorlin, T. F. Jaramillo, *J. Am. Chem. Soc.* **2010**, *132*, 13612.

[3] M. Morita, C. Iwakura, H. Tamura, *Electrochim. Acta* **1977**, *22*, 325.

[4] M. M. Najafpour, K. C. Leonard, F.-R. F. Fan, M. A. Tabrizi, A. J. Bard, C. K. King'ondu, S. L. Suib, B. Haghighi, S. I. Allakhverdiev, *Dalton Trans.* **2013**, *42*, 5085.

[5] M. Huynh, D. Bediako, D. Nocera, *J. Am. Chem. Soc.* **2014**, *136*, 6002.

[6] M. Huynh, D. K. Bediako, Y. Liu, D. G. Nocera, *J. Phys. Chem. C* **2014**, *118*, 17142.

[7] T. Takashima, K. Hashimoto, R. Nakamura, *J. Am. Chem. Soc.* **2011**, *134*, 1519.

[8] G. Lodi, E. Sivieri, A. De Battisti, S. Trasatti, *J. Appl. Electrochem.* **1978**, *8*, 135.

[9] G. Bergerhoff, R. Hundt, R. Sievers, I. D. Brown, *J. Chem. Inf. Model.* **1983**, *23*, 66.

[10] A. Jain, S. P. Ong, G. Hautier, W. Chen, W. D. Richards, S. Dacek, S. Cholia, D. Gunter, D. Skinner, G. Ceder, K. a. Persson, *APL Mater.* **2013**, *1*, DOI 10.1063/1.4812323.

Paper IV

In-situ investigation of Au-MnO_x thin films with improved activity for the oxygen evolution reaction
Rasmus Frydendal, Linsey Seitz, Dimosthenis Sokaras, Tsu-Chien Weng, Dennis Nordlund, Ib Chorkendorff, Ifan E.L. Stephens, Thomas F. Jaramillo
In preparation

DRAFT

In-situ investigation of Au-MnO_x thin films with improved activity for the oxygen evolution reaction

Rasmus Frydendal,[a] Linsey Seitz,[b] Dimosthenis Sokaras,[c] Tsu-Chien Weng,[c] Dennis Nordlund,[c] Ib Chorkendorff,[a] Ifan E.L. Stephens,[a] Thomas F. Jaramillo,[b,c]

[a] Center for Individual Nanoparticle Functionality, Department of Physics, Building 312, Technical University of Denmark, DK-2800 Kgs. Lyngby, Denmark

[b] Department of Chemical Engineering, Stanford University, Stanford, California 94305, United States

[c] SLAC National Accelerator Laboratory, 2575 Sand Hill Road, Menlo Park, California 94025, United States

Abstract

The electrochemical splitting of water holds great potential as a method for producing clean fuels by storing electricity from intermittent energy sources. The efficiency of such a process would be greatly facilitated by incorporating more active catalysts based on abundant materials for the oxygen evolution reaction. Manganese oxides are promising as catalysts for this reaction. Recent reports show that their activity can be drastically enhanced when modified with gold. Herein, we investigate highly active mixed Au-MnO_x thin films for the oxygen evolution reaction, which perform more than five times better than the pure MnO_x. These films are thoroughly characterized with in-situ X-ray Absorption, which reveal that Mn assumes a higher oxidation state under reaction conditions when Au is present. At the same time, the magnitude of the enhancement is correlated to the size of the Au domains where larger domains are the most beneficial. These observations serve as a solid starting point for better understanding of the beneficial interaction between gold and manganese oxide.

1. Introduction

The electrolytic production of synthetic fuels provide a promising means to average fluctuant energy supply from renewable sources. It is evident that the water oxidation reaction, known as oxygen evolution, is set to play a key role in such transformations.[1–4] Whether the goal is to produce pure hydrogen, reduce CO_2 to hydrocarbons or upgrade biomass it is crucial to find a suitable source of hydrogen. For this purpose, water is ideal due to its abundance and the relative ease of water splitting, which leaves no harmful byproducts. However, the electrochemical evolution of oxygen, OER, imposes a large overpotential, due to sluggish kinetics at the electrode.[5–7] More specifically, the difficulties in catalyzing the reaction arise from non-optimal binding energies to the three reaction intermediates, even on the most active catalysts.[5,8–10] This is because the binding to the reaction intermediates, *O, *OH and *OOH, correlate linearly with each other: their relationships to each other are known as the scaling relations. For all surfaces which obey scaling relations, no catalyst will exhibit optimal binding to all three intermediate. For this reason, there is a need for novel strategies that circumvent the scaling relations and lead to catalytic surfaces with lower overpotential.[11]

A possible strategy for improving catalyst properties is to modify a catalytic surface with another material. There are several examples in the literature where such mixtures have been successful in achieving improved performance. In acidic media ruthenium oxides mixed with either Ni or Co has been reported to be more active than the pure oxide.[12–15] Recently, Ti has also been shown to stabilize MnO_2 thin films against anodic dissolution in acidic media.[16] In alkaline media Ni and Fe based oxides are currently utilized in commercialized electrolyser systems and combinations of the two elements have been shown to increase activity significantly.[17–19] Furthermore, Mn and Co based oxygen evolution catalysts have shown good performance in alkaline environment and various strategies have been proposed to improve the activities.[20–28] Interestingly, the presence of metallic particles or support has a profound influence on the activity of both Mn and Co based oxide catalysts.[29–35] Mn nanoparticles deposited above or below gold clusters can lead to a 20-fold increase in turnover frequency.[29] A possible explanation for the beneficial interaction was later proposed by two of the authors of the current manuscript on the basis of stabilized *OOH adsorption on neighboring Mn and Au sites, due to a proton transfer mechanism.[30] Kuo et al. experimentally investigated the role of gold nanoparticles for five different MnO_x polymorphs: they argued that the increase in OER activity could be correlated to facile formation of active Mn^{3+} sites in the presence of gold.[33] This conclusion was reached primarily from ex-situ X-ray Absorption Near Edge Spectroscopy, XANES, which indicated a lower oxidation state of Mn sites when combined with gold nanoparticles. However, judging from stability regions of the Mn-O system in aqueous

environment it seems unlikely that a high concentration of Mn^{3+} should be present at the surface while turning over oxygen.[36,37]

In the present study, we will characterize the behavior of MnO_x in situ under oxygen evolution conditions, using XANES to measure the Mn K-edge. To achieve a high concentration of Mn/Au neighbors the samples investigated are co-sputtered thin films.

2. Experimental details

Thin films of MnO_x and Au-MnO_x, with a nominal thickness of 40 nm, were prepared with reactive sputter deposition using a method previously reported.[38] The amount of material deposited was controlled by an in-chamber Quartz Crystal Microbalance, with which the deposition rates of both Mn and Au were calibrated. Mn was deposited with 140 W and Au with power dependent on the desired concentration (30 or 50 %). The deposition pressure was kept at 5 mTorr consisting of Ar and O_2 in a 25/3 ratio and the substrate temperature was 200 °C. Glassy carbon disks or wafers were used as substrates (Sigradur G, HTW GmbH), both polished to a mirror finish. To facilitate film adhesion, the glassy carbon substrates were cleaned with radio frequency (RF) sputtering in an argon atmosphere for 10 minutes prior to deposition. The glassy carbon wafer preparation has been reported previously.[29] They were prepared to be 100-200 μm thick from GC rods and polished to an RMS roughness of less than 50 nm.

Tests of activity towards oxygen evolution were performed in a standard three electrode glass cell using 1 M KOH. A carbon rod was used as counter electrode and a Hg/HgO electrode as reference. The reference electrode potential was calibrated with a reversible hydrogen electrode (RHE) in the same electrolyte by bubbling hydrogen over a platinum mesh. All potentials are reported with respect to the RHE scale and have been corrected for Ohmic losses, evaluated with Electrochemical Impedance Spectroscopy; range 1-200000 Hz and DC potential 10 mV. The Ohmic resistance was between 5-9 Ω for all samples.

Ex-situ characterisation of the thin films was performed using X-ray Photoelectron Spectroscopy (Thermo-Fisher, base pressure of 5 x 10-10 mbar and X-ray source monochromatized $Al_{K\alpha}$ 1486.7 eV), Scanning Electron Microscopy (SEM, FEI, Magellan, secondary electron detector, beam voltage of 5 kV, beam current of 50 pA) and X-ray Diffraction (PANanalytical X'pert PRO equipment having an X-ray wavelength of 1.54 Å for the $Cu_{K\alpha}$ line).

In-situ XAS measurements probing the Mn K-edge were performed at the SSRL Beam-line 6-2 ES2. The electrochemical setup for these measurements has been reported previously.[29,39] A double crystal Si(311) monochromator equipped with Rh-coated mirror was used to operate the beamline. Furthermore, a parabolic mirror was used to focus the beam to a spot size of 230x400 μm^2 (FWHM) at the sample position. Six spherically bent analyzer crystals of germanium ‹333› resolved the $Mn_{K\alpha}$ signal which could then be detected by an Si drift detector, SDD, in photon counting mode. The spectra presented here have all been normalised to have an edge jump of one after the linear background is subtracted. Error bars represent ±1 standard deviation from Poisson statistics and standard error propagation.

3. Results and Discussion

To investigate the beneficial interaction between Au and Mn for oxygen evolution, thin films of MnO_x mixed with two different amounts of gold were prepared. The mixed films contain 30 % or 50 % Au and are compared to pure MnO_x and a polycrystalline Au surface. The percentage values are on a total metal basis, so that 30 % Au means that 30 % of the manganese are now replaced with Au.

From XPS measurements the Mn 2p and Au 4d peaks were used to evaluate the Mn:Au stoichiometry. It should be noted that a small Cu contamination (1-3 %) was found for two samples used for electrochemical tests, but the activity towards OER remained the same as without contamination. See more details in supporting information. The XPS spectra can be seen in Supplementary Information, Figures S1-3. The Mn2p½ satellite distance and Mn3s multiplet splitting can also be used to evaluate the initial Mn:O stoichiometry.[20,40] Comparing the results obtained for as-prepared samples to literature references, indicates an Mn:O stoichiometry consistent with Mn_3O_4.

The thin films were also characterized with Glancing Angle X-ray Diffraction, to investigate whether the sputter deposition method yields crystalline Mn oxide or Au phases. The results for pure MnO_x can be seen in Figure 1a and the results for mixed Au-MnO_x films in Figure 1b. There are nine peaks from the MnO_x film matching with a Mn_3O_4 phase which is plausible from a low amount of oxygen present during deposition. Interestingly, the Mn_3O_4 peaks vanish for the mixed films where gold peaks are instead visible, for both concentrations. For 30 and 50 % Au, four peaks can be identified which match with a gold face centered cubic (FCC) phase. These results clearly show that Au particles are formed. The difference between the two concentrations is the broadening of the peaks. Using Scherrers equation it is possible to compare the Au domain size for the two films based on this broadening. For 30 % Au the domains are approximately 2 nm while for 50 % Au they are 3

nm. For details regarding domain size estimation, see supporting information. This method is not very accurate due to the assumptions used to derive the equation. It is also possible that microstrain in the gold domains could influence the peak broadening. However, the estimation here serves as a comparison between the two very similar films.[41] The results indicate that from 30 to 50 % the Au domains within the MnO_x films grow approximately 150 %.

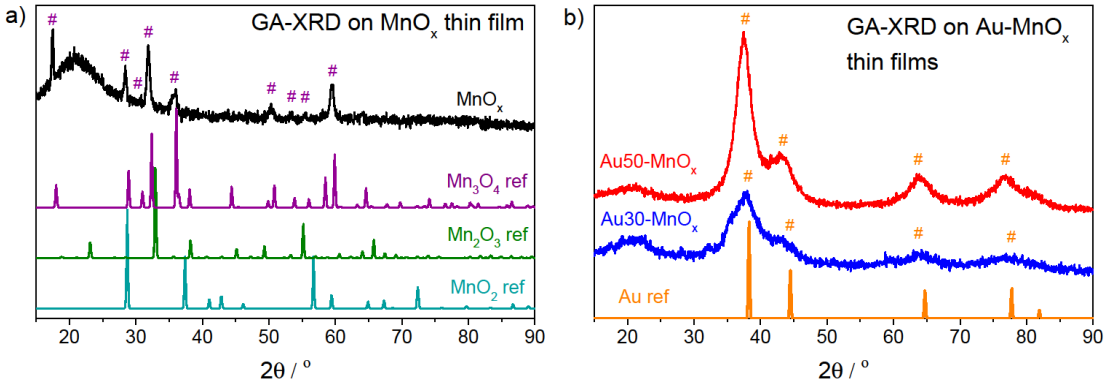

Figure 1. a) X-ray Diffraction for pure MnOx film, in purple, together with references for Mn_3O_4 (blue), Mn_2O_3 (red) and MnO_2 (black). The peaks matching Mn_3O_4 lines are indicated with blue #. b) X-ray Diffraction results for Au-MnO_x films, 50% Au in green and 25 % Au in teal. A gold reference is shown in orange. The four main peaks for Au is indicated with orange #.

The characterization of surface morphology was performed with Scanning Electron Microscopy. From figure 1a-c it is evident that the surface of MnO_x change with increasing gold content. The pure MnO_x consists of pyramid shaped features, whereas the mixed films exhibit roundish features. These images also indicate that the films with Au have a slightly more open structure which could lead to a higher surface area.

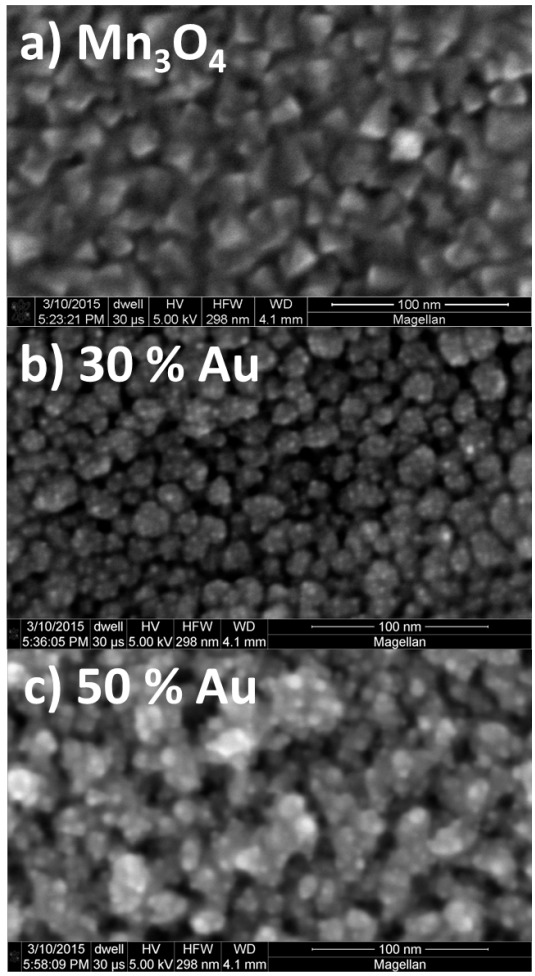

Figure 2. Scanning Electron Microscopy images for a) pure Mn_3O_4 b) MnO_x with 30 % Au and c) MnO_x with 50 % Au.

The activities of these films were then characterized with cyclic voltammetry in 1 M KOH using a scan rate of 20 mV/s. For each thin film the activity measurements were repeated three times. In Figure 2a the initial CVs can be seen and in Figure 2b they are compared at 400 mV overpotential with error bars.

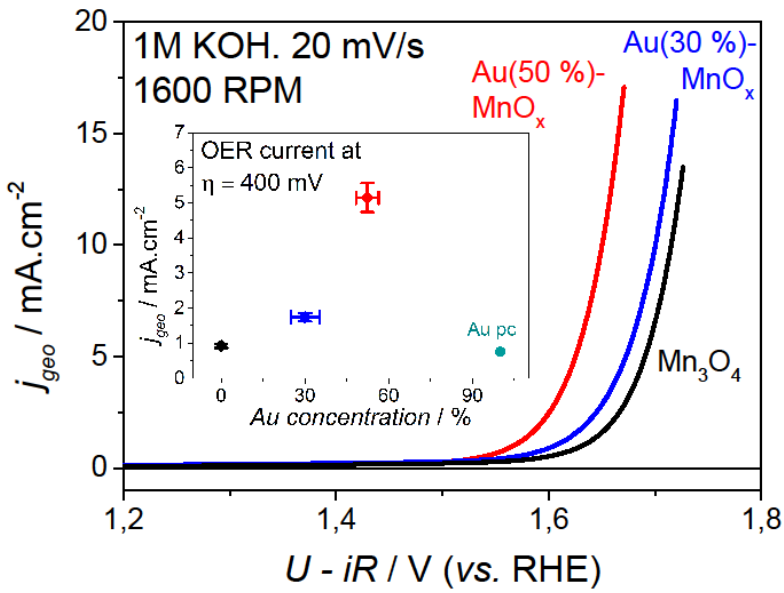

Figure 3. Initial cyclic voltammetry for Mn_3O_4 films with 0, 30 and 50 % Au. The results were obtained for Rotating Disk Electrodes which were performed in 1M KOH using a scan rate 20 mV/s and a rotation speed of 1600 RPM. Inset: At each concentration the activities are compared at an overpotential of 400 mV. The error bars are based on three independent measurements and the Au concentration is evaluated with XPS.

From the electrochemical results in Figure 3 it is clear that a significant increase in current density is obtained with increased concentration of Au in the MnO_x films. Most striking is a 5-fold improvement in activity at 400 mV overpotential for the MnO_x with 50 % Au. When comparing the overpotential at the benchmark value of 10 mA/cm^2,[42,43] the presence of Au results in a decrease in the overpotential of 65 mV.

The gold could improve the conductivity of the MnO_x film, however, the similar Tafel slopes of pure and mixed films indicate that differences in uncompensated Ohmic losses are not a dominant effect. Changes in the surface morphology could lead to a higher electrochemically accessible surface area. The pseudo capacitance measured electrochemically is considered proportional to the active area.[43] The change in capacitance between pure MnO_x and Au(50%)-MnO_x is below a factor of two as shown in figure S2.

With the XRD and XPS data a simple model can be made to estimate how many Mn-Au interacting sites that are present for the two concentrations. Here we will use domain size (2 or 3 nm) as particle size for spherical gold particles distributed on a flat Mn_3O_4 surface. If the circumferences of such particles are assumed to be proportional to the number of Mn-Au interacting sites, then the Au(50%)-MnO_x should have less than 1.3 times

more than Au(30%)-MnO_x. This increase in interacting sites is not enough to explain the factor three in difference measured in current density. For details on this model see supporting information.

With such an improvement it is of great interest to understand the interactions between Au and MnO_x under reaction conditions. In-situ XANES characterisation of the thin films was therefore carried out, specifically probing the Mn K-edge and Au LIII-edge while applying more oxidative potentials. In Figure 4a-c the Mn K-edge spectra are shown for each of the three Au concentrations, 0, 30 and 50 %, respectively.

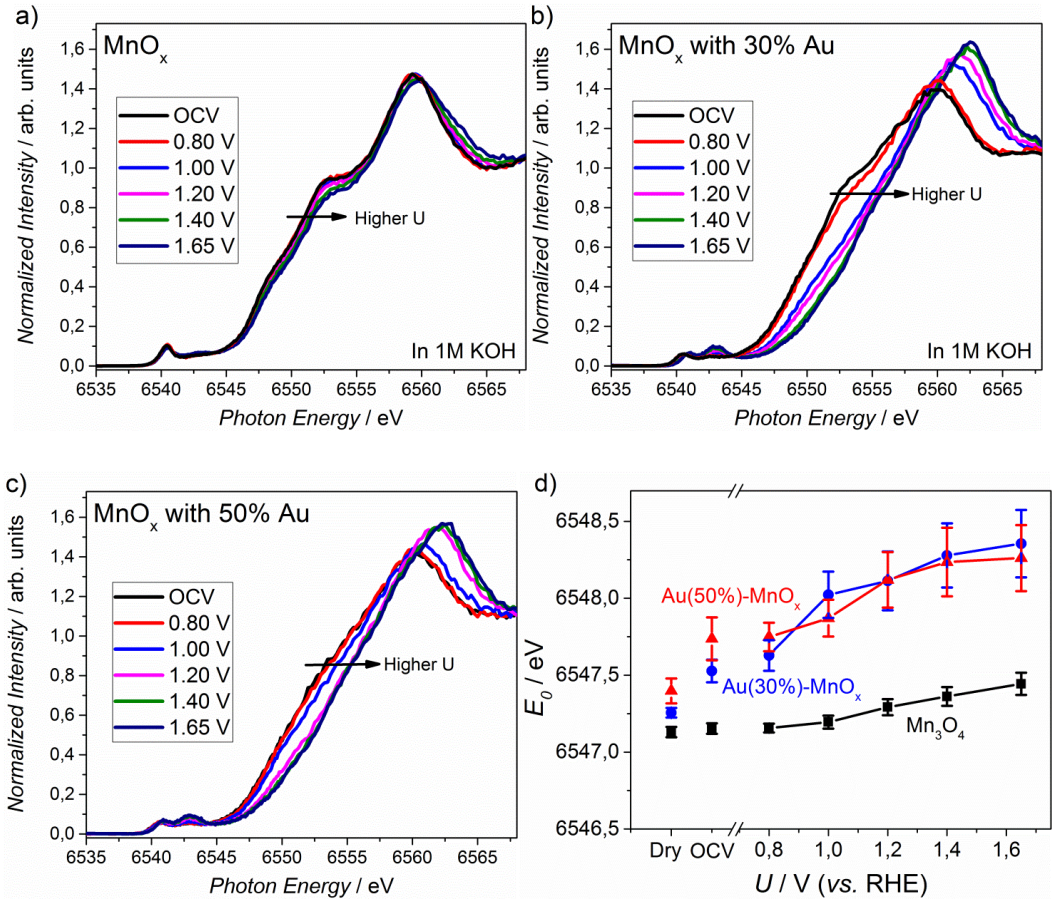

Figure 4. a) Normalised Mn K-edge results for the pure MnOx thin film. **b)** Normalised Mn K-edge results for the MnOx thin film with 30 % Au. **c)** Normalised Mn K-edge results for the MnOx thin film with 50 % Au. **d)** Moment analysis of Mn K-edge data for the three thin films. This method takes into account the general shift of the K-edge features in a large energy range instead of focusing

on a single feature. In grey, values for known references have been included for comparison. The error bar are based on varying the integral range in the first moment equation.

In Figure 4a a slight change in the Mn K-edge can be observed for the gradual increase in potential. at more positive potentials, the overall edge shifts towards higher energies, which is consistent with a small degree of oxidation of the Mn atoms, as expected from applying an oxidizing potential. For the samples with Au incorporated, Figures 4b and c, the same overall trend can be seen; at increasing potentials the edge shifts towards higher energies. However, the change is significantly more drastic for the mixed films, compared to the pure MnO_x. Two specific features should be noted. The shoulders visible around 6548 and 6552,5 eV for the initial measurements disappear for the films with Au, while it is still visible for pure MnO_x, even at 1.65 V. These two shoulders are normally seen for Mn oxides in lower oxidation states, Mn^{2+}.[44,45] Another feature is the pre-edge located around 6540.5 eV for the dry measurements. For the pure MnO_x there is little to no change in the pre-edge, whereas for the mixed films a very clear splitting into two peaks is seen for both concentrations after around 1 V. Farges attributed this pre-edge splitting, which he observed on several different types of Mn compounds, to oxidation states of 3+ or higher.[45] However, Mn compounds with the same oxidation state can exhibit very different K-edge features dependent on the structure and due to the fact that mixed oxidation states can be present at the same time.[46] To account for such a possibility, we analyze the overall shift of the edge using a moment method where we calculate the weighted integral of the spectrum.[47] The results of that analysis are shown in Figure 4d, where data for each of the films are included together with literature values for two known Mn oxidation states. Consistent with the Farges' interpretations described above, this analysis shows that the incorporation of Au leads to a significant shift of the Mn K-edge towards higher energies. Even at the open circuit conditions a clear difference is observed between the pure MnO_x and the mixed films. At the highest potential, 1.65 V, the mixed films have a Mn K-edge shifted 1 eV higher than the pure Mn_3O_4. It is unlikely that the Mn exists in a single oxidation state based on the data presented here. We emphasize, that since the Mn K-edge energies are in the hard X-ray regime the entire bulk of the film is contributing to the signal, together with the surface atoms. We expect the electrochemically active Mn atoms to be more oxidized when the potential is increased, than the bulk atoms.

The Au LIII-edge was also measured for the samples containing gold, and the resulting spectra are shown in figure 5a and b. At OCV, figure 5a, the spectra for Au(30%)-MnO_x and Au(50%)-MnO_x are almost identical. However, at 1.65 V_{RHE} there is a distinct in the white line for the lower Au concentration. A higher white line indicates that the Au is oxidized.[48,49] From the Pourbaix diagram of gold the oxidation to a +3 state can occur at potentials close to 1.46 V_{RHE} so it is not a surprising feature. Nevertheless it is a feature that is missing for the

higher concentration of Au, indicating that a significant amount of the gold in the 30% sample is oxidized, not just the surface.

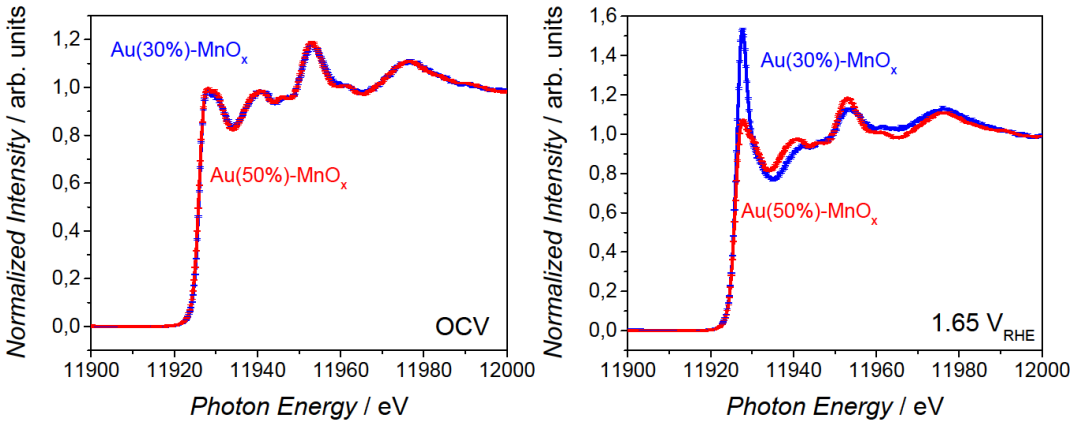

Figure 5. a) Au LIII-spectra for Au(30%)-MnO_x (blue) and Au(50%)-MnO_x (red) at open circuit conditions. b) Au LIII-spectra for Au(30%)-MnO_x (blue) and Au(50%)-MnO_x (red) at 1.65 V_{RHE}.

Since the XANES results showing a higher oxidation for MnO_x film mixed with gold, it raises the question; why does a higher oxidation state lead to higher OER activity. The binding energies for Mn sites in a higher oxidation state is closer to the optimal strengths. This notion can be justified with the DFT calculations reported in [8,36] where MnO_2 is predicted to have a lower overpotential than Mn_2O_3, Mn_3O_4 and MnO.

It is therefore interesting that the two Au concentrations results in very similar Mn oxidation state from the in-situ XANES, while the activity enhancement is much more significant at 50 % Au. An important difference between the two concentrations is the Au domain size, which was markedly larger at 50 %. Furthermore, the Au LIII-edge spectra revealed that the sample with 30% gold was oxidized at high potentials, whereas the sample with 50 % was not. Assuming the domain size estimated with XRD to be a suitable measure of the particle size it should be noted that size effects for oxygen electrochemistry is very significant in the range of 1-5 nm.[50] A possible explanation for the observations is that a certain size of Au particles is necessary for the full enhancement. This enhancement could be related to the type of Au sites available at the surface of such particles during oxygen turnover.[30,51] Greeley et al. have reported that the binding to OER intermediates for Au surfaces is stronger for undercoordinated sites.[52] Specifically, *OH binding to Au(211) was 0.17 eV stronger than to Au(100). Furthermore, the number of undercoordinated sites for Au particles increase dramatically when the size of particles is decreased from 5 to 1 nm.[51] For the smaller Au domains this is consistent with

oxidation at more cathodic potentials as observed with XAS. It is therefore noteworthy that the Au particles used in the study by Kuo et al. have an average size of 4 nm,[33] which are likely to contain less undercoordinated sites. These observations indirectly indicate that Au terrace sites are important for the interaction with Mn oxides. From the theoretical model proposed in [30] *OH adsorbed to the terrace sites of bulk Au(111) was used as proton acceptor. A particle size dependency on the activity could suggest that these sites are indeed important and play a role in the reaction mechanism.

However, to fully establish such an effect more specific measurements much be carried out. From these measurements it is, however, clear that gold promotes the activity towards OER and leads to higher oxidation state of Mn under reaction conditions. In future studies it would also be of great interest to mimic this interaction and beneficial effect using a non-noble metal activity promoter instead of Au.

4. Conclusion

In this study we have investigated mixed Au-MnOx films as catalysts for the oxygen evolution reaction. Films with 30 % Au exhibited modest increase in current density over the pure Mn_3O_4 film . At 50 % Au more than five times higher current densities were measured. From X-ray Diffraction measurements it was found that Au forms particles in the MnO_x matrix, with sizes dependent on the Au concentration. At 30 % the crystallite size was approximately 2 nm, while at 50 % Au it increased to 3 nm. The films were studied with in-situ X-ray Absorption where the Mn K-edge and Au LIII-edge were probed as a function of electrochemical potential. At increasingly anodic potentials all films showed a shift of the Mn K-edge towards higher photon energies. However, the films with Au showed a significantly larger shift, indicating that the Mn atoms on average reach a higher oxidation state. The Au LIII-edge revealed that at a low Au concentration, 30 %, significant oxidation could be seen, which was not the case at 50 %. The combined study suggests that a beneficial interaction between Mn oxide and Au depends on more than just number of neighboring Mn-Au sites. It is likely that the type of Au sites available next to active Mn sites has a strong impact on the increase in OER activity.

Acknowledgements

The authors gratefully acknowledge financial support from the Danish Ministry of Science's UNIK initiative, Catalysis for Sustainable Energy. The Center for Individual Nanoparticle Functionality is supported by the Danish National Research Foundation (DNRF54).

References

(1) Greeley, J.; Markovic, N. M. *Energy Environ. Sci.* **2012**, *5* (11), 9246.
(2) Gasteiger, H. A.; Markovic, N. M. *Science* **2009**, *324* (April), 48.
(3) Maeda, K.; Domen, K. *J. Phys. Chem. Lett.* **2010**, *1* (18), 2655.
(4) Lewis, N. S.; Nocera, D. G. *Proc. Natl. Acad. Sci. U. S. A.* **2006**, *103* (43), 15729.
(5) Rossmeisl, J.; Logadottir, A.; Nørskov, J. K. *Chem. Phys.* **2005**, *319* (1-3), 178.
(6) Rossmeisl, J.; Qu, Z.-W.; Zhu, H.; Kroes, G.-J.; Nørskov, J. K. *J. Electroanal. Chem.* **2007**, *607* (1-2), 83.
(7) Trasatti, S. *J. Electroanal. Chem.* **1980**, *111*, 125.
(8) Man, I. C.; Su, H.-Y.; Calle-Vallejo, F.; Hansen, H. A.; Martínez, J. I.; Inoglu, N. G.; Kitchin, J.; Jaramillo, T. F.; Nørskov, J. K.; Rossmeisl, J. *ChemCatChem* **2011**, *3* (7), 1159.
(9) Koper, M. T. M. *J. Electroanal. Chem.* **2011**, *660* (2), 254.
(10) Abild-Pedersen, F.; Greeley, J.; Studt, F.; Rossmeisl, J.; Munter, T.; Moses, P.; Skúlason, E.; Bligaard, T.; Nørskov, J. *Phys. Rev. Lett.* **2007**, *99* (1), 016105.
(11) Doyle, A. D.; Montoya, J. H.; Vojvodic, A. *ChemCatChem* **2015**, *94025*, 738.
(12) Reier, T.; Oezaslan, M.; Strasser, P. *ACS Catal.* **2012**, *2* (8), 1765.
(13) Halck, N. B.; Petrykin, V.; Krtil, P.; Rossmeisl, J. *Phys. Chem. Chem. Phys.* **2014**, *16*, 13682.
(14) Petrykin, V.; Macounová, K.; Okube, M.; Mukerjee, S.; Krtil, P. *Catal. Today* **2013**, *202*, 63.
(15) Macounová, K.; Jirkovský, J.; Makarova, M. V.; Franc, J.; Krtil, P. *J. Solid State Electrochem.* **2009**, *13* (6), 959.
(16) Frydendal, R.; Paoli, E. A.; Chorkendorff, I.; Rossmeisl, J.; Stephens, I. E. L. *Adv. Energy Mater.* **2015**, *n/a*.
(17) Trotochaud, L.; Young, S. L.; Ranney, J. K.; Boettcher, S. W. *J. Am. Chem. Soc.* **2014**, *136* (18), 6744.
(18) Friebel, D.; Louie, M. W.; Bajdich, M.; Sanwald, K. E.; Cai, Y.; Wise, A. M.; Cheng, M.-J.; Sokaras, D.; Weng, T.-C.; Alonso-Mori, R.; Davis, R. C.; Bargar, J. R.; Nørskov, J. K.; Nilsson, A.; Bell, A. T. *J. Am. Chem. Soc.* **2015**, *137* (3), 1305.
(19) Song, F.; Hu, X. *Nat. Commun.* **2014**, *5* (4477), 1.
(20) Gorlin, Y.; Jaramillo, T. F. *J. Am. Chem. Soc.* **2010**, *132* (39), 13612.
(21) Dau, H.; Limberg, C.; Reier, T.; Risch, M.; Roggan, S.; Strasser, P. *ChemCatChem* **2010**, *2* (7), 724.
(22) Jiao, F.; Frei, H. *Angew. Chemie* **2009**, *48*, 1841.
(23) Suntivich, J.; May, K. J.; Gasteiger, H. A.; Goodenough, J. B.; Shao-Horn, Y. *Science (80-.).* **2011**, *334* (6061), 1383.
(24) Grimaud, A.; May, K. J.; Carlton, C. E.; Lee, Y.-L.; Risch, M.; Hong, W. T.; Zhou, J.; Shao-Horn, Y. *Nat. Commun.* **2013**, *4* (May), 2439.
(25) Mette, K.; Bergmann, A.; Tessonnier, J.-P.; Hävecker, M.; Yao, L.; Ressler, T.; Schlögl, R.; Strasser, P.; Behrens, M. *ChemCatChem* **2012**, *4* (6), 851.
(26) Nocera, D. G. *Acc. Chem. Res.* **2012**, *45* (5), 767.
(27) Rosen, J.; Hutchings, G. S.; Jiao, F. *J. Am. Chem. Soc.* **2013**, *135*, 4516.
(28) Hong, W. T.; Risch, M.; Stoerzinger, K. A.; Grimaud, A.; Suntivich, J.; Shao-Horn, Y. *Energy Environ. Sci.* **2015**, *8* (5), 1404.
(29) Gorlin, Y.; Chung, C.-J.; Benck, J. D.; Nordlund, D.; Seitz, L.; Weng, T.-C.; Sokaras, D.; Clemens, B. M.; Jaramillo, T. F. *J. Am. Chem. Soc.* **2014**, *136* (13), 4920.
(30) Frydendal, R.; Busch, M.; Halck, N. B.; Paoli, E. a.; Krtil, P.; Chorkendorff, I.; Rossmeisl, J. *ChemCatChem* **2015**, *7* (1), 149.
(31) Lu, X.; Ng, Y. H.; Zhao, C. *ChemSusChem* **2014**, *7* (1), 82.
(32) Yeo, B. S.; Bell, A. T. *J. Am. Chem. Soc.* **2011**, *133* (14), 5587.

(33) Kuo, C.; Li, W.; Pahalagedara, L.; El-Sawy, A. M.; Kriz, D.; Genz, N.; Guild, C.; Ressler, T.; Suib, S. L.; He, J. *Angew. Chemie Int. Ed.* **2014**, *127*, 2375.
(34) El-Deab, M. S.; Awad, M. I.; Mohammad, A. M.; Ohsaka, T. *Electrochem. commun.* **2007**, *9* (8), 2082.
(35) Yeo, B. S.; Bell, A. T. *J. Phys. Chem. C* **2012**, *116* (15), 8394.
(36) Su, H.-Y.; Gorlin, Y.; Man, I. C.; Calle-Vallejo, F.; Nørskov, J. K.; Jaramillo, F.; Rossmeisl, J. *Phys. Chem. Chem. Phys.* **2012**, *14* (40), 14010.
(37) Pourbaix, M. *Atlas of Electrochemical Equilibria in Aqueous Solutions*, 1st ed.; Pergamon Press, 1966.
(38) Frydendal, R.; Paoli, E. A.; Knudsen, B. P.; Wickman, B.; Malacrida, P.; Stephens, I. E. L.; Chorkendorff, I. *ChemElectroChem* **2014**, *1* (12), 2075.
(39) Gorlin, Y.; Lassalle-Kaiser, B.; Benck, J. D.; Gul, S.; Webb, S. M.; Yachandra, V. K.; Yano, J.; Jaramillo, T. F. *J. Am. Chem. Soc.* **2013**, *135*, 8525.
(40) Di Castro, V.; Polzonetti, G. *J. Electron Spectros. Relat. Phenomena* **1989**, *48* (1), 117.
(41) Langford, J.I. and Wilson, A. J. C. *J. Appl. Crystallogr.* **1978**, *11*, 102.
(42) Walter, M. G.; Warren, E. L.; McKone, J. R.; Boettcher, S. W.; Mi, Q.; Santori, E. A.; Lewis, N. S. *Chem. Rev.* **2010**, *110* (11), 6446.
(43) McCrory, C. C. L.; Jung, S.; Peters, J. C.; Jaramillo, T. F. *J. Am. Chem. Soc.* **2013**, *135* (45), 16977.
(44) Jiao, F.; Frei, H. *Chem. Commun.* **2010**, *46* (17), 2920.
(45) Farges, F. *Phys. Rev. B - Condens. Matter Mater. Phys.* **2005**, *71* (15), 1.
(46) Manceau, A.; Marcus, M. A.; Grangeon, S. *Am. Mineral.* **2012**, *97* (5-6), 816.
(47) Weng, T. C.; Hsieh, W. Y.; Uffelman, E. S.; Gordon-Wylie, S. W.; Collins, T. J.; Pecoraro, V. L.; Penner-Hahn, J. E. *J. Am. Chem. Soc.* **2004**, *126* (26), 8070.
(48) Haider, P.; Grunwaldt, J. D.; Seidel, R.; Baiker, A. *J. Catal.* **2007**, *250* (2), 313.
(49) Konishi, Y.; Tsukiyama, T.; Saitoh, N.; Nomura, T.; Nagamine, S.; Takahashi, Y.; Uruga, T. *J. Biosci. Bioeng.* **2007**, *103* (6), 568.
(50) Perez-Alonso, F. J.; McCarthy, D. N.; Nierhoff, A.; Hernandez-Fernandez, P.; Strebel, C.; Stephens, I. E. L.; Nielsen, J. H.; Chorkendorff, I. *Angew. Chem. Int. Ed. Engl.* **2012**, *51* (19), 4641.
(51) Brodersen, S. H.; Grønbjerg, U.; Hvolbæk, B.; Schiøtz, J. *J. Catal.* **2011**, *284* (1), 34.
(52) Greeley, J.; Rossmeisl, J.; Hellman, A.; Nørskov, J. K. *Zeitschrift für Phys. Chemie* **2007**, *221* (9-10), 1209.

DRAFT VERSION

Supporting Information

In-situ investigation of Au-MnO_x thin films with improved activity for the oxygen evolution reaction

Rasmus Frydendal,[a] Linsey Seitz,[b] Dimosthenis Sokaras,[c] Tsu-Chien Weng,[c] Dennis Nordlund,[c] Ib Chorkendorff,[a] Ifan E.L. Stephens,[a] Thomas F. Jaramillo,[b,c]

[a] Center for Individual Nanoparticle Functionality, Department of Physics, Building 312, Technical University of Denmark, DK-2800 Kgs. Lyngby, Denmark

[b] Department of Chemical Engineering, Stanford University, Stanford, California 94305, United States

[c] SLAC National Accelerator Laboratory, 2575 Sand Hill Road, Menlo Park, California 94025, United States

X-ray Photoelectron Spectroscopy

The films were characterized for elemental composition with X-ray Photoelectron Spectroscopy, using the Mn2p, Au4d and O1s peaks, as seen in figure 1a,c and d. Due to adventitious carbon it is difficult to assess the Mn:O stoichiometry which was instead evaluated from Mn2p½ satellite distance and Mn3s,[1,2] shown in figure 1b, multiplet splitting. The Au concentration used for denoting the samples are based on total metal basis, so that 30 % means that Au/(Au+Mn) corresponds to 30 %:

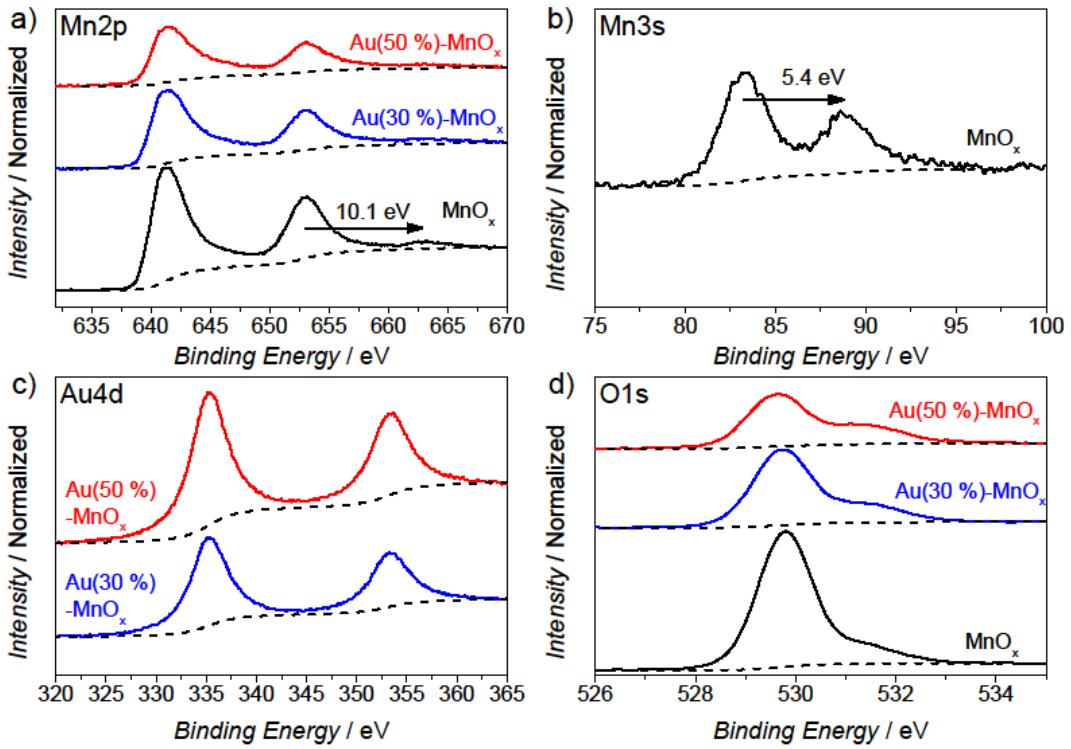

Figure 1: X-ray Photoelectron Spectroscopy for the thin films. Pure MnO_x film is shown in black, Au(30%)-MnO_x is shown in blue and Au(50%)-MnO_x is shown in red. a) Mn2p. b) Mn3s. c) Au4d. d) O1s.

Domain size estimation from the Scherrer equation

The Scherrer equation relates the size of crystallites, τ, to the broadening (after instrumental line broadening is subtracted), *B*, of peaks seen in X-ray Diffraction with the following expression:[3]

$$\tau = \frac{K\lambda}{B\cos\theta}$$

where *K* is a dimensionless shape factor, λ is the wavelength and θ is the Bragg angle. There are multiple other factors beyond crystallite size that can affect the peak broadening which is why the estimations should be considered tentative. It should be noted that the instrumental peak broadening are taken into account for the estimations here. The instrumental peak broadening was measured as a function of the Bragg angle with a Si powder reference. The Scherrer calculator in HighScore Plus from PANalytical.[4] The peak broadening was estimated from three Au peaks: (111), (220) and (113). The three broadenings lead to average crystallite sizes of 1.9±0.2 and 2.8±0.3 nm. Due to the inaccuracy of the method, the sizes are shown as 2 and 3 nm, respectively.

Model for estimation of Mn-Au sites

The number of sites with Mn and Au in close vicinity could have a strong impact on the activity. For the two concentrations of Au in MnO_x it is therefore interesting to estimate this number. For Au(30%)-MnO_x we will assume that spherical 2 nm particles are half immersed and dispersed on a flat Mn_3O_4 surface, so that the Au particles never touch each other. For Au(50%)-MnO_x the same assumptions are made but for 3 nm particles. The ratios found from XPS will be used to evaluate the gold surface area. In this way the maximum circumference, *C*, of the particles are in contact with the oxide while accessible for the electrolyte. The total circumference, C_{tot}, of all gold particles present at the surface is therefore proportional to the number of Mn-Au sites. Then the ratio between the total circumference for Au(50%)-MnO_x and Au(30%)-MnO_x is a measure of the difference in interacting sites for the two concentrations. This ratio can be written as:

$$\frac{C_{tot,50\%}}{C_{tot,30\%}} = \frac{\frac{A_{tot} \cdot Au_{XPS,50\%}}{\pi(\frac{3nm}{2})^2}\pi \cdot 3nm}{\frac{A_{tot} \cdot Au_{XPS,30\%}}{\pi(\frac{2nm}{2})^2}\pi \cdot 2nm} = \frac{3 \cdot Au_{XPS,50\%}}{2 \cdot (1.5)^2 Au_{XPS,30\%}} \approx 1.3$$

Where A_{tot} is total area, $Au_{XPS,50\%}$ is the ratio of Au from XPS measurements and 3 or 2 nm comes from the domain size estimations from using the Scherrer equation as described above. For cube shaped particles the result is the same. From this model it is therefore estimated that the samples with 50 % gold has 1.3 times as many Mn-Au sites as the sample with 30 %. This difference is not enough to explain a factor 3 difference in current density. If the gold particles are allowed to touch other gold particles the ratio will instead be close to 1.1 and the difference is therefore lower.